SOUND INSULATION OF BRICK DIAPHRAGM WALLS

Thesis submitted in accordance with the requirements of the University of Liverpool for the degree of Doctor of Philosophy by

RORY DANIEL SULLIVAN

April 1994

VOLUME CONTAINS CLEAR OVERLAYS

OVERLAYS HAVE BEEN SCANNED SEPERATELY AND THEN AGAIN OVER THE RELEVANT PAGE

ANY MAPS, PAGES, TABLES, FIGURES, GRAPHS OR PHOTOGRAPHS, MISSING FROM THIS DIGITAL COPY, HAVE BEEN EXCLUDED AT THE REQUEST OF THE UNIVERSITY

DAMAGED TEXT IN ORIGINAL

PAGE NUMBERING AS ORIGINAL

To Julie
&
my parents

SUMMARY

Diaphragm wall constructions are increasingly used for tall single storey buildings such as sports halls and warehouses, but their acoustic qualities have not previously been considered and hence their use for noise sensitive buildings such as theatres and studios. This study examines the sound insulation characteristics of such constructions.

1:8 scale models of single, fin and diaphragm walls were built and their transmission loss was measured in a small transmission suite by the standard ISO 140/3 method and by non-standard sound intensimetry. The latter was later used for field measurements. The measured transmission loss curves showed that a loss in sound insulation occurs below the leaf critical frequency, producing a plateau, the frequency width of which increases as the wall is stiffened.

Prediction using existing isotropic wall theory fitted well for the single wall. Fin wall performance can also be predicted by modifying simple theory to include a second bending stiffness along the ribs and thus a second lower critical frequency. Interpolation between the two critical frequencies approximates the required plateau region. Simple theory could not be modified for the diaphragm wall due to the complicated bridging effect.

Transmission of energy between the leaves of the diaphragm wall was examined. Existing impedance models used to describe such transmission are found inapplicable. Wave analysis compared a 'bending wave only' model with an 'all wave type' analytical model for transmission between cross-rib and leaf, showing the former to give results to within ± 2 dB over the building acoustics frequency range. Due to the width of the cross-rib, resonances were shown possible between leaves, but were not observed in measurement.

To better analyse the diaphragm wall a Statistical Energy Analysis (SEA) approach was used. This allowed consideration of the wall's radiation resistance, cavity path and the effect of variations in the geometric and the material characteristics of the cross-rib and leaves. It is shown that energy transmission between leaves is dominated by the large number of cross-ribs and the cavity path can be neglected for frequencies up to 1250 Hz. The agreement between measurement and theory was acceptable.

Field measurements of the transmission loss of in-situ diaphragm walls were carried out using sound intensimetry. These were successful only on internal walls where flanking transmission was negligible. SEA prediction also fitted well for these walls.

Using a parametric approach it is shown that SEA predicts a typical transmission loss rating for the diaphragm wall of between 52 - 56 dB. Variations in material and geometry alter the transmission loss by no more than 2 dB. Where one leaf is theoretically de-coupled from the rest of the wall higher sound insulation can be obtained, but it is then necessary to include the cavity path.

ACKNOWLEDGEMENTS

Throughout this thesis many people have aided me in my endeavours. My most grateful thanks go to Dr. Barry M. Gibbs, my supervisor, who has encouraged, persuaded and taught me much more than any written text could do. My thanks also to Mr. Garry Seiffert without whom few experiments would have ran as smoothly, and to all the other members of the Acoustic Research Unit who have made my time here particularly enjoyable and interesting; including Dr. John Goodchild, Dr. Andrew Moorehouse, Dr. Richard Lyons, Mr. Ross Fulford, Mr. Hussein Akil, Prof. David Oldham and Dr. Philip Banfill.

This work could not have been as thoroughly carried out without the help of the schools, leisure centres, council departments and consultants who allowed me access to buildings, drawings and details. Particularly I would like to thank the Richard Ellis partnership and John Lewis.

Especially I would like to thank my wife who listened to my grumbles and whose support, encouragement and patience was endless (and needed to be)!

The financial support of the Science & Engineering Research Council and the Brick Development Association is gratefully appreciated, without which this research could not have been undertaken.

Finally I thank God who has watched over me, cared for me and kept me on track.

"No temptation has overtaken you that is not common to man. God is faithful, and he will not let you be tempted beyond your strength, but with the temptation will also provide the way of escape, that you may be able to endure it."
1 Corinthians Ch. 10 v 13.

CONTENTS

FIGURES

TABLES

SYMBOLS

A	total sound absorption, area
a	acceleration
B	bending stiffness
b	width of an element, spacing of line connectors
c	speed of sound in a medium (air = 344 m/s)
c_L	longitudinal wave speed
c_b	bending wave speed
c_s	shear wave speed
C	field non-uniformity constant
d	depth of an element, width of cavity
D-	ANSI S12.12-199X draft standard field indicators
E	energy in a sub-system, Young's modulus
f	frequency (Hz)
f_0	mass-spring-mass resonance frequency (lower London frequency)
f_b	bridging frequency
$f_{90°}$	upper London frequency
f_{res} or f_d	frequency of first cross-cavity resonance ($f_d = c / 2*d$)
f_l	limiting frequency
f_c	critical frequency
$f_{c,u}$	upper critical frequency
$f_{c,l}$	lower critical frequency
f_{cut}	Shroedor cut-off frequency
f_{11}	frequency of first resonant mode
F-	ISO/DIS 9614-1draft standard field indicators
F	force
G	shear modulus
G_{ab}	cross spectrum between the two channel spectrums

Hz	cycles per second
h	thickness
H	cross-spectral density
I	sound intensity, current
$\bar{I}$	average sound intensity
Im	imaginary part of the complex function
I_n	normal incidence sound intensity
I_o	reference sound intensity (10^{-12} Wm^{-2})
I_x	one-sided intensity
I_{xx}	moment of inertia along the x-axis
I_{in}	one directional intensity upon the panel
I_{out}	one directional intensity out from the panel
j	complex component ($\sqrt{-1}$)
k	wave number, stiffness
l, L	length of wall or total room edge length
L.d.	level difference
L_p	time and spatial-averaged sound pressure level
L_i	time and spatial averaged sound intensity level normal to the area under test
$L_{k,o}$	residual pressure-intensity index
$L_{p,o}$	sound pressure level at normal incident intensity in the calibrator
$L_{I,o}$	sound intensity level at normal incident intensity in the calibrator
$\bar{L}_I$	mean intensity level
$\bar{L}_{\|I\|}$	mean intensity level from the modulus of the intensities
L_k	is the reactivity index
$L_{i,r}$	residual intensity index
Ld	dynamic capability
$L_{eq,T}$	equivalent continuous sound pressure level of a time period T.
m	surface density (Kg/m^2)

M	total mass, moment
M_o	modal density
n	integer value
N	mode count, number of measurement locations
n_r	modal density of a room
n_w	modal density of a wall
p	sound pressure
Pa	sound pressure: Channel A
Pb	sound pressure: Channel B
p(t)	instantaneous sound pressure at a point.
P	sound pressure amplitude
p^2_{rms}	mean square pressure of a room
P-I index	pressure-intensity index or reactivity index
R	mass resistance term
R_{rad}	radiation resistance
R_w	single figure rating
r	resistance coefficient, radius of gyration
Re	real part of a complex function
S	surface area
T	reverberation time, integrated time period
t	transmissibility, time
TL	transmission loss
$\bar{u}(t)$	instantaneous particle velocity at the same point.
u	particle velocity
V	volume
v_{rms}	velocity (root mean squared)
W	sound power
Y	mobility
Z	impedance

α	surface absorption
Δf	width of mode at half power
Δp	pressure gradient between the two microphones (Pa - Pb)
Δr	separation distance of the microphones.
df	distance between modes
Φ	phase
γ_{ir}	transmission coefficient between the ith and rth sub-systems
$\bar{\gamma}$	angle average transmission coefficient
η	loss factor
η_{ir}	coupling loss factor from ith to rth sub-system
η_i	internal loss factor of ith sub-system
η_{nr}	non-resonant coupling loss factor
λ	wavelength
λ_c	wavelength at critical frequency
λ_a	acoustic wavelength
π	pi (= 3.141592654)
θ	oblique angle, temperature
ρ	density of air (1.19 Kg/m^3)
ρ_c	material density
σ	poisson ratio (0.3 for most building elements)
$\sigma_{rad}^{2\pi}$	radiation efficiency into half space
τ	transmission coefficient
τ_s	transmission across stud
τ_a	transmission across air cavity
$\bar{\tau}$	average transmission coefficient
ω	angular frequency
χ, φ	junction relationship expressions
Π	power flow

Subscripts

b	bending wave energy, bridging path
b/g	background
c	critical
corr	correction factor
eff	effective
eq	equivalent
f	field incidence
i	incident component, ith sub-system
l	longitudinal wave energy
m	mass, model
ort	orthotropic
r	reflected component, random incidence, room, rth sub-system
rw	room-to-wall
s	transverse shear wave energy
t	transmitted component
w	wall
wr	wall-to-room
x,y,z	co-ordinate direction
0 or n	normal incidence
1, 2 etc.	element numbers

1 INTRODUCTION

1.1 INTRODUCTION

The purpose of this study was to examine the sound insulation characteristics of a particular type of wall construction known as the 'Diaphragm Wall.'

The diaphragm wall is an all masonry construction developed over the past 20 years and increasingly used in the U.K for tall single storey buildings. At present it is a popular alternative to steel frame cladding systems, commonly used for sports centres or factory units, offering advantages in terms of structure, construction and cost. To date there has been no comprehensive study of the sound insulation properties of the construction and it has simply been assumed to be equivalent to or better than a traditional double wall.

The wall consists of two widely spaced leaves, typically 0.35 m apart, which are bridged at regular intervals by vertical cross-ribs, typically at 1.25 m centres. Figure 1.1 shows the general layout of a diaphragm wall. Traditional cavity brick constructions can be built to a height of 3 - 4 m if lightly pre-stressed, while diaphragm and fin walls are commonly between 7 - 10 m high. In terms of sound insulation it might be assumed that compared with a double wall, the wide spacing of the leaves is beneficial, but the acoustic coupling through the cross-ribs is detrimental.

Community noise problems exist when there is excessive sound transmission between connected buildings or between the external environment and a building. The building fabric, including walls, roof, windows etc., plays a key role in reducing the noise level between source and receiver. The sound insulation of each element is normally characterised by its 'transmission loss', defined as the ratio of

sound energy emitted by a surface to that of the sound energy incident on its other side.

At present, the diaphragm wall has been used for purposes where noise, generated either internally or externally, is not a significant issue. It was the intention of the author, in response to the wishes of the sponsors of the research, the Brick Development Association (B.D.A.), to explore the sound insulating character of the wall, determine its transmission loss and propose improvements to its performance. The construction may then be used in noise sensitive areas such as sound studios, theatres, cinemas etc., or anywhere there is a design criteria for sound insulation.

It will be seen that the diaphragm wall is a hybrid masonry construction which relates little to commonly examined walls types such as single walls, double walls and double walls bridged by point or line connections. Initially it might be thought that the diaphragm wall, because of its geometry, relates to the latter wall type, but these normally relate to conventional cavity walls or lightweight stud partitions. Hence detailed analysis was necessary to determine the transmission loss of the wall in terms of theoretical prediction as well as model and field measurement. Sound insulation measurements of in-situ heavyweight facades have always been problematic and therefore the non-standard technique of sound intensimetry was used as a more effective measurement method.

1.2 BACKGROUND TO THE DIAPHRAGM WALL

The common approach to the enclosure of large spaces is by composite material constructions using for example, a steel portal frame with infill walls. These are typically of a primary frame of steel columns and beams, strengthened by cross struts at corners against lateral loading and purlins for the fixture of large cladding panels. Construction of this type of environmental envelope requires the co-ordination of

several trades on site and a high degree of manufacture and construction accuracy is required at joints, particularly between different materials. Human error can often lead to a poor weather tightness of the structure with increased costs for rectification.

The diaphragm wall typically uses only 10 % more masonry than a cavity wall but will be many times stronger, allowing it to be built to greater heights. As the diaphragm wall is an all-masonry construction it requires only one trade on site to erect the walls between foundation and roof, which gives reduced co-ordination problems leading to cost savings. There will also be savings from less returns to site for alterations as the problems of dimensional tolerance between different materials is almost eliminated. An all-masonry envelope, compared with composite constructions, are also more durable with respect to the problems of degradation from moisture penetration and ultra-violet radiation.

Most research to date has concentrated on the structural behaviour of the wall. W.G. Curtin first proposed the diaphragm wall and at present there are at least a few thousand diaphragm walls built in the U.K. Many good examples are in the North West designed by Curtin & Partners, including churches and as earth-retaining walls [1]. Curtin admits the concept of the diaphragm wall came about by accident while designing a large school with load-bearing brickwork walls, where an internal and external plane surface was required. At the time this was thought only possible by building an uneconomically thick wall. A double leaf piered wall was considered with the piers placed internally, see figure 1.2. It remained to reduce the width of the piers and to link to the second leaf, so forming a construction which could be described as a series of box or I-sections [2]. Figure 1.3 gives the range in cross-rib centres and cavity widths, which vary in steps of half bricks for ease of construction. Many diaphragm walls have since been built by Curtin and others, allowing architects to express the structure by variations in design [1]. Significant research into the structural characteristics were carried out in 1978 at Liverpool University by

Curtin [3], followed by a series of papers [4, 5]. The Brick Development Association has sponsored and published much of this research in a booklet [1].

1.3 DETAILS OF THE DIAPHRAGM WALL

Figures 1.1 - 1.7 give general details for the diaphragm wall. The internal width between leaves varies from 1 - 3 bricks and spacing between cross-ribs from 4 - 7 bricks, including mortar, see figure 1.3. To ensure a stiff structural construction between leaves and cross-ribs the bonding must be correct. This is either bonding with interlocking full or three-quarter bricks, or with metal ties to one or both leaves. In the latter case care must be taken with more stringent site checking, which will give a stretcher bond appearance to the leaves [13]. Flat fishtail or equivalent shear ties should be used, but not butterfly ties, and these must be embedded to at least 50 mm. The brick types for the cross-rib and leaf are usually similar, but not necessarily identical in material character to avoid cracking along joints. Tying the cross-rib and leaf allows for greater differential movement, while the use of concrete blocks in the cross-ribs, will increase the vibrational impedance mis-match between leaves, but can cause difficulties in tying. The spacing of ties is important, varying with height between 1 to 4 course spacing. Closer spacing is required at the base of the wall where shear stresses are highest and wider cross-ribs can even accommodate double ties, see figure 1.4.

The roof loads are carried by a concrete capping or ring beam around the top of the wall, which transfers the loads to the wall. This beam may be designed to be hidden within the leaves, or exposed either internally, externally or both. Ring beams may be built at lower levels or on a thickened inner leaf to carry or fix equipment, i.e. a crane arm in a machine room. Figures 1.5a and 1.5b show two solutions. The void between leaves can be designed for greater architectural expression, i.e. to form alcoves or can be utilised for building services. Extra or thicker ribs may be built to

carry lintels over wide openings, or where construction joints are required, see figure 1.1. Between foundation level and the ground level the diaphragm wall will be filled for drainage and to add stability to the wall, see figure 1.6. The thermal insulation of the wall can be improved by the fixing of rigid insulation batts against the inner leaf, see figure 1.7.

A possible problem is that of moisture penetration to the inner leaves across the ribs. Research by the London Brick Company [14] showed that there was very little penetration to the inner leaf under conditions equivalent to a week of severe driving rain. Preventative measures should be applied where walls are less than 450 mm thick, or cross-ribs are constructed of calcium silicate or concrete block. One common measure is to paint a vertical DPM (Damp Proof Membrane) onto the internal surface of the external wall along the line of the cross-ribs before tying the ribs into the leaf. Vents can be also used to evaporate water passing through the wall.

1.3.1 Load-bearing masonry

The advantage of brickwork over other building elements is in its ability to satisfy several requirements simultaneously, providing structure, a sub-division of space, thermal and acoustic insulation as well as fire and weather protection [7]. Load-bearing brickwork is used in structures where there is a regular sub-division such as in flats, hotels and residential buildings, so that no one area need carry unduly heavy concentrated loads. Vertical load-bearing walls are generally cavity or one brick thick walls. Diaphragm or fin walls (introduced later), used for tall single storey constructions, are unique and do not fit easily into the traditional load-bearing masonry categories.

Masonry brickwork varies in its properties (frost resistance, soluble salt content, water absorption, compressive strength) and designs (cellular, frogged, solid,

perforated, pressed). Three categories broadly separate a brick's usage: 'common bricks' for general building work, 'facing bricks' where a standard of surface finish is required and 'engineering bricks' which have higher compressive strength and lower water absorption. Most bricks have a dry density between 1680 - 1940 kg/m^3, and Engineering bricks between 1980 - 2340 kg/m^3. When saturated the brick density will increase by typically 10% [8]. Load-bearing brickwork can range from 5 - 100 N/mm^2, while engineering bricks will have higher densities. The brickwork density assumed for a diaphragm wall, including mortar, where no details are known is assumed as 1850 Kg/m^2. Details on load bearing brickwork are given by BS 5628 [9] and CP111 [10].

1.4 DETAILS OF THE FIN WALL

The masonry fin wall can be thought of as the 'brother' of the diaphragm wall, developed for greater architectural expression. The external leaf is a series of T-sections alike the diaphragm wall but without a second leaf and at wider centres. The inner leaf is tied to the outer leaf like a traditional cavity wall [6]. Figure 1.8 shows the general details. The wall is used on similar structures to the diaphragm wall, with the fins allowing the wall to be built to similar heights. Fins are built on the external facade to maximise the internal space and to add a feature. The fin wall has greater moments of inertia, radius of gyration and section modulus than a tradition cavity construction but less than a diaphragm wall. The structural stability of the wall and its resistance to vertical and lateral loadings is given by the fin, built at typical centres of 3.6 - 3.8 m.

Fin walls are not the key interest of this thesis, but are included as the external leaf of the wall is in essence a diaphragm wall with a leaf missing and therefore is the linking step from a single wall to a diaphragm wall. (Thus no inner leaf is included in the models built). Fin walls modelled in this study are used for the purpose of

understanding the diaphragm wall and therefore the distance between fins are at centres typical for a diaphragm wall rather than a fin wall.

1.5 CONCRETE & PRE-STRESSED CONSTRUCTIONS

The key problem with high single storey structures is the ability to withstand lateral loadings, predominantly wind loads. The performance of diaphragm walls has been improved by post-tensioning. Diaphragm walls have also been designed in concrete blockwork, hollow, infilled and pre-stressed forms. This work is published in booklets by the A.C.B.A. [15, 16]. Different bonding patterns are possible using concrete blocks (100 mm thick x 440 mm wide) and single ties may travel across both leaves, producing different rib centres, mechanical connections and stresses. Figure 1.9 illustrates some bonding and tying patterns [15]. Pre-stressing can significantly benefit a diaphragm wall and its wide cavity is ideal for a post-tensioning system of unbonded vertical bars. A.C.B.A. show that pre-stressing of just 1.5N/mm^2 can increase the walls strength against lateral loading by seven times. Further pre-stressing can eliminate any tensile stress on the leaves and avoid cracking. Figure 1.10 illustrates this method [16].

1.6 APPROACH TO THE RESEARCH

Aims:

The objectives of the thesis are to determine the sound insulation characteristics of the diaphragm wall, to define its typical transmission loss, to show the present range in transmission loss and that possible through optimisation. Sound intensimetry is examined as both a laboratory and field measurement technique for transmission loss of high insulation elements and facades.

Chapter 1:

This chapter introduces the reader to the diaphragm wall. The wall is shown to be a significantly different design to traditional wall constructions. The history of the wall is described as well as its present uses and benefits compared with composite structures. Its structural characteristics are described and its similarities to a complimentary construction type, the fin wall. It is shown that, at the time this research programme commenced there was little knowledge relating to the sound insulation qualities of diaphragm walls. The present study is aimed to benefit future constructions with regard to acoustic design and thus lead to a possible expansion in building applications.

Chapter 2:

Presently available theories for traditional wall constructions are considered for the prediction of transmission loss of diaphragm walls. It is found that no existing theory directly applies for the case of a heavyweight construction with regular cross-ribs of similar materials to the leaves. It is suggested that a new theory may be developed from present theory. Therefore theories for single, double and double bridged walls are reviewed and their suitability discussed.

Chapter 3:

To validate theory for the diaphragm wall, measurement of the construction is required. In-situ field measurement is difficult, with numerous problems, such as flanking transmission and background noise; while the existing measurement method, ISO 140/5, is only suitable for lower insulation elements. The structure is too large to be adequately represented in a standard laboratory facility and the construction and re-construction of such large walls would be both costly and time consuming. Therefore model walls are used, which were built and tested in a small transmission suite according to the standard ISO 140/3 laboratory measurement procedure for transmission loss. The model walls had the advantage that they could be tested, rebuilt and re-tested. These walls were geometric models of roughly 1:8 scale and allowed the diaphragm wall to be examined by components. Hence, a single wall, a ribbed single wall (fin wall) and a diaphragm wall could be investigated, as well as the affect of altering the walls bending stiffness. The full scale frequency range of interest was 50 Hz - 2 kHz, at 1:8 scale this was equivalent to 400 Hz - 16 kHz. The standard ISO 140/3 [67] method was unreliable for the test suite available as it suffered from significant flanking transmission. Therefore a different measurement approach was applied in chapter 4. Measurements of transmission loss for a 1:4 scale diaphragm wall were also available from two dissertations produced in 1982 and 1986.

Chapter 4:

A laboratory measurement method was required which would not be influenced by flanking energy radiating from the receiver room walls and would allow measurement up to 16 kHz. Sound intensimetry was found to satisfy both requirements. For the measurement of transmission loss the approach is non-standard; at present only standards [90] and draft standards [91 - 93] relating to sound power measurements exist, though many papers and discussion documents relating to transmission loss measurements have been published. Re-measurements of almost all model walls were possible, using scanning and discrete point

techniques. The reliability of the measurement method was evaluated using a series of 'field indicator' tests. The sound intensimetry approach also offered the possibility of an improved method of field measurement, which was attempted later.

Chapters 5:

Chapters 5 and 6 consider the acoustic character of the diaphragm wall in two parts. Chapter 5 principally considers the acoustic effect of ribbing on an isotropic panel. The concept of orthotropicity is introduced and existing theory for single isotropic walls is adapted for the fin wall case. Proposals are given to define the acoustic radiation resistance of an orthotropic wall, and finally the effect of de-coupling the leaves of a diaphragm wall is considered by model measurement.

Chapter 6:

Chapter 6 considers the effect of the ribs as bridges between the leaves of the diaphragm wall. Model and full scale vibrational level difference measurements are examined. Initially prediction is considered using an impedance analysis approach and found inapplicable. Prediction is then considered using a wave analysis approach for 'bending only' and 'bending and in-plane' waves at normal and oblique incidence. Prediction is given of transmission across cross-rib/leaf junctions and also direct transmission between leaves using oblique incidence bending waves, where standing waves are examined. The transmission coefficients obtained are included later in a Statistical Energy Analysis approach, which allows a more sophisticated analysis of the diaphragm wall.

Chapter 7:

Statistical Energy Analysis (SEA) is invoked as an approach which enables the diaphragm wall to be considered as separate sub-elements. This allows examination of the effect of varying material constants for ribs and leaves and of including cavity transmission. Single and fin walls are considered and the effect of orthotropicity is

included using the radiation resistances discussed in Chapter 5. SEA models are described where the cavity path is included and excluded and where the cross-rib is considered as a resonant sub-system or non-resonant path. Measured and predicted vibrational level difference between leaves of scale and full size walls are compared, and similarly for the transmission loss of scale walls.

Chapter 8:

Measurement of the transmission loss of a selection of full scale diaphragm walls was attempted. Sound intensimetry is used due to the presence of significant flanking transmission and as an evaluation of the technique for such measurements. Vibrational level difference measurements on the sports halls and a free-standing wall are also described.

Chapter 9:

The SEA prediction is first compared with the most reliable of the full scale wall transmission loss measurements described in chapter 8. The variation in transmission loss of diaphragm walls resulting from likely changes in material and geometric parameters is predicted. This variation, typical and maximum values are given in terms of a single figure rating according to ISO 717/1 [24]. Finally, optimisation of the walls transmission loss by de-coupling one leaf from the rest of the wall is considered theoretically.

Chapter 10:

The final chapter draws together the key conclusions of the study and offers further related areas of research.

1.7 CONCLUDING REMARKS

The diaphragm wall is an increasing popular masonry wall construction in the U.K and its structural characteristics are well known and well published. As an environmental envelope it has been considered in terms of its thermal properties, water penetration and its aesthetic qualities which are increasingly expressed with each new construction. To date there has been no significant research in to its acoustic properties, indeed assumptions which have been made in trade literature are optimistic. It would seem timely therefore to study this construction with respect to its sound insulation.

To examine the sound insulation of the diaphragm wall the second chapter reviews present theory of sound transmission through single, double and bridged double walls. This is in order to establish if diaphragm walls lie within the range of existing theory.

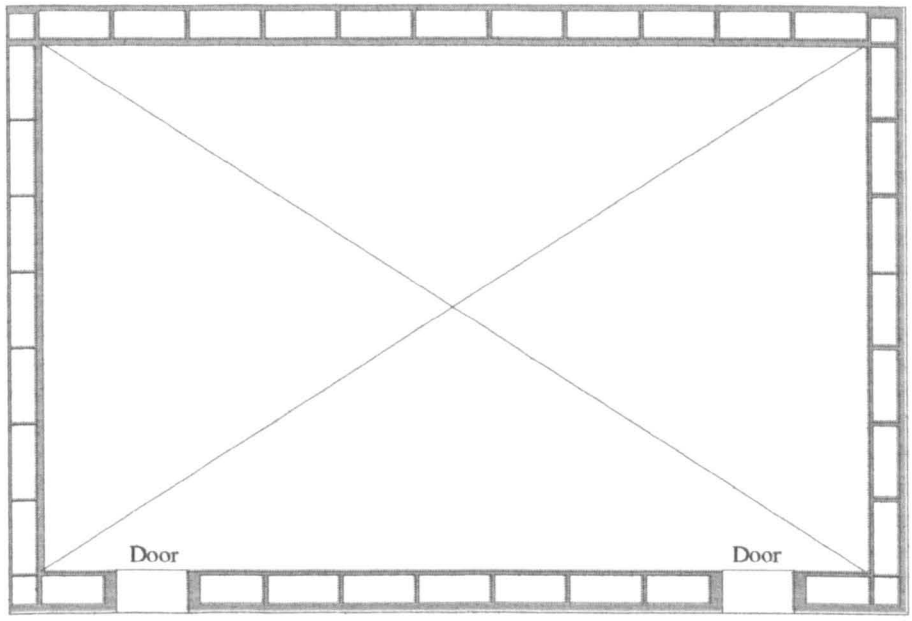

Typical arrangement

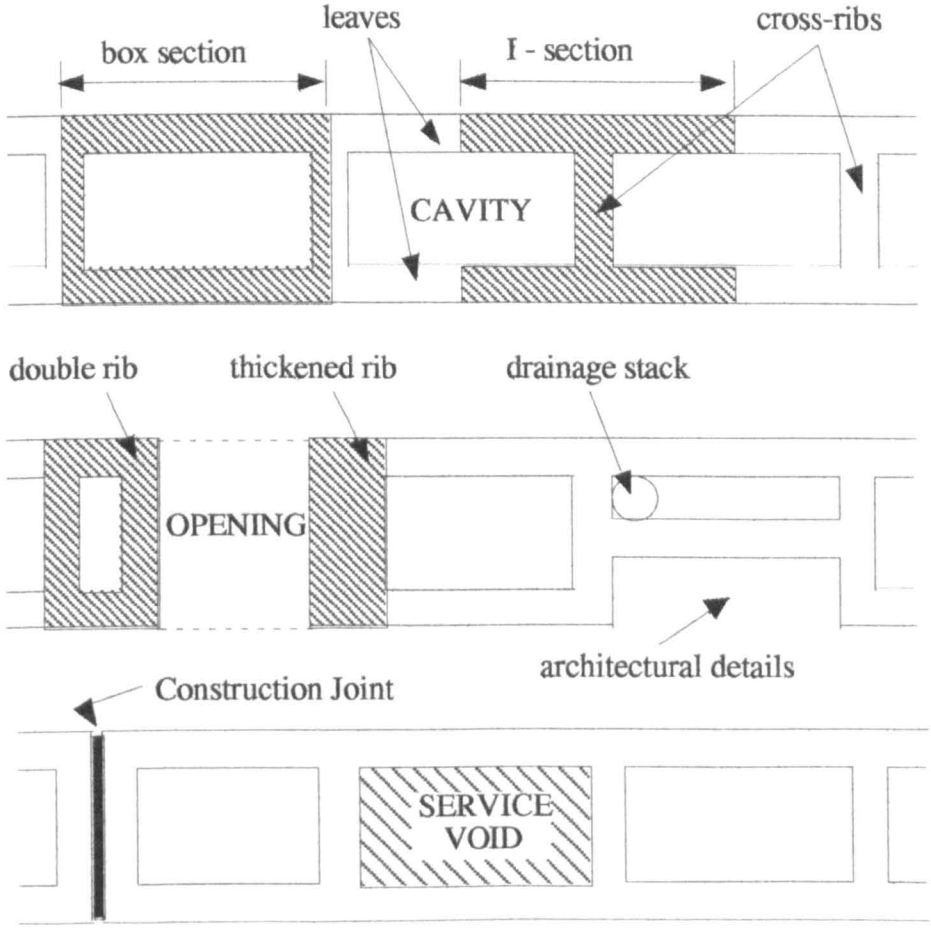

Figure 1.1: General details of the diaphragm wall: plan views

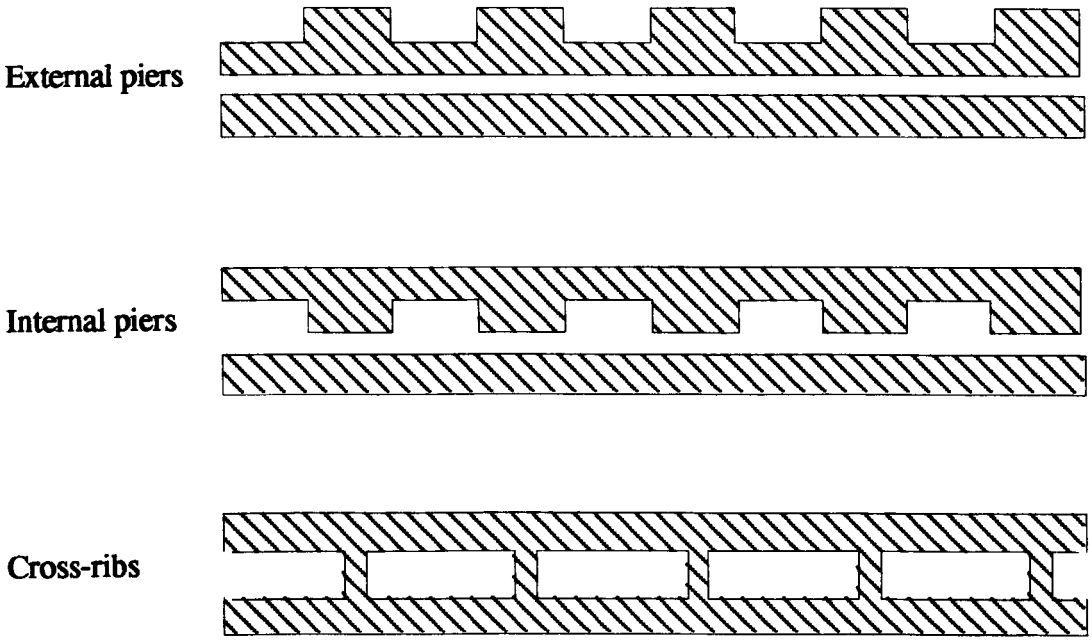

Figure 1.2: Development from piered wall to diaphragm wall

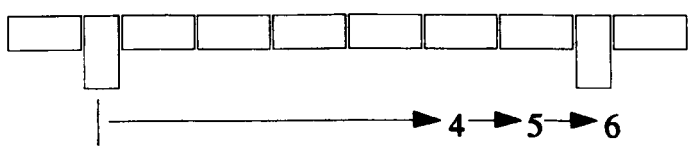

4 bricks wide = (4 x 215mm) + (5 x 10mm) + (2 x 0.5 x 102.5mm) = 1.0125m
bricks mortar half of 2 ribs

5 bricks wide = 1.2375m

6 bricks wide = 1.4625m

Rib centres

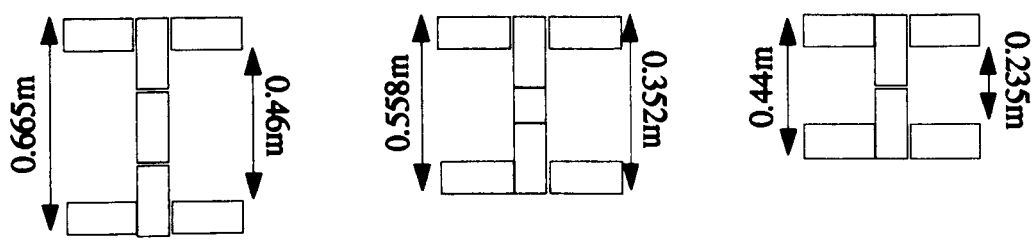

Typical internal leaf spacing: 1 - 3 bricks

Rib width

Figure 1.3: Cross-rib and leaf spacings

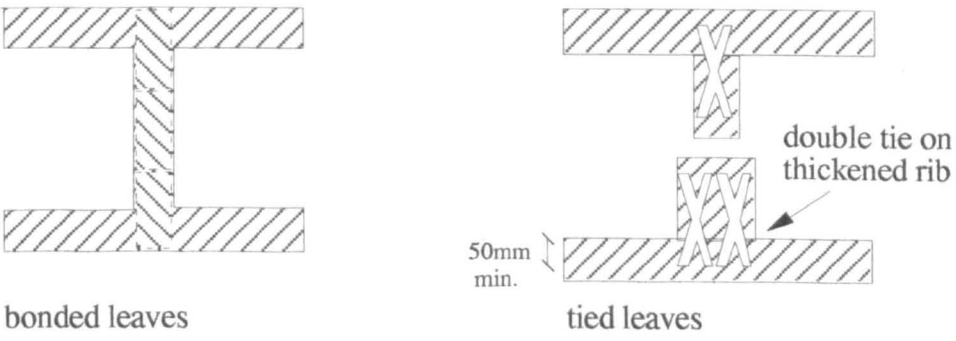

Figure 1.4: Bonding and tying of cross-ribs

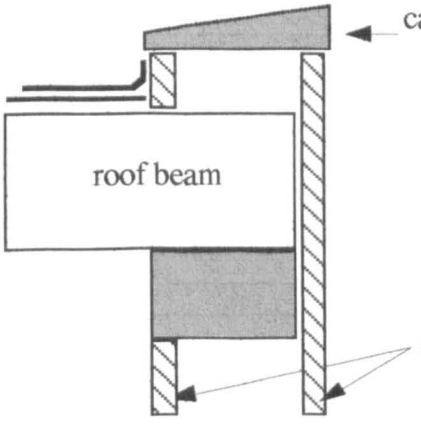

Figure 1.5a: Example 1 of capping beam

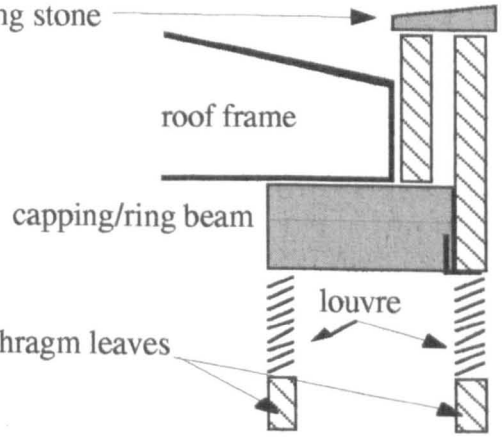

Figure 1.5b: Example 2 of capping beam

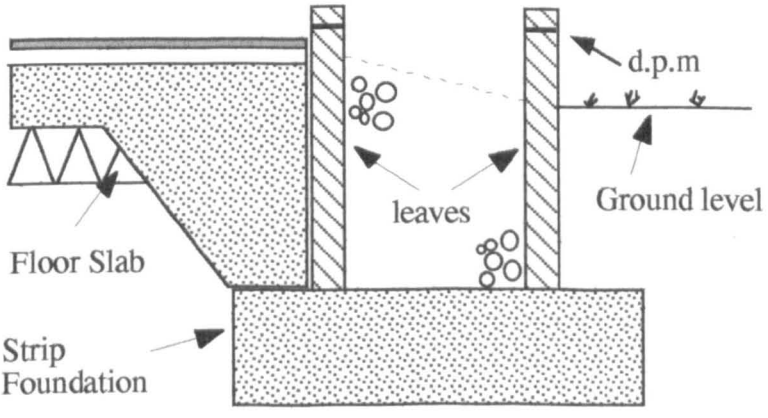

Figure 1.6: Foundation detail

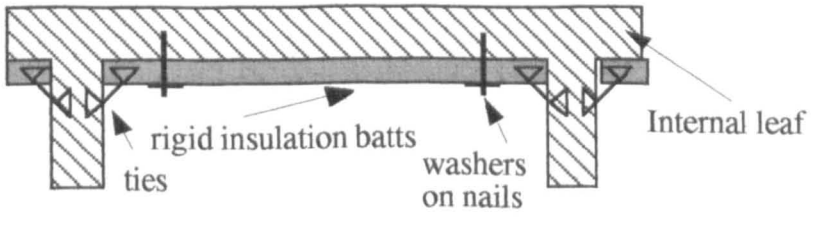

Figure 1.7: Thermal insulation detail

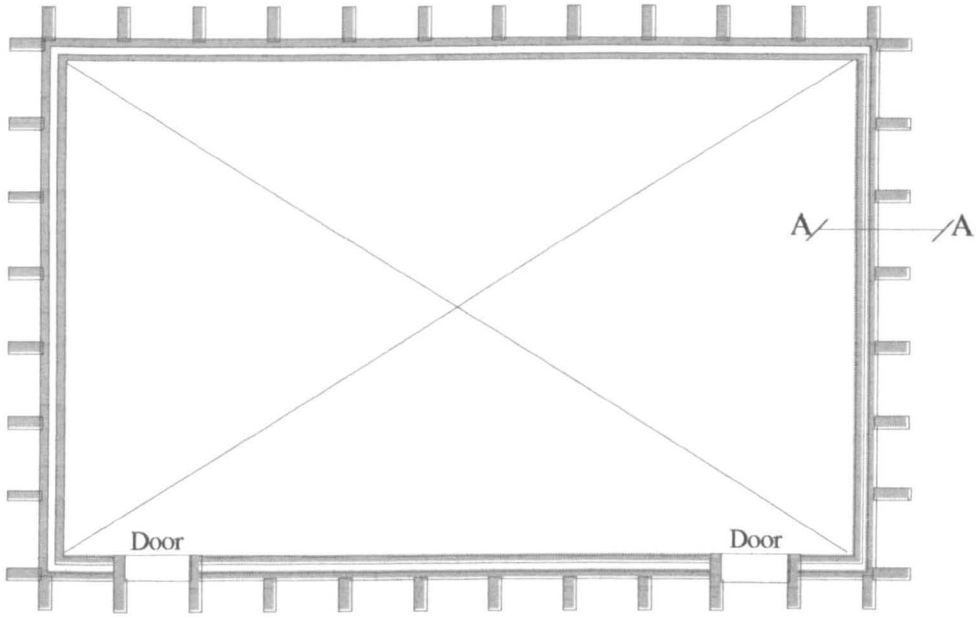

General Layout

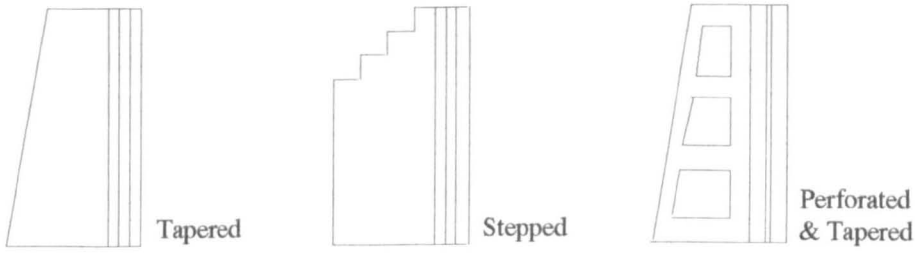

Variations in fin design

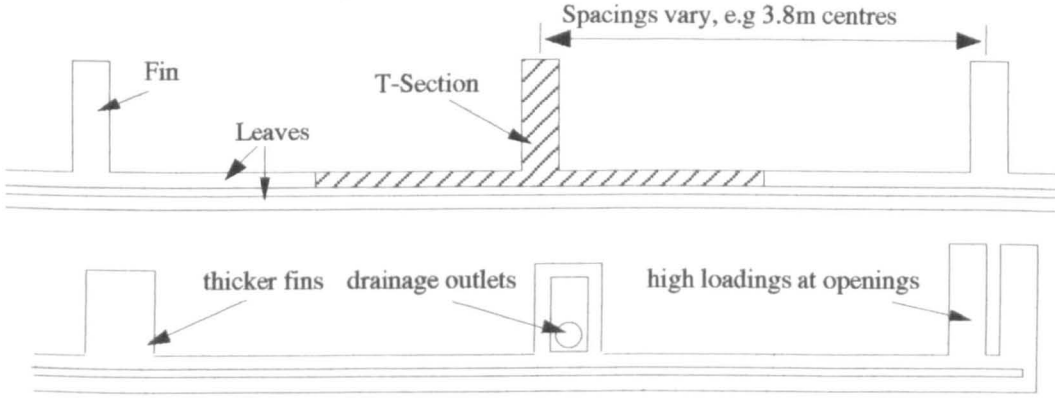

Variations

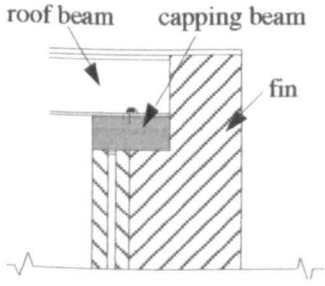

Typical detail at roof (Section A-A top):

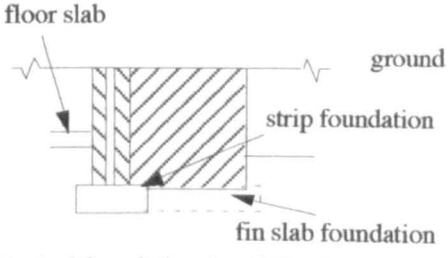

Typical foundation detail (Section A-A bottom)

Fig ure 1.8: General details of the fin wall

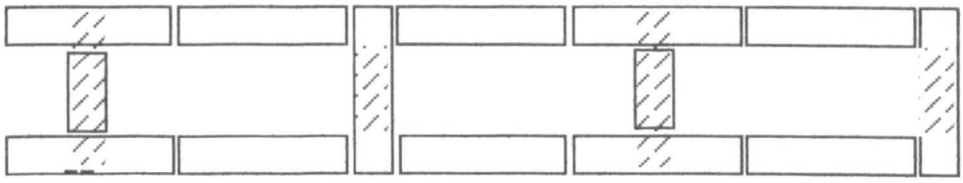

Bonded concrete blockwork wall

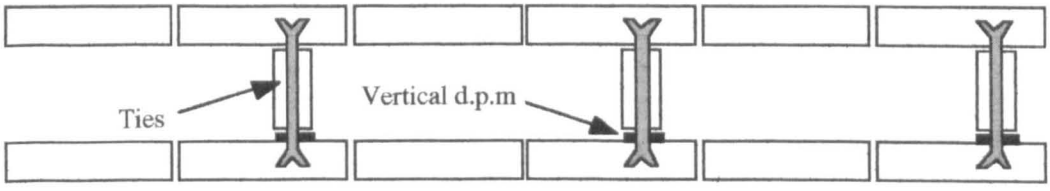

Tied concrete blockwork wall

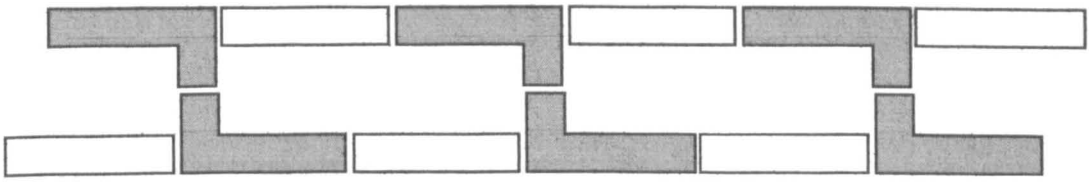

Quoin bonded blockwork wall

Figure 1.9: Concrete diaphragm bonding patterns

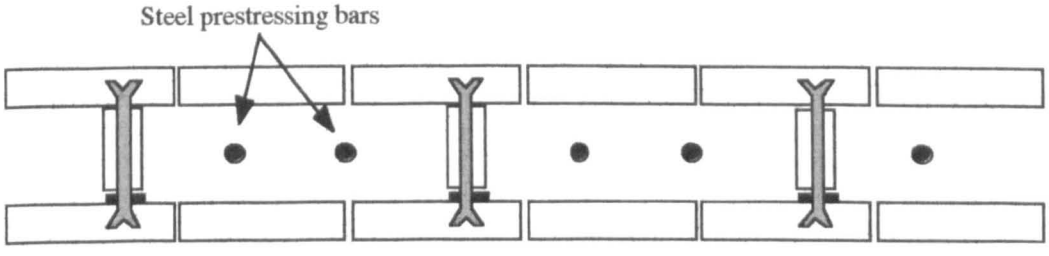

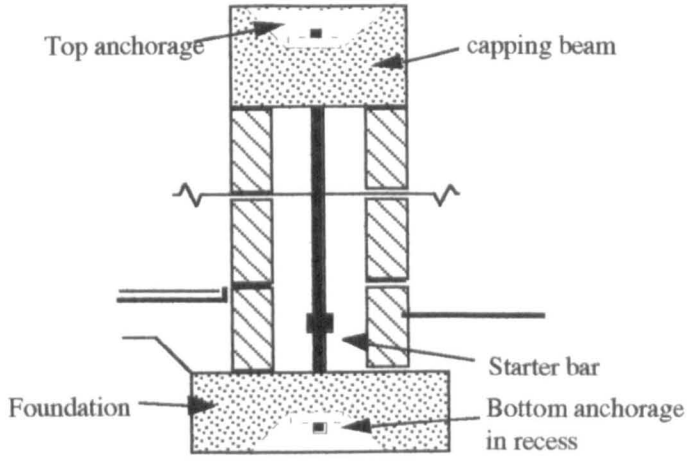

Vertical section through wall

Figure 1.10: Prestressed concrete bonding pattern

2 SOUND TRANSMISSION THROUGH WALLS

2.1 INTRODUCTION

An understanding of sound transmission theory relevant to the diaphragm wall is essential in order to predict transmission loss. Existing theory which might be relevant is now reviewed. As no theory is, at present, directly applicable to the diaphragm wall, model walls were built and measured, and some full scale walls were measured, in order to validate any theory developed for such constructions. These measurements are described in later chapters and compared with theory given in this chapter.

Due to its large mass the diaphragm wall might be described simply as an isotropic single wall. However the existence of two leaves and a cavity implies transmission mechanisms as are found with a double wall. Whereas the numerous cross-ribs suggest transmission across these bridges is also important. The wall's geometry also requires us to consider a stiffening and orthotropic effect, (considered in chapter 5), but the surfaces will be assumed to have an isotropic radiation behaviour initially. Hence theory for single, double and double bridged walls will be examined.

2.2 PREVIOUS RESEARCH

Very little work on the sound insulation of masonry diaphragm walls has been reported in literature. The only known published work is that by Gibbs & Lewis [17] at Liverpool University, where it is suggested that a monolithic diaphragm wall (where all material parameters are the same) is at best only equal in sound insulation to a single wall of the same equivalent mass. (In the BDA booklet [1] it is tentatively offered to the reader that the wall will give, at least, as good a performance as a traditional cavity wall). In addition, since 1982, there has been an internal report of

the same title and three dissertations by undergraduate final year Building Services Engineering students, at the same university. The first of which reported the construction and measurement of a 1/4 scale model [18]. The second included a report of the same model and analysis of the sound transmission using SEA [19]. An attempt to measure the sound insulation of a diaphragm wall in the field is reported in the third [20].

There are many papers on the transmission loss of masonry walls, e.g. [21, 22], and standards texts [36, 38] including general estimates for single leaf and traditional double leaf constructions. In addition, a large number of field measurements have been made over many years on masonry party walls between dwellings [23]. Laboratory and field measurement of transmission loss are carried out on low and medium building elements and facades according to various parts of ISO 140 (BS 2750) and others, which will be referred to as required throughout this study. Measurements are generally carried out over the building acoustics range of 100 Hz - 3.15 kHz, although there is some interest in reducing the lower limit to 50 Hz.

Stud partitions have similarities with diaphragm walls in that they are regularly (line) bridged. Such partitions have been studied theoretically [41, 57] and by measurement [50, 58]. Differences which do occur will be examined in later chapters, such as the high impedance mis-match at rib/leaf junctions and an assumed rigid [37] and often massless rib [41], neither of which can be as easily assumed for the diaphragm wall.

We shall now review theory for single, double and double bridged walls and discuss the relevance of such theory to the diaphragm wall. We shall also consider if it is necessary to consider thick plate theory for the diaphragm wall or whether extending thin plate theory up in frequency is sufficient.

2.3 SINGLE WALLS

It is the intention in this review to summarise and extract the theory relevant to this study. Detailed descriptions of the theory and fuller derivations are found in many papers including [28, 37, 38]. The fundamental principle of sound transmission through a wall was given early by Rayleigh who stated that; " It is easy to verify that the energies of the reflected and transmitted waves account for the whole energy of the incident wave" [27]. Subsequent significant research into the attenuation of sound by panels was reported in the 1940's to 60's [28 - 33]. It has been identified that the transmission of sound through a wall is principally dependant on mass, frequency, flexural stiffness, damping and finite dimensions.

2.3.1 Mass Law

The simplest theoretical model assumes a limp massive wall of negligible flexural stiffness. It is assumed to be infinite in size, incompressible, homogeneous and with no leaks. The surface density, m, mass per unit area (kg/m^2) is a governing factor in determining the insulation of the wall. This was examined for masonry constructions in 1923 by Sabine [34]. The 'mechanical impedance', also known as the 'specific transmission impedance' is given by:

$$Z_w = j\omega m \qquad (2.1)$$

and is the complex ratio of the difference in pressures on either side of the wall and the velocity of the wall. Where ω is the angular frequency, $\omega = 2\pi f$, f is the frequency in Hertz, and j shows it to be complex. Consider a plane wave travelling in air incident on an infinite panel at normal incidence. It has an incident sound pressure, $P_{i,0}$, and two waves result, a reflected pressure wave, $P_{r,0}$, on the incident side and a transmitted pressure wave, $P_{t,0}$, on the opposite side. The reduction factor in sound

pressure amplitude on either side of the panel is given by the complex ratio. From which, (without derivation):

$$p_i + p_r - p_t = j\omega m v \tag{2.2}$$

and,

$$v_i + v_r = v_t \tag{2.3}$$

where v is the particle velocity. It is common to assume that P_t is much smaller than P_i, and that P_i is approximately equal to P_r. The transmitted intensity is proportional to the square of the sound pressure and hence the normal incidence mass law transmission loss through an infinite limp wall is given by:

$$TL_0 \approx 10 \log \left| \frac{P_i}{P_t} \right|^2 \approx 20 \log \left[\frac{m\omega}{2\rho c} \right] \tag{2.4}$$

Where ρ is the density of air (1.19 kg/m^3) and c is the speed of sound in air (344 m/s). If the reflected component is eliminated, one obtains:

$$TL_0 = 10 \log \left[1 + \left(\frac{\omega m}{2\rho c} \right)^2 \right] \tag{2.5}$$

Equation 2.5 is commonly known as the normal incidence 'Mass Law.' Transmission loss increases proportionally at 6 dB per octave with a doubling of mass or frequency. The reciprocal of the term inside the widest bracket is the transmission coefficient, τ_0.

At an oblique angle θ, the transmission coefficient is given by:

$$\tau_\theta = \left[\frac{p_t}{p_i}\right]^2 = \left|1 + \frac{\omega m \cos\theta^2}{2\rho c}\right|^{-1} \qquad (2.6)$$

and,

$$TL_\theta = 10 \log \left[\frac{1}{\tau_\theta}\right] \qquad (2.7)$$

If sound waves are assumed incident on the wall at all angles, then the average transmission coefficient is obtained from integration over all angles of incidence.

$$\bar{\tau} = \frac{\int_0^\theta \tau \cos\theta \sin\theta \, d\theta}{\int_0^\theta \cos\theta \sin\theta \, d\theta} \qquad (2.8)$$

This gives the random incidence transmission loss, TL_r, as:

$$TL_r = TL_n - 10 \log [0.23\, TL_n] \qquad (2.9)$$

Cremer [35] and Kosten [40] suggested that the angle of incidence should be limited to between 75° or 80°, since angles above this, close to grazing incidence, are less influential and overweight the average transmission coefficient. This results in what is now defined as the field incidence value, TL_f, which lies between values at normal and random incidence. This is generally taken to be:

$$TL_f = TL_n - 5 \text{ dB} \qquad (2.10)$$

Field incidence often gives good agreement with measurements but it has been suggested [36] that this is not due to lack of sound at grazing incidence, but rather is

due in some way to the finite size of the panel. Figure 2.1 shows the typical relationship between normal, field and random incidence transmission loss for a 1/2 brick thick (102.5 mm) masonry wall with a material density of 1850 Kg/m^3.

London [28] found from measurement that values of transmission loss for lightweight walls were between normal and random incidence mass law prediction. Good agreement was achieved by the introduction of a mass resistance term 'R' to the wall impedance, Z_w, where $R = r / \rho c$. Thus equation 2.5 is altered to include:

$$\frac{p_i}{p_t} = 1 + \frac{r}{\rho c} + j\frac{\omega m \cos\theta}{2\rho c} \qquad (2.11)$$

The resistance coefficient, r, was based solely on the empirical data to give a best fit to measurements.

The specific transmission impedance of the wall, based on equation 2.1, is described here for an infinite plate. According to Schoch [29], and discussed by London [28], this is only appropriate at frequencies well above the first order resonance, such that the vibrating surface can be assumed to be of small elements which act independently of each other.

2.3.2 Finite Size Walls at Low Frequencies

At very low frequencies, below the first order resonance frequency or fundamental natural frequency, f_0, the transmission is controlled by stiffness. Doubling of mass or damping will be ineffective, but doubling the stiffness or frequency will reduce the transmission loss by 6 dB. The transmission loss where $f \ll f_0$ is given by Fahy [37] as:

$$TL_n = 20\log A_w - 20\log f - 20\log(4\pi\rho c) \qquad (2.12)$$

where A_w (= l_x x l_y) is the area of the wall. f_0 for a rectangular thin plate, supported at its boundary is:

$$f_{n_x n_y} = \frac{\pi}{2}\sqrt{\left[\frac{B}{m}\right]}\left[\left[\frac{n_x}{l_x}\right]^2 + \left[\frac{n_y}{l_y}\right]^2\right] \qquad (2.13)$$

f_0 occurs where the integral values, $n_x = 1$ and $n_y = 1$. Further resonant frequencies occur above f_0, where $n_{x,y} = 1, 2, 3$ ...etc. The degree to which they infringe into the mass-controlled region depends upon the size, mass, internal and edge damping of the wall. Schiller [32] suggests that edge effects can be assumed unimportant when:

$$L \gg \sqrt[4]{\frac{B}{m\omega^2}} \qquad (2.14)$$

B is the bending stiffness and L is the shortest wall length. At 50 Hz (the worst case) for a typical masonry wall L » 1.5 m, thus for a 8 m high diaphragm wall edge effects are of little importance. The degree to which the wall is fixed to its boundary and the impedance mis-matching dictates vibrational energy loss. The boundaries will also establish modes due to free returning bending waves from the edges. These radiate sound energy with increasing efficiency at higher frequencies. Measurements of internal damping and the radiation efficiency of diaphragm walls are discussed in chapter 5.

2.3.3 Coincidence Region

The phenomenon of coincidence, discussed in Fahy [37], was first described by Pierce in 1933 [61], and by Sanders, with respect to ultrasonics, in 1939 [62]. Cremer explains this phenomena with respect to sound transmission through plates in a well referenced paper [35]. The initial premises of the effect are; that the wall is surrounded by a fluid such as air, the velocity of acoustic waves in fluid are

frequency independent, while the speed of the bending waves in the wall are frequency dependant. Radiation of sound from a surface is dominated by the bending wave, where its wavespeed is given by:

$$c_b = \sqrt[4]{\frac{B}{m}}\sqrt{\omega} \qquad (2.15)$$

For a thin isotropic plate of thickness, h, the bending wavespeed can be approximated to [39]:

$$c_b \approx \sqrt{1.8\ c_L h\ f} \qquad (2.16)$$

where c_L is the longitudinal wavespeed. In a plate, this is defined as [39]:

$$c_L = \sqrt{\frac{E}{\rho_c(1-\sigma^2)}} \qquad (2.17)$$

ρ_c is the material density, E is the Young's modulus and σ is the Poisson ratio commonly of the order of 0.3 for most building materials.

A bending wave can be termed as a 'free' wave when it is only dependant on its elastic constants. Coincidence will occur when the free bending wavelength along the wall surface matches the 'forced' trace-wave produced by an incident airborne wave at angle θ to the normal ($\lambda_{free} = \lambda_{forced}$). The 'forced' trace-wavelength is given by

$$\lambda_{forced} = \frac{\lambda}{\sin\theta} \qquad (2.18)$$

Where λ is the wavelength in air. This wave coupling forces the wall at a free wavespeed, producing a maximum response. Theoretically, total transmission will occur at coincidence when there is no damping ($\eta = 0$), though inevitably there will always be some damping of the wall due to frictional or dissipative forces which will

reduce the amplitude of displacement. (Damping will be discussed in chapter 5). Under a diffuse sound field there are many angles of incidence, so there will be a series of 'coincidence angles' where λ_{free} equals λ_{forced}. The earliest this will occur is where $\theta = 90^\circ$ known as 'grazing incidence,' where $\lambda_{forced} = \lambda$. This frequency is defined as the critical frequency, f_c, which is given by:

$$f_c = \frac{c^2}{2\pi}\sqrt{\frac{m}{B}} \tag{2.19}$$

where B is the bending stiffness and m is the surface density. For an isotropic plate this is simplified to:

$$f_c = \frac{c^2\sqrt{3}}{\pi h c_L} \tag{2.20}$$

where h is the wall thickness and c_L is the longitudinal wavespeed. The coincidence frequency will increase as the incident angle approaches the normal, producing a 'coincidence region', given by [38]:

$$f_{coincidence} = \frac{f_c}{\sin^2\theta} \tag{2.21}$$

The transmission loss above critical frequency is given by Cremer [35] and Kosten [40]:

$$TL_\theta = 10\log_{10}\left\{1 + \left[\frac{\omega m \cos\theta}{2\rho c}\left(1 - \frac{c_{free}^4 \sin^4\theta}{c^4}\right)\right]^2\right\} \tag{2.22}$$

Sharp [41] rewrites Cremer's expression in terms of field incidence transmission loss, including damping, as:

$$TL_f = 20\log_{10}\left[\frac{\omega m}{2\rho c}\right] + 10\log_{10}\left[\frac{2\eta\omega}{\pi\omega_c}\right] \tag{2.23}$$

The region above f_c is often termed the 'recovery region.' As after the coincidence effect has initially produced a 'dip' in the transmission loss curve below mass law, the curve can be described as attempting to recover, with increased frequency, to the value which mass law would give if extended in frequency. For a single wall this recovery gradient is approximately 10 dB / octave but is dependant on other factors such as edge conditions, internal damping and the finite size of the wall. Fuller discussions of coincidence can be found in many references such as [32, 37, 38].

f_c varies greatly between materials, increasing with decreased longitudinal wavespeed and thickness. For masonry constructions the coincidence dip occurs between 50 and 300 Hz, the lowest region of the audio frequency range. This frequency region corresponds to that predominant from traffic noise and therefore is often a weak link in the wall's transmission loss. It may be desirable to redesign the wall to ensure that either the f_c does not occur in the frequency range, or dampen the wall to lessen transmission about f_c. For masonry walls both options are difficult. Generally for heavyweight thick walls the dip around coincidence is not great due to the inherent damping of the wall. Watters [43], introduces an empirical transmission loss design curve for single leaf masonry walls to cope with poor agreement found near and below critical frequency, which incorporates a plateau transmission loss region around f_c of between 2 - 3.5 octave band width.

Figure 2.2 shows the four regions which traditionally describe the transmission loss of a single isotropic wall. The degree to which any of these regions predominates depends on the particular element.

To summarise, where:

$f < f_0$	Stiffness controlled
$f < 0.5\ f_c$	Mass controlled
$0.5\ f_c < f < f_c$	Extrapolated region (straight line)

Recovery region Coincidence controlled (damping)

Single wall theory would at first seem the least applicable to the complicated geometry of the diaphragm wall. Yet, if the large number of cross-ribs forms a strong structural link between the leaves such that this path dominates, then the transmission of energy across the wall compared to the cavity will dominate, and the leaves act in phase. Then it may be possible to consider that the diaphragm wall, at least over part of the frequency range of interest, behaves as a single wall of the same equivalent mass.

2.4 DOUBLE WALLS

As the diaphragm wall is a double leaf construction with cavities it is useful to review the theory of sound transmission through such walls in order to understand the influence of the cavities and as a prelude to bridged double walls. Double walls are described in the literature, both theoretically [44 - 48] and by measurement [49 - 52]. The two leaves of a traditional double wall are acoustically coupled by an air cavity and by ties, and at the boundaries by foundations, flanking walls, floors, leaf returns etc. Prominent theories for unbridged double walls have come from London [44], Beranek [45] and Mulholland [46].

London [44] considered transmission by an oblique incident wave through two identical leaves. An angle averaged sound attenuation is derived and it is shown that the transmission loss of a double wall in low and mid frequency regions can be less than that of a single wall of the same equivalent mass and it certainly does not result from the simple addition of the effect of both leaves. London again introduced his resistance term R to give a better fit between theory and measurement. Transmission through the wall will be effected not only by the behaviour of each leaf but also by the air coupling. At low frequencies the stiffness of the cavity is equal to the mass

reactance of the leaves. This is called the oblique mass-spring-mass frequency, given by:

$$f_\theta = \frac{1}{2\pi \cos\theta}\left\{\left[\frac{\rho c^2}{d}\right]\left[\frac{m_1 + m_2}{m_1 m_2}\right]\right\}^{\frac{1}{2}} \qquad (2.24)$$

m_1 and m_2 are the surface densities of each leaf. The frequency of the lowest mass-spring-mass resonance is obtained at normal incidence. With increased angle, f_θ increases creating a resonance dip. The upper resonance frequency occurs at the limiting angle of 90°, which can be equal to 5 f_0. At frequencies below f_0 the two leaves will act almost in phase [31], with negligible excess pressure in the cavity. Transmission loss below f_0 is assumed as the mass law, where m is the sum of both leaves. For a traditional cavity masonry wall f_0 lies between 15 - 30 Hz which is below the building acoustics frequency range.

At frequencies above f_{90} transmission loss increases at approximately 18 dB / Octave until the first cross-cavity resonance, given by:

$$f_{res} = \frac{c\,n}{2d \cos\theta} \qquad (2.25)$$

where n = 1, 2, 3..., and d is cavity width. For a cavity wall, the first cross-cavity resonance will occur between 1.7 - 3.4 kHz, while for a diaphragm wall which has a much wider cavity, this is between 374 - 735 Hz. In this region transmission loss rises at approximately 12 dB / Octave.

Beranek & Work's [45] theory is a more accurate solution than London's [44] but gives the same result as London where R = 0. The approach was for normal incidence and infinite walls only, solving the wave equation for different regions of a

multiple wall. This allowed for any media ratios to be calculated including the transmission coefficient.

Mulholland et al [46 - 48] produced the multiple reflection theory which allows consideration of a random incidence sound field, sound absorptive material in the cavity and finite size. The theory follows the ray's multiple reflections within the cavity and transmission through each leaf. The fraction of intensity of the ray which is reduced by each reflection and transmission is calculated according to mass law. Calculations were made for a diffuse field with a limiting angle of 80°. Initially results gave poor agreement with measurement. Sound absorption was then included in the cavity, on both internal faces, and a reflection coefficient 'α' was derived which gave good agreement between theory and measurement. These derived values of α were not confirmed by measurement to be those of the material under test, therefore were questionably little better than London's best fit resistance term. Mulholland [46] also considered finite double walls where the absorption is only at the boundary edges of the cavity. Agreement with measurement was again good using a best fit α term.

White & Powell [53] used a mode/coupling approach to derive the coupling between a transmission suite room separated by a double wall. The modal response of the wall was predicted with good agreement with measurement under broadband random excitation. This multi-modal statistical method was essentially an SEA approach, which will be applied to the diaphragm wall in chapter 7.

Sewell [54] considered a double wall with an infinite cavity in a rigid baffle. Good agreement was gained above and below the critical frequency by altering the internal loss factor of the cavity. Sewell criticised Mulholland's multiple reflection theory as not applicable where the wavelengths are greater than the cavity width.

Donato [55] predicted the transmission loss for a infinite double wall via an electrical analogy. At low frequencies a correction factor is introduced for a finite wall. The internal loss factor of the panel gave best results using values of $\eta = 0.01\text{-}0.015$, which are typical figures for building elements. Donato also gives a crude analysis of the effect of stud bridges between leaves.

Sharp [41] gives an approximate expression for a double wall based on London's theory where:

$$\begin{array}{ll} TL_M & f < f_0 \\ TL_{m1} + TL_{m2} + 20\log_{10}[fd] - 29 & f_0 < f < f_l \\ TL_{m1} + TL_{m2} + 6 & f > f_l \end{array} \qquad (2.26)$$

Where M is the total surface density of both leaves, $M = m_1 + m_2$, and TL is calculated by mass law. f_l is called the 'limiting frequency' which is approximated by:

$$f_l = \frac{c}{2\pi d} = \frac{55}{d} \qquad (2.27)$$

Equation 2.27 is essentially equation 2.24 excluding the walls surface density. It approximates well for a wide range of leaf masses up to a limiting angle of 80°. Figure 2.3 shows a transmission loss for an infinite double wall at normal incidence, with Beranek & Work and Sharp's theory applied. It is important not to forget the coincidence effect of each individual leaf which may also be seen in the resulting transmission loss.

In real walls cavities are of finite dimension large enough to enable resonant waves to occur along the cavity within the building acoustic frequency range. This is true in the case of the diaphragm wall where the cavities are vertical columns of air. At cavity anti-nodes strong coupling may exist between leaves. This coupling can be dampened

by including an absorptive layer at both the mass-spring-mass and cross-cavity resonance frequencies. Even a sheet of sound absorptive material much thinner than the cavity can significantly improve the sound insulation of lightweight walls. It is less effective as the walls become heavier or the air gap smaller. Hence with masonry constructions the heavy leaves limit the effect of the cavity absorption. Hung [18] made measurements of a 1/4 scale diaphragm wall (described fully in chapter 3) with and without a mineral wool batten against one internal face. This resulted in only a 1 dB difference above 2500 Hz.

Double wall theory can only be directly applicable to the diaphragm wall if the cavity path is significant compared with the cross-rib bridging. To get an initial estimation of the degree of importance of the two bridging paths between the leaves let us consider theory relevant to bridged double walls.

2.5 BRIDGED DOUBLE WALLS

Traditional cavity wall constructions are inevitably bridged over their surface with wall ties in a regular matrix and by masonry returns at doors and windows. This bridging reduces the transmission loss of the wall dramatically compared with an unbridged double wall. Recently Wilson [52] gave a comprehensive study of the bridging effect of wall ties. Measurements showed that a doubling of the number of ties produces a fall of 3 dB in airborne level difference and a doubling of tie stiffness results in a reduction of 6 dB.

The diaphragm wall can be best described as a vertically line bridged double wall. Bridges are principally to stabilise the wall against lateral loadings. Research on this geometry of wall has overwhelmingly been devoted to lightweight constructions such as timber or plasterboard partitions [37, 41, 56 - 59] which are usually found in internal, domestic and office locations. In lightweight partitions the bridges are

commonly vertical metal or timber studs fixed at regular centres between two panels. Figure 2.4 shows examples of bridging for this type of construction. The structural connection between stud and panel can be fixed by line or small point connections on one or both faces. With respect to the diaphragm wall a continuous line connection exists on both leaves. With masonry constructions, laboratory measurement and field measurement are more difficult and the lower critical frequency of the wall means the frequency range of interest is predominantly super-critical.

No comprehensive theory exists for lightweight double partitions but a useful approximation is given by Sharp [41]. Two key assumptions are generally made; that each stud reacts independently of any other and each stud is considered as a rigid body simply transmitting forces along its plane. Sharp also assumes the bridge is massless. The degree to which the sound bridge will degrade the sound insulation of the partition wall is determined by comparing the sound power radiated by the bridged path, W_b, to that radiated by the acoustic path alone, W_p. The transmission loss of the bridge can be written as:

$$TL_b = 10 \log \left[1 + \frac{W_b}{W_p} \right] \qquad (2.28)$$

If the power radiated due to the sound bridges is equal to that from the cavity path then the transmission loss will fall by 3dB. If W_b is dominant the bridge path will cause a fall in transmission loss from double wall theory (equation 2.26) by 12 dB / octave where $f < f_l$ and 6 dB / octave where $f > f_l$. (f_l is given by equation 2.27). The predicted transmission loss will then rise at only 6 dB / octave between the bridging frequency, f_b, and $f_c/2$. f_b is where the bridge becomes significant and limits the effect of the overall wall performance, determined by the intersection between the 12 or 6 dB / octave curves. Therefore, in the region $f_b < f < f_c/2$, The transmission loss is given by:

$$TL = TL_M + \Delta TL_M \qquad (2.29)$$

Where TL_M is that in equation 2.26 and ΔTL_M for line connections is given by:

$$\Delta TL_M = 20\log_{10}(b\, f_c) + K - 45dB \qquad (2.30)$$

where K equals:

$$K = 20\log_{10}\left[\frac{m_1(Z_1 + Z_2)}{Z_1(m_1 + m_2)}\right] \qquad (2.31)$$

and where Z_1 and Z_2 are the line impedance's of the two leaves per unit length, given by [41]:

$$Z = 2(1+j)mc\left[\frac{f}{f_c}\right]^{\frac{1}{2}} \qquad (2.32)$$

Similar results are given for point connections by Sharp. Bies gives expressions for the cases of line-point and point-line bridges [36]. For the line-line case (connected by lines along both faces) the transmission loss can be written as:

$$TL = 10\log_{10}[Mbf_{c2}] + 20\log_{10}[f] + 20\log_{10}\left[1+\frac{m_2}{m_1}\sqrt{\frac{f_{c1}}{f_{c2}}}\right] - 77dB \qquad (2.33)$$

This is shown graphically in figure 2.5, where the dashed line is that of an isolated double wall and the solid line includes all paths. f_{c1} and f_{c2} are the critical frequencies of the two leaves where always $f_{c2} \geq f_{c1}$ and the region $f_{c1}/2 < f < f_{c2}$ is interpolated. Above the higher critical frequency transmission loss rises at 15 dB / Octave.

The significance of the bridge path compared to the cavity path between the leaves is approximated by Fahy [37] as a ratio of stud to air cavity transmission coefficients:

$$\frac{\tau_s}{\tau_a} = \frac{0.7nc\cos\theta}{f_c} \qquad (2.34)$$

where n is the number of bridges. Using a typical incident angle of 45° he concludes that where this ratio is ≥ 1 the transmission loss will be equal to little more than the equivalent mass of the wall. Applying equation 2.34 to the diaphragm wall, will always produce a ratio » 1 (typically 7-18), due to the low critical frequency and large number of cross-ribs. This indicates that the strong bridging of the cross-ribs would be expected to dominate the transmission path, and cavity will have little effect except at very high frequencies (>8 kHz) where it is not typically necessary [18]. Ingemansson and Kihlman [60], reproduced in Fahy [37], also illustrated this ratio by comparing two stud partitions with identical leaves, with a mineral filled cavity. Where the leaves are of a high critical frequency the effect of the absorption on the transmission loss is clearly seen (10 dB increase). For the leaves with a lower critical frequency the absorption has negligible effect up to $f_c/2$, effectively by-passing the cavity path.

Therefore, as soon as the bridge becomes the significant transmission path it is useful to consider ways of reducing this path without any loss of structural integrity. Gu & Wang [57] found a 5 dB higher sub-critical transmission loss could be obtained by bridging with a metal stud compared with a wooden stud. The metal bridge is significantly different from the rigid bridge effect predicted by Sharp. The metal stud acts more like a spring between the leaves and thus Gu & Wang included a lateral equivalent stiffness which gives a predicted transmission loss of 12 dB / Octave where $f_b < f < f_c/2$. It was also shown that by adding resilient pads at points between the stud and panels this would create extra changes in impedance and the compressional nature of the pads would add extra damping to the wall. Hence, the vibrational transmission between stud and panel is reduced and the overall transmission loss particularly around critical frequencies is increased.

Lin and Garrelick [59] mathematically modelled a double stud partition. They showed that partition resonances at low frequencies could produce transmission loss curves lower than predicted by the equivalent mass law curves, where minima occurred not at the fundamental mode of the panel.

Lee [58] employs Statistical Energy Analysis in a unified approach to the air and stud paths and showed that the stud path did not contribute greatly and measurement fitted well with prediction assuming the air path only.

The ribs also act as stiffeners to the leaves, and the relationship between rib and leaf in terms of a changing wall bending stiffness and impedance mis-match are discussed in chapters 5 and 6 respectively. Von Venzke [63], reproduced in Fahy [37], shows that by stiffening a panel its transmission loss is reduced over most of the frequency range (particularly about coincidence).

2.5.1 Bridging at Boundaries

To simplify this study it is useful to be able to eliminate sound transmission paths through the diaphragm wall other than the direct path (across the cavity by air and cross-rib coupling). Horizontal bridges occur at roof level by the concrete capping beam and at the base by the foundation. Vinokur [64] considered the reduction in airborne sound insulation of two identical separated leaves, caused by the inclusion of such edge conditions. He examined principally window frames of double glazed systems and also a masonry double wall. Transmission through the foundation and capping beam can be assumed rigid and non-resonant, as they are both of concrete and for simplicity are assumed the same thickness. Using Vinokur's expressions, sound transmission via these paths is estimated and compared with transmission via

the direct path through the wall. The airborne transmission loss of the edge path, TL_{edge}, is given by equations 2.35-2.37. Where $f \leq 0.5f_c$:

$$TL_{edge} \approx TL_n + \Delta TL_f + 20\log\left[\frac{f_c \pi A_w}{c\,l}\right] + 15\log\left[1 - \frac{f}{f_c}\right] + 10\log\eta + 5\log\left[\frac{f}{f_c}\right] + 12 \qquad (2.35)$$

and where $f \geq 2f_c$:

$$TL_{edge} \approx TL_n + \Delta TL_f + 6 \qquad (2.36)$$

l is the length of the linear links around the perimeter, TL_n is the normal incidence transmission loss of a single leaf and ΔTL_f is given by:

$$\Delta TL_f = 10\log\left[1 + \left[\frac{\pi^3 m_{link} A_w \eta f_c f}{2m c^2 l}\right]^2\right] \qquad (2.37)$$

where m_{link} is the surface density of the link element (the foundation and capping beam), given by:

$$m_{link} = m_f[h + d + h_f] \qquad (2.38)$$

where h is the thickness of the leaf, d the cavity width and h_f is the link thickness. Figure 2.6 shows the difference in airborne transmission loss between the direct path and the sum of the direct and edge paths. As the error is < 1 dB it is assumed that this path can be eliminated as an important transmission route for the rest of the study. The probability of this path being important for the diaphragm wall is very small due to the large number of cross-rib bridges. Wilson [52] measured the airborne level difference via this path for a masonry double wall and found Vinokur predicted too high by 5 - 20 dB. He concludes that Vinokur's theory is probably not valid for heavyweight construction.

2.6 THIN PLATE THEORY & HEAVYWEIGHT WALLS

The diaphragm wall is clearly a heavyweight construction, and there is generally less literature concerned with sound transmission through heavy, thick walls [39, 42] than for theory with respect to thin, lightweight structures. Thin plate theory applies where rotational inertia and shear deformation is not included in the bending wave equation. In thick plates traverse shear waves become important travelling through the thickness of the wall, their bending speed is given by [39]:

$$c_s = \sqrt{\frac{Gh}{m}} \qquad (2.39)$$

where G is the shear modulus. The full bending wave equation for thick plates was derived by Mindlin and is given by Cremer [39]. An arbitrary limit is given by Cremer for thin plate theory, where the material thickness is small compared with the bending wavelength, given below:

$$\frac{\lambda_B}{6} < h \qquad (2.40)$$

where the Helmholtz number is unity (kh = 1, where k is the wavenumber). At this limit Cremer argues that solutions assuming thin plate theory are 10 % different from the full bending wave solution. At frequencies up to this limit the surfaces of a single wall are assumed to vibrate in phase.

For many elements in the aerospace or shipping industries the thin plate approximation is acceptable as most vibrating / radiating elements will be thin with high longitudinal wavespeeds. Hence the limit given by equation 2.40 is far above the audio frequency range (e.g. 5 mm steel plate $h > \lambda_b/6$ above 52.7 kHz). Whereas for the diaphragm wall, as for many building elements, the acceptability of thin plate

analysis over the whole frequency range is less obvious. Particularly with concrete and masonry materials, the arbitrary limit often falls within the building acoustics frequency range (100 Hz - 3150 Hz). Therefore the question arises, is thin plate theory sufficient for this type of masonry construction? Ljunggren [42] gives evidence that for thick plates, the thin plate expressions can be used to approximately 2 octaves above the limit of equation 2.40, which is equivalent to changing the 6 to a 3, or a Helmholtz number of 2 (kh = 2). Table 1 below gives the cut-off frequency for thin plate theory for a variety of typical walls using equation 2.40 (kh = 1) and also includes a cut-off limit given by Ljunggren [49] of kh = 2:

Table 1: Cut-off Frequencies for Thin Plate Theory

Material	kh = 1 (Hz)	kh = 2 (Hz)
Masonry (1/2 brick)	1163	4651
Masonry (1 brick)	548	2190
Concrete (light, 150 mm)	574	2296
Concrete (dense, 150 mm)	1129	4515
Perspex (13 mm)	8028	32636

Importantly for the 1/2 brick thick walls of the diaphragm wall, this offers evidence that thin plate theory is theoretically applicable up to 4.7 kHz, rather than only 1.2 kHz, by altering equation 2.40. This is then above the traditional upper limit to the building acoustics frequency range of 3150 Hz. It is also above the measurable frequency range that was found possible on site, of 2 kHz for airborne sound transmission and 4 kHz for structure-borne transmission (see chapter 8). Also, the 16 kHz upper measurement range for the 13 mm perspex model walls, introduced in chapter 3, is now within the theoretical thin plate limit, set by Ljunggren.

At higher frequencies Ljunggren includes a plateau region (roughly 2 octaves wide) in the transmission loss curve to accommodate longitudinal (P wave) resonances which

are dominated by the loss factor. This is reproduced below, but was not included later as it is outside the measurement range for validation.

$$TL_{plateau} = 20\log\left[\frac{\rho_c c_p}{4\rho c}\right] + 10\log\left[\frac{\eta}{\eta_0}\right] \qquad (2.41)$$

Where η_0 is the reference damping equal to 0.02 and c_p is the propagation speed of the P wave.

Ljunggren also compared thin and thick plate theory with the transmission loss measurements for various building materials (brick, concrete, plywood) of arbitrary thickness. Thin plate theory over-estimated measurement above the thin plate limit by 0.5 - 1.6 dB, while thick plate theory under-estimated by 2.0 - 2.9 dB. If we are to accept these results then thin plate theory can be used to much higher frequencies. As Ljunggren argues there has been little research into this field and there is no justifiable reason therefore why an arbitrary limit cannot be changed with measurement validation.

As a guide to the importance of including shear wave transmission Rindel [65] compared the influence of the shear waves upon the bending waves with increasing frequency. It is assumed the bending and shear stiffness are connected in parallel by incorporating the shear wave speed, c_s, within the bending wave speed, c_b, to produce an effective bending wave speed, $c_{b,eff}$. Equations 2.15 and 2.39 give the expressions for bending and shear waves respectively and equation 2.42 is the combined expression for the effective bending speed.

$$c_{b,eff} = \frac{c_b^2}{c_s}\sqrt{\left[-\frac{1}{2} + \frac{1}{2}\sqrt{1 + 4\left[\frac{c_s}{c_b}\right]^4}\right]} \qquad (2.42)$$

Rindel could then substitutes $c_{b,eff}$ for c_b wherever necessary, to accommodate shear waves within thin plate analysis, which would effect, for example, the critical

frequency and modal density of an element. The degree to which the shear wave influences the bending wave is shown in figures 2.7 and 2.8, which plot the bending wave speed, effective bending wave speed and shear wave speed for a 13 mm perspex wall and for a 1/2 brick masonry wall, respectively. c_s is frequency invariant and when c_b is significantly slower than c_s, then $c_{b,eff}$ is essentially identical to c_b. When the speeds are closer, $c_{b,eff}$ deviates from c_b, and tends towards c_s. The arrows on the figures denote the calculated frequency at which $c_{b,eff}$ differs from c_b by 10 %. For the 13 mm perspex walls this is at 13 kHz and for the 1/2 brick masonry wall at 1.8 kHz. Although these do not quite reach the upper frequency limit of measurement the influence of the shear waves is believed not to be greatly significant. As mentioned earlier , this is still above the field measurement frequency limit for the diaphragm wall. Therefore for purposes of measurement and theory, comparison and validation, thin plate theory was assumed. Thus the author concludes that it is not necessary to invoke thick plate theory as the cut-off frequencies of thin plate theory are high enough or above the frequency range of interest for both the model and full size walls.

2.7 CONCLUDING REMARKS

In this chapter a review has been given of existing theories of sound transmission through walls, in particular, those which might best be applied to best predict the sound insulation character of the diaphragm wall. The near monolithic nature of the wall and the strong bonding between leaves by the cross-ribs has shown that it may be possible to theoretically model the diaphragm wall as a single wall. Yet this can only be the case where the leaves act in phase (at low frequencies) and where the cavity path is not important (at some higher frequency).

Sound transmission at the boundaries of the wall, at roof and foundation, returns on doors etc., can been assumed negligible due to the large number of cross-ribs already bridging the leaves.

Further, it is shown that thin plate theory is adequate for analysis of the diaphragm wall, particularly as measurement validation is only possible over this frequency range anyway. Work by Ljunggren and Rindel suggests an extension of the arbitrary thin plate limit can be justified.

The accuracy of any theoretical analysis of the diaphragm wall is determined by validation from measurement. Full scale in-situ measurements of masonry facades are very difficult. For this reason model walls were used initially. Chapter 3 describes the models built and tested, and the results obtained.

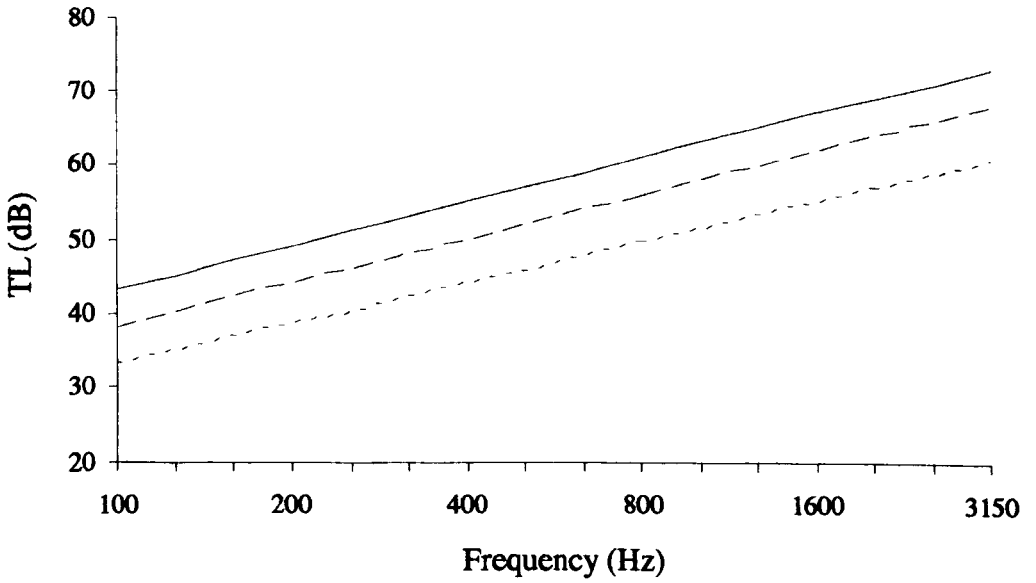

Figure 2.1: Transmission loss prediction according to mass law for a 1/2 brick thick wall (m = 185 Kg/m2)

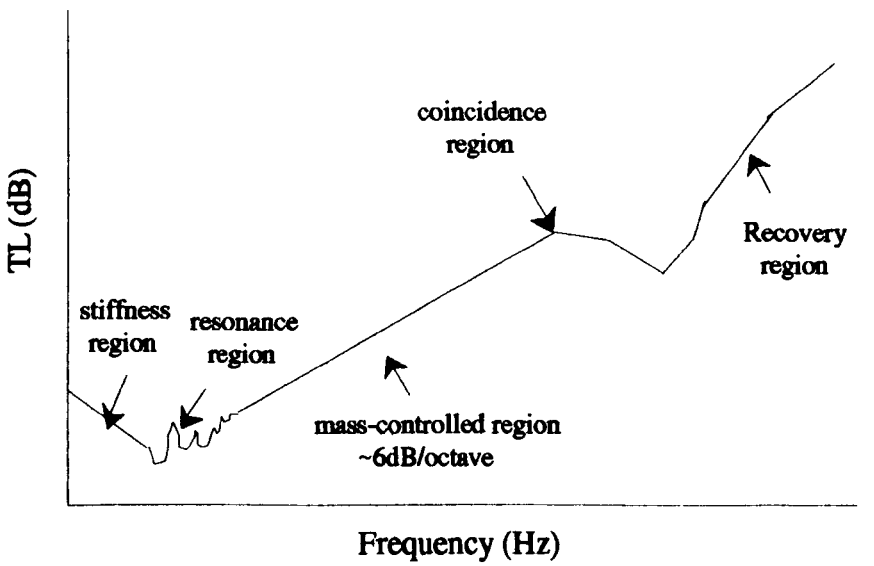

Figure 2.2: Typical transmission loss behaviour for a single isotropic wall

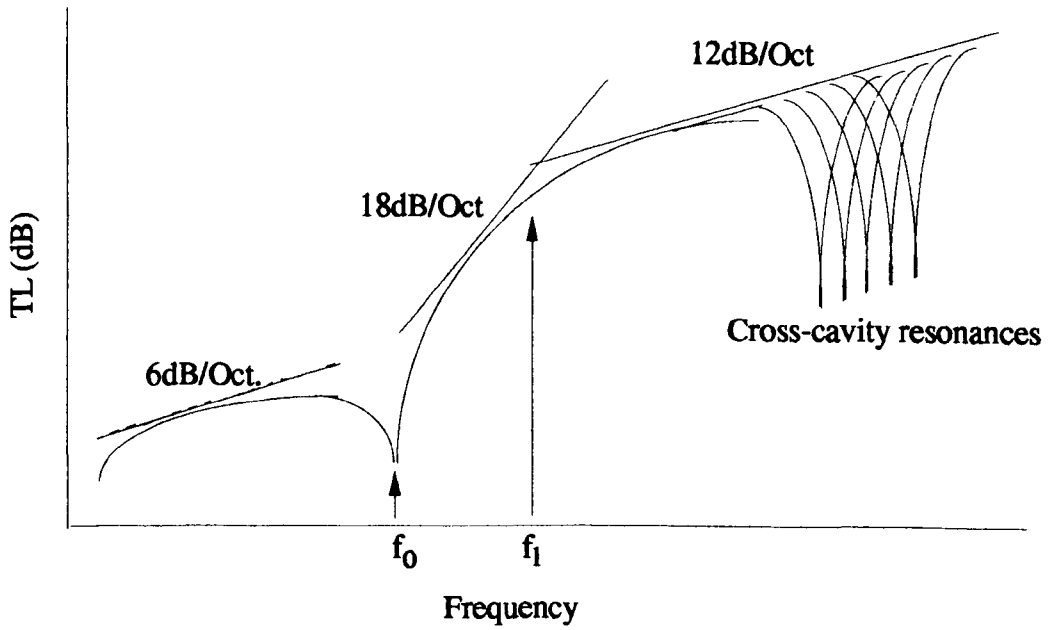

Figure 2.3: Transmission loss prediction for an infinite double wall

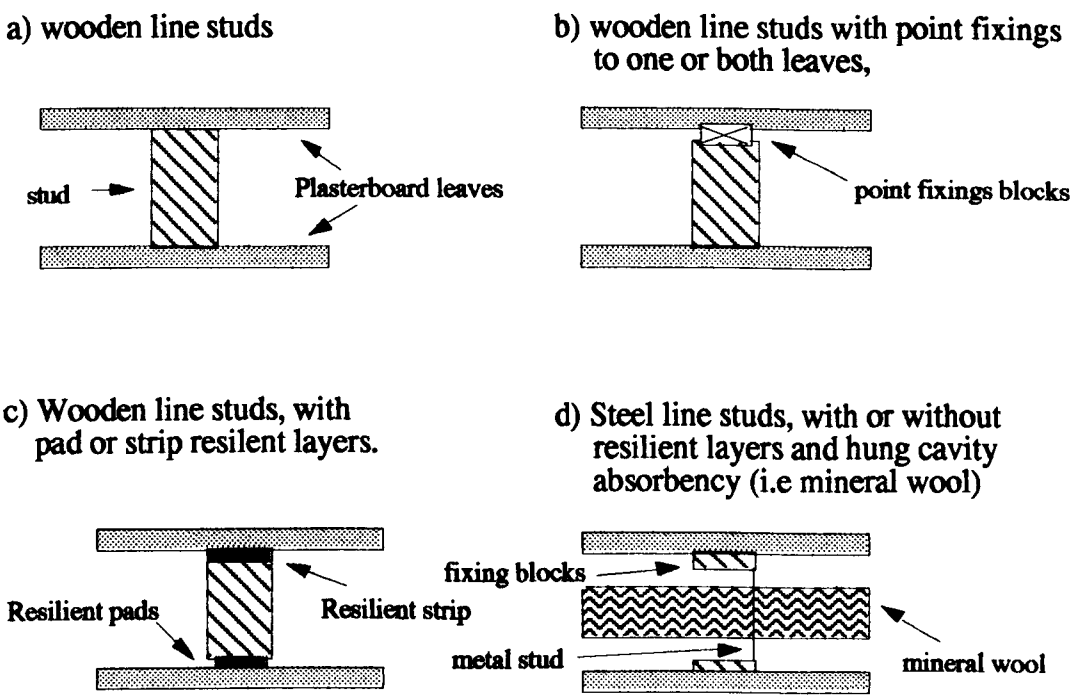

Figure 2.4: Bridged lightweight partitions (plan views)

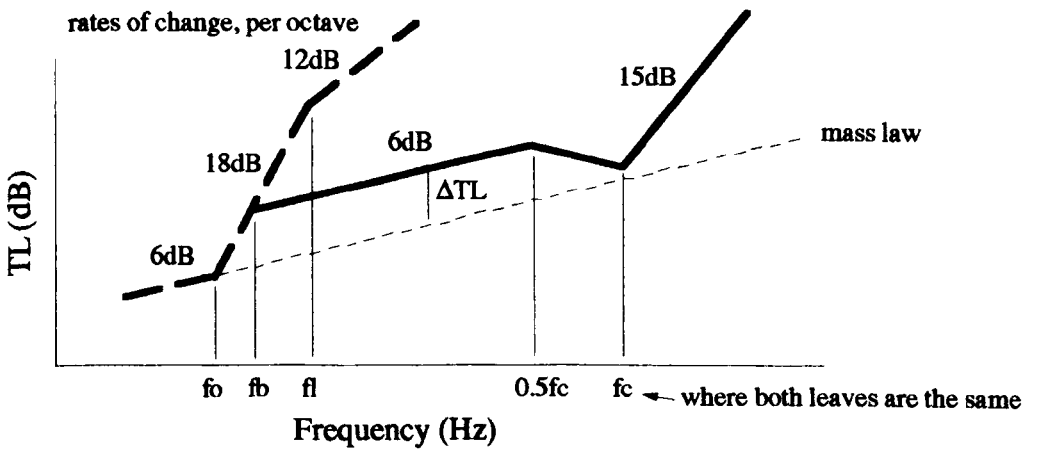

Figure 2.5: Transmission loss prediction for a double bridged wall

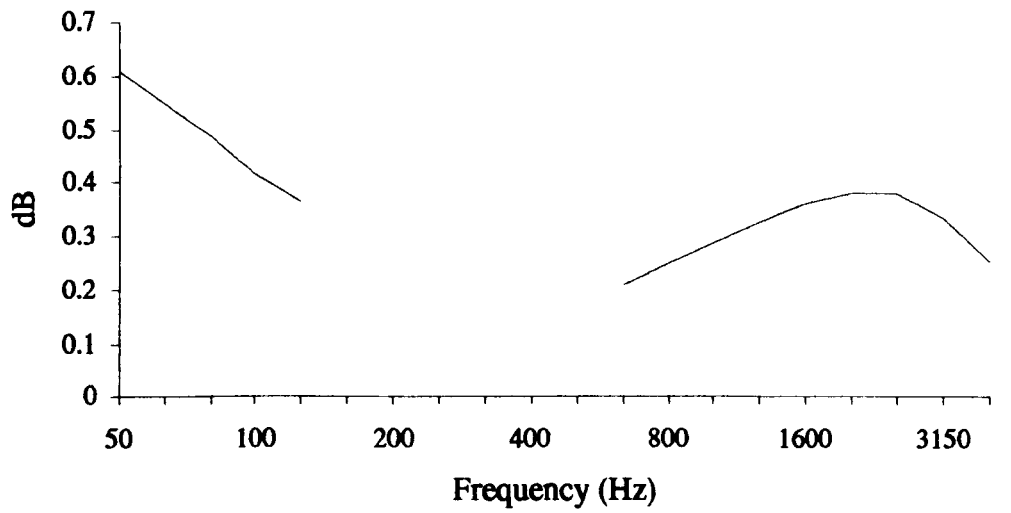

Figure 2.6: Edge effect on overall transmission loss

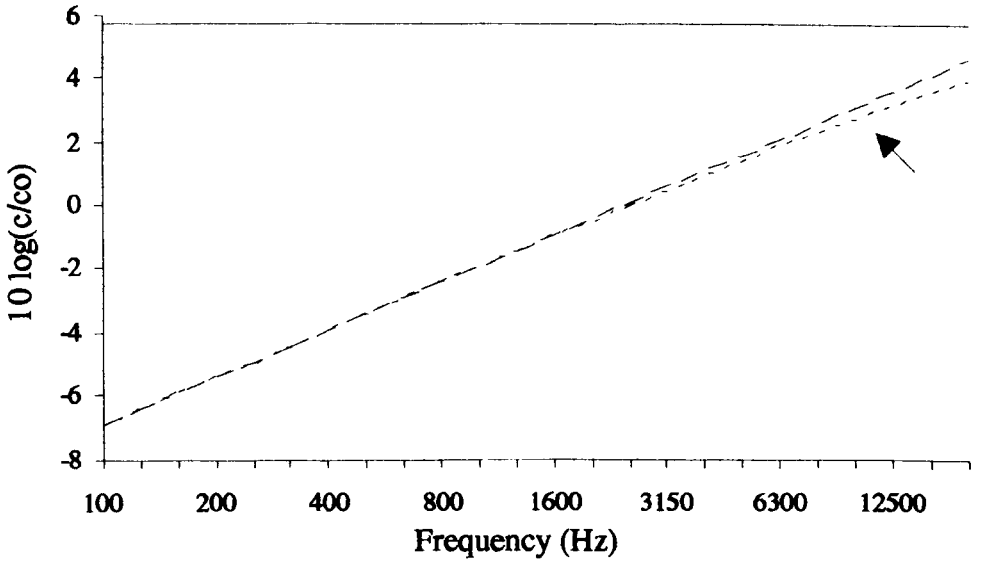

Figure 2.7: Phase speeds for 1:8 scale perspex wall

shear wave only — — — — bending wave only - - - - - - - - effective bending wave

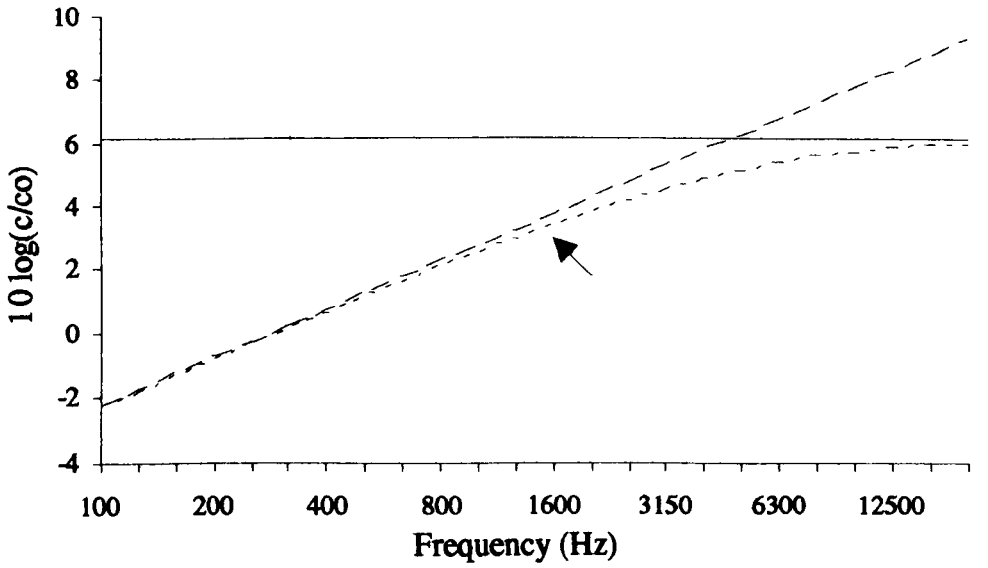

Figure 2.8: Phase speeds for 102.5mm masonry wall

shear wave only — — — — bending wave only - - - - - - - - effective bending wave

3 SCALE MODELLING & ISO 140/3 MEASUREMENT

3.1 INTRODUCTION

A model can be defined as a representation of an existing or planned object. Physically, this often involves a change of scale. A small scale model offers the advantage of being constructed and reconstructed quickly. Effects can be identified that would otherwise not be easily measurable on their full scale equivalents. Hence, they allow a degree of control that would otherwise be extremely difficult. Model measurement is often used in validation of theoretical prediction before application to the full scale problem. It is for this purpose that the models were used as part of this study.

The model measurements were used to validate theories of transmission loss, as initially full scale measurements were not considered to be feasible using standard recommended methods. Even with non-standard intensimetry techniques, discussed in chapters 4 and 8, there seemed little possibility of finding acceptable measurement conditions for such high insulation facades.

Acoustic scale modelling is based on the necessity to ensure that all relevant parameters in the real case are replicated in the model case. Exact design detailing of models is not necessarily that important, as it is not often required to reproduce the sound field at each point within the model but only to determine average energy levels [66]. There is a particular need to preserve the interaction between the structure and the impinging acoustic wave. Hence, there is a minimum requirement that the ratio of wavelength and structural dimension is preserved, and ideally the absorption, transmission, and diffraction mechanisms should also be preserved. The relationship between an acoustic scale model wall and an actual wall should be such that:

$$\frac{\lambda_m}{h_m} = \frac{\lambda_w}{h_w} \qquad (3.1)$$

Where λ and h are the sound wavelength (which can be either an air-borne or structure-borne wave) and thickness respectively, and subscripts m and w are the model and wall respectively. This relationship is achieved by increasing the frequency by a scale factor. For example, a scale factor of 8 requires the frequency range of measurement to be increased by three octaves. Thus model measurement often requires changes in facilities and instrumentation to measure up to these higher frequencies. Other scaling considerations with respect to the standard measurement procedure [67] and facilities [68] should also be met.

3.2 REVIEW OF MODELLING

In acoustics, the earliest physical modelling may have been the use of ripple tanks in Germany in 1840 with studies of reflection, diffraction and transmission [69]. Since then scale modelling has become an integral part in architectural acoustics, though often expensive to build. Technological developments in electro-acoustic transducers and associated instruments enable measurement up to 100 kHz. Applications in building acoustic models have been less common since, for example, many building elements can simply be cut to fit into transmission suite apertures and their sample area is sufficient to characterise the whole element. For large facades such as diaphragm walls where there is a changing internal geometry, a sample element between 10 - 20 m^2 [67] would be uncharacteristic and thus to model the facade is advantageous.

Comparisons between 1:10 scale and full scale measurements in auditoria by Harwood and Burd [70] showed inaccuracies in reverberation times of no more than 20 % which were considered not audibly different. While analysis using scale model

measurement for building facades or environmental (traffic) noise situations often requires scaling of 1:25 - 1:100. Acceptable results have been obtained using very crude models, such as by Delany et al [71] where a 1:30 scale model for the prediction of urban noise propagation deviated by only 2.5 dB from field measurement on complex sites. Barrier models were used successfully by Fujiwara et al [72, 73] giving good agreement with diffraction theory and field measurement.

3.3 SCALE FREQUENCY RANGE

The standard frequency range when measuring the transmission loss of a building element under laboratory conditions is 100 Hz - 3.15 kHz at 1/3 octaves intervals [67]. Hence for a 1:8 scale model, measurements should be between 800 Hz - 25.2 kHz. However, Fothergill [74] indicates that future revisions of ISO 140/3 may include measurement down to 50 Hz. Therefore the frequency range chosen for measurement of all the models was 400 Hz - 16 kHz, relating to 50 Hz - 2 kHz full scale. It became clear that due to signal to noise problems measurements above 16 kHz would not be possible. Indeed some model constructions were only measured up to 10 kHz. This was not thought a practical restriction, as in general the performance of most heavy-weight constructions are acceptable or good at mid to high frequencies and it was observed that the super-critical prediction of the models gave good agreement with measurement. Also it will be seen in chapter 8 that full scale diaphragm wall measurements above 1.25 kHz were unreliable (and unnecessary). Hence an upper limit of 16 kHz (2 kHz times 8) was believed sufficient.

3.4 MODEL WALLS

The models constructed were not 'scale' models in terms of being dimensionally an exact representation of the real walls, rather they only characterised the geometry of the wall. Structural transmission across junctions was believed to be adequately

identified by preserving these basic relationships. As will be shown in chapter 6 with respect to transmission coefficients across these junctions, the value is the same irrespective of material or thickness.

Notionally, the scale factor was 1:8, given by the ratio of the thicknesses, h_m/h_w, and shall be referred to as such subsequently. For ease of construction the models were made of perspex. Hence, they were not specifically models of brick walls since they were not constructed to an equivalent surface density and Young's modulus. However, perspex has acoustic properties not dis-similar to those of brickwork, e.g. a typical longitudinal wavespeed of 2200 m/s compared with 2300 m/s for brickwork. Models with the correct material properties were constructed prior to this investigation by Hung [18] and Ma [19] and are described later.

According to the scaling relationship given by equation 3.1, at 50 Hz a typical full size wall ($h = 0.1025$ m, $c_L = 2350$ m/s) ≈ 28.7, while for the perspex models at 400 Hz ($h = 0.013$ m and $c_L = 2172$ m/s) ≈ 27.4. Thus the 1:8 scale perspex model and a 1/2 brick thick masonry wall, are closely equivalent.

Finally, it was considered whether the facade of a masonry wall could be modelled as a homogeneous material. This was assumed the case as at the highest full scale frequency of interest 2 kHz, which is the worst case, the bending wavelength λ_b is greater than 6 brick and mortar courses and the acoustic wavelength λ is greater than 2 brick and mortar courses. It was also assumed that surface variations would not effect bending propagation in the wall.

3.4.1 Construction of model walls

Various 1:8 scale models were constructed and measured, some of these are shown in figure 3.1, i.e. one single isotropic wall (figure 3.1a), one double wall (60 mm

cavity), three fin walls (figure 3.1b) and three diaphragm walls (figure 3.1c). Each of the fin and diaphragm walls were re-built with additional ribs, firstly one, then three and finally seven ribs, which in turn halved the distance between rib centres. The addition of the ribs increased the total mass of the wall and changed its moment of inertia. Other models built are described in later chapters. Plate A.7.1 shows the single, seven rib fin and diaphragm wall models. All models were made from 13mm perspex with the following properties:

Size = 1 m x 1 m $\quad m = 15.47\ Kg/m^2 \quad \rho_c = 1190\ Kg/m^3$

$c_L = 2172\ m/s \quad f_c = 2328\ Hz.$

Where, m is the surface density, ρ_c is the material density, c_L is the longitudinal wavespeed and f_c is the critical frequency of the single isotropic wall. The cross-ribs and fins were 50 mm wide (equivalent to a full scale width of 400mm) with their edges milled smooth. Ribs were added as required and glued perpendicular to the leaves at regular vertical centres; (the glue was a composite mix of 'Tensol' cement No. 70). Models were sealed into the aperture with plasticine and heavy tape and weak links were checked for, originally with a stethoscope and later using intensimetry.

3.5 TEST FACILITIES

Transmission loss measurements were made of all the model walls. The measurement criteria used to define the airborne sound transmission loss of a building element is given by ISO 140/3 [67]. It requires two isolated rooms where a highly diffuse sound field can be created. The only connection between the rooms should be the aperture where the test elements are placed. Where the rooms are connected by the same party wall, or elsewhere, this should have a significantly higher transmission loss than the element under test to reduce any flanking transmission. Background noise levels and

sound transmission by flanking paths should be low enough so as not to be influential upon measured room levels.

Model measurements were carried out in the small transmission suite at the Acoustic Research Unit, Liverpool University. The suite consists of two almost equally sized rooms, the details of which are given in table 2 below:

Table 2: Small Transmission Suite Rooms

	Volume (m^3)	Surface Area (m^2)	Dimensions (m)
Source Room :	12.97	33.74	2.875 x 1.819 x 2.48
Receiver Room :	13.08	33.91	2.875 x 1.835 x 2.48

The aperture area is 1 m^2 with a 300 mm reveal, centred in the 1.8 m x 2.48 m wall. The two rooms are isolated by a 50 mm cavity containing an absorbent fibrous mat. Each room is constructed of 0.1 m masonry walls, an in-situ concrete roof and screeded floor. Walls and ceiling are plastered with a minimum 13 mm hard plaster and each room has a small window (0.04 m^2) of thickened glass (25 mm) and a 1 m x 2 m sealed steel insulated door. Both rooms are isolated from the structural floor by a thick fibrous mat. The research unit is on the second floor of the Mechanical Engineering Building where nearby rooms contain heavy plant and equipment in frequent use. These can produce low frequency vibrations throughout the building and occasionally hamper measurements.

Let us consider the acceptability of the transmission suite rooms for transmission loss measurement. ISO 140/1 [68] requires the source and receiver room to be at least 10 % different in volume and shape, which is not met by these rooms. The minimum room volume (50 m^3) also cannot be met, yet at the lowest frequency of interest, 400 Hz, at least 2 wavelengths occur across the shortest room dimension. For transmission loss measurements it is required that room is able to produce a diffuse

sound field over the frequency range of interest. Schroeder [75, 76] considers the room to be 'sufficiently diffuse' at frequencies above a cut-off frequency, f_{cut}, given by,

$$f_{cut} = \sqrt{\frac{T M_o c^3}{V \pi 8.8}} \qquad (3.3)$$

Where T is the reverberation time, V is the room volume, c is the speed of sound in air and M_o is the modal overlap. The modal overlap describes the configuration of modes within a finite space or element for an excited frequency band and will be of concern at various points within this study. It is given by:

$$M_o = \frac{\Delta f}{df} \qquad (3.4)$$

Where Δf is the width of a mode at its half power amplitude (3 dB down) and ∂f is the difference in frequency between adjacent mode centres. Where the modal overlap is less than 1, there are few modes within the excited bandwidth. Higher modal overlaps describe an increasing closeness between modes and/or increased damping of their resonances, collectively contributing to the room response. Therefore a value of 3 describes a high density between modes producing a diffuse sound field within the room. Schroeder [76] used a modal overlap value of 3, but Crocker [77] found an overlap of 0.3 to be acceptable. Where $M_o = 0.3$, $f_{cut} = 293$ Hz for the transmission suite rooms, which was considered acceptable as this was below the lower frequency limit of 400 Hz. Any concern about the sound field at low frequencies was not such a worry due to the use of intensimetry for many of the measurements described in chapter 4. For the 1:4 scale model walls, described later, $f_{cut} = 98$ and 110 Hz for the suite rooms, again below the 400 Hz lower measurement frequency. Also, with respect to the field measurements of full size walls in the sports hall described in chapter 8, f_{cut} was always less than 30 Hz, therefore again below the lowest measured frequency.

The dimensions of the transmission suite rooms should allow a uniform spacing of the natural room modes, so as to produce diffuse sound fields over the frequency range of interest. Long reverberation times are characteristic of reverberant rooms, but should not be excessively long at low frequencies (> 2 seconds). A long reverberation time does not necessarily indicate a diffuse sound field i.e. if the room is very large. Meyer and Kuttruff [78], as described in Cremer [79] show that reverberation can be considered in a statistical fashion if there are sufficient room modes. Lubman [80] describes three frequency regions for a room. Where, f_0 is the first room resonance, f_{cut} is given by equation 3.2 and f_{air} is the frequency above which air absorption becomes significant.

$f_0 < f > f_{cut}$:

The modal overlap is low and the source cannot couple efficiently with the room and therefore the room spatial variance of sound pressure is high. This frequency range is termed the 'volume control region' as an increase in the room volume increases the modal density (equation 7.12) and thereby reduces the spatial variance.

$f_{cut} < f < f_{air}$:

The modal overlap is high with a low spatial variance of sound pressure. This variance decreases with an increased product of bandwidth and reverberation time, termed the 'statistically controlled region' and is usually a number of octaves wide.

$f > f_{air}$:

The field becomes semi reverberant and is controlled by moist air absorption, termed the 'air absorption or direct field region.'

According to ISO 140/1 [68] the transmission suite test aperture can be less than the 10 m^2 as long as the wavelength of the free flexural wave in the test element at the lowest frequency is less than half the minimum dimension of that element. Thus:

$$\lambda_b < \frac{L_{min}}{2} \qquad (3.5)$$

Where L_{min} is the shortest dimension of the test element. The test aperture is 1m x 1m, so for the 13 mm perspex models λ_b = 0.356 m at 400 Hz giving a panel dimension of 2.8 bending wavelengths. The transmission suite rooms at a 1:8 scale are equivalent to full size rooms of a volume of 6670 m^3, which is similar to that of the sports halls constructed with diaphragm walls measured in Chapter 8.

Hence, the small transmission suite rooms were accepted as meeting the general qualitative requirements of ISO 140 parts 1 and 3 [67, 68] and were suitable for transmission loss measurements between 400 Hz - 16 kHz.

3.6 MEASUREMENT OF TRANSMISSION LOSS

The reader is reminded of some basic definitions of the measured quantities. The airborne transmission loss of an element, TL, can be defined in terms of sound power:

$$TL = 10\log_{10}\left[\frac{W_1}{W_2}\right] \quad dB \qquad (3.6)$$

where W_1 and W_2 are the sound powers incident on the test element from the source room (1) and transmitted into the receiver room (2) respectively. The 'insertion loss' of an element is simply the change in sound pressure level within the receiver room before and after placing the panel in the aperture. The 'level difference' is the difference in room averaged pressure levels. Measured values for the same element vary in different facilities and therefore results are standardised by accounting for the receiver room sound field.

The rate of transfer of sound energy through an element, given by Halliwell and Warnock [81] is:

$$\tau S \frac{p_1^2}{4\rho c} \tag{3.7}$$

where τ is the transmission coefficient through the aperture, S is the area of the test element, p is the rms sound pressure, ρ is the density of air and c the speed of sound in air. For steady state conditions to exist between the two rooms:

$$\tau S \frac{p_1^2}{4\rho c} = \frac{b p_2^2 V_2}{\rho c^2} \tag{3.8}$$

where:

$$b = \frac{Ac}{4V_2} \tag{3.9}$$

A and V are the absorption and volume of the receiver room respectively. By assuming no test element in the aperture, $p_1^2 = p_2^2$ and rearranging equations 3.8 and 3.9, gives:

$$\frac{1}{\tau} = \frac{S}{A} \tag{3.10}$$

Therefore, assuming perfectly diffuse conditions and sound transmission only through the test element, TL is given as:

$$TL = L_1 - L_2 + 10\log_{10}\left[\frac{S}{A}\right] \quad dB \tag{3.11}$$

where L_1 and L_2 are the room averaged sound pressure levels in both rooms. What is measured is the apparent transmission loss, TL', which includes any sound transmitted from source to receiver room by 'flanking paths' i.e. through the wall, floor or roof. Suite design tries to limit transmission via these paths to a minimum.

Variations in laboratory design can also influence the measured transmission loss. Craik [82] examined theoretically variations in measured transmission loss between one laboratory design and another using Statistical Energy Analysis. He predicted a 2 dB level difference in transmission loss due only to the separating wall being connected to one room, then both rooms; thus changing its damping.

3.7 TRANSMISSION LOSS MEASUREMENTS OF 1:8 SCALE WALLS

3.7.1 Source signal

The sound source was a broadband random signal produced from the signal generator of an FFT analyser with a band width of 12.5 Hz - 20 kHz. The signal was transferred through a Mosfet amplifier, via a switch box, to two interchangeable speakers - a mid range and an omni-directional high frequency speaker. The frequency spectrum of a typical mid-range speaker was found sufficient for the lower insulation model walls, but for the diaphragm and double wall models a second omni-directional speaker was introduced consisting of a boxed array of 6 tweeters. This gave sufficiently higher sound pressure levels in the source room up to 16 kHz. The speaker array reduced any undesirable directional characteristics produced in the source room. Between the signal generator and amplifier the signal was transferred through a high pass filter set to 2 kHz which was switched in when using the high frequency speaker to protect it from low and mid-frequencies damage. This omni-directional speaker was placed above the mid range speaker which faced into a far corner of the source room and was suspended to allow all of its six speakers to be utilised. Figure 3.2 shows the source room response of both speakers, the mid-range speaker peaks at 800 Hz and the high frequency speaker at 6300 Hz. Where repeatability measurements were carried out the speakers were re-positioned in the

opposite far corner of the source room. Measurement variations were within the limits in accordance with ISO 140/2 [83].

3.7.2 Measurement procedure

The method adopted for the measurement of the 1:8 scale walls was according to ISO 140/3 [67]. The layout for the small transmission suite and measurement set-up is shown in figure 3.3. The Instrumentation used is listed in Appendix A.4.

The room sound field was measured using either a precision integrated type 1 sound level meter with an attachable 1/3 octave filter set, or, a ZONIC-AND Fast Fourier Transform (FFT) analyser allowing values at all 1/3 octave frequencies to be measured simultaneously. This was fed to a revolving boom in the source or receiver room. The boom was positioned slightly off centre with the room and at an angle such that the microphone revolved through a non-horizontal axis. A 1/4" pressure microphone was used as the frequency range required was up to 16 kHz. As the same microphone was used for both rooms any loss of sensitivity at higher frequencies was negated. The boom revolved through two 16 second cycles and an $L_{eq(32s)}$ was taken to give the room averaged sound pressure level. L_{eq} is the equivalent continuous sound pressure level which has the same amount of acoustic energy as that measured over the given time period.

The microphone was kept at least 0.215 m from the wall boundaries which is $\lambda/4$ at the lowest frequency of interest. This gave a revolving boom circumference of 4.36 m and a total averaging rotating distance of 9.27 m. $\lambda/2$ is often given as a minimum distance away from boundaries but this would have reduced the rotating distance significantly. A precedent for using a $\lambda/4$ is as the minimum microphone distance away from rotating diffusers is given in ISO 3741: 1988 (E) [84].

At frequencies up to 8 kHz a building acoustics analyser was used to measure the reverberation time. A level recorder was used above this frequency. Three sets of measurements were taken at each frequency, with the microphone in different positions. The measurements were repeated a further 6 times and the mean of the 18 reverberation times were used.

3.7.3 Measurement of surface acceleration

Surface acceleration measurements were also made on the single, fin and diaphragm 1:8 scale walls to compare with Statistical Energy Analysis prediction. The wall was excited using random broadband source from an attached driver and measurements of mean acceleration levels were taken on the leaf surfaces. Eight randomly chosen points were measured and the logarithmic surface average was calculated for each 1/3 octave frequency band. One 4.2 g miniature accelerometer (DJB A23/E) was used so as to reduce the added mass on the wall.

3.7.4 Measurement difficulties

Results are presented with a scaled frequency x-axis but a lower and upper point indicating the equivalent full size frequency range will be given where required, denoted by > and < respectively. Results in this chapter are given in order to highlight measurement problems and developments in the measurement method. Comparison with theory will be shown in chapter 5 onwards.

Initial measurements of single and double leaf models gave concern with regard to flanking transmission. One significant path between the rooms was the wooden spigot surrounding the test aperture. The spigot bridged the insulated cavity between the aperture walls. This was cut to produce a central 10 mm gap. The difference in transmission loss between the single and double walls before and after cutting of the

spigot can be seen in figure 3.4. A positive value shows an increase in transmission loss after cutting the spigot. The single wall transmission loss improved at all frequencies and at low and mid frequencies significantly. The change in double wall transmission loss is difficult to interpret though improvements do occur at the frequencies of lowest transmission loss, at low frequencies and about coincidence.

Figure 3.5 shows the measured transmission loss for the single and double leaves after cutting the spigot. It was difficult to measure transmission loss at frequencies greater than 6.3 kHz where levels began to flatten for the single model wall and fall dramatically for the double model wall. This was believed due to a combination of poor signal in the receiver room and flanking transmission.

3.8 RESULTS FROM PREVIOUS MODELS

A previous material scale model of a diaphragm wall has been constructed and measured at Liverpool University. The research was carried out as two undergraduate final year dissertations [18, 19] supervised by Dr. B.M. Gibbs. The measurements are of importance to this research as the model was a 1/4 scale wall where the material density and Youngs modulus of a real masonry diaphragm wall were matched to within 10 %.

The wall was initially built in 1982 by Hung [18]. It was tested in the large transmission suite at the Acoustics Research Unit, built into an aperture 2.26 m x 1.80 m. A lightweight concrete mix was used, cured to within 4 % of the desired material density. Six pre-cast panels were required per leaf, and the gaps filled with mortar. Cross-ribs were butted and bonded to the leaves. Transmission loss was measured as the model was constructed, first as a single wall, then as a 7 rib fin wall, a diaphragm wall and an insulated diaphragm wall. Details of the scale wall are given in table 3. On dismantling of the model vertical cracks were found along one side at

the cross-rib/leaf junctions which brought into question the bonding and thus the results for the diaphragm wall.

In 1986 Ma [19] repaired and re-measured the wall. This time better rib to leaf bonding was assured and measurements of transmission loss and vibrational level difference between leaves were conducted. The measurement range was 400 Hz - 12.5 kHz in 1/3 octaves, equivalent to a 100 Hz - 3150 Hz full scale. Plate A.7.2 shows the 1:4 scale model fixed in the test aperture.

Some of the results by Hung and Ma were published by Gibbs & Lewis [17]. Measurements generally were dubious above 8 kHz, with a plateau in the transmission loss curves due to a poor signal/noise ratio. Figure 3.6 shows the transmission loss of the single wall & fin wall measured by Hung. The theoretical critical frequency, f_c, for the single model wall was 1093 Hz which appears to be 1/3 octave lower than measured (to 1/3 octave resolution). For the fin wall f_c is difficult to discern though a change in gradient does occur at about 800 Hz. Sub-critically the transmission loss is less than the single wall and a plateau region occurs. This was taken as evidence of an orthotropic effect introduced by the ribs. There was no measurable increase in transmission loss due to the additional mass of the ribs super-critically, but there was clear improvement about f_c.

Figure 3.7 shows the measured vibrational level difference between the diaphragm wall leaves before and after repair. The degree to which the earlier model by Hung was not bonded correctly is seen. Vibrational level difference is close to zero at low frequencies and increases slowly with frequency. Figure 3.8 shows the measured transmission loss of a model diaphragm wall by Ma and an SEA prediction by Gibbs [17]. Agreement is good and both curves, again, indicate a plateau region below critical coincidence.

To summarise, the early work by Gibbs [17], Hung [18] and Ma [19] indicated that the addition of fins to the single wall and the addition of cross-ribs to the diaphragm wall changed the character of the walls transmission loss from that of an 'isotropic' to an 'orthotropic' plate. However the measurements are limited with little data in the sub-critical region.

Two critical frequencies occur with orthotropic walls. The 'upper' critical frequency, $f_{c,u}$, for both the fin and diaphragm wall is that of a single isotropic leaf of the same material. The 'lower critical frequency, $f_{c,l}$, is based on the bending stiffness across the ribs. Above $f_{c,u}$ a recovery to mass law curve is seen in transmission loss and the wall behaves as a single isotropic wall. Below $f_{c,u}$ the transmission loss rises at a slow gradient for the diaphragm model and stays relatively flat for the fin model.

Strong bonding results in a low vibrational level difference between the leaves, which increases slowly with frequency, from 1 dB to 7 dB.

3.9 CONCLUDING REMARKS

This chapter has explained the purpose and practicalities of scale modelling, the construction of a series of 1:8 scale model walls, the previous research and the measurement of transmission loss made according to ISO 140/3.

The problems of flanking transmission, particularly with higher insulation model walls and a weak signal above noise in the receiver room at frequencies above 6.3kHz limited the standard approach. Therefore it was decided that another method should be considered; that of 'sound intensimetry'. This remained a non-standard method through most of this study, but ISO 9614-1 [90] was introduced during the final 12 months. It was hoped that intensimetry, which senses sound as a vector, would discriminate against the effect of flanking transmission and give greater bias

toward the sound transmission through the test aperture. It was also hoped that intensimetry would improve the signal to noise ratio and thus increase the upper frequency limit of measurement to 16 kHz. Importantly, an investigation of intensimetry under laboratory conditions was seen as a prelude to field measurement trials of diaphragm walls in-situ.

Chapter 4 will describe the theory and application of sound intensimetry to transmission loss measurements.

Specification:

	Limits of Model Spec.	Brickwork	Actual
Density (Kg/m^3)	1665-2035	1850	1774
Dyn. Youngs Mod. ($N\ m^{-2}$)	$8.55x10^9$ - $1.05x10^{10}$	$9.5x10^9$	$1.01x10^{10}$

Concrete scale mix:

	Mortar sand	Perlite	Agg.(10mm)	Cement	Water	Total
Spec. Gravity	2.8	0.28	2.65	3.15	1	
Volume (m^3)	0.213	0.261	2.555	0.073	0.198	1
Weight (Kg)	596.4	73.1	675.8	230	198	1773.5
Pulse velocity	2577.3 m/s					
Calculated C_L	2508 m/s					

Dimensions of 1/4 Scale Model Wall:

Scale	1/4	Full
Thickness (m)	0.025	0.1025
Cavity Depth (m)	0.11	0.4-0.9
Rib Centres (m)	0.283	1-1.5
I_{xx}	$2.39x10^{-4}$	
$f_{c,l}$	80.5 Hz	
$f_{c,u}$	1093 Hz	
Panel length (m)	2.26	
Panel heights (m)	1.81 & 1.5	

Transmission suite dimensions:

	Length	Width	Height
Source room	5.75	4.9	4.3
Receiver room	5.75	3.1	4.3

Table 3: Details of 1982 1/4 scale material model wall

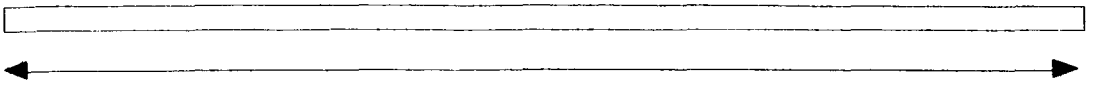

Figure 3.1a: Single isotropic wall

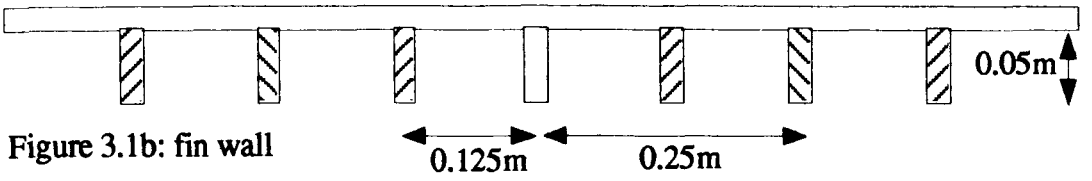

Figure 3.1b: fin wall

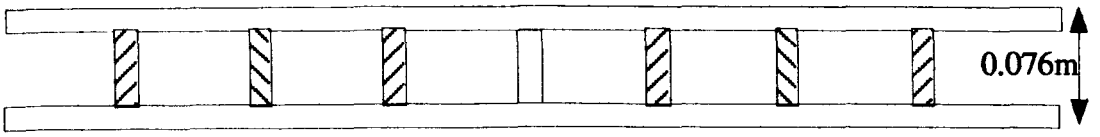

Figure 3.1c: diaphragm wall

Figure 3.1: Dimensions of 1:8 scale walls

1 rib location 3 rib locations 7 rib locations

Model material : perspex
Sheet & rib thickness : 0.013m
Panel area : 1m x 1m

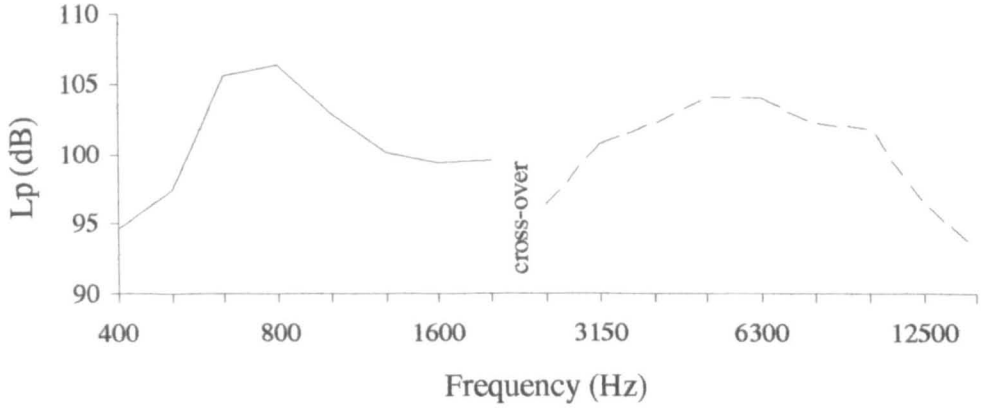

Figure 3.2: Typical source room sound pressure levels

Low-mid frequency speaker

High frequency speaker

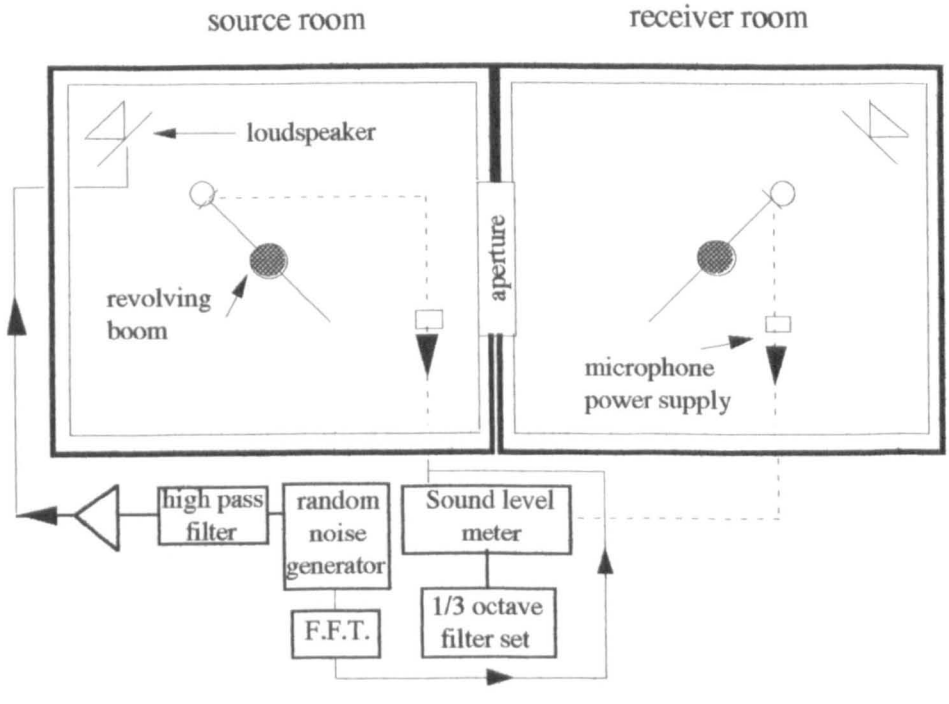

Figure 3.3: Layout for ISO 140/3 measurement

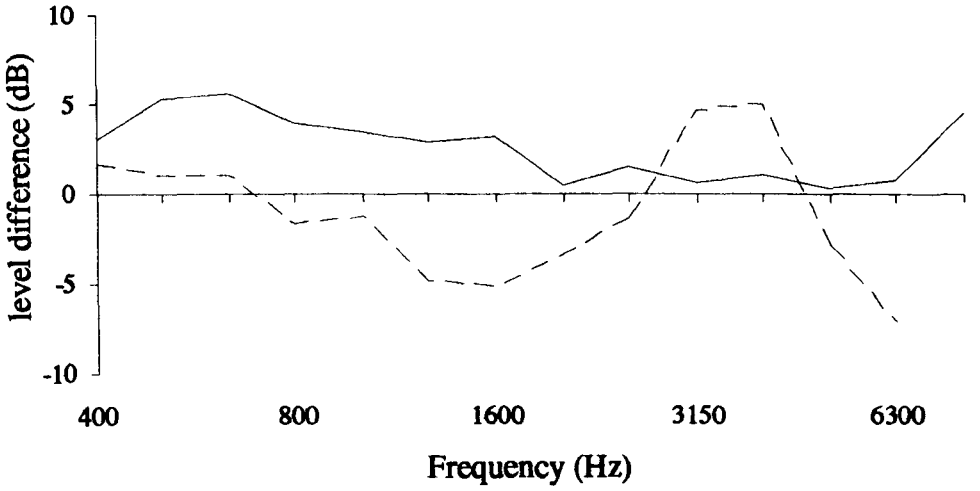

Figure 3.4: Difference in transmission loss before and after cutting spigot

Single

Double

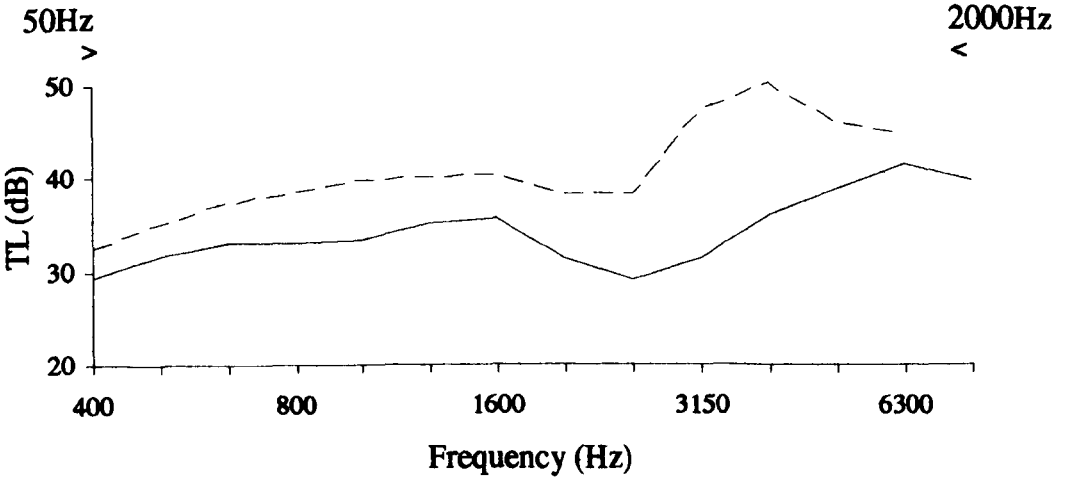

Figure 3.5: Transmission loss of single and double walls after cutting spigot

Single

Double

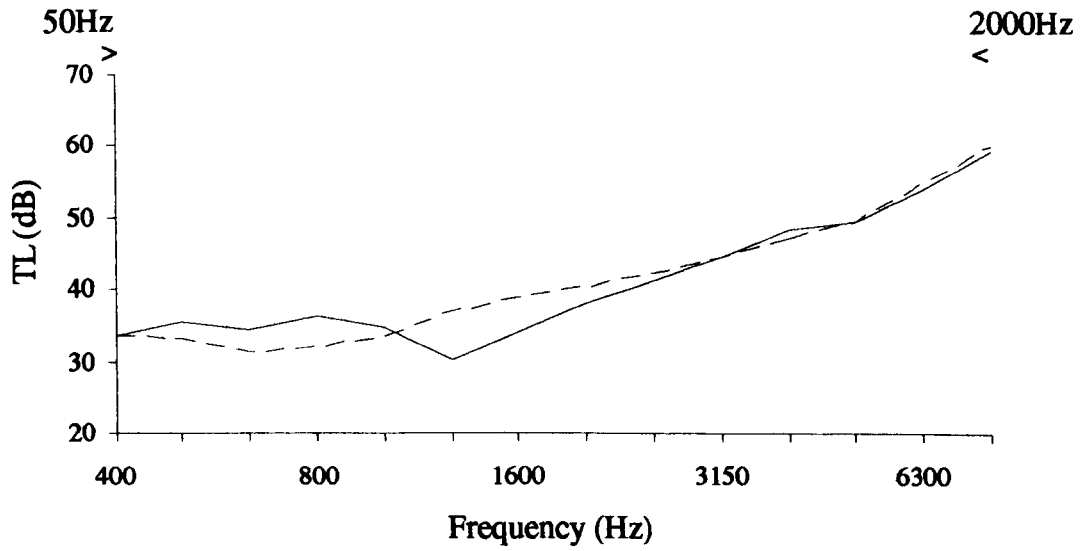

Figure 3.6: Transmission Loss of 1/4 scale single and fin walls

Single Fin

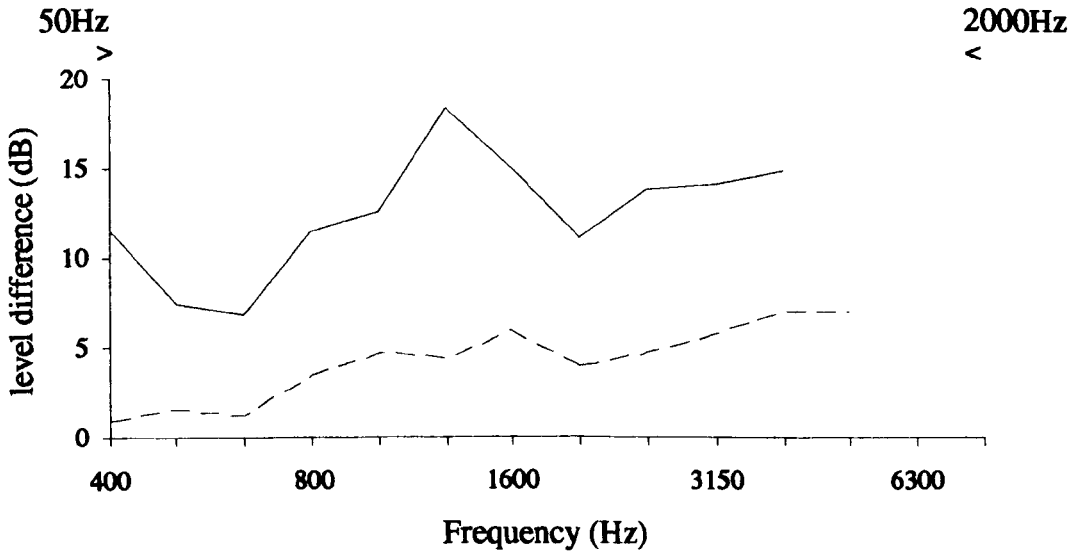

Figure 3.7: Vibration level difference between leaves of the 1/4 scale diaphragm wall

Hung measurement [18]

Ma measurement [19]

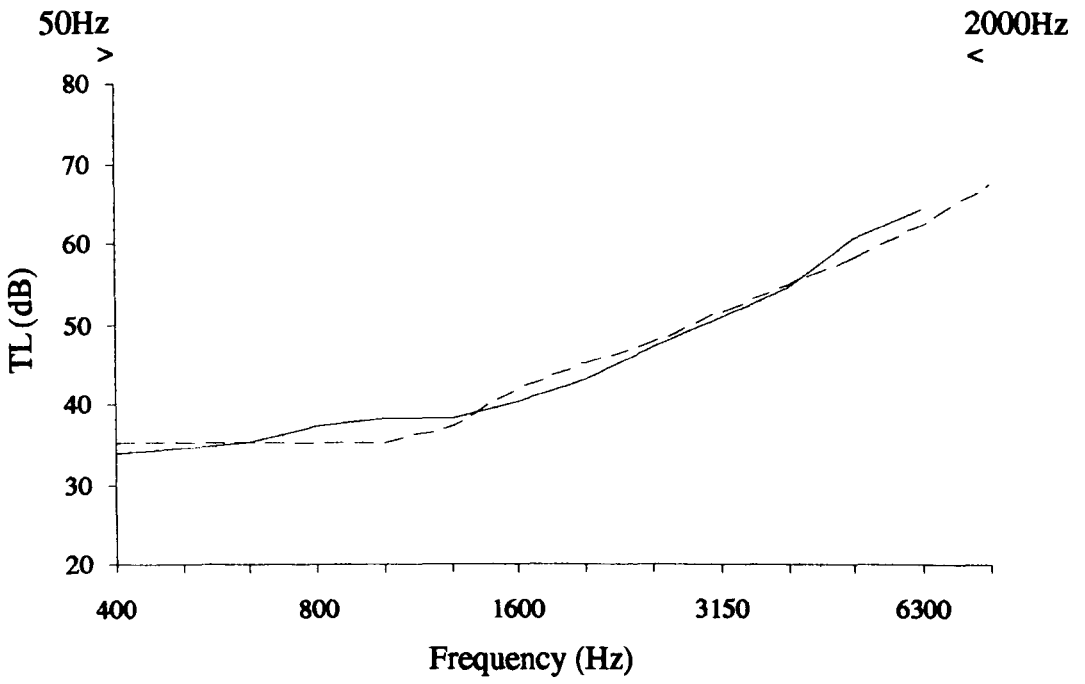

Figure 3.8: Transmission loss of 1/4 scale diaphragm wall

——— Measurement [19]

– – – – – SEA Prediction [17]

4 TRANSMISSION LOSS MEASUREMENT BY INTENSIMETRY

4.1 INTRODUCTION

As transmission loss measurements suffered from flanking transmission through the side walls and from poor signal at high frequencies with the standard ISO 140/3 method, another measurement method was required. This chapter introduces the non-standard technique of sound intensimetry and applies it to the transmission loss of the scale model walls. In chapter 8 the method is applied to the field measurement of full scale diaphragm walls. Sound intensimetry describes the method of measuring the average sound intensity level over a measurement area. As the method was non-standard throughout most of the research much consideration has been given to the adaptation of previous work using intensimetry. ISO (International Standards Organisation) and ANSI (American National Standards Institute) draft standards were used for guidance and as indicators of measurement accuracy for both model and field measurements. This chapter discusses the background to, and theory of, sound intensity; the application of sound intensimetry to transmission loss measurements, the models measured, and finally the use of field indicators to determine the accuracy of results.

Instantaneous sound intensity can be defined as the rate of flow of sound energy per unit surface area, where the area is perpendicular to the instantaneous particle velocity vector [85]. A simpler definition for sound intensity is the product of the particle velocity and the sound pressure at a point in a sound field. As particle velocity is a vector quantity, with both magnitude and direction, therefore so is sound intensity, measured in Watts / m^2 in a direction normal to the specified unit area. Energy flow in real sound fields is in many directions at any instant and therefore sound intensity is 'time-averaged' so that continual dominant net flows of energy can be identified in particular directions.

Sound intensity probes consist commonly of two pressure microphones, usually face to face or side to side. This design allows the measurement and calculation of the particle velocity from the pressure gradient between the two microphones and the average pressure level across them. Previously and less commonly a back to back pressure microphone configuration has been used, or pressure and particle velocity microphones in conjunction. For this research a B&K Type 3519 face to face probe was used, with two B&K Type 4135 6 mm phase-matched pressure microphones (for model measurement) shown in figure 4.1.

4.2 A SHORT HISTORY OF SOUND INTENSIMETRY

The progress of sound intensity as a feasible method of measurement has been rapid in the last 20 years with the advent of digital processing techniques. Recently, the first international standards have appeared [90] and the practical uses of sound intensity are being more widely appreciated.

Expressions for sound intensity appear as early as 1878 [27], but measurement technology has taken almost a century to catch up. A comprehensive work on sound intensity to date is given by Fahy [86] with a full historical review. In 1931 Olsen [87] patented an acoustic wattmeter which would work only under ideal free field conditions. During the 50's and 60's sporadic work followed. Wolff & Massa's 'Field Wattmeter' processed separate signals from pressure and particle velocity microphones. In 1941 Clapp & Firestone [88] used pressure microphones with a ribbon velocity microphone and obtained good results in an impedance tube up to 2 kHz. T. D. Schultz in 1956 [89] investigated the determination of sound power under reverberant conditions and expressed certain well founded reservations. The requirement for high quality transducers and phase matched circuits was essential, but this would have to wait until the mid-seventies for development. Important work in

the early 70's by Zyl, Anderson & Burger and Lambrich & Stahel resulted in the first reliable sound intensity meters for field measurement over a wide frequency range, described by Fahy [86].

In the mid-seventies the introduction of integrated circuit devices and dual channel digital filters have solved the problems identified by Schultz. There has been prominent work throughout the 70's and 80's by Fahy in the U.K., Chung in the U.S.A. and Lambert & Badie-Cassagnet in France [86]. Fahy in 1975, preparing for an undergraduate project by Miller, showed how two phase-matched frequency microphones and a dual channel frequency analyser could be used to measure intensity. The time-dependant intensity could be expressed as the imaginary part of the cross-spectrum density function in the frequency domain. This relationship has been the basis of commercially available software today.

At present, ISO has produced a two part standard for the regulation of sound intensity measurement with respect to the determination of sound power levels of sources. ISO 9614-1 was adopted in December 1991 [90] while ISO/DIS 9614-2 [91] (and ANSI S12.12 [92]) are still under discussion. These all consider the definition of the measurement surface, the procedure of integration and field indicators. IEC Working Group 11 has also issued a draft standard, IEC 1043 [93], for instrumentation. This standardisation of convenient sound power measurement methods is part of the regulations toward the enforcement of EC Directives 89/392/EEC and 91/368/EEC concerning health and safety legislation for new types of machinery. The standards are primarily developed for the determination of sound power levels for machine sources, they are not written directly with regard to transmission loss measurement. ISO DIS/9614-2 was unfortunately only available to the author after all field measurements had been completed, nevertheless most, but not all, of its criteria were met.

Sound intensimetry allows for the determination of the sound power of a source under situations, such as in the presence of significant background, parasitic or extraneous noise. Parasitic noise refers to background and room effects characterised by sound intensity vectors in directions other than normal to the measurement surface. Present intensimetry methods allow large complex sources to be measured and regions of separate sound power identified. Measurement can also be made on-site where non-ideal conditions exist, and noise source identification from complex sources is possible in real situations such as on factory floors, offices, production lines etc., where other peripheral noise sources may be active. On-site sound pressure level measurements used to calculate sound power levels are only possible under special conditions which rarely occur. Sound intensity therefore offers technical advantages previously unavailable. In addition, the method can be applied to the measurement of sound transmission loss giving advantages in both laboratory and field testing compared over the standard pressure level difference method.

4.3 THEORY OF SOUND INTENSITY

Let I(t) be the rate of flow of sound energy per unit surface area in the direction of the local acoustic particle velocity at an instant in time. This is given by:

$$I(t) = p(t)\, u(t) \qquad (4.1)$$

where p(t) and u(t) are the rms sound pressure and particle velocity instantaneously at a point in space.

Sound intensity is expressed as the product of the pressure and particle velocity in the time domain and normally a time-averaged value, $\bar{I}$, in a time stationary sound field is measured, given by:

$$\bar{I} = \frac{1}{T}\int_0^T I(t)\, d(t) \qquad (4.2)$$

We are concerned with the normal sound intensity, $\bar{I}_n$, which is the component perpendicular to the measurement surface by the unit vector , n, such that I_n is :

$$I_n = I \cdot n \qquad (4.3)$$

Its logarithmic expression is the normal sound intensity level, L_i; an unsigned value given by:

$$L_i = 10 \log\left[\frac{|I_n|}{I_o}\right] \quad \text{dB} \qquad (4.4)$$

where I_o is the reference intensity level 10^{-12} W/m^2. The particle velocity u is described as 'active' where the u is in phase with the pressure and 'reactive' when 'u' is 90° out of phase. At other phase angles, u has both active and reactive components. An example of a purely active field is a plane wave propagating under free field conditions, here all energy flow produces a positive net intensity. The acoustic impedance, Z, is given by:

$$Z = \frac{p}{u} = \rho c \qquad (4.5)$$

Where ρ is the density of air and c the speed of sound in air. The magnitude of the intensity is given by [86]:

$$|I| = \overline{p\,u} = \frac{p_{rms}^2}{Z} \qquad (4.6)$$

An example of a highly reactive field is a diffuse field in a reverberation room. All energy flow at a point would be equal and random, giving a time averaged intensity of zero. A relationship can be made between pressure and intensity even though the intensity is zero. We can say that one-sided intensity, I_x, (that is the intensity in one direction, or on one wall of a room), is related to the pressure in a purely diffuse field by [94]:

$$I_x = \frac{p^2_{rms}}{4\,\rho c} \qquad (4.7)$$

Generally, sound fields have active and reactive components. In normal conditions, (semi-diffuse with extraneous noises) sound pressure is an unreliable measure of the power radiated from a source, as the field is not directly related to that source. However, sound intensimetry distinguishes the active and reactive components from the source and therefore the net energy flow.

4.3.1 Finite Difference Approximation

The measurement of intensity by a microphone pair is based on an approximation of the pressure gradient along the axis between the two microphones. According to Euler the pressure gradient and density of the fluid determines the particle acceleration. The particle velocity is then obtained, where:

$$u = -\frac{1}{\rho}\int \frac{dp}{dr}\,dt \qquad (4.8)$$

dp and dr are a small change in sound pressure and distance respectively.
A straight line approximation of the pressure gradient is given by:

$$\frac{dp}{dr} = \frac{\Delta p}{\Delta r} = \frac{Pa - Pb}{\Delta r} \qquad (4.9)$$

where Δp is the difference in sound pressure between the microphones, denoted a and b, and Δr is the distance between a and b. This is termed the finite difference approximation and depends on the frequency and microphone spacing chosen. The particle velocity is now written as:

$$u = -\frac{1}{\rho}\int \frac{Pa - Pb}{\Delta r}\, dt \qquad (4.10)$$

The pressure is simply the average of the two microphones :

$$p = \frac{Pa + Pb}{2} \qquad (4.11)$$

Therefore substituting equations 4.10 and 4.11 into equation 4.6, gives the instantaneous sound intensity at a point in space:

$$I = -\frac{Pa + Pb}{2\rho\Delta r}\int (Pb - Pa)\, dt \qquad (4.12)$$

4.3.2 Frequency Domain Formulation

Work in the late 1970's by Lambert, Miller, Fahy and Chung, described in Fahy [86], derived expressions for intensity based on complex Fourier transforms of two closely spaced microphone signals. The intensity can be related to the imaginary part of the cross spectrum of the two sound pressures. The cross spectrum is defined as the cross spectral density multiplied by the frequency resolution of the Fourier transform [95]. Cops [94] gives Chung's [95] expression in digital form as:

$$I = \frac{1}{2\pi\rho\Delta r}\sum_{n=1}^{N}\frac{\mathrm{Im}\langle G_{ab}\rangle}{f}\Delta f \qquad (4.13)$$

G_{ab} is the one sided cross-spectral density. A correction is required for phase-mismatch between the microphones, so the true value of G_{ab} is given by [94]:

$$|G_{ab}| = \frac{|\widetilde{G_{ab}}|}{|H_a| \cdot |H_b|} \qquad (4.14)$$

where $\widetilde{G_{ab}}$ is the measured cross-spectral density of H_a and H_b, the transfer function of the two signals. Phase error correction is minimised by using phase-matched microphones. A full derivation and explanation is given by Fahy [86] and Chung [95], while practical aspects are discussed later in the chapter. This method allows for a 'real time' analysis only limited by signal sampling, computational and frequency synthesis. With the advent of FFT analysers and digital filter systems this cross-spectral approach gives a versatile system. A ZONIC-AND 3524 dual channel FFT analyser, with sound intensity and accelerator processor cards, was used for all intensity measurements in this research. Advantages and disadvantages occur with both digital filters and FFT analysers. The versatility of an FFT approach is limited by errors in 1/3 and 1/1 octave filter synthesis and computational processing time, while digital 1/3 octave filters will allow real time parallel processing upto around 20 kHz. With all FFT processors, overlapping is required to reduce the data loss errors caused by windowing, but for steady state signals, as used in this study for transmission loss measurements, both methods will give equally valid results.

Figure 4.2 shows a narrow band spectrum of L_i for the 250 Hz calibration signal using 4096 FFT points; this is clearly difficult to decipher and of limited use in its raw form. Figure 4.3 shows the 1/3 octave spectrum giving an interpretable result and manageable numbers.

4.4 LABORATORY MEASUREMENT OF TRANSMISSION LOSS BY SOUND INTENSIMETRY

The benefits of sound intensity have been predominantly applied as a multiple source or complex source sound power descriptor, such as for work place noise problems. Much research has been carried out into the use of sound intensimetry for the measurement of airborne sound insulation [94, 96 - 101] and recent standards identify 'field indicators' in describing the reliability of measurement result [102, 103]. The Nordtest Project 746 - 88, by S.N.T.R.I. (Swedish National Testing and Research Institute) [107] carried out a large set of independent measurements at different laboratories in order to validate the proposed method. Small high insulation elements were used and results were compared with those obtained by the ISO 140 method with good agreement. S.N.T.R.I. also produced an appendix [105] to ISO 140/5 [106], using the sound intensimetry scanning technique for field measurement. Measurement precision is said to overestimate by 0.5 - 1.5 dB compared to the ISO 140/3 method between 63 Hz - 5 kHz.

Intensimetry has a number of advantages over the standard pressure method. It allows small elements and sub-areas of an element to be measured and the measurement of high insulation elements is possible in the presence of flanking transmission and where a diffuse field in receiver room is not required or preferred. Only the source room is still required to produce a diffuse sound field and the receiver room absorptive characteristics need not be known. Importantly, with respect to transferring the technique to field measurement, less equipment is required and a better extraction of signal from background is possible. The scanning technique allows large facades to be measured and by placing the source signal inside the building this will allow higher source levels to be produced without disturbing the locality. Also local areas of different sound power such as cracks may be identified within a facade. Sound

intensity therefore offers a new development and potential improvements in measurement where ISO 140/5 presently is limited to low insulation facades and ISO 140/3 to laboratory conditions.

4.4.1 Intensity Theory for Transmission Loss

The airborne sound transmission loss of an element under laboratory conditions, according to ISO 140/3, is given by equation 3.10. Under steady state conditions the incident sound power across the open aperture equals the transmitted power. In terms of sound intensity:

$$I_{in} A_w = I_{out} A_w \qquad (4.15)$$

Where A_w is the area of the wall under test and I_{in} and I_{out} are the incident and transmitted sound powers respectively. Substituting equation 4.7 into equation 4.15, for a diffuse incident source field, gives:

$$\left[\frac{p^2}{4\rho c}\right] A_w = I_{out} A_w \qquad (4.16)$$

Knowing the transmission loss is given by equation 3.10 and rearranging equation 4.16, gives:

$$TL = 10 \log\left[\frac{p^2}{\rho c}\right] + 10 \log\left[\frac{1}{I_{out}}\right] + 10 \log\left[\frac{1}{4}\right] \qquad (4.17)$$

This can be rewritten as:

$$TL = L_p - L_i - 6 \qquad (4.18)$$

where L_p is the spatial averaged pressure level in the source room and L_i is the average intensity level over the measurement surface.

4.5 PRACTICALITIES AND LIMITATIONS

The method is promising in that it offers a simple expression for transmission loss, it requires less facilities and equipment and can theoretically operate under problems of extraneous noise and flanking transmission. In reality the reliability of results depends upon the microphone, probe and analyser system, the characteristics of the room sound energy field, extraneous noise sources and the measurement technique. It is important to be able to quantify these factors, and field indicators are used to identify problems with the capability of the analyser, reactivity of the sound field, background and extraneous noise. The main considerations, important for any sound intensity measurement, specific to the model wall and field transmission loss measurements are discussed below.

4.5.1 The Measurement System

Sound intensity measured in a purely reactive field should give a value of zero. This is also true for a single wave travelling normal to the probe axis which can be replicated in a sound intensity coupler (i.e. the B&K Type 3541 - which was used for all calibrations in this research). Any measured intensity which exists is an apparent acoustic flow due to phase error between microphones and/or analyser inputs and is known as residual intensity, $L_{i,o}$. Both microphones should be identically phased matched with a flat amplitude response to limit this error. The difference in phase angle between the two channels determines the low frequency limit of the system. The phase angle is given by [107]:

$$\Phi = \frac{\Delta r \,.\, f \,.\, \rho \,.\, I}{p^2_{rms}} \,.\, 360^\circ \qquad (4.19)$$

Typically the difference in phase angle may be $\pm 0.3^{\circ}$.

The high frequency limit of the system depends on the finite difference approximation, given by equation 4.9. If the wavelength is too small, the finite difference approximation is inaccurate. Therefore a smaller distance between microphones, Δr, allows a higher frequency limit. To a 1 dB accuracy, Chung sets this limit as $k\Delta r \approx 1$ [95], where k is the wavenumber. This is equivalent to approximately 1/6th of a wavelength across the spacer, or a phase angle = 60°. Hence a difference in phase angle of 0.3° is insignificant.

The residual intensity, (the measure of an instruments difference in phase angle) will increase or decrease constantly with the respective sound pressure level. Thus a frequency spectrum of constant level difference can be produced called the 'residual pressure-intensity index', $L_{k,o}$. This is measured in the intensity coupler where a pink noise source is applied normal to the microphones, such that:

$$L_{k,o} = L_{p,o} - L_{i,o} \qquad (4.20)$$

where $L_{p,o}$ is the mean sound pressure level of the two microphones in the coupler. For 1dB accuracy, the phase change must be 5 times the phase mis-match across the spacer, which relates to a constant K. Therefore the limits of an analyser and microphone set up can be given as:

$$Ld = L_{k,o} - K \qquad (4.21)$$

where Ld is termed the 'dynamic capability' of the system. For survey work K = $10\log(1/5) \approx 7$ dB. For precision measurement a higher accuracy is given by

Rasmussen [107], where K ≈ 10 dB. This is compared to the reactivity of the field in which the measurements are taken.

The reactivity of the sound field under test is defined by the 'Reactivity index', L_k, or 'Pressure -Intensity index', given as:

$$L_k = L_p - L_i \tag{4.22}$$

where L_p and L_i are the instantaneous sound pressure and sound intensity measured in the sound field. The index will vary from point-to-point in a field, so a global value is obtained by space-averaging. The field reactivity must be less than the dynamic capability so that measurements are not effected by the residual intensity of the instrument. Therefore:

$$L_k < L_{k,0} - 7 \text{ dB} \tag{4.23}$$

This may also be written in terms of the 'residual intensity index', $L_{i,r}$, where:

$$L_{i,r} = L_p - L_{k,0} \tag{4.24}$$

and,

$$L_i > L_{i,r} + 7 \text{ dB} \tag{4.25}$$

Standard spacers between microphones of 50 mm, 12 mm and 6 mm are presently used, with 12 mm and 6 mm microphone heads. The frequency range for the various microphone/spacer configurations can be found in many manuals/booklets [112]. For all laboratory measurements 6 mm head microphones were used with a 6 mm spacer, which limited the upper frequency limit to 10 kHz. Above this frequency a 3 mm

spacer was used, described later. (For all field measurements a 12 mm microphone head and 50 mm spacer were used, described in chapter 8). Figure 4.4 shows the dynamic capability of the measurement system for the various configurations. At low frequencies the upper limit is highest, varying considerably, while at higher frequencies the curves smooth up to 8 kHz. The reason for the low value at 10 kHz is unknown except it is on the limit of the system.

To check the system the probe was tested for the various microphone size/spacer configurations under free field conditions in the anechoic chamber at the ARU. The intensity probe was positioned facing a loudspeaker 3 m away. In ideal free field conditions it would be expected that $L_p = L_i$, so that $L_k = 0$. Figure 4.5 shows the reactivity indices for 5 different configurations. For all the conventional spacers, generally the reactivity index is less than 0.5 dB, probably due to phase mis-match. At some points this index is negative. Guy [108] examined the occurrence of negative reactivity indices under similar conditions, concluding it to be due to standing waves where the measurement location is near or on a pressure minima. At low frequencies the index rises significantly due to the room being non-anechoic because of its small volume and the depth of absorptive wedges. All configurations show the poorest agreement at their highest frequency limit when the finite difference approximation does not apply. Between 10 - 16 kHz a non-standard 3 mm spacer and 6 mm microphone combination was used. This clearly produces a greater value of L_k reducing the field conditions it can be used in to within the instruments dynamic capability.

The 3 mm spacer was specially made previously and is not commercially available. Through private conversation with B & K such a spacer was believed unsuitable due to the microphones being too close together causing wave interference. As there were reservations towards the use of the spacer it was necessary to test its performance against other conventional configurations. Measurements of sound intensity on a

single model wall using the 3 mm spacer were compared with 12 mm and 6 mm spacers from 1 kHz to their frequency limit. Figure 4.6 shows the difference between L_i values for the 3 mm spacer and other combinations. The curves are all within 1 dB, showing a frequency invariant discrepancy of approximately 3 dB. Therefore 3 dB was deducted from L_i values above 10 kHz. It is recognised that this was not a conclusive test and the conditions of use for such a spacer are probably limited to only good laboratory conditions. Problems of calibration were not encountered as the spacer was only used for level difference measurements.

To summarise, the scale wall laboratory measurements were made with 6 mm head microphones and a 6 mm spacer for 1/3 octave readings between 400 Hz - 10 kHz and a 3 mm spacer between 12.5 - 16 kHz.

4.5.2 Field Reactivity

Intensity measurements in free field conditions produce values of L_k easily within the dynamic range of the instrument system (as seen in figures 4.4 and 4.5). Intensity can be measured in semi-reactive and reactive fields as long as this and other criteria are met. Measurements by Krishnappa [109], where an erroneous noise source is introduced into a free field, recommended a maximum L_k of 5 dB. The smaller the reactivity index, the greater is the range of the spacer available to the operator. Further calculations of phase errors are given by Rasmussen [107].

Cops, Minten & Myncke [100] considered the influence of the various factors such as loudspeaker and microphone positions, diffusers etc. Of particular relevance was a comparison of transmission loss where the reverberant receiver room reactivity was changed by adding absorbent wedges. The difference was seen to be negligible. A reactivity index limit of 10 dB was considered reasonable for such measurements.

In order to determine the influence of the sound field in the receiver room the sound intensity of a 1 rib diaphragm wall was measured under 3 different room conditions. These were, with the receiver room empty; only the back wall covered with sound absorbent wedges (0.3 m long); and where all surfaces were covered. Rectangular absorbent slabs, 0.1 m thick, were placed around the walls and the floor was covered with two absorbent mats, 0.05 m thick. Measurement of reverberation times showed the room to be very 'dead'. Figure 4.7 shows the difference in mean intensity level between the empty room and the two other room conditions. It is seen that except at the lowest frequencies the effect of changing the receiver room conditions is less than 1 dB between any condition. Hence, for all scale wall tests the receiver room was left empty for ease of measurement.

4.5.3 Establishing a Measurement Surface

The measurement surface must completely enclose the sound source so no sound energy is lost. This may take various shapes, depending on the source surface; box-shaped, hemispherical etc., with the probe axis normal to that surface. For our case the test element in the aperture was flush with the receiver wall. Hence the measurement surface is that parallel to the test element plus the perimeter surface created by the probe distance away from the test element. The majority of radiated sound power will pass through the parallel measurement area, but with some leakage at the perimeter which will decrease by reducing the distance from probe to surface [97].

Measurement involving integration over the parallel area, S_o, will be called an 'open box' measurement. Inclusion of the perimeter area will be called a 'closed box' measurement, denoted S_c. The closed box accounts for all radiated power leaking between the test element and S_o. Therefore it is always important to 'close the box' by including the perimeter area. In a test suite it is hoped that extraneous and flanking

noise will be minimal so the difference between a 'closed box' and 'open box' surface integration would indicate the effect of leakage by this perimeter area. Figure 4.8 shows the difference in average intensity level for measurement of the single 1:8 scale wall. The difference is inconclusive, varying around zero with a maximum of ± 3 dB above 500 Hz.

'Closing the box' will also eliminate any extraneous noise sources. Sound from a source, other than the test element, entering the measurement area will produce a non-zero intensity which should be cancelled by the same sound leaving the test area. In practice, where there is strong extraneous noise and complex sound fields, this is not usually the case and van Zyl [97] and Nordtest [104] indicate errors of 1-2 dB when the measurement surface is not correctly closed. This is highly dependant on factors such as the receiver room diffusivity, parasitic noise and flanking transmission.

An important consideration is the measurement distance from the surface. Complex near field patterns occur close to a radiating surface where circulatory effects cause changes in the polarity of the active intensity, resulting in a high reactivity index [86]. To avoid these effects it is recommended that the distance from the surface should be no less than 0.1 m and for box-shaped measurements no greater than 0.3 m. It is suggested [105] that such polarity problems will occur below 0.05 m. Field measurements by Lai & Burgess [110] used between 0.05 m and 0.1 m, while measurements by van Zyl, Erasmus & Anderson [96] were between 0.03 m - 0.07 m from the test surface. Note that if this distance is set to the centre of the spacer then the distance to the surface will vary with changes in spacer size. Fahy [111] recommends for large heavyweight facades that the measurement distance should be no less than 0.1 m from the surface. ISO/DIS 9614-2 suggests a distance no greater than 0.2 m with the possibility of reducing to 0.1 m under very good field conditions. For all the laboratory and field measurements, the distance from the centre of the spacer to the

wall surface was 0.1 m. When integrating over the perimeter of the 'box' the probe was positioned half the distance from test surface to measurement surface, 0.05 m.

The shape of the measurement surface and thus the measured result varies depending upon the position of the test element within the aperture. A niche is always created in the aperture between the test element and room surface, unless the element is the same width as the aperture. Halliwell & Warnock [98] suggest a lower transmission loss will result when the test object is placed centrally rather than at either edge of the aperture. This discrepancy increases with decreasing frequency. Cops, Minten & Myncke [100] showed the niche effect is not seen super-critically, while sub-critically large errors of up to 5 dB were measured for a test object positioned between the extremes of central and edge locations within an aperture. A central positioned panel increases the transmitted energy particularly at normal mode frequencies, but also deep niches should be avoided. Lining of the niche on the receiver side has been considered by Guy & Mey [101], but little effect is seen on the resulting transmission loss particularly at low-mid frequencies due to the poor absorption of the material. The above research considered low insulation elements in deep niches, while the aperture in the transmission suite at Liverpool was 0.3 m wide and therefore any niche position effect was assumed very small. All the model walls were positioned flush with the aperture opening into the receiver room.

Such details as given in this section are generally not published in papers, but should be considered and are relevant to the accuracy of results.

4.5.4 Averaging over the Measurement Surface

The measurement of the average normal intensity requires a technique of spatial sampling. Two methods of integrating over a surface are presently used; discrete point

averaging and scanning or swept averaging. Both require a grid system and initially both were employed for the laboratory measurements.

4.5.4.1 Discrete Point Averaging

The number of measurement positions should be adequate for determining the average intensity from the source with 'sufficient accuracy'. ISO/DIS 9614-1 states that measurements should be at a minimum of one position per m^2, and at least 10 positions, distributed evenly. This is quantified by the use of the field indicator tests, discussed later. The scale model walls had a number of advantages that meant that a only a small grid was required. They were materially monolithic with a flat radiating surface, and measurements were at frequencies where there was a sufficiently high modal density and modal overlap.

The 1:8 scale walls were sub-divided into a grid of 25 equal squares (200 mm x 200 mm). This was marked on the surface of the scale walls and gave 16 measurement positions at the corners of the squares (see figure 4.9). The measurement positions were never closer than $\lambda_b/2$ away from the side of the aperture. The number of positions along the perimeter of the measurement box was such that the sample density was equal to the front measurement surface. This gave a further 8 positions, 2 per side, and a total of 24 positions. For all discrete point measurements the probe was held by a stand and clamp 100 mm from the test element at each position. The mean surface intensity was calculated by:

$$\overline{L_i} = 10 \log \left[\frac{1}{n} \sum_{1}^{n} 10^{L_n/10} \right] \qquad (4.26)$$

where L_n is mean normal intensity at each position and n is the number of positions.

To calculate the number of samples required at any position the time-averaged intensity level at a single position was measured repeatedly, each time doubling the sample number. Number averages of 2, 4, 8, 16, 32, 64 and 128 samples were taken. Figure 4.10 shows the difference in the surface averaged L_i by doubling the sample number. The difference shown is the mean of the differences at each 1/3 octave centre frequency. The standard deviation of the difference at each of the frequencies is also shown. At 64 samples the difference and standard deviation are both approximately 0.5 dB, therefore this sample number was measured at each position.

4.5.4.2 Continuous Scan Averaging

In scanning, the probe is simply swept over the surface either by hand or by an automated system, resulting in a single figure time and space average. The method is easier and quicker than the discrete approach and therefore better suited to field measurement. As with the discrete point method the surface is sub-divided, but the measurement location is not a fixed point but a path over which the probe scans.

No fixed speeds have been set for scanning as this would be difficult with the inevitable variation of hand-held scans and different operators. Automated systems could be standardised but these are much less practical in the field; the B & K Type 9654 - Microphone Positioning System, has a maximum speed in the vertical and horizontal direction of only 0.075 m/sec. ANSI S12.12 [92] recommends an initial moderate rate of between 0.1-0.5 m/sec, but this can be increased as long as differences in intensity level varies within given tolerance limits to a maximum of 3 m/sec. ISO/DIS 9614-2 [91] recommends speeds not exceeding 0.3 m/s. The Nordtest method [104] recommends speeds <0.24 m/sec and CSTB (France) offers 0.05 m/sec; while work by Krishnappa [109] with different speeds and extraneous noise sources agrees with Nordtest. Annex E. to ISO/140-3 [105] advocates a steady

speed between 0.1 - 0.3 m/sec. From this information a scanning speed of approximately 0.15 m/sec was chosen.

The walls were scanned as indicated in figure 4.11, using the same grid array as for discrete point measurements. The FFT analyser measured 128 samples at approximately 1 sample/second which gives a total scan distance of 19.2 m. Since the 'closed' scan distance is 7.66 m long it is therefore 'passed over' 2.5 times with one measurement every 35 mm. A further 72 averages, 18 per side, were scanned around the measurement box perimeter. In order to ensure a steady measurement the total average was paused between measurement box faces so the operator could adjust his position to be sure of an even scan. The probe was hand held with the operator standing to its side and at arms length, whenever possible. The measurement area was scanned at least twice in directions mutually perpendicular to each other, as recommended [92]. ISO/DIS 9614-2 requires any scan to be a minimum of 20 seconds, which was exceeded in all cases.

4.5.4.3 Waterhouse correction

The Waterhouse correction is used to take account of the increased energy density at the wall boundaries of a room where there is interference between incident and reflected waves. It is given by:

$$10 \log\left[1 + \frac{\lambda S}{8 V}\right] \qquad (4.27)$$

where S is the internal surface area of the room and V the volume. It has greatest effect at low frequencies. It is often incorporated as a correction between conventional ISO 140/3 measurements and intensity measurements of transmission loss at low frequencies [96, 98, 100]. ISO 140/3 requires measurement of the sound level $\lambda/4$

away from the room boundaries, so a correction should strictly be made; but as the two rooms are usually roughly the same size a general cancellation occurs.

With the intensity method the average receiver room pressure level is not required and thus the correction should be applied only to the source room, which increases the transmission loss [96]. The correction also requires the room to be diffuse which is questionable at low frequencies. Tests by Nordtest [104] suggest that the correction gives an over-estimate of transmission loss, while its absence will underestimate the transmission loss.

The exact benefits of its inclusion are not fully proven although it would seem intuitively correct to include it for the source side. For the small transmission suite the correction was 1 dB at 400 Hz (and cancelled for ISO 140/3 measurements). For a typical full size sports hall, considered in field measurement, the correction is 1.3 dB at 50 Hz. Hence it was decided to neglect the correction term from all model and field measurements whether by ISO 140/3 or intensity methods.

4.6 INTENSIMETRY MEASUREMENTS OF TRANSMISSION LOSS

A summary of the intensimetry details for the 1:8 scale wall measurements is given below:

Frequency range:	400 Hz - 16 kHz
Microphone head size:	6 mm
Microphone spacing:	6 mm (up to 10 kHz) & 3 mm (up to 16 kHz)
Number of discrete points:	16 (open scan), 24 (closed scan)
Grid spacing:	200 mm
Scanning speed:	0.15 m/s
Measurement distance:	0.07 m (end of probe)

Measurement bandwidth:	1/3 Octave
Number of point averages:	64 per point.
Number of scan averages:	128 (open scan), 200 (closed scan)

Figure 4.12 shows the transmission loss measurement set-up for the 1:8 scale walls using sound intensimetry. The source side is the same as the ISO 140/3 measurement method and on the receiver side the dual signals from the intensity probe pass through a microphone power supply to a 2 channel FFT analyser. This was located outside the room for discrete point measurements and inside for scanned measurements. Plate A.7.3 shows the measurement of the 7 rib diaphragm wall, photographed from the receiver room side.

All the scale walls were measured by intensimetry except for the 1 and 3 rib fin walls which had already been modified into a 7 rib fin wall before the intensity system was available. The measurement results of the single, fin and diaphragm walls are discussed in chapters 5, 6 and 7. Figure 4.13 shows the difference in average surface intensity level between discrete point and scanning measurements for the single, fin and diaphragm walls. The values of L_i measured using the discrete point technique are almost always slightly higher than via the scanning technique, although agreement is within 3 dB except at the extremes, where it rises slightly. The fin wall error is slightly higher super-critically, which may be due to a random error because of the small number of measurements taken. A key factor could be the influence of the operator disrupting the receiver room sound field during scanning. Figure 4.14 shows the reactivity index measured under anechoic conditions with and without an operator standing behind the probe (using a 12 mm microphone and 12 mm spacer configuration). The difference is generally less the 0.5 dB although this does not replicate measurement conditions where a greater difference might be expected in a more reactive room.

Figure 4.15 shows the transmission loss for the model single wall gained by using the intensity method compared with the ISO 140/3 method. Both curves give the same characteristic shape, dipping about the calculated coincidence - 2300 Hz. The higher intensity curve suggests that the conventional method is degraded by flanking transmission. The intensity method also enables measurement up to 16 kHz, compared with 6300 Hz for the standard method. Figure 4.16 shows the measured transmission loss of the 7 rib fin wall. Here agreement is better particularly at mid-high frequencies, although the intensity method always gives a higher value. Results for the 1 rib diaphragm wall are given in figure 4.17, showing a similar difference to figure 4.15.

To estimate the contribution due to flanking transmission the average sound intensity was measured from the six receiver room surfaces. The sound power due to the 6 receiver room surfaces was estimated and in figure 4.18 is shown compared with the sound power from the 7 rib diaphragm wall. The sound power from the walls lies between 3 - 23 dB below that from the test element. The curves are closest at low frequencies and between 5 - 10 kHz. This closeness between the curves implies that the ISO 140/3 measurements are effected by flanking transmission in these frequency bands. Typical background intensity levels in the receiver room are also shown in figure 4.18.

The field indicator tests were carried out to confirm that the transmission loss measurements via intensimetry would be valid in the small transmission suite. Also, that they would be unaffected by the flanking power levels, as the intensity procedure would bias measurement toward the test element.

4.7 FIELD INDICATOR TESTS

Field indicators allow consideration of the adequacy of the measurement equipment, strong extraneous directional noise, the measurement array and the non-stationarity of the sound field. One standard [90] and two draft standards [91, 92] are presently in circulation for sound intensity measurements. The field indicators described within are used to "qualify the measurement environment [90]." In other words, these indicators establish guides to ensure adequate measurement parameters depending upon the sound field particular to each case. In this section we shall refer to ISO and ANSI standards which both establish a series of 'field indicators'. In many respects they are identical although different coding systems are applied. It is not the purpose here to review these indicators but just to consider those which apply in our case. ANSI standards give 73 indicators in 7 sub-sets, coded D1 - D7. Guy [102] offers the hypothesis that in most cases a limited number of indicators are sufficient for validation purposes. His recommendations for the ANSI indicators are adopted here for application to scale wall and field measurements. The ISO standards are less copious and apply criteria coded as F2 - F5. Each relevant criterion should be met before the measurement is acceptable.

Indicators results are shown for the single wall. We shall concentrate on those given by ISO /DIS 9614-1 [90] but ANSI [92] indicators are referred to throughout as they were found more comprehensive and useful.

The initial criterion requires Ld > F2 where F2 is the same as the reactivity index (L_k). This ensures that the reactivity of the sound field is within the dynamic range of the instrument and is identical to equation 4.23 discussed previously.

Background or intrusive noise levels are not likely to be problematic within a transmission suite, but will be important for field measurements. Also the steady state source signal means that time variable indicators need not be considered.

4.7.1 Parasitic noise

Parasitic noise refers to background or room effects described by intensity in directions other than normal to the measurement surface. This noise is considered minimal if;

$$F3 - F2 > 3 \text{ dB} \tag{4.28}$$

where,

$$F3 = \overline{L_p} - \overline{L_i} \tag{4.29}$$

$\overline{L_p}$ and $\overline{L_i}$ are the spatial and time averaged sound pressure and sound intensity levels respectively, and where $\overline{L_i}$ is the signed intensity. According to ISO 9614-1 [90] if the inequality of equations 4.23 does not hold and/or equation 4.29 does hold, then alterations to the sound field are required. Options offered are shielding the measurement surface or measuring closer to the source, thereby improving the active intensity level relative to the overall pressure level.

F2 does not consider directionality by taking the modulus of the signed intensity, $\overline{L_{|i|}}$. Hence, equation 4.28 can be re-written as:

$$\overline{L_{|i|}} - \overline{L_i} > 3\text{dB} \tag{4.30}$$

This is the same equation as given by ANSI field indicator D21 [92], where a stricter criterion is used:

$\overline{L_{|i|}} - \overline{L_i} > 0$ there is significant parasitic noise (4.31)

$\overline{L_{|i|}} - \overline{L_i} = 0$ there is low/moderate parasitic noise (4.32)

This second expression implies that even if all the intensity measured is positive and from the source direction, there may still be background or room effects. While the limit of 3 dB, set by ISO 9614-1 [90], allows the sum of the unsigned intensity to be twice as large as the positive intensity before the measurement is unacceptable.

For all single and fin walls no negative intensity values occurred with the discrete point technique and are therefore within the criterion set by equation 4.28. Only when the insulation of the wall is increased, leading to reduced signal through the wall or at some lower frequencies did negative intensities occur. Table 4 below gives values of $\overline{L_{|i|}} - \overline{L_i}$ for the three model walls where the value was not zero.

Table 4: $\overline{L_{|i|}} - \overline{L_i}$ for Non-zero 1:8 Scale Model Walls

Frequency (Hz)	1 rib diaphragm (dB)	3 rib diaphragm (dB)	Double wall (dB)
400	0.6		
500	0.3		1.0
630	0.2	2.7	0.9
800		0.1	2.5
1000			1.3

The ISO criterion is met as the values at each frequency are lower than the 3dB, though parasitic noise may be significant.

ANSI indicator D23 [92] is offered by Guy [102] to measure the reactivity of the field, where the scanning technique can be used to measure $\overline{L_i}$.

$$D23 = \overline{L_p} - \overline{L_i} + 10\log\left[\frac{p_o^2}{\rho c\, I_o}\right] \qquad (4.33)$$

D22 is a measure of the intensity level above background:

$$D22 = \overline{L_{|i|}} - \overline{L_{i|\,b/g}} \qquad (4.34)$$

where $\overline{L_{i|\,b/g}}$ is the unsigned background intensity level. Figure 4.19 gives results of the indicators D22 and D23 for the 1:8 scale single wall. D22 has values between 20 - 40 dB. Draft ANSI S12.12 [92] states that D22 should be greater than 10 dB for background levels to be negligible, and therefore easily meets this criterion. Levels of almost 10dB for field indicator D23, show significant parasitic interference. As the L_i values were all positive this is the same as the reactivity index. Therefore plotting also the dynamic capability of instrument, D23 should be, and is, just below this line. Note that present draft standards do not include any mention that the D23 indicator or equivalent can become negative where standing waves exist [108].

A further indication of measurement accuracy with respect to clearly identifying the direction of the predominant noise source is to rotate the probe through 180°, and repeat the measurement. This simple test should give identical results albeit with the opposite sign. Figure 4.20 shows the mean difference from reversing the probe at 4 random measurement positions for the single wall. The mean error over all frequencies is 0.7 dB, with a standard deviation of 0.6 dB.

4.7.2 Adequate Surface Averaging

A suitable surface average is required to ensure adequate integration of the signal character emitted from the test element. ISO 9614-2 [90] states that the distance between adjacent imaginary scan lines should not exceed half the average distance between measurement and source surfaces. If such a requirement was known previous to the measurements the criterion would have been met, though this would have required a much denser grid. It is suggested that such a dense scan area is partially dependent on the type of sources (machines) the standard is designed for; usually having a significantly variable surface sound power levels. In this case such a criterion is probably over-strict.

With respect to discrete point measurements Criteria 2 of ISO/DIS 9614-1 requires:

$$N > C\,F4^2 \qquad (4.35)$$

where N is the minimum number of required measurement positions. C is a constant and F4 is a field non-uniformity indicator defined by:

$$F4 = \frac{1}{\bar{I}} \sqrt{\frac{1}{N-1} \sum_{i=1}^{N} [I_i - \bar{I}]^2} \qquad (4.36)$$

Figure 4.21 shows the minimum number of positions at each frequency calculated for three degrees of accuracy, which are determined by the value of C. At all frequencies, except for one at the precision grade, all values are below 16. Therefore 16 positions were considered acceptable. The draft ANSI standard [92] gives two simple indicators to determine adequate surface averaging. These are D31 and D32:

$$D31 = |L_i - L_i'| \qquad (4.37)$$

$$D32 = \left| L_i' - L_i'' \right| \qquad (4.38)$$

where L_i' is the surface sound intensity level with 4 times the number of measurement locations and L_i'' is the surface sound intensity level using a difference measurement array. Both indicators are based on the idea of convergence, given by the difference in measurements between one array and the next array. The decrease in the difference between arrays is acceptable when below a set tolerance limit. Figure 4.22 shows the results for the D31 indicator by comparing the difference between various arrays up to 32 positions, using 8x, 4x and 2x the number of measurement points. Again 16 positions seems reasonably acceptable, always below the tolerance limit. Figure 4.23 shows the result for D32. Here a shifted array of points is compared to the original 16 point array (see figure 4.9). This new array is shifted 100 mm horizontally and vertically from the original. Results show measurements below tolerance limits except at lower frequencies, but this is by less than 0.5 dB.

The results of these field indicator tests suggest the intensity method has overcome the difficulties of flanking and poor signal level incurred by the ISO140/3 method and can be accepted as giving the truer measurement result. This may not be surprising as measurement conditions are controlled in the laboratory environment where small numbers of surface averaging are acceptable to give repeatable results. In Chapter 8 such indicators will become more important when applied to the field measurement of in-situ diaphragm walls. As an example of applying these standards to field measurements, ISO/DIS 9614-1 [90] states that for surface areas greater than 50 m^2, 50 measurement locations should be distributed evenly, which is applicable to large workshop machinery. However, for the field measurement of large building facades this would be impractical without the expense of a large scaffold system to reach all parts of the facade.

4.8 CONCLUDING REMARKS

The background and theory of sound intensity has been described and the application of sound intensimetry to the scale models has been given. The advantages and difficulties of the method were discussed, particularly with respect to the standard transmission loss measurement.

The intensity method was shown to give higher values of transmission loss than the standard method overcoming the flanking problems of the non-standard transmission suite, and allowed an extension of the measurable frequency range up to 16 kHz, by using a 3 mm spacer above 10 kHz. Field indicators carried out on the single wall confirm the receiver room to be suitable for intensity measurement, and the number of surface averages to be enough to adequately approximate the radiated energy from the test walls.

The importance of including the perimeter of a measurement surface is emphasised, particularly for field measurements where the sound field deteriorates.

Presentation and analysis of the scale wall measurements are now possible in the following chapters.

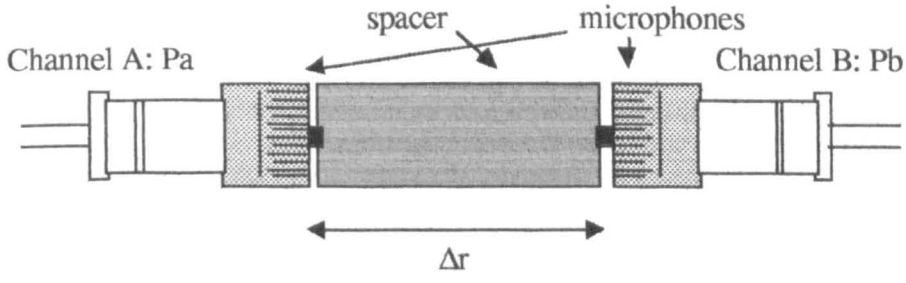

Figure 4.1: Sound intensity probe: face to face microphones

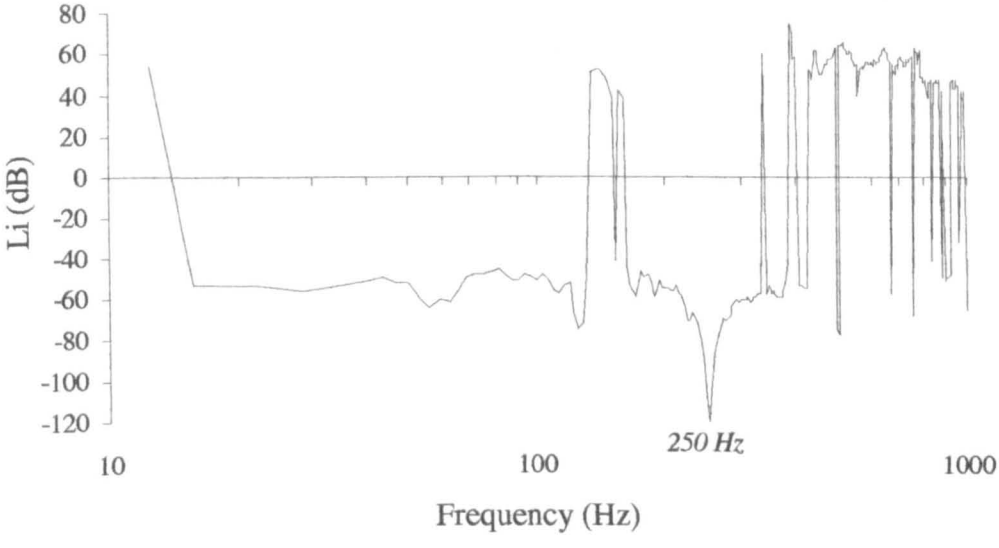

Figure 4.2: Typical narrowband calibration spectrum

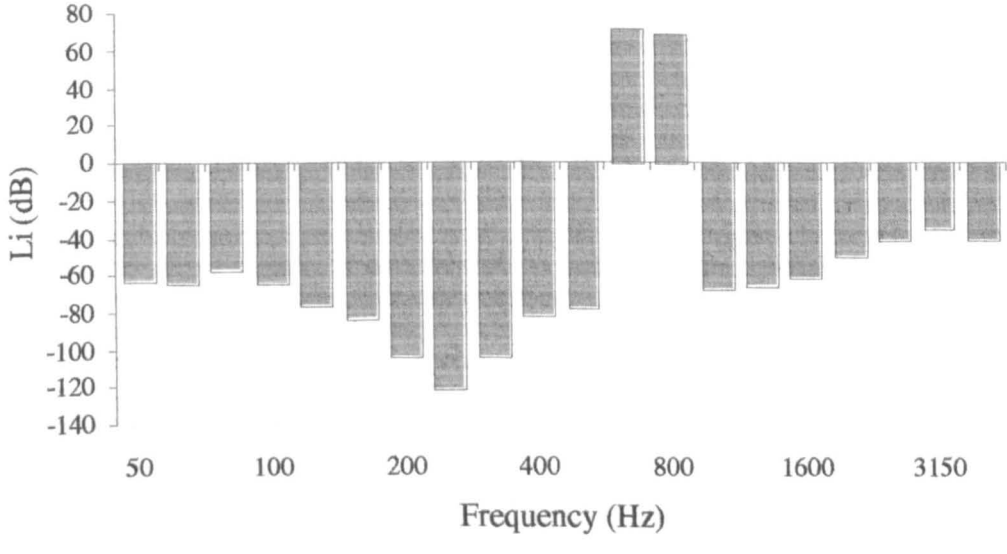

Figure 4.3: Typical 1/3 Octave calibration spectrum

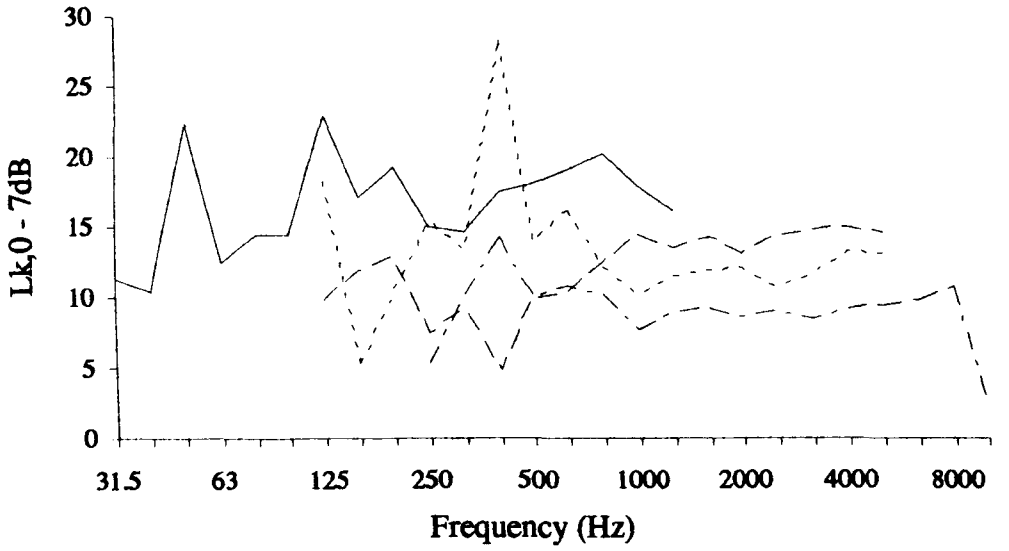

Figure 4.4: Dynamic capability of the measurement system

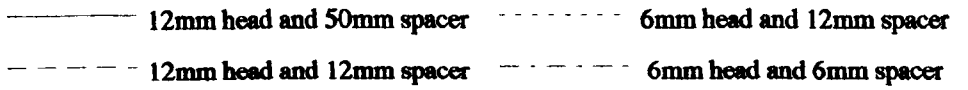

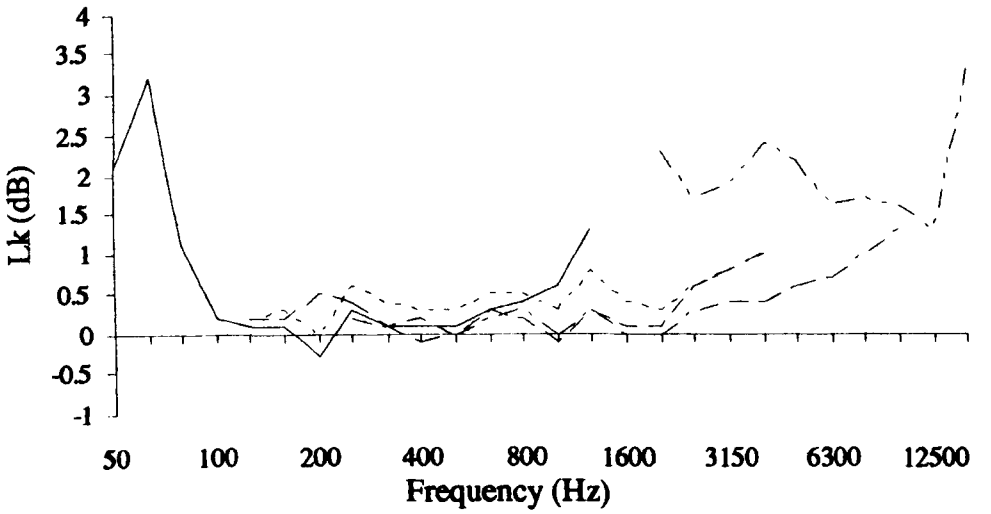

Figure 4.5: Reactivity indices under anechoic conditions

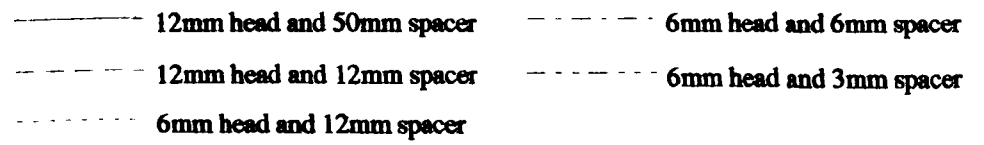

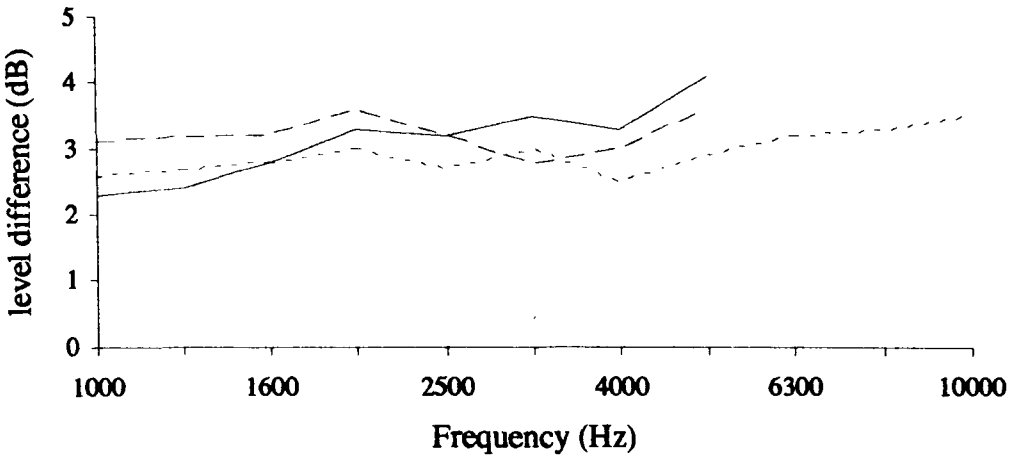

Figure 4.6: 3mm spacer compared to conventional microphone and spacer configurations

12mm heads and 12mm spacer

6mm heads and 12mm spacer

6mm heads and 6mm spacer

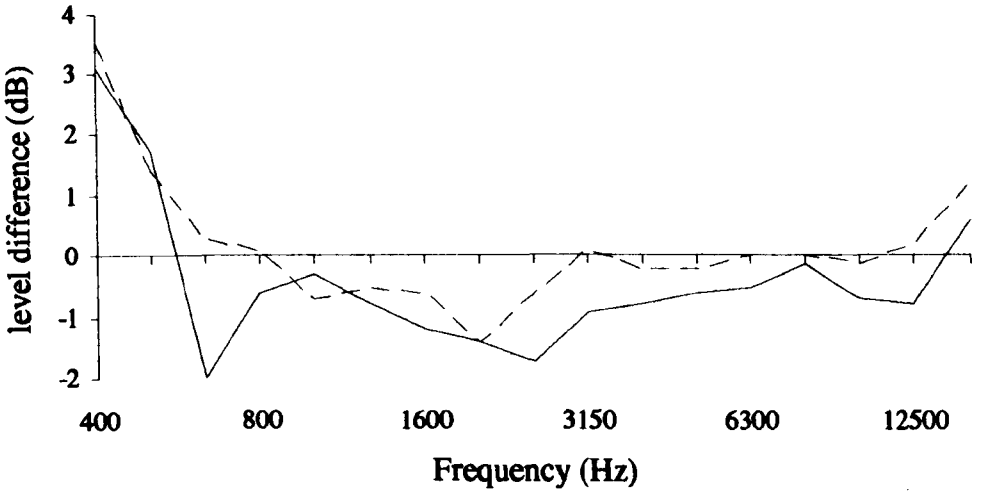

Figure 4.7: Effect of varying receiver room absorption

empty room - absorption only on backwall

empty room - absorption on all surfaces

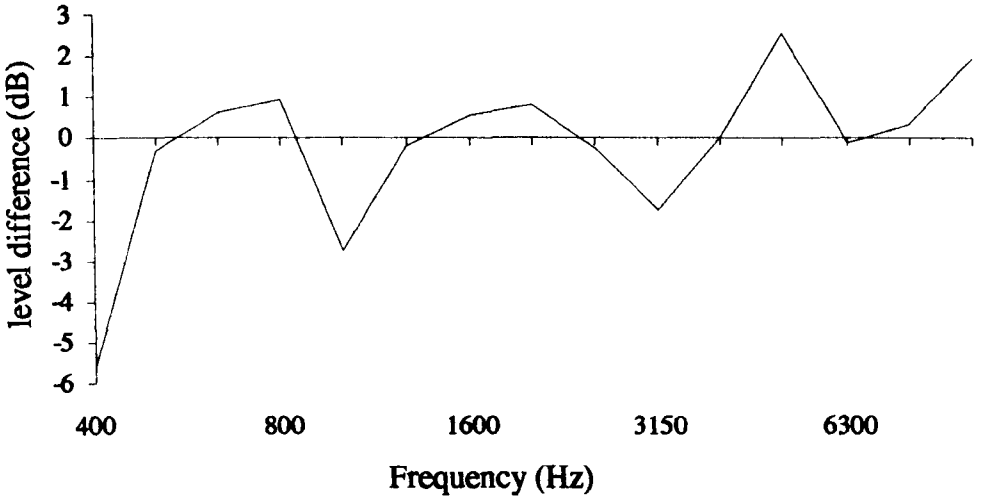

Figure 4.8: Difference between 'closed' and 'open' box average intensity levels

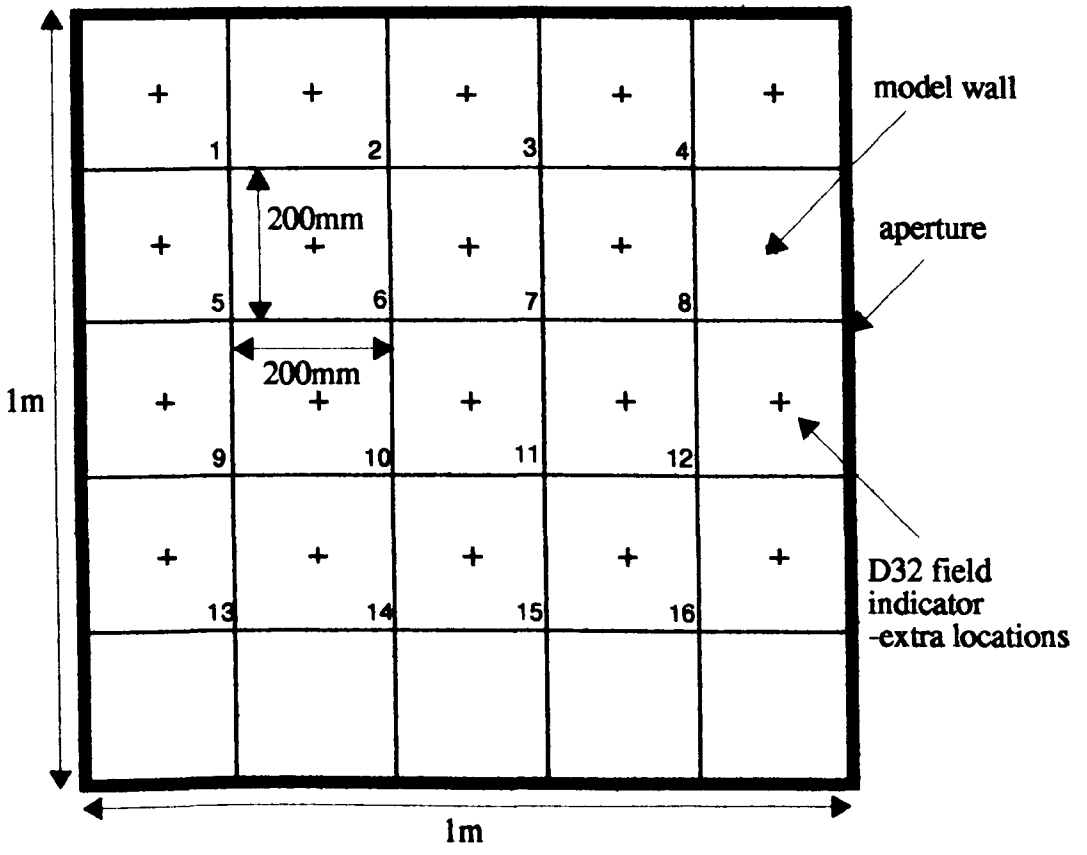

Figure 4.9: Averaging by discrete points

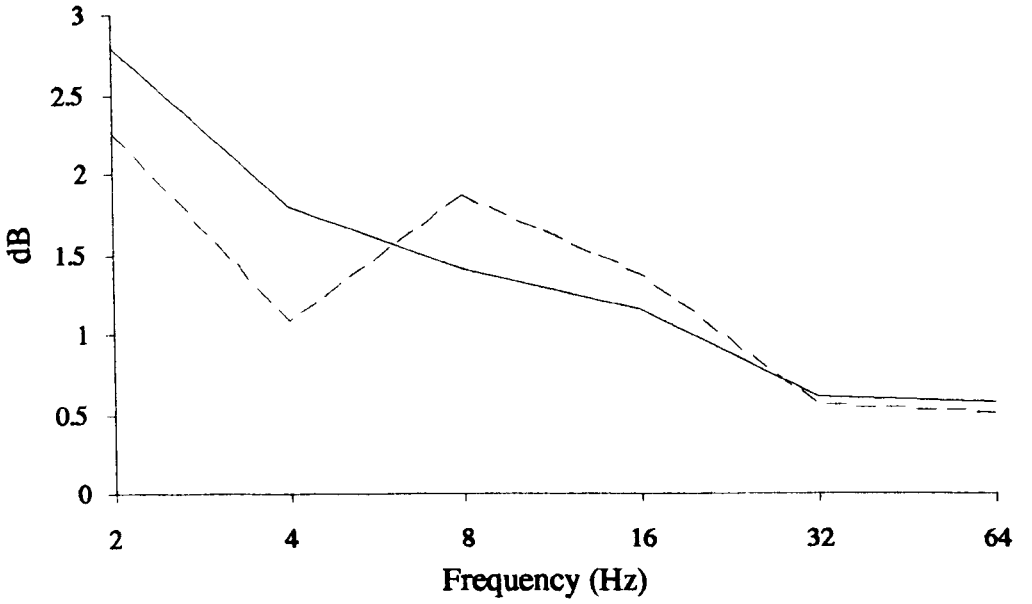

Figure 4.10: Effect of doubling sampling average at 1 location

Mean difference in average intensity at each frequency

Standard deviation

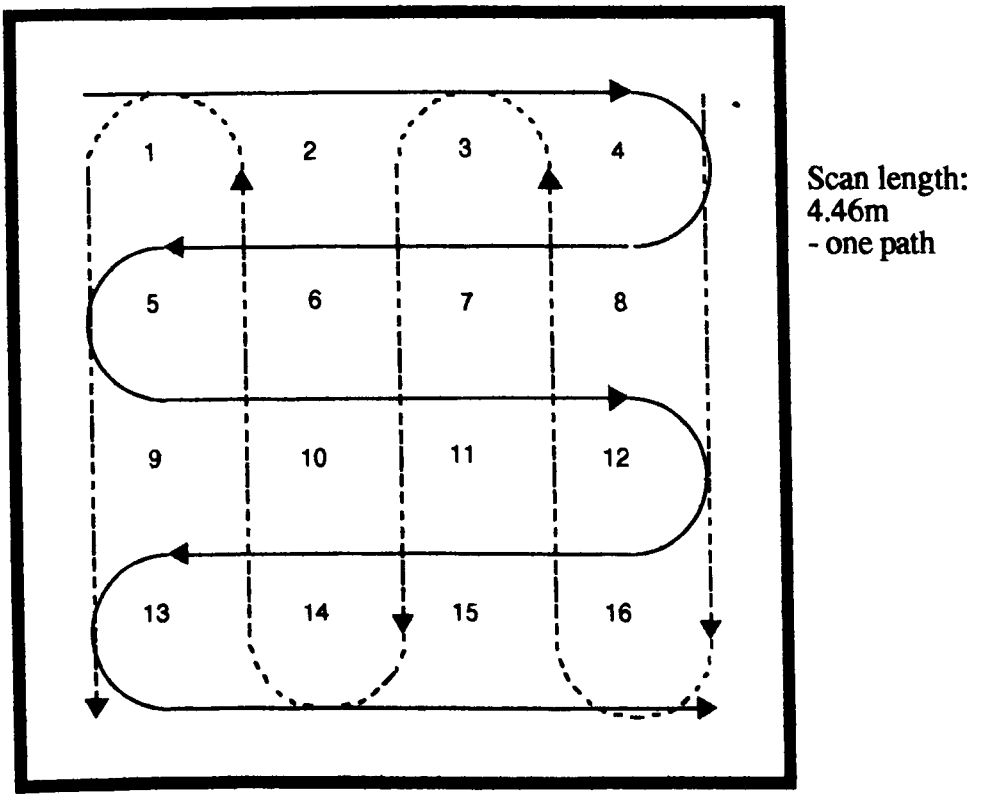

Figure 4.11: Averaging by scanning

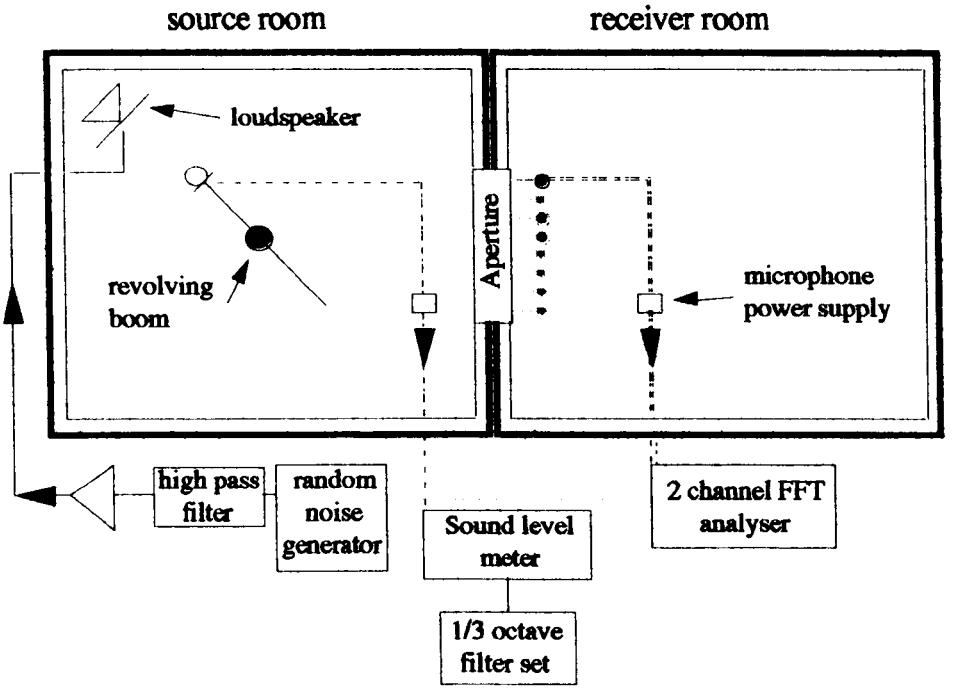

Figure 4.12: Transmission loss measurement set-up for 1:8 scale walls using sound intensimetry

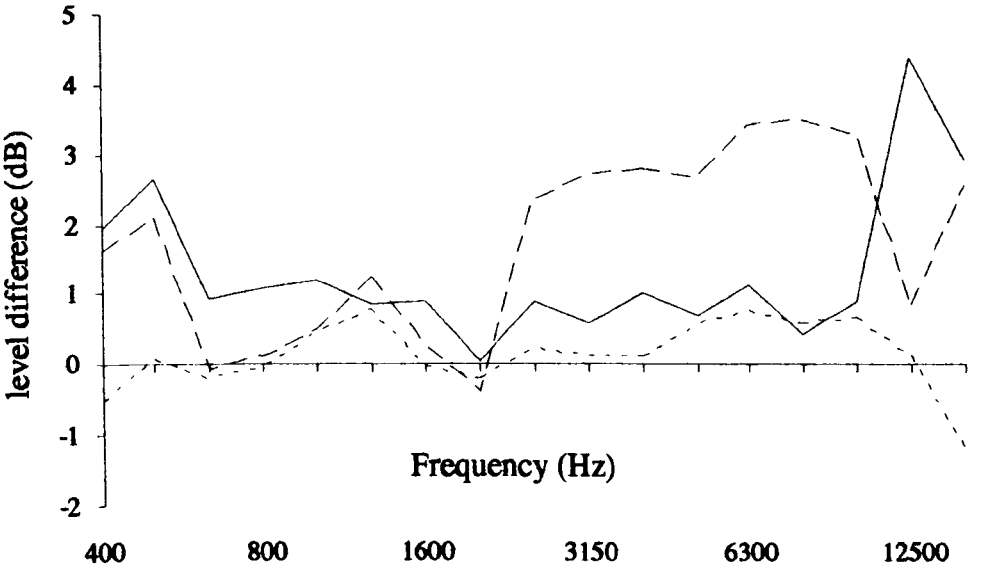

Figure 4.13: Difference in measured intensity level between discrete point and scanning techniques

single walls — fin walls - - - - diaphragm walls

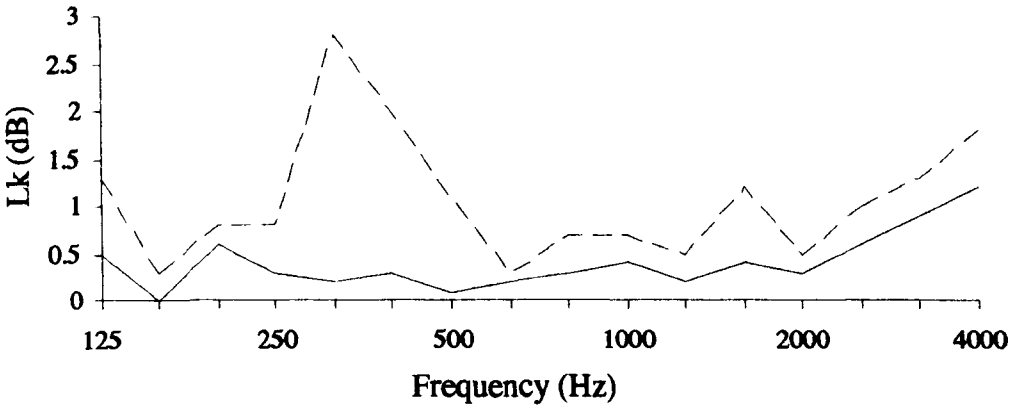

Figure 4.14: Influence of operator on reactivity index under anechoic conditions

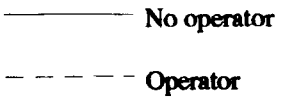

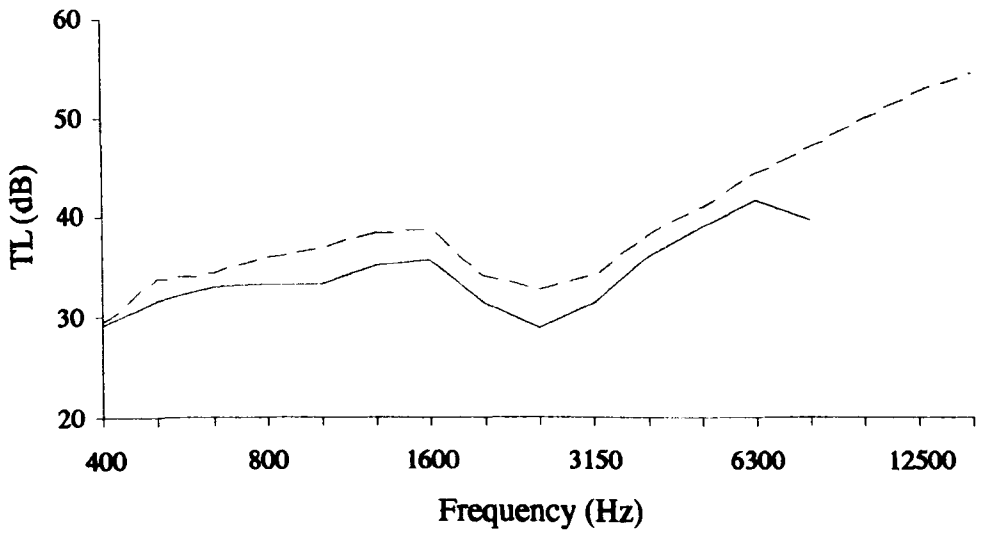

Figure 4.15: Transmission loss of single wall

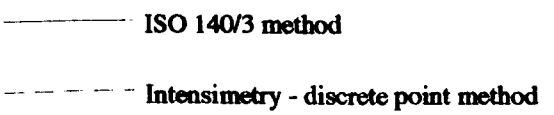

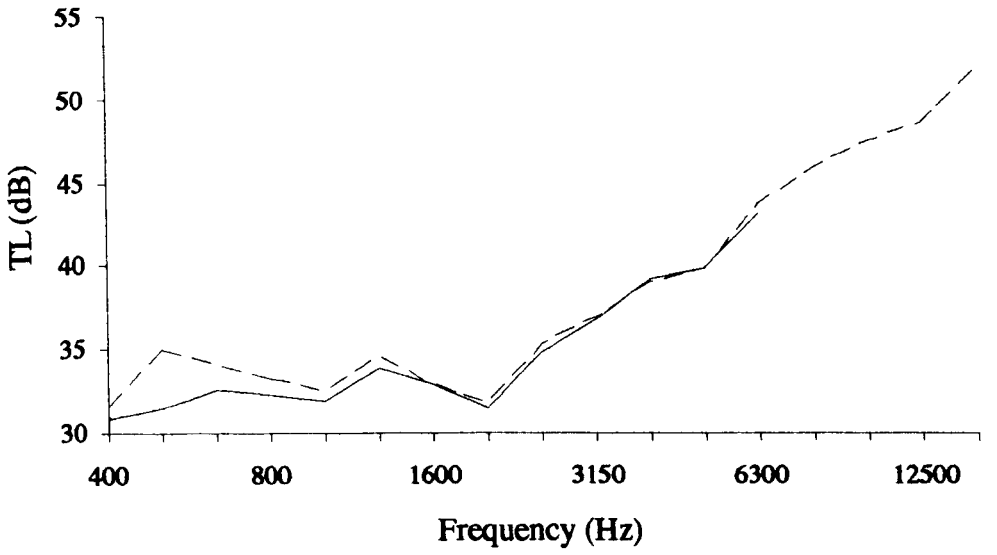

Figure 4.16: Transmission loss of 7 rib fin wall

ISO 140/3 method

Intensimetry - Discrete point method

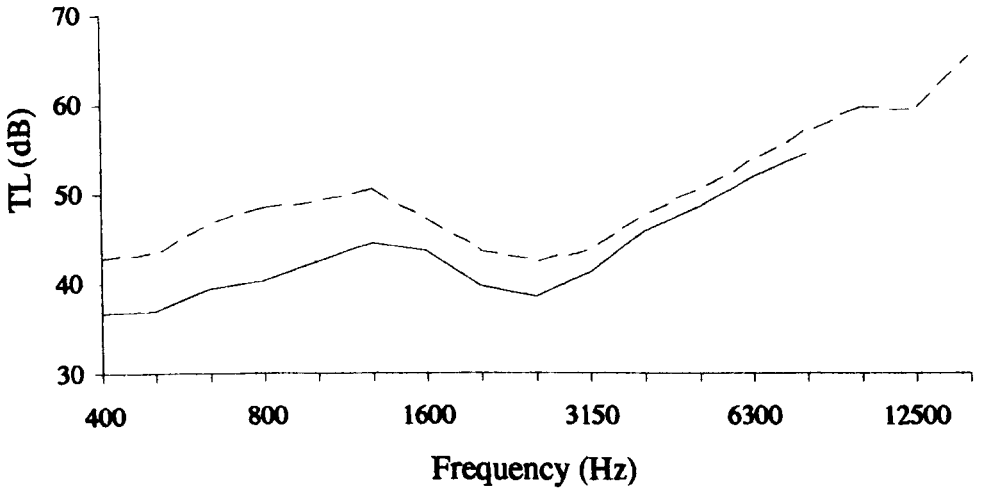

Figure 4.17: Transmission loss of 1 rib diaphragm wall

ISO 140/3 method

Intensimetry - discrete point method

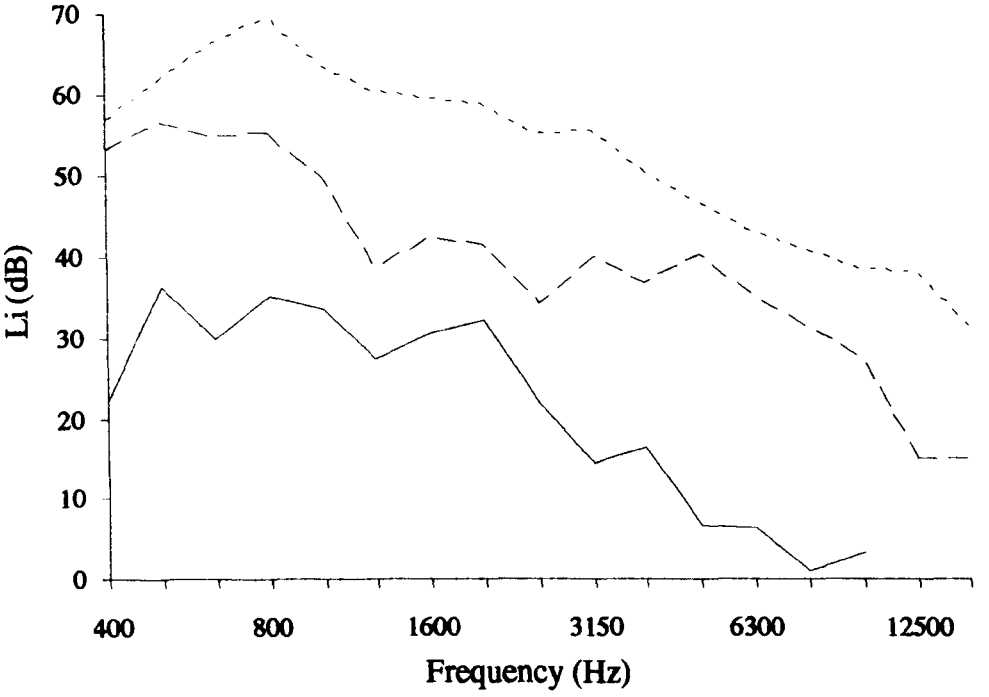

Figure 4.18: Sound power levels and background levels in receiver room

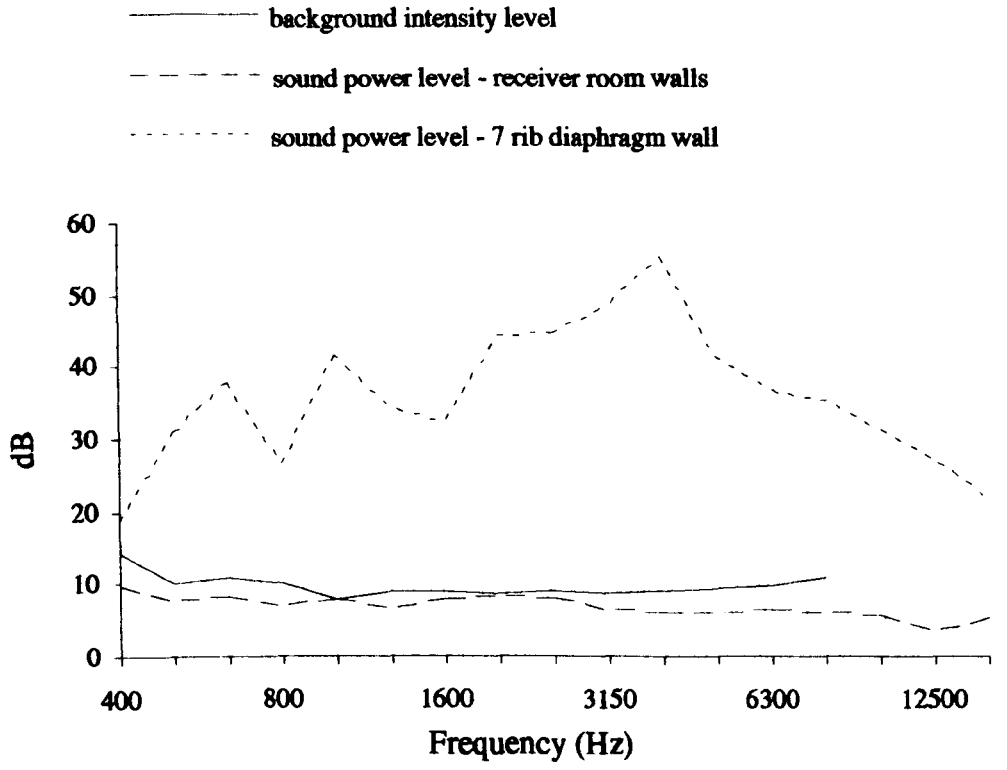

Figure 4.19: D22 & D23 indicators for single wall

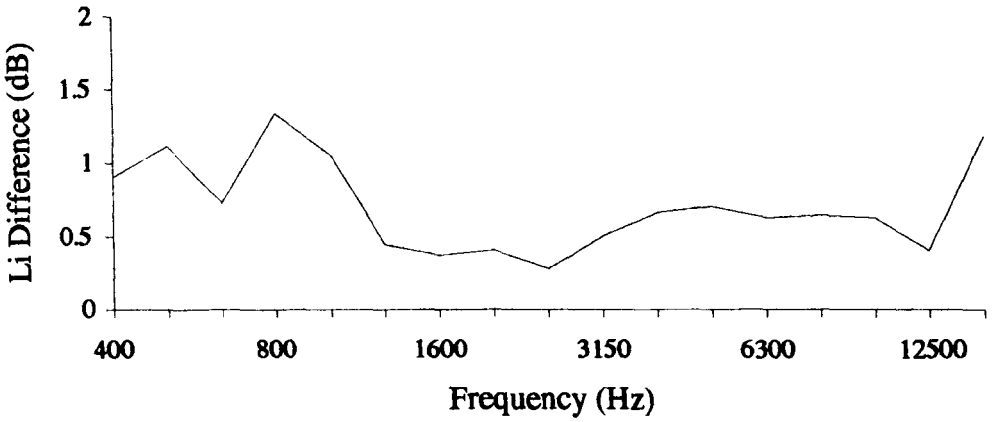

Figure 4.20: Reversability test - mean of 4 measurement locations

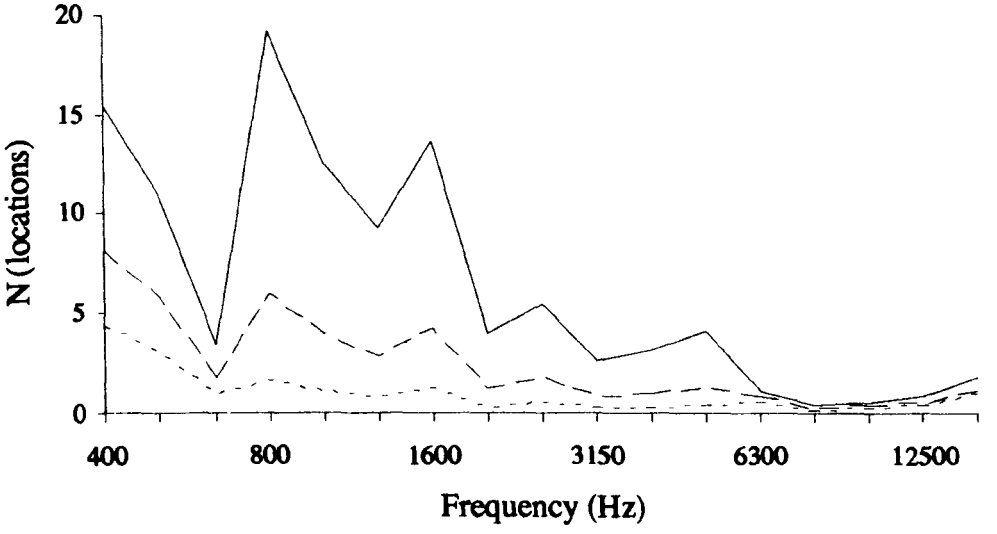

Figure 4.21: Minimum number of measurement locations

Precision

Engineering

Survey

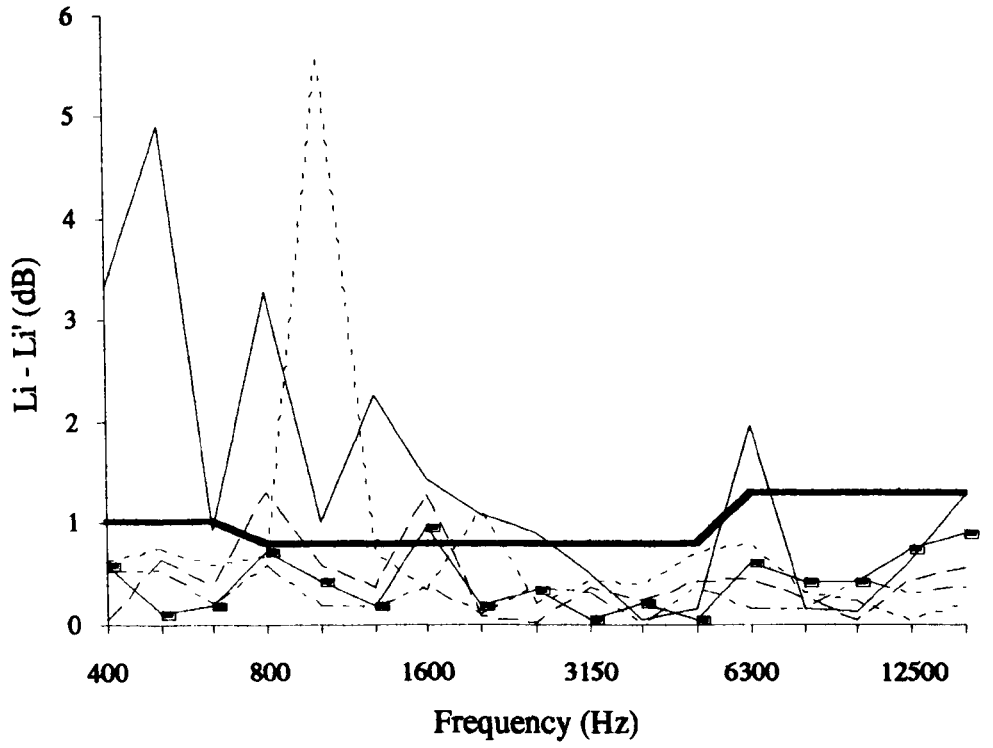

Figure 4.22: D31 indicator for single wall.

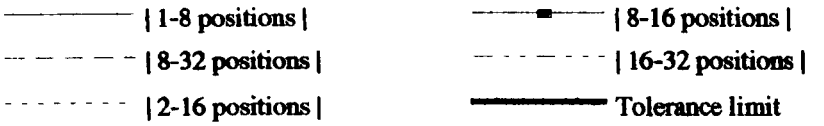

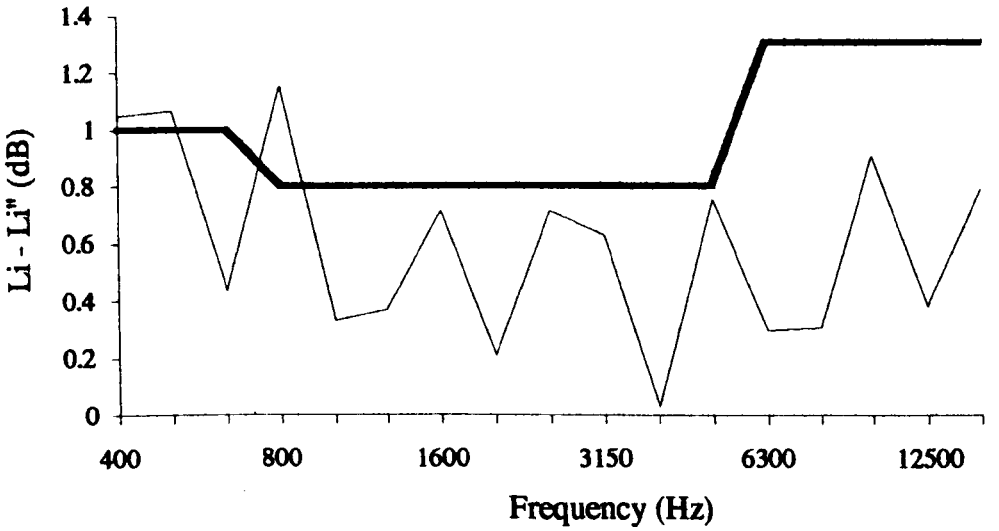

Figure 4.23: D32 indicator for single wall

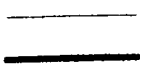

5 ORTHOTROPICITY & SURFACE RADIATION

5.1 INTRODUCTION

In this chapter and that following, an attempt is made to predict the transmission loss of the diaphragm wall by developing existing theory for heavyweight and bridged wall constructions. Two mechanisms were believed significant in the transmission of sound through a diaphragm wall. Both involved the cross-ribs, first as stiffening, and second, as a bridge between leaves. The behaviour of the ribs as a stiffening influence upon the diaphragm wall is described in this chapter by examining walls of increasing complexity from a single isotropic wall to a fin wall. Theory for the transmission loss of a fin wall will be developed. The influence of ribs on the sound radiation character of the diaphragm wall is discussed and proposals are given for inclusion in Chapter 7. Predictions are compared with measurements of the scale walls (and full size walls in later chapters).

5.2 SINGLE ISOTROPIC WALLS

The fin wall cannot be examined without first understanding the transmission loss of isotropic walls. An isotropic wall may be defined as having only one bending stiffness and thus only one critical frequency. Isotropic walls have a characteristic transmission loss curve, shown in figure 2.2, although this will vary depending on material parameters. For lightweight or lightly damped walls the characteristic coincidence dip is clearly observed. For heavier walls, such as of masonry it is harder to detect and is often seen as a change in slope.

Three single walls were measured in this investigation; the 1:8 scale wall, the 1:4 scale wall measured by Hung [18], and a wall of the large transmission suite. The latter was a 120 mm 1/2 brick dense masonry wall, hard plastered internally, with a

calculated critical frequency of 231 Hz. Figure 5.1 shows the measured transmission loss of the three walls with appropriate frequency adjustment for the model walls. The three curves show the same characteristic shape, rising initially, dipping about their critical frequency and rising in close agreement at 9 dB/octave. There is no reason why such close agreement should be obtained, particularly above critical coincidence, as all three walls are not of equivalent surface density, although they all have roughly the same scaled thickness and longitudinal wavespeed. The greater total damping of the masonry wall produces a less obvious dip about coincidence. These results give a reference when considering the change in transmission loss caused by the addition of ribs.

A theoretical reference was also required for the single wall transmission loss. Figure 5.2 shows the predicted transmission loss of the 1:8 scale wall according to mass law. Normal, field and random incidence predictions are given according to equations 2.9, 2.14 and 2.13 respectively. There is little agreement with measurement over the whole frequency range. It is only in the sub-critical non-resonant mass controlled region that some agreement with measurement would be expected and is found - the field incidence curve gives the best fit. Normal incidence prediction over-estimates the transmission loss as a diffuse incident sound field was always used. It was generally observed throughout the research that field incidence gave better agreement with measurement than random incidence, reasons for this were given in Chapter 2. Therefore, all conventional theoretical predictions that follow assume field incidence.

Equation 2.30, given by Sharp [41], was employed in the super-critical region to account for the influence of coincidence and damping. Hence, predicted values were obtained in three frequency regions as follows.

Mass law	$f_0 < f < f_c/2$	Equation 2.14	
Interpolation	$f_c/2 < f < f_c$		(5.1)
Recovery	$f > f_c$	Equation 2.30	

Equation 2.16 is not included, where $f < f_0$ (the first order resonance frequency) as f_0 for the 1:8 scale, 1:4 scale and masonry wall is 25 Hz, 14 Hz and 12 Hz, respectively, all of which fall below the measurement frequency range. The region between $f_c/2$ and f_c is interpolated. Sharp does not indicate a theoretical basis for $f_c/2$, as it was obtained empirically. However this assumption is supported by the present results, where at approximately $f_c/2$ a change in slope away from mass law begins to occur.

Figures 5.3, 5.4 and 5.5 show the predicted transmission loss for the three single isotropic walls. Figure 5.3 shows results for the 1:8 scale wall. The predicted critical frequency is 2328 Hz, and is observed in all measurements. Discrete point measurements are shown in subsequent figures unless otherwise stated. Measurement by intensimetry, using scanning and discrete point techniques, both showed very close agreement, with prediction and each other. The interpolated slope is slightly long and would have given better agreement if it began at 1600 Hz. Figure 5.4 shows the 1:4 scale wall, where again agreement is very good super-critically and good at all but the lowest frequencies. This may be due to the nature of the construction, the joints were of a less dense infill mortar producing weaknesses and thereby slightly reducing the measured transmission loss. These joints may also have affected the longitudinal wavespeed and Young's modulus of the wall. Figure 5.5 gives prediction for the full size masonry wall. Measurement appeared to be an underestimate at high frequencies due to poor signal to noise above 1250 Hz. The calculated critical frequency was 231 Hz and agreement here and in the interpolated region is very good. Intensity measurements below 100 Hz were suspect as they

were below to limit of the probe configuration and a high field reactivity at the measurement surface, of around 10 dB, was measured.

To further validate the prediction theory for single walls more broadly, comparisons with five other isotropic walls were made. Results were taken from previous research work where exact material details were available. The five materials were two 3 mm and one 6 mm aluminium sheets, one hollow concrete block wall and one masonry wall plastered both sides. These results are each shown as a level difference, measurement minus prediction, in figure 5.6. Agreement is within ± 2 dB in the mid-frequencies and worse at the low and high frequencies. Better agreement might not be expected as values of damping, η, and longitudinal wavespeed, c_L, had to be estimated. The concrete and masonry walls deviated from prediction at the high frequencies probably due to the measurement limits of the test suite.

5.3 MEASUREMENT OF DAMPING

Overall, the prediction of single isotropic walls gives good agreement with measurement. One parameter that can significantly affect prediction above critical frequency is the value of damping, or loss factor, η. A range of values for different materials are found in the literature [37]. For building materials such as brick, concrete, asphalt, plywood etc., values between 10^{-2} and 10^{-1} are given. For other materials typical values are $\eta \approx 3 \times 10^{-2}$ for perspex, 10^{-1} for copper and 10^{-3} for aluminium or steel. Damping treatments only effectively benefit lightly damped materials. Figure 5.7 predicts the transmission loss for the 1:8 scale single wall using three values of loss factor. The importance of correctly determining the loss factor is seen by the wide range between the curves, 4.7 dB. No effect is expected below $f_c/2$ as this is mass law controlled but the value of damping will affect the gradient of the interpolated region. It was beneficial therefore to measure the loss factor for the 1:8

scale perspex walls while in the test aperture so that this value could be included as a known parameter in subsequent measurements.

Measurement of a material loss factor is problematic. Many influences may effect the measured result, such as the positioning of the material and how it is supported, as well as the coupling with the surrounding air. The total loss factor, η_{tot}, of a test wall in a transmission suite aperture includes radiation and coupling components, to the rooms and to the chamber walls respectively. Such that:

$$\eta_{tot} = \eta_{rlf} + \eta_{clf} + \eta \qquad (5.2)$$

Where η_{rlf} is the radiation loss factor into the rooms and η_{clf} is the coupling loss factor to the aperture wall and η the internal loss factor. It is often assumed that η is greater than ($\eta_{rlf} + \eta_{clf}$), but this assumption is not always true. For lightweight panels many factors such as those noted above will have a significant affect and may dominate a measurement result. Radiation coupling between a panel and a room will decrease with increased transmission loss, so for building elements structural coupling rather than radiation coupling is more important in determining the total loss factor. In measurements of 3mm aluminium panels Cummings [49] produced values 50 - 350 times greater than typical published figures which was suggested to be due to radiation damping controlling the measured loss factor. Hence in general, the determination of a material loss factor is highly variable, with little repeatability.

Two approaches were used to measure the loss factor of the 1:8 scale single wall, the envelope decay technique and the reverberant decay method. The former is a 'narrowband method' which involved identification of individual resonant modes. The approach is generally the more accurate, but is dependant upon the modal density and overlap, so with higher frequencies and complex shapes the technique becomes increasingly unworkable. The logarithmic decrement of the decay is

obtained from a repetitive impulse excitation. The signal response is gated in the frequency domain between band-limits to capture a single mode. By auto-correlation the imaginary part of the time waveform is displayed, which is called the Hilbert transformation. The damping factor is given by:

$$\eta = C\left|\frac{\Delta Y_{axis}}{\Delta X_{axis}}\right|\frac{1}{f} \qquad (5.3)$$

Where C is the constant equal to 18.32×10^{-3}. Measured values of η were between 2.2 - 12×10^{-2} for the single 1:8 scale wall but measurement proved difficult due to the relatively high modal density.

Where there is an increased modal density, band averaging of the measurement gives statistically better results. Hence the 'reverberation decay' method was used. This band-limited approach is faster but less accurate. The wall is excited using a random broadband source via a non-contact electromagnet. Cutting off the source produces a decay which is averaged and digitally filtered. Surface averaging statistically decreases any errors. The loss factor is given by:

$$\eta = \frac{Ln\ 10^6}{\omega T_{60}} \approx \frac{2.2}{f T_{60}} \qquad (5.4)$$

where f is the centre 1/3 octave frequency and T_{60} is reverberation time for a 60 dB fall in signal amplitude.

Figure 5.8 shows the measurement set-up. The panel was excited using a speech coil attached to the wall with a permanent magnet brought close, but without touching. An electromagnetic driver was not used as additional contact stiffness would influence the wall's response. A building acoustics analyser (B & K Type 4417) produced the signal and the response decay was measured by the analyser using a 12g accelerometer (B & K Type 4371), attached to the surface via beeswax. The

mean reverberation time of six random measurement positions was calculated four times and the overall average taken as RT_{60}. By using a 1/3 octave filter system for the output and input signals to the analyser, any unwanted noise was reduced. Further, it was important that the response system of the analyser would be able to measure the decay. The instrumentation could measure decays greater than 0.25 sec below 315 Hz and greater than 0.08 sec above 400 Hz, to a resolution of 0.01 sec. Measurements were possible between 125 Hz and 4 kHz, although above 1.25 kHz the furthest positions from the exciter were not always measurable as the decay was too fast. The frequency response of the accelerometer was flat up to 10 kHz and the thin layer of beeswax was not believed influential until above 5 kHz.

Figure 5.9 shows the measured loss factor for the wall. η is approximately 0.02 over most of the frequency range, up to 1.25 kHz. At higher frequencies, where measurement was less reliable, the value decreases. Therefore, from these measurements, all 1:8 scale walls were predicted using a loss factor of 0.02. This flat response is confirmed for building materials from measurements of concrete and masonry rods by Gibbs [113]. He considered bending, longitudinal and torsional waves separately, by exciting and measuring the vibrational response in rods along different axes. Loss factors were calculated by sweeping through the frequency band of excitation and evaluating the half-power bandwidths. It was discovered that for all wave types and materials the loss factors could be regarded as independent of frequency. For the brickwork and reinforced concrete rods all values of η for all wave types were found to be similar, between $0.8 - 1.3 \times 10^{-2}$.

5.4 FIN WALLS

So far we have considered the transmission loss of a single isotropic wall, presented a suitable theoretical prediction, and determined the damping parameter for the 1:8

scale walls. We can now examine the affect on the transmission loss of adding ribs to an isotropic wall.

Three 1:8 scale fin walls were measured. One, three and seven ribs were added to an isotropic single wall. In each case the addition of the ribs halved the distance between centres, as shown in figure 3.1. Figure 5.10 shows the measured transmission loss of the 1 rib, 3 rib and 7 rib fin walls and the isotropic single wall. The 1 and 3 rib fin walls were measured according to ISO 140/3 and the 7 rib and single wall by intensimetry - the latter two being measurable up to 16 kHz. Super-critically, i.e. above 2328 Hz, all the curves rise with roughly the same gradient. The 1 and 3 rib walls are slightly lower than the 7 rib and single walls due to the failure of the ISO 140/3 method (already discussed in Chapters 3 and 4).

An important effect of ribbing is seen sub-critically. There is a distinctive change in shape between the isotropic wall, which has a 'hump' in transmission loss, and the fin walls which tend to produce a 'plateau region'. The effect is less obvious for the 1:4 scale walls (see figure 5.11) but was repeatable. In all cases there is a reduced transmission loss in the sub-critical region when fins are added to an isotropic wall. Also, the transmission loss around critical frequency of the 1:8 scale 7 rib fin wall (figure 5.10) and the 1:4 scale fin wall (figure 5.11) is already rising, possibly suggesting a lower critical frequency. Furthermore, as more ribs are added, the 'plateau region' extends to a lower frequency (figure 5.10).

5.4.1 Prediction for Fin Walls

A distinctive difference in transmission loss is observed between the fin and single walls. As this effect is likely to also influence the diaphragm wall performance it was decided to analyse and predict the fin walls transmission loss. If the ribs are considered to have no other influence apart from an addition in mass; then the wall

can be predicted as a single wall of equivalent mass. Table 5 below shows the rib/leaf width ratio, the equivalent thickness, h_{eq}, and equivalent surface density, m_{eq}, for the 1:8 scale fin walls.

Table 5: Equivalent Surface Density of Model Fin Walls

No. of ribs:	Rib/leaf width ratio	h_{eq} (m)	m_{eq} (Kg/m^2)
0 (single)	0	0.013	15.47
1	0.05	0.014	16.24
3	0.15	0.015	17.79
7	0.35	0.018	20.88

Firstly, the walls are predicted as single isotropic walls as described by equation 5.1 where m is replaced by m_{eq}. Figure 5.12 shows the measured minus predicted transmission loss for the 1:8 scale fin walls. Prediction for all the walls show the same characteristics, an under-estimation sub-critically, and an over-estimation about coincidence, with reasonable agreement, within 1 - 2 dB, at higher frequencies. The difference between prediction and measurement is greatest for the 7 rib case, which would be expected as it shows the flatter plateau region. It appears that super-critically transmission loss is a function of equivalent surface density, but it should be noted that change in surface density between the 7 rib wall and the single wall is only an increase of 1.3 dB. An approach is now required which allows the stiffening effect of the ribs to be included in theory.

Lee [114] gives an expression for the transmission loss of a single stud panel as:

$$TL = -10\log\left\{\left[1 + \left[\frac{\omega m}{4\rho c}\right]^2\right]^{-1} + \left[\left[\frac{\omega m}{2\rho c}\right]^2 \left[\frac{f}{f_c}\frac{2}{\pi}\frac{\eta}{(\sigma_{rad})^2}\right]\right]^{-1}\right\} \qquad (5.5)$$

The expression includes the term σ_{rad} for the radiation efficiency of a panel given by Maidanik [115]. The radiation efficiency of a plate is defined in section 5.6, where

σ_{rad} is given by equations 5.10 - 5.17. Sub-critically the radiation efficiency is a function of the perimeter length, and the separation of the panel into sub-areas by ribs increases the perimeter by a factor of two times the total rib lengths. Figure 5.13 compares theory with measurement for the 7 rib fin wall. Two predictions curves are given, the first excludes the additional perimeter length and is the same as a prediction of a single isotropic wall, and the second includes the extra perimeter length. Both predictions give poor agreement with measurement. The isotropic prediction over-estimates the coincidence region and does not indicate a plateau effect. Including the ribs perimeter length increases the discrepancy, simply reducing the transmission loss sub-critically, with no change in shape. This is to be expected since Maidanik's theory of radiation efficiency is only suitable for panels where the ribs are rigid and the sub-panels act as isotropic plates. This is not the case for the fin and diaphragm walls.

An alternative approach is to consider the wall as 'orthotropic'. An orthotropic wall has two bending stiffnesses. In the vertical axis the ribs are simply additional masses to the leaf and the bending stiffness is the same as the isotropic wall. In the horizontal axis the ribs give an increased bending stiffness. The bending stiffness is given by:

$$B = EI_{xx} \qquad (5.6)$$

Where E is the Young's modulus, which can be estimated by re-arranging equation 2.17. I_{xx} is the moment of inertia, either horizontally across the ribs, or vertically parallel with the ribs; calculated according to Appendix A.2 (x-x is the axis of bending along the wall). In its simplest form I_{xx} depends on the cube of the wall's depth. The bending stiffness effects the speed of the propagating flexural waves across the wall, so different bending speeds will occur vertically and horizontally. As it is the interaction of bending and acoustic wavelengths in air which cause

'coincidence,' in the orthotropic case this will begin at two different critical frequencies, calculated from equation 2.26. The upper critical frequency, $f_{c,u}$, is based on the bending stiffness of the leaf; and the lower critical frequency, $f_{c,l}$, is based on the horizontal bending stiffness of the whole wall. As more ribs are added the centroidal axis changes producing different values of I_{xx}, and $f_{c,l}$. Table 6 shows the values of I_{xx}, B and $f_{c,l}$, for the 1:8 scale fin walls.

Table 6: Lower Critical Frequencies of Model Fin Walls

No. of ribs:	I_{xx} (m^4)	B ($Kg/m^2\ s^{-2}$)	$f_{c,l}$ (Hz)
0 (single)	183e-9	934.9	2423 ($f_{c,u}$)
1	9.3e-7	4764.9	1073
3	2.3e-6	11617.1	687
7	4.5e-6	22871.5	490

From the measurements it is seen that no second coincidence dip is seen at $f_{c,l}$, but rather it extends the region affected by coincidence from $f_{c,l}$ to $f_{c,u}$, and creates a plateau region. Equation 5.1 for isotropic walls can be modified as follows: f_c remains the same as $f_{c,u}$, but $f_c/2$ is replaced by the lower critical frequency, $f_{c,l}$, and linear interpolation is used between critical frequencies to give a plateau region. Now the mass law region only occurs below $f_{c,l}$, and above $f_{c,u}$ the recovery expression is unchanged except that an equivalent mass, m_{eq}, is used. Therefore the transmission loss for the fin walls is predicted as:

Mass law	$f_0 < f < f_{c,l}$	Equation 2.14	
Interpolation	$f_{c,l} < f < f_{c,u}$		(5.7)
Recovery	$f > f_{c,u}$	Equation 2.30 using m_{eq}.	

Hence, as ribs are added the bending stiffness increases and the lower critical frequency decreases, thus extending the plateau region down in frequency.

Figures 5.14 - 5.16 show predictions of transmission loss for the 1,3 and 7 fin walls respectively, using equation 5.7. The interpolated region is shown between calculated values of $f_{c,l}$ and $f_{c,u}$ rather than the nearest 1/3 octave frequency. Agreement, sub-critically, between prediction and measurement is much improved. A negative gradient is indicated in all cases, along with an increasing transitional region which seems to agree well with measurement. For the 1 and 3 rib walls agreement is within 2dB. For the 7 rib case agreement is less good due to a slight double dip in transmission loss below $f_{c,u}$. Figure 5.17 is for the 1:4 scale fin wall [18] where $f_{c,u}$ = 1111 Hz, $f_{c,l}$ = 190 Hz, and m_{eq} = 59.4 Kg/m^2. Agreement is very good over the whole frequency range . As measurements were only down to 400 Hz, the region below $f_{c,u}$ is all plateau. This would also be the case for full scale walls where $f_{c,l}$ is much lower than 50 Hz.

Overall, prediction using equation 5.7 fits well with measurement, and could in theory be applied to any type of fin construction. The assumption to include the bending stiffness of the whole wall has been shown to be important, producing a lower critical frequency and a change in transmission loss.

5.5 ORTHOTROPIC WALLS

The indication is that orthotropicity will influence the performance of the diaphragm wall and therefore must be considered in more detail. To do this we shall examine the stiffening effect of the ribs on a diaphragm wall with respect to other stiffened constructions. Many structural elements are stiffened by ribs such as a ship's hull or aircraft's fuselage. Examples in buildings are in the form of stud partitions or profiled industrial cladding. Three common ways of stiffening a surface are a grillage, by profiling the surface, or by line stiffening. The surface of a grillage is stiffened equally in mutually perpendicular directions and therefore is unlike the fin

or diaphragm wall, except for its flat radiating surface. Cummings [49] & Maidanik [115] have considered the transmission loss and radiation efficiency of this construction. A corrugated panel is an example of profiled stiffening, and of orthotropic transmission characteristics. Like both fin and diaphragm walls it has two critical frequencies and an extended coincidence region. Stud partitions are examples of line stiffened walls, comprising typically of a plasterboard or plywood panel attached to vertical timber or metal studs at regular centres. A single stud partition superficially seems similar to the fin wall, with a flat surface stiffened linearly in one direction. Likewise, a double stud partition is superficially similar to a diaphragm wall. Yet it will be seen that none of these constructions apply well to either masonry fin or diaphragm walls.

Figure 5.18 shows the measured results of a single and double stud partition reproduced by Lee [114]. Both partitions are built of 12 mm plywood panels and 50mm x 50 mm studs at 0.5 m centres. The transmission loss shape for the partitions suggest an isotropic wall with one critical frequency based on the panel only. There is a 'hump' in transmission loss sub-critically and no clear plateau region ($f_c \approx 2$ kHz). Hence some stiffened walls exhibit isotropic and others orthotropic sound transmission characteristics. It is suggested that the difference depends on two factors, the number of bending wavelengths between rib centres and the rib /leaf impedance ratio.

Let us first consider the distance between rib centres. For the prediction of bridged walls it is assumed that each bridge acts independently [37, 41]. For this to be true the bridges should not be within the 'near field' of each other. Kihlman [116] considers that where the distance between bridges is 5 - 10 times greater than the bending wavelength at the critical frequency, then they shall act independently and not affect the isotropic surface radiation. Using this approach for the 1:8 scale walls, the bridges should be a minimum of 0.74 - 1.48 m apart. Hence for the 3 and 7 rib

cases of fin and diaphragm walls the ribs will interact to affect the surface radiation, while the 1 rib wall is on the border. For a 1/2 brick unplastered masonry wall $\lambda_b \approx$ 1.3 m, giving a minimum distance of 6.3 - 12.7 m between ribs centres, where the diaphragm wall has ribs 1 - 1.5 m apart.

Let us consider the number of bending wavelengths, λ_b, between rib centres. By rearranging equation 2.20 and including equation 2.19, λ_b equals:

$$\lambda_b = \frac{\sqrt[4]{\frac{B}{m}}\,\sqrt[2]{2\pi}}{\sqrt[2]{f}} \qquad (5.8)$$

The frequency limit at which there are 'n' bending wavelengths between rib centres, is given by:

$$f_{limit} = \frac{c}{n\,\lambda_b} \qquad (5.9)$$

f_{limit}, with respect to 1 and 2 bending wavelengths, was calculated for the cases of 1:8 scale fin and diaphragm walls and a selection of other walls.

Table 7: F_{limit} at One and Two Bending Wavelengths

Wall type	f_{limit} at 1 λ_b (Hz)	f_{limit} at 2 λ_b (Hz)
Fin/Diaphragm wall - 1 rib	195	782
F/D wall - 3 rib	782	3126
F/D wall - 7 rib	3126	12505
1/2 brick masonry wall - 1.25 m c/c	280	1120
Plywood stud partitions - 0.5 m c/c [114]	261	1045
Pl/bd double stud partition - 0.61 m c/c [41]	153	2090

It was hoped that a change in transmission loss would occur at one of these frequency limits, suggesting some alteration in rib-to-rib interaction. Consider again figure 5.18, and figures 5.10 and 6.1 showing the measured transmission loss of the 1,3 and 7 rib fin and diaphragm walls respectively.

For $f_{limit} = 2\lambda_b$, most walls are in the super-critical region and indicate isotropic behaviour above and below this limit. For $f_{limit} = 1\lambda_b$ a change in the transmission loss curve is suggested by some of the results. Lee's measurements of single and double stud walls both suggest a flattening of the transmission loss curve below the $1\lambda_b$ frequency, indicated by the arrows in figure 5.18, then rise significantly producing a traditional isotropic 'hump.' For the 7 rib fin and diaphragm wall f_{limit} is slightly above $f_{c,u}$. Below f_{limit} is a flat plateau region, while above it the wall acts as a single isotropic wall of equivalent mass. For the 1 rib wall isotropicity is still indicated below f_{limit} and for the 3 rib walls results are 'bumpy' and less easy to interpret.

Deductions based on the above are purely from observation and it is appreciated that other factors considered in this and following chapters strongly affect the shape of the transmission loss curve. However it is suggested that the assumption that ribs act independent of each other is only valid at frequencies where at least one wavelength lies between the leaves. Where the distance between the ribs is greater than two wavelengths the sub-wall or whole wall will behave isotropically. Therefore, walls might be described as orthotropic in transmission loss character where the ribs are within one wavelength of each other, but this will also depend on the impedance matching between rib and leaf.

The impedance mis-match between rib and leaf, and the rigidity of the ribs is discussed in section 5.6 with regard to radiation efficiency of the surface, and in Chapter 6 with regard to the bridging effect. It appears that three cases exist,

depicted in figure 5.19. A high impedance case is a lightweight partition where the stud is rigid with a higher impedance and bending stiffness than the plasterboard panel. The studs behave as fixed boundaries with the panels between them performing as small isotropic sub-panels. A common low impedance case is light ties between masonry cavity walls which will exert no influence on the wall's isotropic radiation character and the whole wall will act as a single wall. The matched impedance case applies to the fin and diaphragm walls. The ribs and leaves are of identical or similar material, allowing easy vibrational transmission across the junction, and can be considered neither as rigid nor resilient. Therefore the wall is poorly described as simply a stiffened wall and at frequencies where the orthotropicity of the wall effects the sound radiation efficiency, it will be different to that of either an isotropic or stiffened wall.

5.6 RADIATION RESISTANCE OF ORTHOTROPIC WALLS

An isotropic wall has one bending stiffness and one radiation characteristic, while an orthotropic wall has two bending stiffnesses and therefore two radiation characteristics. The problem arises how these should be interpreted or combined to give a suitable total radiation character.

The radiation of sound from a surface is described primarily by its radiation efficiency, σ_{rad}, which can be defined as, the acoustic power from the surface into half space divided by the acoustic power of an infinite piston radiating into the same half space vibrating at the same rms velocity [117]. If we consider an infinite plate, the radiation efficiency above f_c is like that of an infinite piston and therefore σ_{rad} is unity. At $f = f_c$ acoustic and bending wavelengths match and acoustic power theoretically can reach infinity, but will be limited by material damping. Below f_c, the surface bending waves of an infinite plate cannot couple with the air and no radiation occurs.

For a real wall, area and dimensions, edge conditions, damping, bending stiffness and modal response, all effect the sound radiation. If a wall is excited by a broadband source then the wall will respond in a multi-modal form, resonating at its natural frequencies within the excitation bandwidth. Above f_c these modes can couple efficiently with air and the whole surface radiates evenly. Modes above f_c are termed acoustically fast (A.F. modes). Below f_c modes couple poorly with the air and volume velocity cancellation occurs over most of the surface [118]. Where $f < f_c$ all modes are terms acoustically slow (A.S. modes). Where $f < f_{11}$ (first bending resonance) no modes exist and there is no resonant radiation. At low frequencies where the surface modes are slow in both x and y directions the only radiation is from corners of the walls where no cancellation occurs, see figure 5.20a. If far apart, they act as point sources, (usually assumed when $\lambda > 3l_x$, where l_x is the wall length in the x-direction). At frequencies where A.S. and A.F. modes both take place, cancellation will occur everywhere but along the edges parallel to the A.S. modes, see figure 5.20b. Therefore, the degree of modal radiation will depend upon the number of resonant modes within the frequency bandwidth of excitation and whether they are radiating efficiently or poorly.

The radiation efficiency of a finite plate is given by:

$$\sigma_{rad}^{2\pi} = \left[1 - \frac{f_c}{f}\right]^{-\frac{1}{2}} \qquad f > f_c \qquad (5.10)$$

and,

$$\sigma_{rad}^{2\pi} = \left[\frac{l_x}{\lambda_c}\right]^{-\frac{1}{2}} + \left[\frac{l_y}{\lambda_c}\right]^{\frac{1}{2}} \qquad f = f_c \qquad (5.11)$$

l_x and l_y are the lengths of the wall and λ_c the wavelength in air at critical frequency. Where $f < f_c$, σ_{rad} is given by Lyon [119] as an approximation of Maidanik [115], as:

$$\sigma_{rad}^{2\pi} = \left\{ \frac{\lambda_c P}{\pi A_w} \frac{2}{\pi} \sin^{-1} \left[\frac{f}{f_c} \right]^{\frac{-1}{2}} \right\} \beta \qquad (5.12)$$

where A_w is the wall area and b defines the edge conditions; $\beta = 1$ for the simply supported case and $\beta = 2$ for the clamped case. Lyon uses $\sqrt{2}$ as the general case. Maidanik's expression for σ_{rad} where $f < f_c$ is correctly given by Crocker & Price [120] and applies to the simply supported case.

$$\sigma_{rad}^{2\pi} = \left[\frac{\lambda_c \lambda_a}{A_p} \right] 2 \left[\frac{f}{f_c} \right] g_1 \left[\frac{f}{f_c} \right] + \left[\frac{P \lambda_c}{A_p} \right] g_1 \left[\frac{f}{f_c} \right] \qquad (5.13)$$

where $f < f_c/2$. g_1 is:

$$g_1 \left[\frac{f}{f_c} \right] = \frac{\left[\frac{4}{\pi^4} \right] \left[1 - 2\alpha^2 \right]}{\alpha \left[1 - \alpha^2 \right]^{\frac{1}{2}}} \qquad (5.14)$$

and where $f > f_c/2$. g1 is:

$$g_1 \left[\frac{f}{f_c} \right] = 0 \qquad (5.15)$$

g_2 is:

$$g_2 \left[\frac{f}{f_c} \right] = \frac{(2\pi)^{-2} \left\{ \left[1 - \alpha^2 \right] \ln \left[\frac{(1+\alpha)}{(1-\alpha)} \right] + 2\alpha \right\}}{\left[1 - \alpha^2 \right]^{\frac{3}{2}}} \qquad (5.16)$$

and α is:

$$\alpha = \left[\frac{f}{f_c} \right]^{\frac{1}{2}} \qquad (5.17)$$

Craik [121] also gives an approximation for σ_{rad} where $f \ll f_c$:

$$\sigma_{rad} = 69.7 \left[\frac{(l_x + l_y)}{l_x l_y}\right] \frac{1}{f_c} \left[\frac{f}{f_c}\right]^{\frac{1}{2}} \qquad (5.18)$$

An approximate design curve for the σ_{rad} under resonant broadband excitation, is given by Norton [122].

The radiation characteristics of a vibrating surface can be described in terms of radiation resistance, R_{rad}, by Maidanik [115] as the sound power radiated by a panel divided by the mean square velocity, averaged over time and space, (Π / $\langle v_p^2 \rangle$). R_{rad}, given as a function of radiation efficiency, is:

$$R_{rad}^{2\pi} = \rho c A_w \sigma_{rad}^{2\pi} \qquad (5.19)$$

Figure 5.21 shows the predicted radiation resistance for the 1:8 scale single wall as predicted by Lyon [119], and Maidanik [115] as given by Crocker & Price [120]. Both curves use identical expressions super-critically. Sub-critically Lyon's prediction produces almost a straight line upto f_c, Maidanik's expression was seen to predict better with measurement than Lyons with early comparisons and is thus used throughout this study.

5.6.1 R_{ort} for Orthotropic Walls

Five proposals were considered for a radiation resistance suitable for an orthotropic wall, denoted R_{ort}. These were applied and examined in chapter 7, in terms of a radiation loss factor, η_{wr}, as part of an SEA analysis. The relationship between η_{wr} and R_{rad} is given in equation 7.8. $R_{rad,l}$ and $R_{rad,u}$ denote the radiation resistances based on the lower and upper critical frequencies, $f_{c,l}$ and $f_{c,u}$ respectively. The

proposals were as follows and are shown in terms of radiation efficiency in figure 5.22:

i) $R_{ort} = R_{rad,u}$

R_{ort} is calculated as for an isotropic plate with one critical frequency, $f_{c,u}$ and takes no account of $f_{c,l}$. It assumes the radiation efficiency is minimal at these lower frequencies due to a reduced number of modes.

ii) $R_{ort} = R_{rad,u}$ (including extended perimeter).

For stiffened panels Maidanik [115] states that the radiation resistance is directly proportional to the perimeter of the panel. For a ribbed panel the perimeter term is increased by 2 times the total length of the ribs. As seen in Figure 5.13 using Lee's theory, this increase in radiation resistance significantly reduces the transmission loss. Figure 5.20c depicts the increase in corner radiation assumed by this alteration. Note that for the diaphragm wall the perimeter of the second leaf is not included, as we are only concerned with the radiation from one side of the wall.

iii) $$R_{ort} = \frac{R_{rad,l}.R_{rad,u}}{R_{rad,l} + R_{rad,u}} \qquad f < f_c \qquad (5.20)$$

$$R_{ort} = 2.\left[\frac{R_{rad,l}.R_{rad,u}}{R_{rad,l} + R_{rad,u}}\right] \qquad f > f_c \qquad (5.21)$$

The radiation resistances, $R_{rad,l}$ and $R_{rad,u}$ were combined according to parallel circuit theory shown by equations 5.25 and 5.26. Above f_c, R_{ort} is multipled by 2 so a value of unity occurs when $R_{rad,l}$ and $R_{rad,u}$ are unity. Figure 5.23 shows the values for the 1, 3 & 7 rib fin walls and $R_{rad,u}$ which does not change for any wall. The parallel circuit approach predicts sub-critically a radiation resistance lower than the $R_{rad,u}$, but the difference is small and about coincidence it produces a more heavily damped dip in the transmission loss curve, which is desirable.

iv) $R_{ort} = \sqrt{R_{rad,l}.R_{rad,u}}$ (5.22)

By calculating the geometric mean of the two radiation resistances, this gives greater emphasis to $R_{rad,l}$. Figure 5.22 shows it to produce a reduction in transmission loss sub-critically which is similar in size to that of the perimeter effect, larger about $f_{c,l}$ and smaller about $f_{c,u}$.

v) $R_{ort} = R_{rad,u}$ $f < f_{c,l}$

R_{ort} - interpolated $f_{c,l} < f > f_{c,u}$ (5.23)

$R_{ort} = \rho c A_w.1$ $f > f_{c,u}$

The final approach was to interpolate the values of radiation resistance between $f_{c,l}$ and $f_{c,u}$. Results were interpolated such that R_{ort} gave a straight line gradient on a log frequency axis, shown in figure 5.22. This final approach is shown in chapter 7 to give best agreement with measurement.

5.7 CAVITY FIN WALLS

This chapter has concentrated on investigating the effect adding ribs has on the radiation characteristics of a single leaf. In terms of the diaphragm wall, connecting a second leaf to the ribs means that it becomes necessary to also consider the ribs as vibrational transmission paths between the leaves.

To exclude the cross-rib path between leaves, the wall could be constructed as two interlocking but un-touching fin walls. Such a model wall was constructed, as shown in figure 5.24a. Its transmission loss is compared in figure 5.25 with that of a double wall, shown in figure 5.24b. It would be structurally possible to build a double fin wall, but it can be seen in figure 5.25 that as both fins are orthotropic there is still a plateau region below $f_{c,u}$. Compared with the double isotropic wall,

the transmission loss of the double fin wall is between 5 - 15 dB lower below $f_{c,u}$. Above $f_{c,u}$ agreement between curves is very close. Only about $f_{c,u}$ is the fin wall transmission loss greater than the double isotropic wall. The reason for this is unknown but is also exhibited for the 7 rib fin walls.

If we split the diaphragm wall at a rib/leaf junction rather than the centre, we create an orthotropic fin wall and an isotropic single wall. Three variations on this were measured, all consisting of a 7 rib fin wall and a single wall, shown in figure 5.24c-e. The difference in transmission loss between the three dis-connected diaphragm walls should be almost identical as the constituent parts of the walls do not change. Figure 5.26 shows the transmission loss of the double wall and these three double fin-single walls. What is apparent is that the loss in transmission loss seen sub-critically in figure 5.26 with the double fin wall, is regained by using a fin and single wall. Hence the isotropic radiation character of the single wall dominates sub-critically over the orthotropic wall. Super-critically agreement is very good except above 10 kHz where results are not reliable because of low signal to noise. The fin-single wall where the leaves are closely spaced has a significantly lower transmission loss sub-critically from the other walls. This is due to the close spacing of the leaves increasing the cavity air stiffness and thus energy transmission across the cavity.

The significance of these results is that any orthotropic influence due to the ribbing of one leaf seems to disappear when used in conjunction with an isotropic leaf. Unfortunately some connection is always required for structural reasons. Although the ideal case cannot be constructed for masonry walls, this implies that any reduced attachment that can be achieved in the link at the cross-rib/leaf junction will benefit the sound insulation by regaining in part some isotropic behaviour sub-critically, as well as reducing the transmission efficiency across the junction. These points are considered further in Chapters 6, 7 and 9.

5.8 CONCLUDING REMARKS

The effect on the transmission loss of single walls by adding ribs has been investigated and a decreased sound insulation has been observed in a plateau region below the critical frequency of the leaf. This is due to an expansion of the coincidence region by the creation of a lower critical frequency based on the bending stiffness across the ribs - hence the fin construction is defined as orthotropic. Isotropic theory was modified by the inclusion of a lower critical frequency and interpolating the transmission loss between the two critical frequencies. Good agreement with measurement was obtained. The addition of ribs lowers the lower critical frequency and thus extends the plateau region.

Present radiation resistance theory is inapplicable to the fin wall and indirectly also to the diaphragm wall as this considers stiffened walls, such as stud partitions, which are still isotropic in radiation and transmission loss character.

It is estimated that the distance between ribs should be at least two wavelengths to consider them acting independently and the area between to radiate isotropically. Although this also depends upon the impedance matching of rib and leaf, discussed further in chapter 6.

Proposals are given to estimate the radiation resistance of an orthotropic wall. These are included in terms of radiation loss factor in Chapter 7 and will then be compared with the measured transmission loss of the fin walls.

Finally, measurement showed it to be better to separate a diaphragm wall at cross-rib/leaf junction rather than down the centre of the ribs. The latter creates two orthotropic fin walls which still produce a plateau region sub-critically, while the former is a combination of an orthotropic fin wall and isotropic single wall. It was

shown that the transmission loss of the isotropic leaf dominates and the plateau region disappears, regaining the sound insulation lost in this frequency region.

Now that the orthotropicity of the diaphragm wall has been examined in isolation, chapter 6 will consider the effect of the ribs as a transmission path between the two leaves.

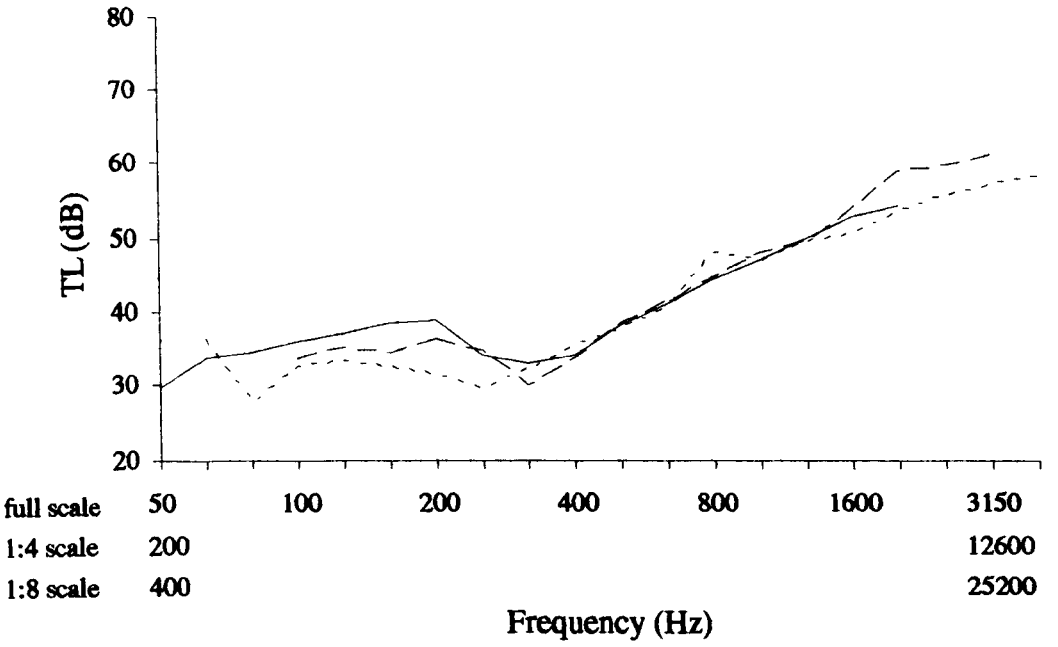

Figure 5.1: Measured transmission loss of single walls

1:8 scale

1:4 scale

Transmission suite wall - 120mm thick, plastered one side

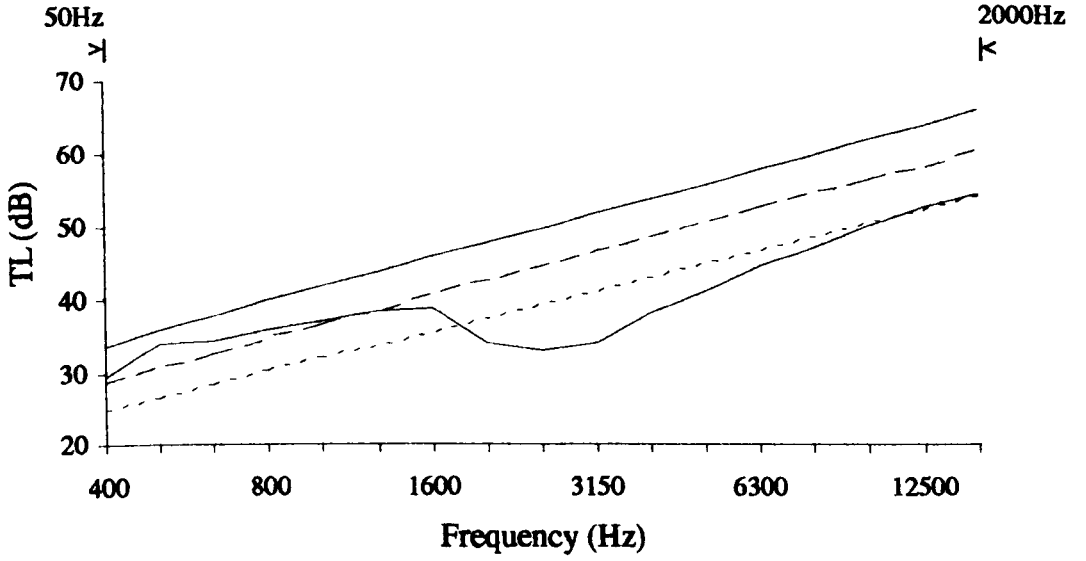

Figure 5.2: Mass law prediction of 1:8 scale single wall

measurement by intensimetry

Prediction - incidence:

random field normal

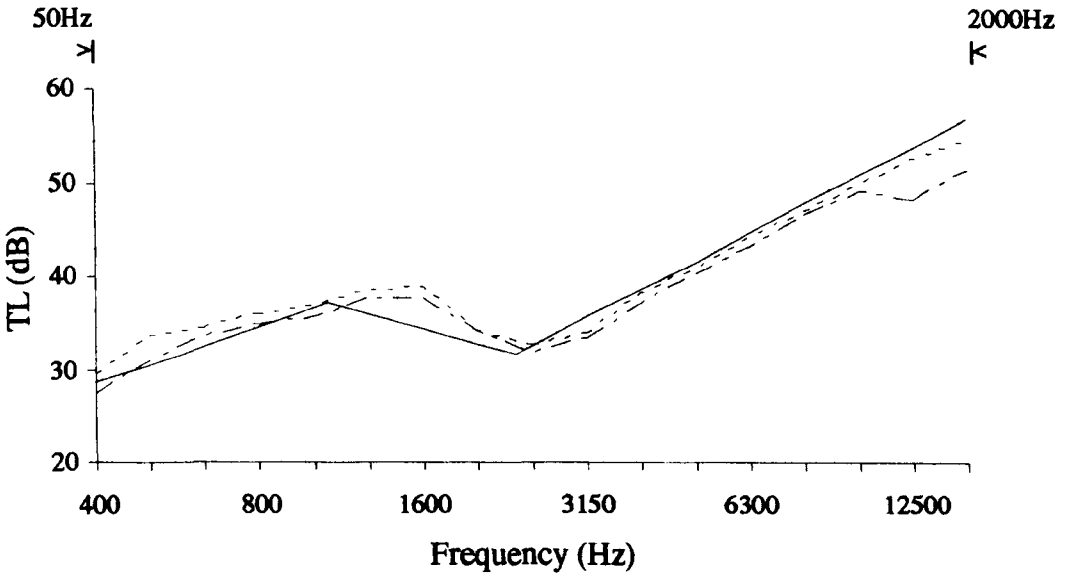

Figure 5.3: Transmission loss of 1:8 scale single wall

prediction

measurement: discrete point

measurement: scanning technique

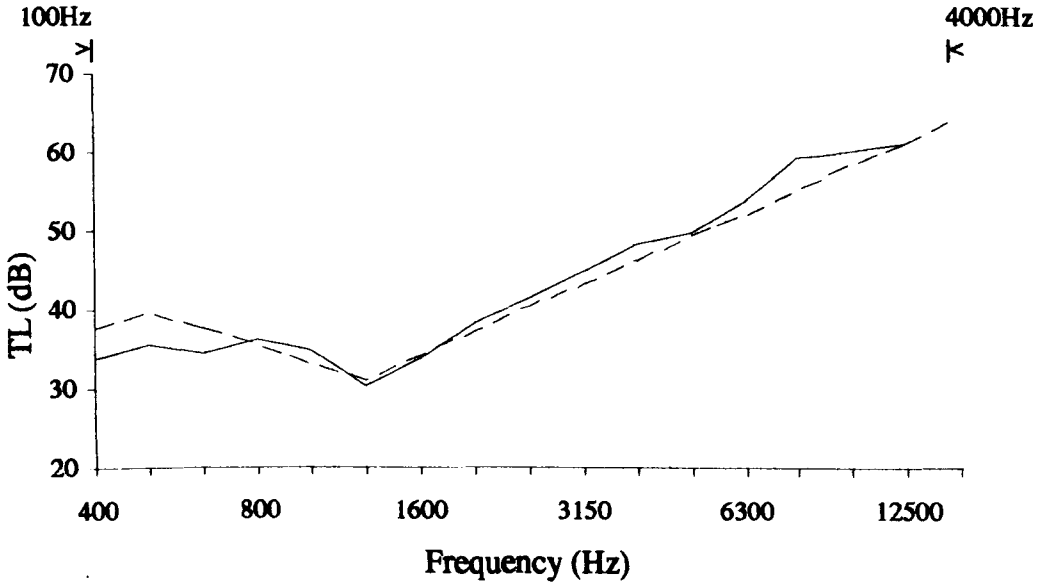

Figure 5.4: Transmission loss of 1/4 scale single wall

measurement: ISO 140/3

prediction

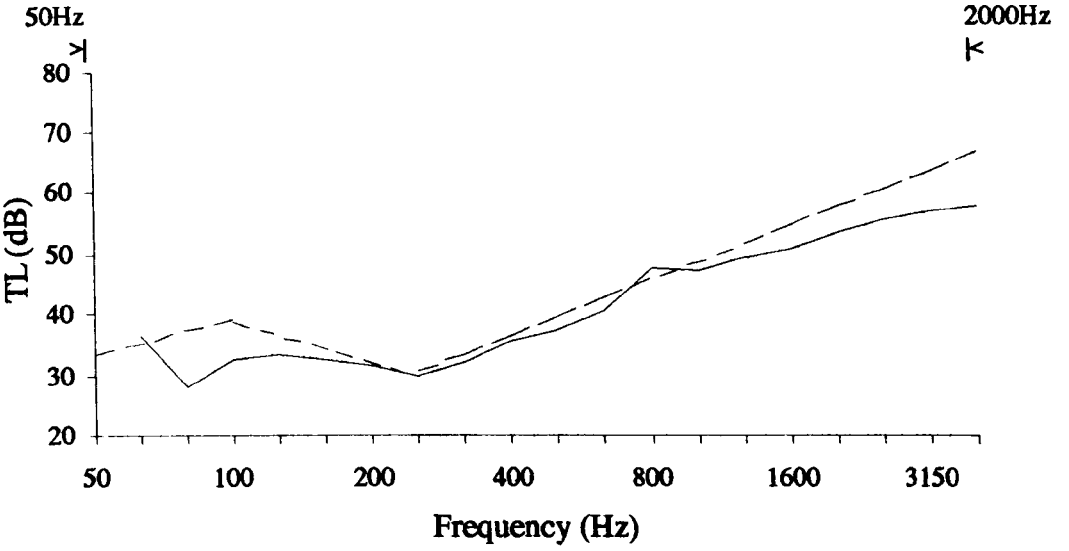

Figure 5.5: Transmission loss of transmission suite wall

measurement: intensimetry

prediction

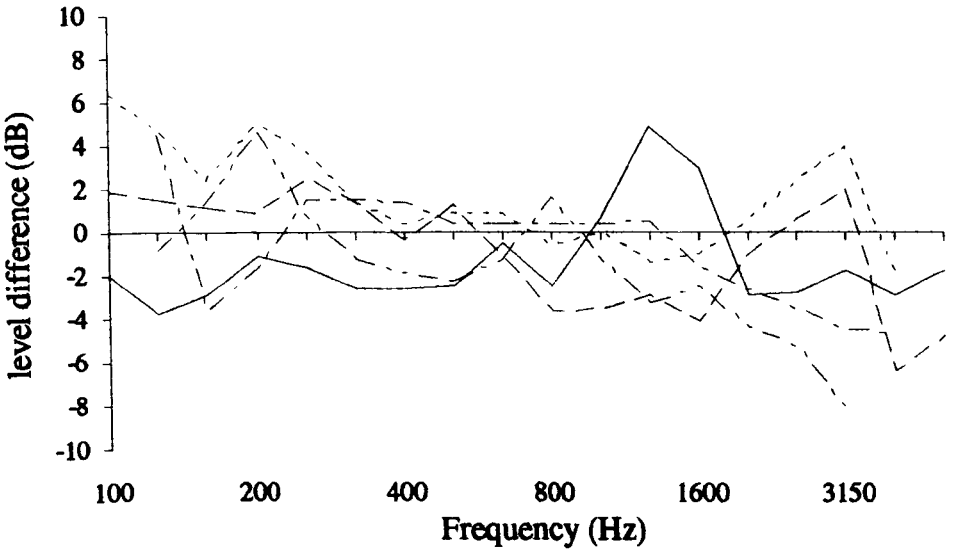

Figure 5.6: Difference between measured and predicted transmission loss for various building elements (measurement - prediction)

aluminium panels:

3mm [49]

6mm [49]

6mm [157]

hollow concrete block wall [157]

masonry wall [157]

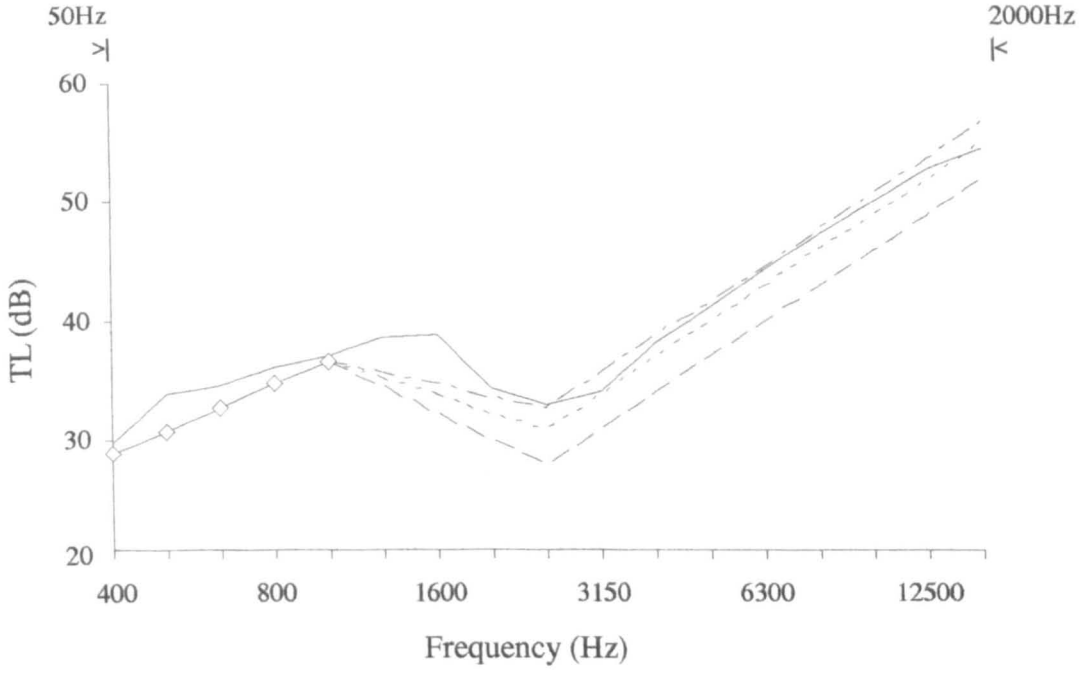

Figure 5.7: Transmission loss prediction of 1:8 scale single wall altering the loss factor

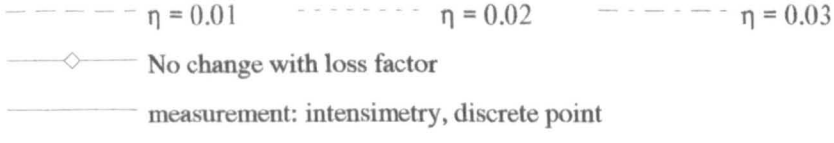

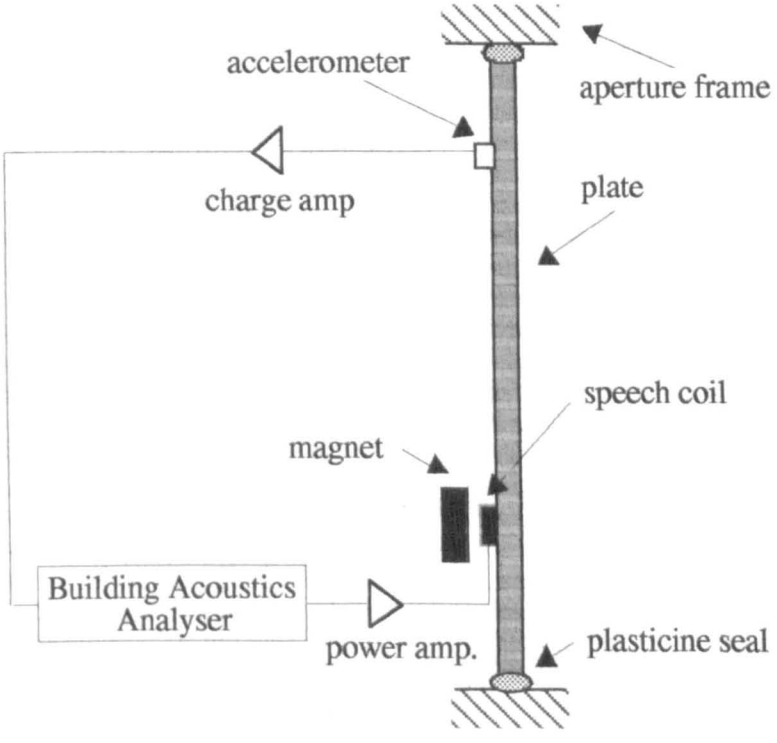

Figure 5.8: Loss factor measurement set-up

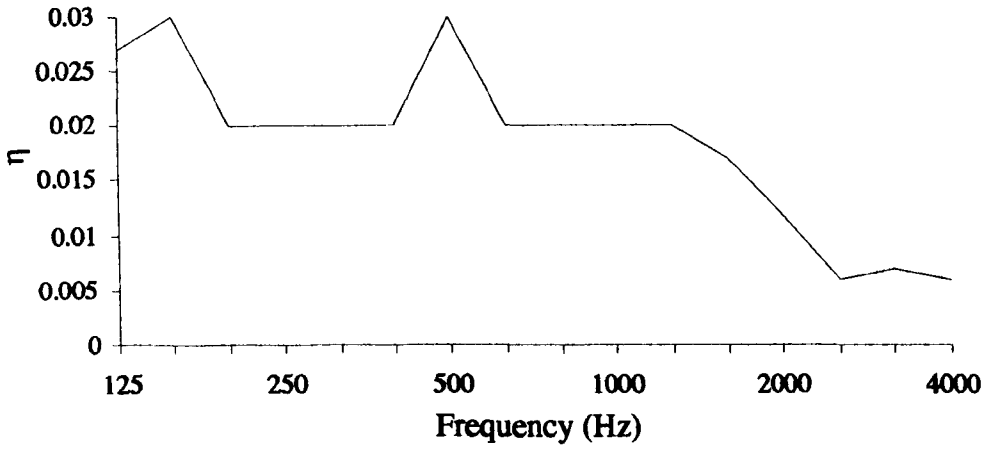

Figure 5.9: Measured loss factor for 1:8 scale single wall.

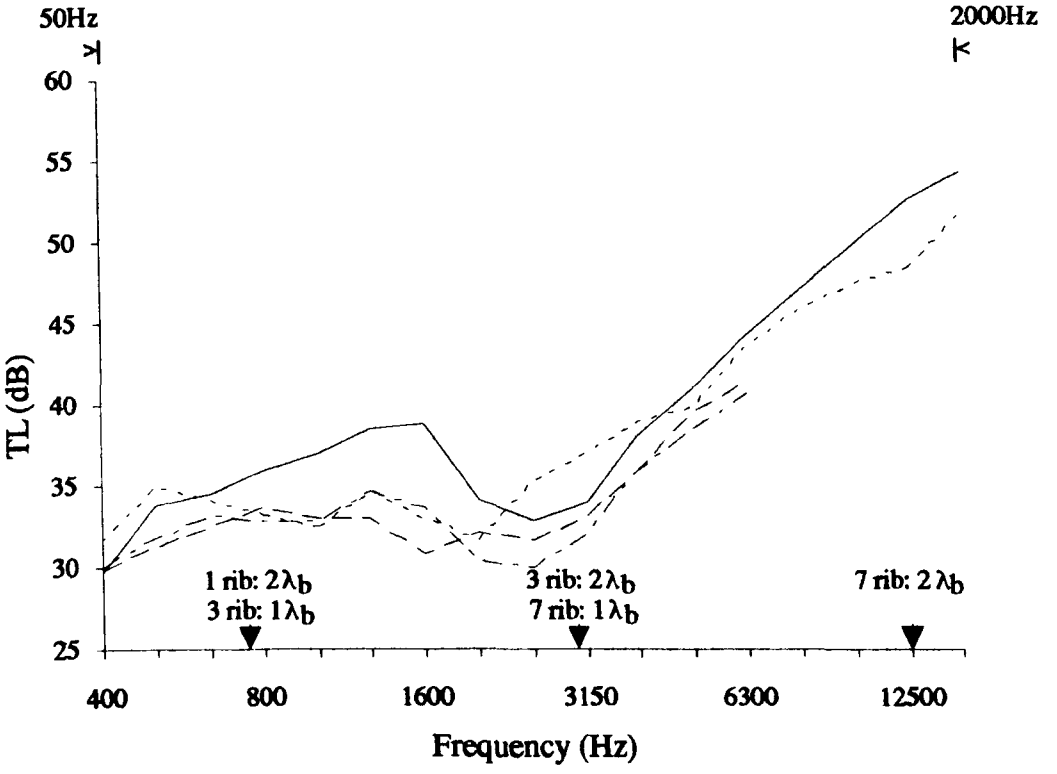

Figure 5.10: Measured transmission loss of 1:8 scale fin walls

- - - - - - 1 rib wall: ISO 140/3

— — — — 3 rib wall: ISO 140/3

. . . . . 7 rib wall: intensimetry - discrete point

——— single wall: intensimetry - discrete point

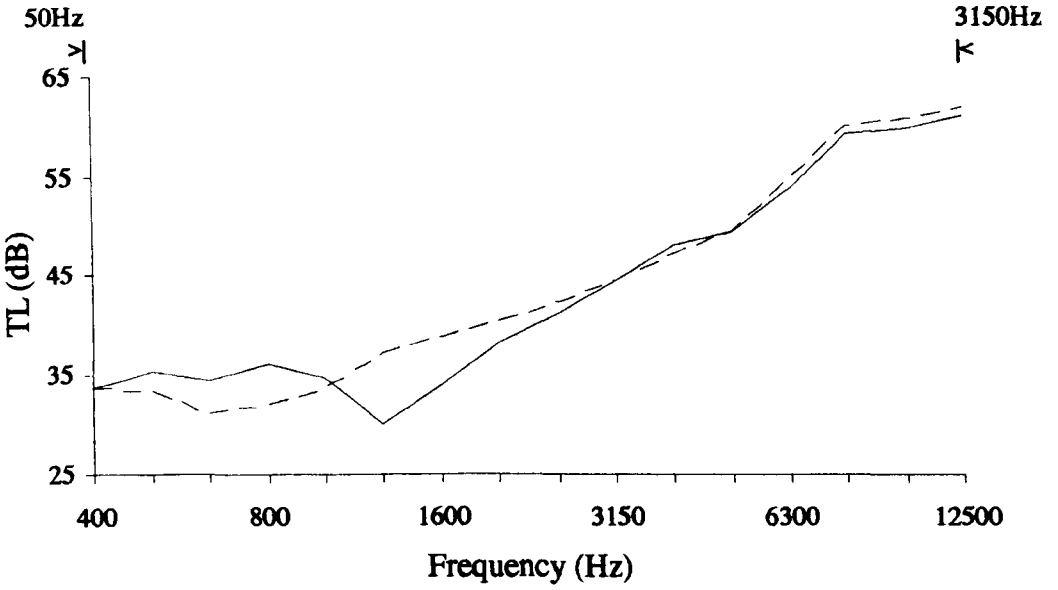

Figure 5.11: Measured transmission loss of 1:4 scale fin wall

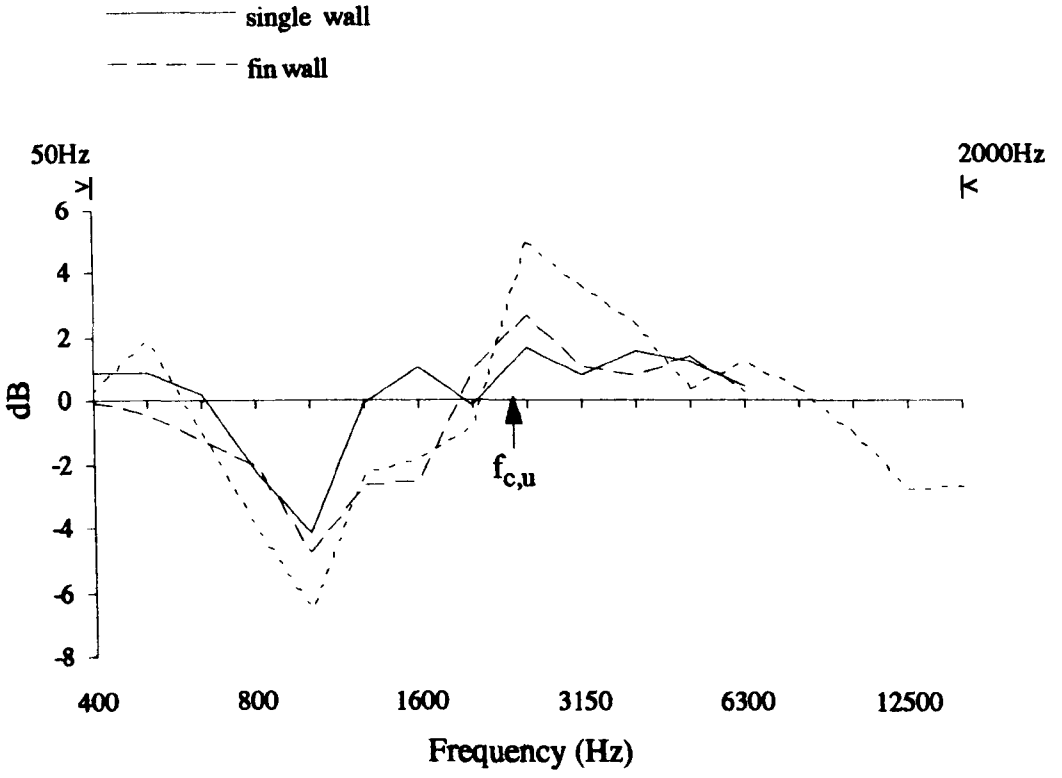

Figure 5.12: Fin wall transmission loss measurement and isotropic prediction

Measurement - Prediction (dB)
1 rib
3 rib
7 rib

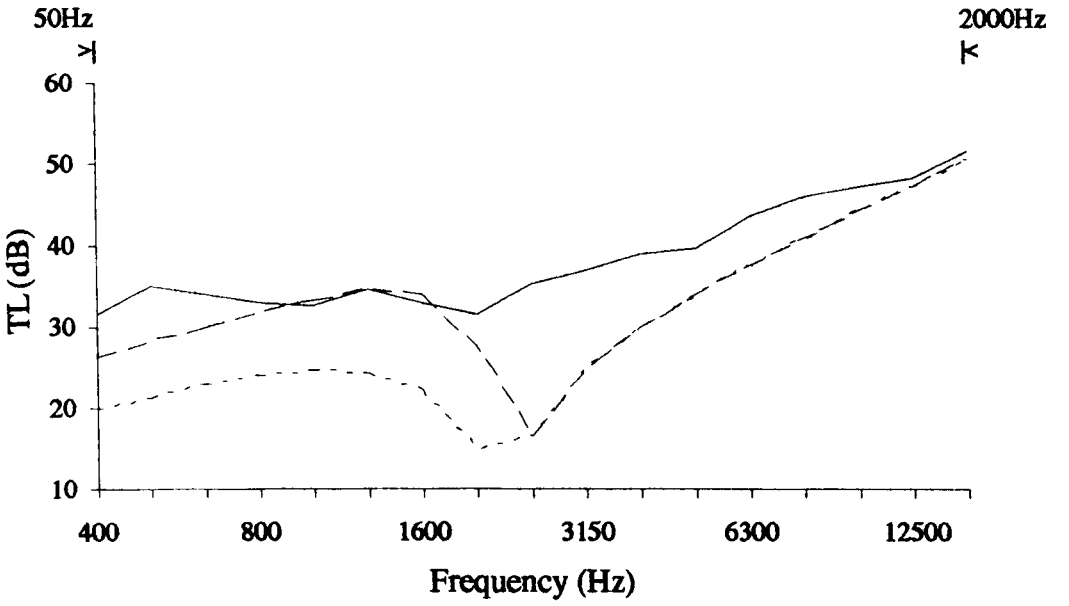

Figure 5.13: Transmission loss of 1:8 scale 7 rib fin wall using Lee's expression [114]

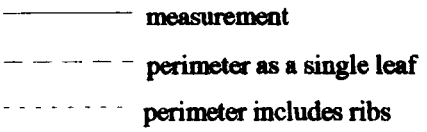

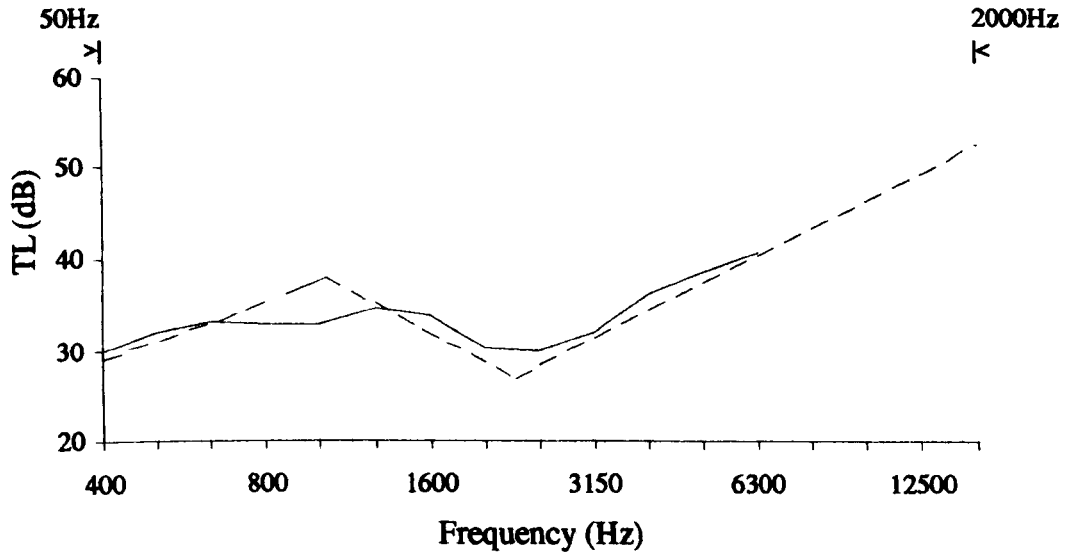

Figure 5.14: Transmission loss of 1:8 scale 1 rib fin wall

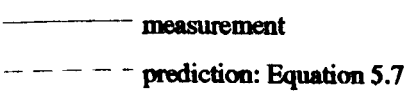

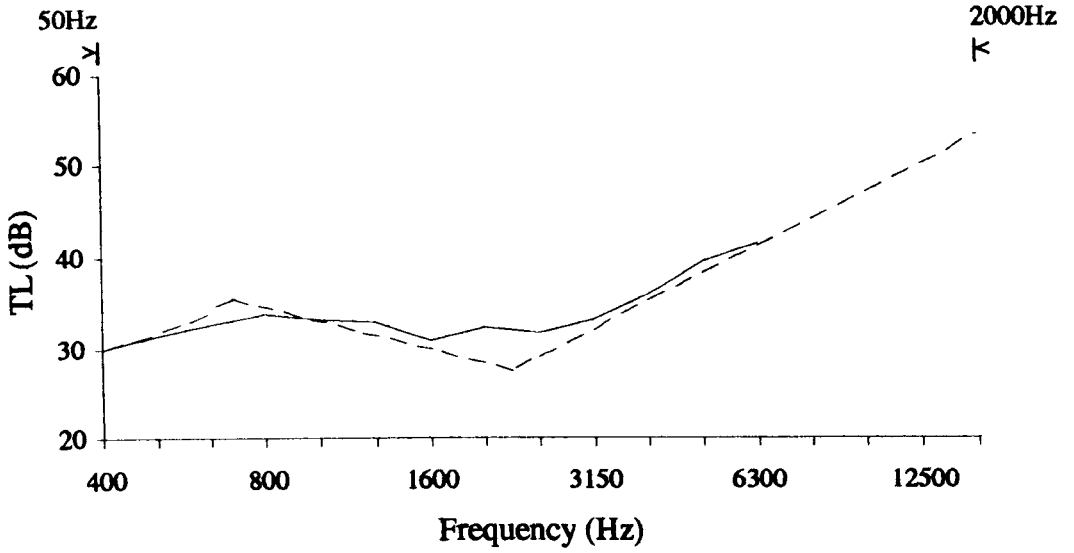

Figure 5.15: Transmission loss of 1:8 scale 3 rib fin wall

——— measurement

– – – – – prediction: Equation 5.7

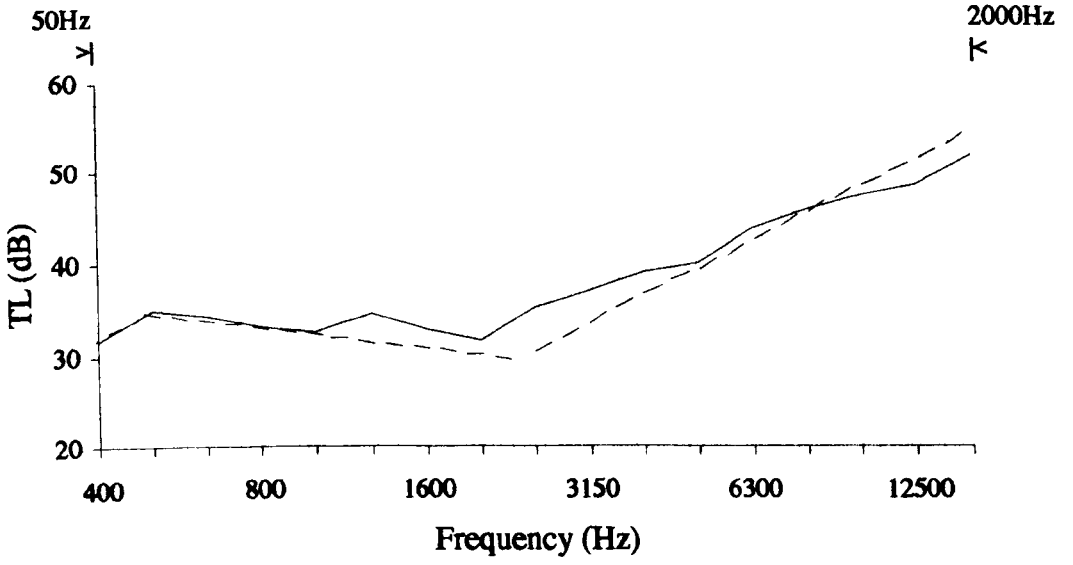

Figure 5.16: Transmission loss of 1:8 scale 7 rib fin wall

——— measurement

– – – – – prediction: Equation 5.7

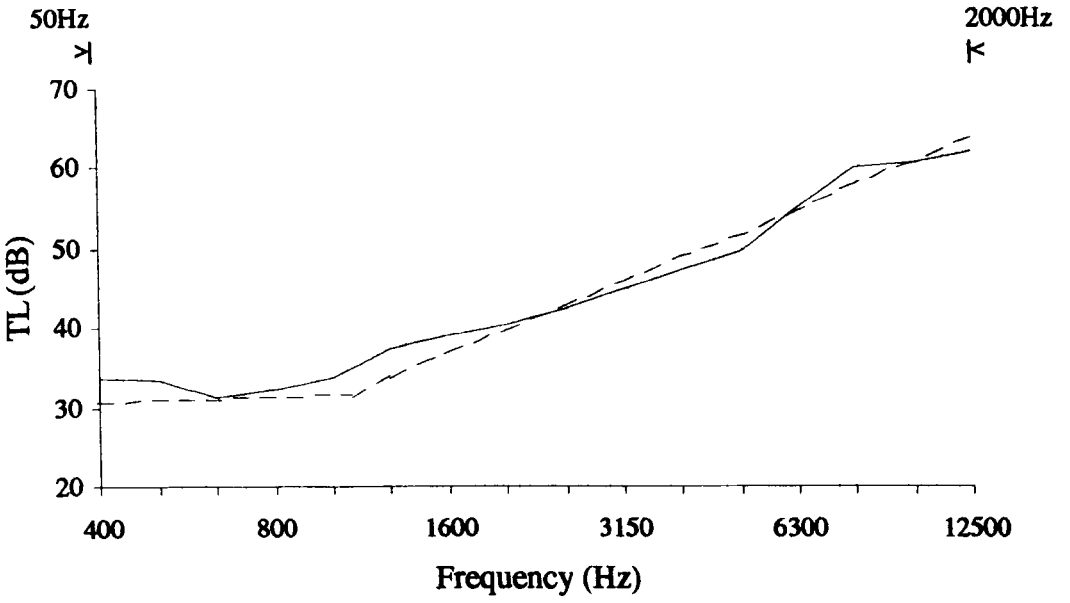

Figure 5.17: Transmission loss of 1/4 scale fin wall

measurement prediction

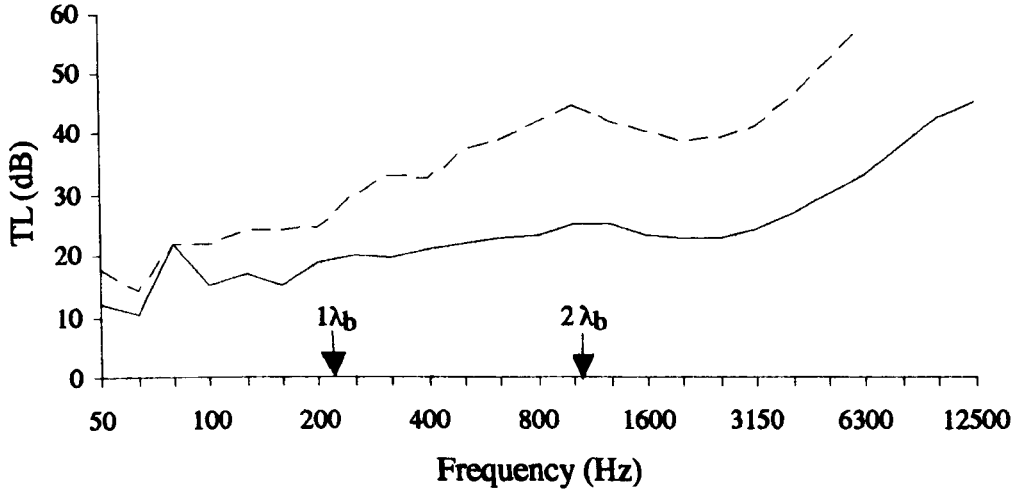

Figure 5.18: Measured transmission loss of single and double stud partitions [114]

single double

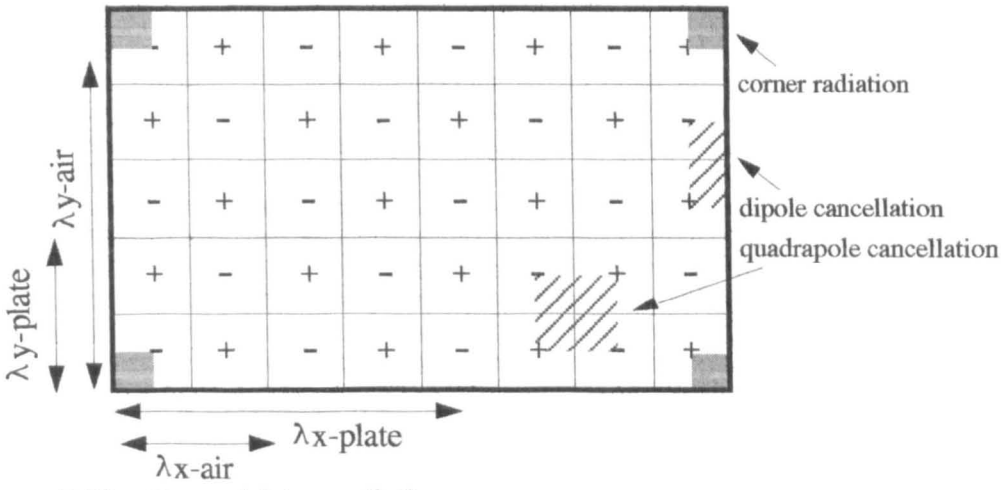

5.20a: Corner/piston radiation

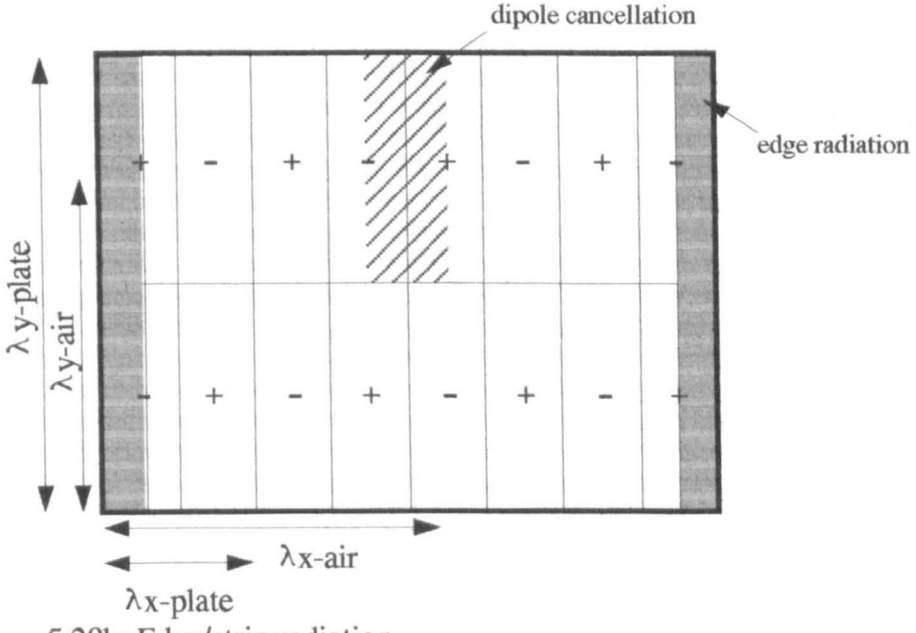

5.20b: Edge/strip radiation

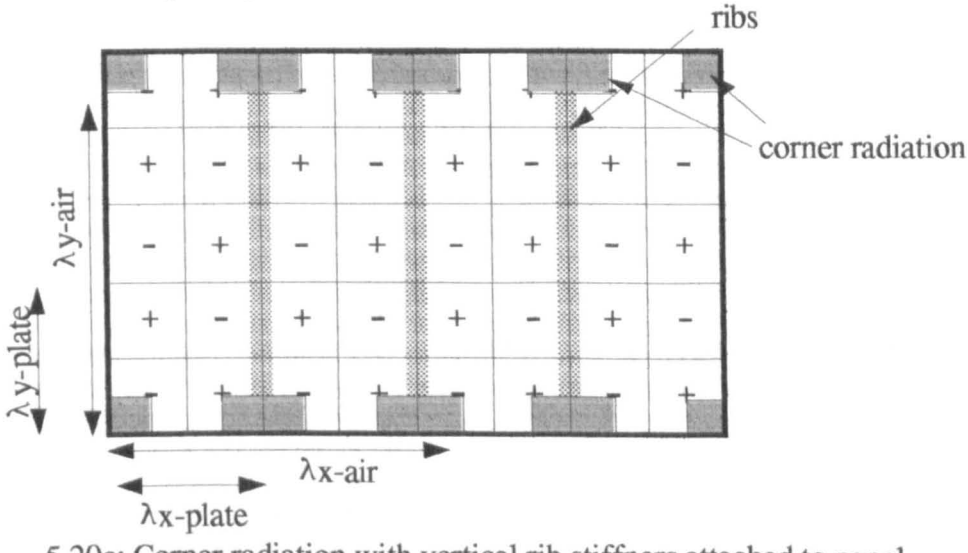

5.20c: Corner radiation with vertical rib stiffners attached to panel

Figure 5.20: Modal radiation patterns for finite plates

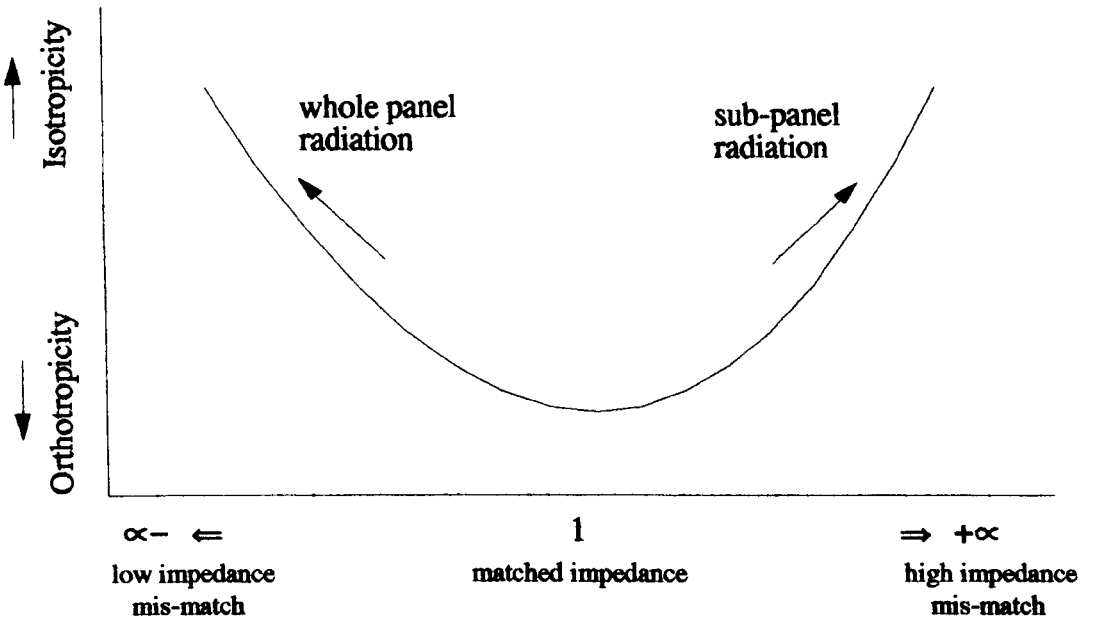

Figure 5.19: Isotropic / orthotropic relationship

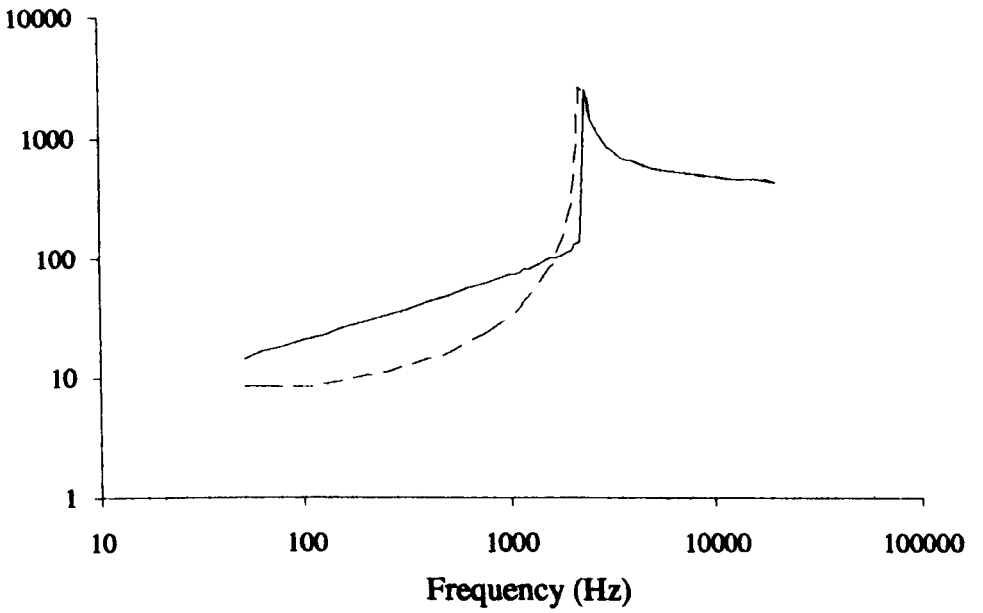

Figure 5.21: Radiation resistance of a 1:8 scale single wall

——— Lyon [119] – – – – – Maidanik [115]

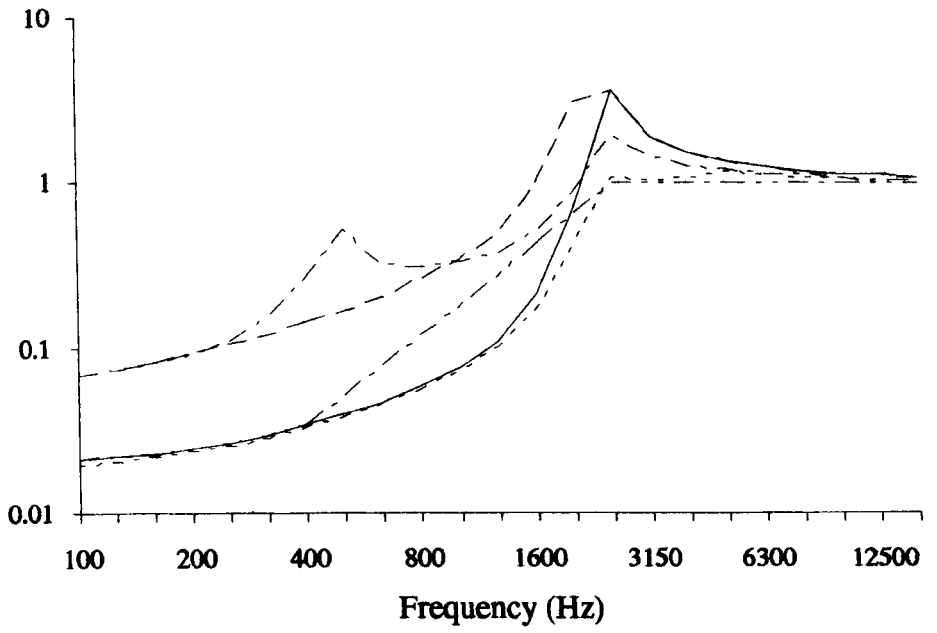

Figure 5.22: Radiation efficiency proposals for an orthotropic wall

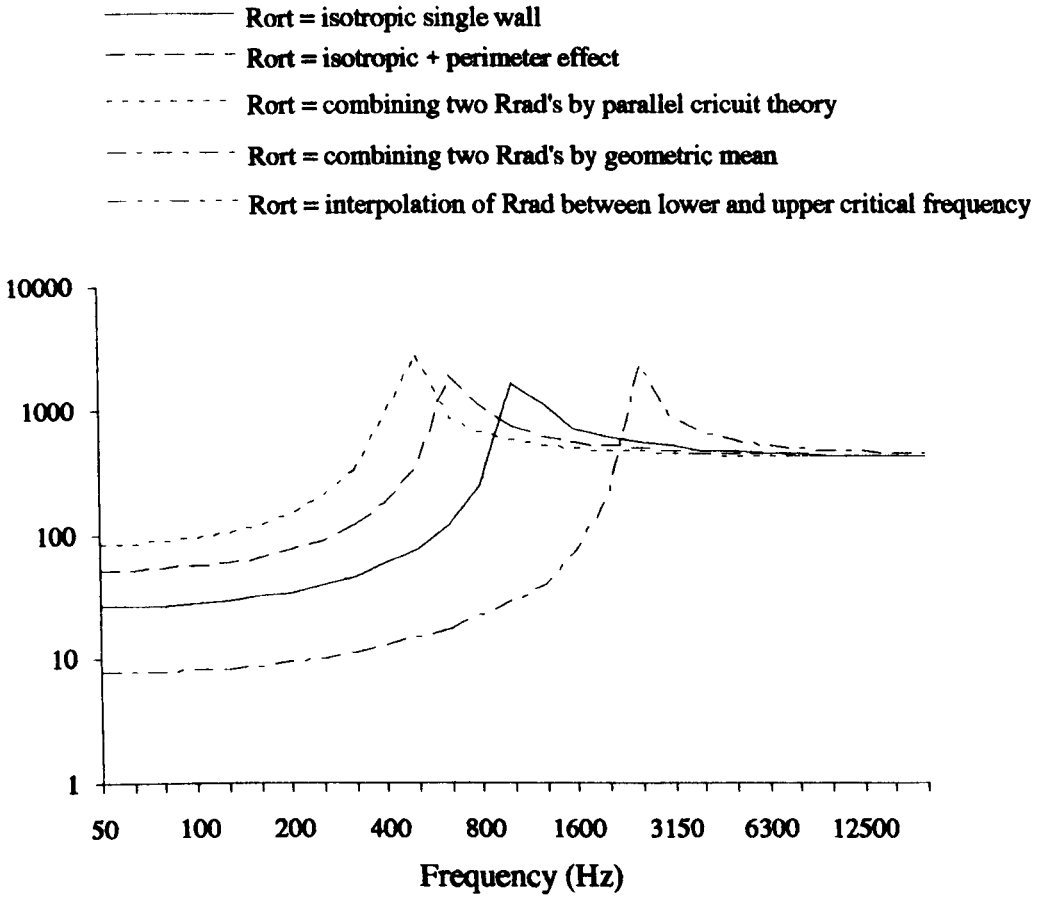

Figure 5.23: Radiation resistance of 1,3 and 7 rib fin walls based on the lower critical frequency

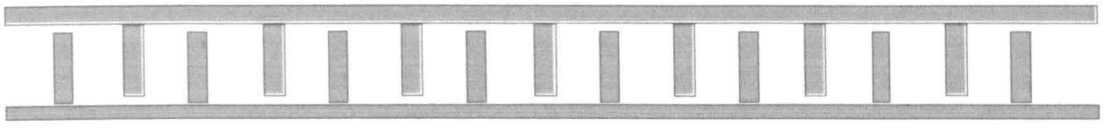

Figure 5.24a: Interlocking double fin wall

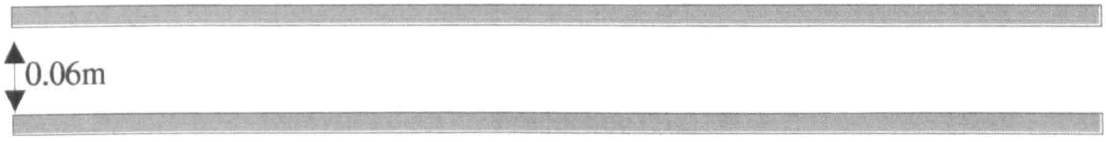

Figure 5.24b: Wide double wall

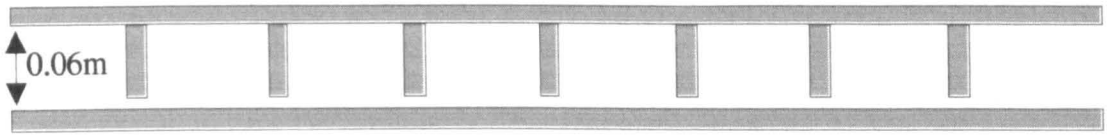

Figure 5.24c: Fins internal

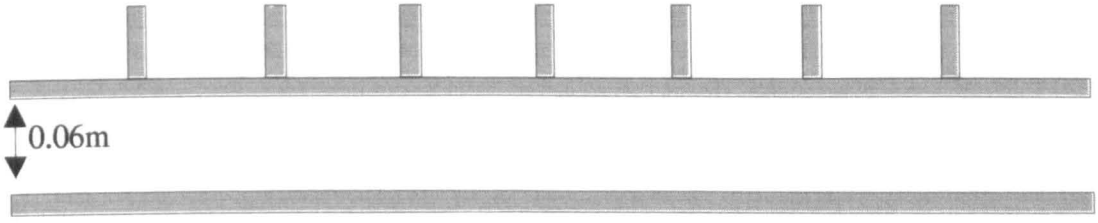

Figure 5.24d: Fins external

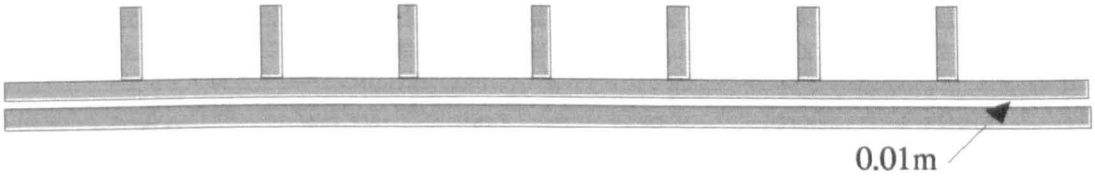

Figure 5.24e: Fins external (small gap)

Figure 5.24: Fin wall combinations and wide double wall

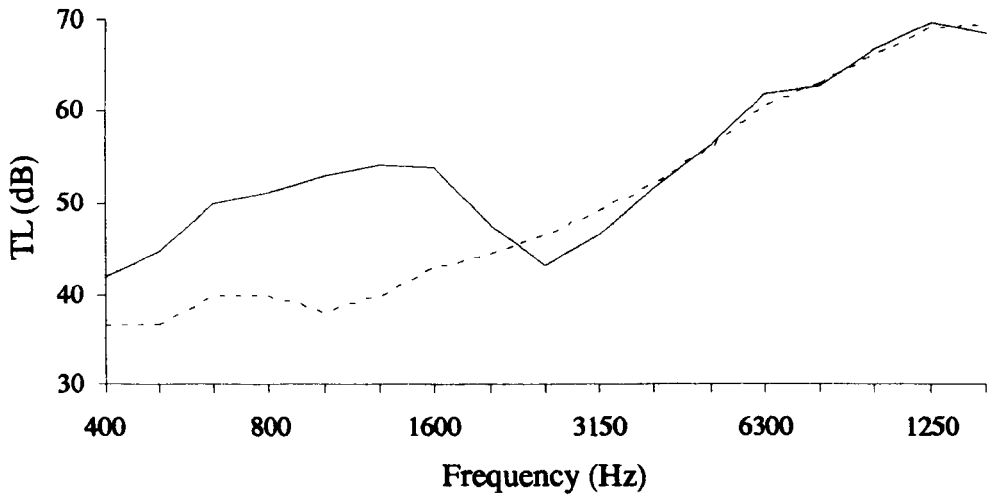

Figure 5.25: Measured transmission loss of the wide double wall and double fin wall

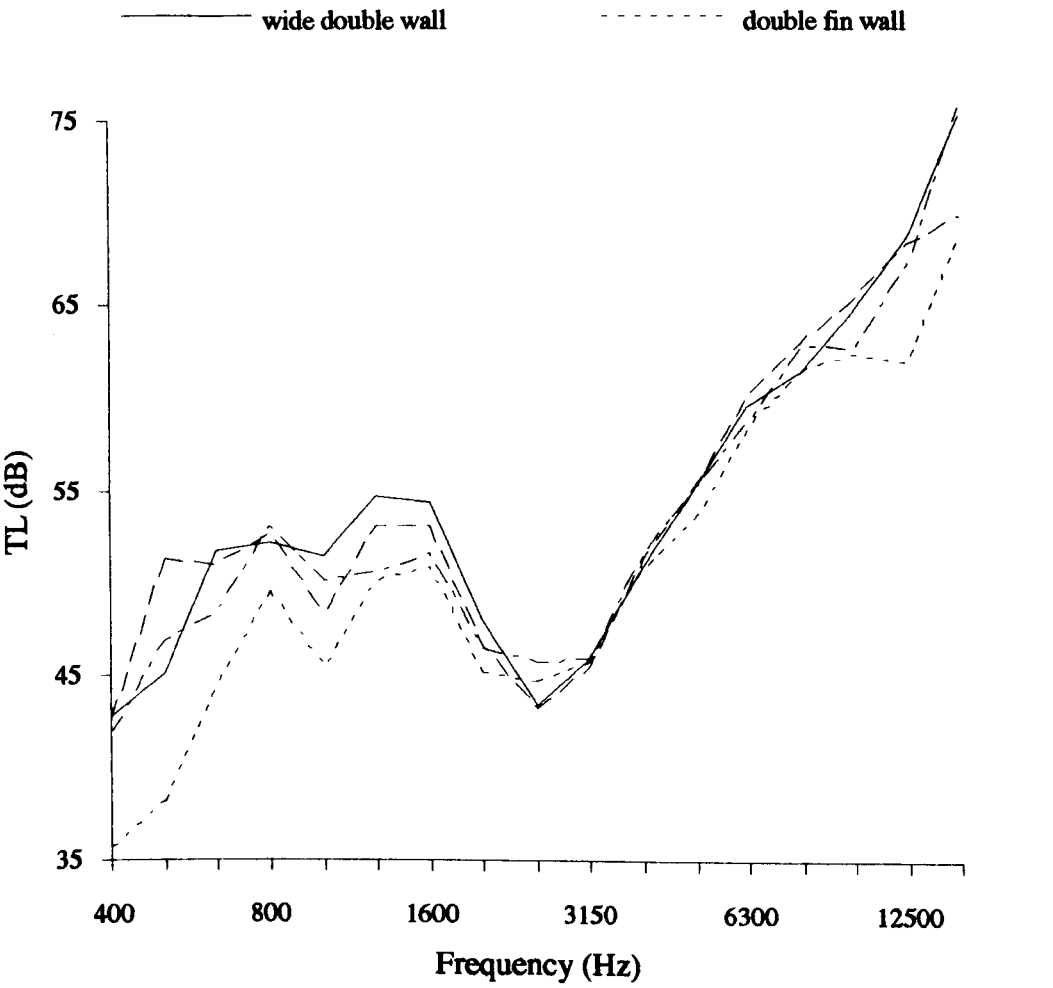

Figure 5.26: Measured transmission loss of cavity fin walls

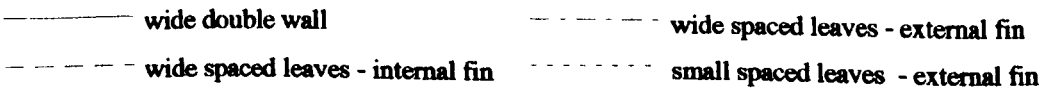

6 STRUCTURE-BORNE SOUND TRANSMISSION BETWEEN LEAVES

6.1 INTRODUCTION

An examination of the fin wall allowed us to consider the effect of orthotropicity on the radiation characteristics of the diaphragm wall. Vibrational transmission between the leaves via the cross-ribs is now analysed. The resultant prediction is compared with measurements of transmission loss and vibration level difference for scale walls and in-situ full scale walls. Details of the latter are described in chapter 8.

6.2 DIAPHRAGM WALL MEASUREMENTS

Figure 6.1 shows the transmission loss of the 1, 3 and 7 rib 1:8 scale walls. Two regions are clearly observed; above the upper critical frequency, $f_{c,u}$, the values are within 1 - 2 dB, with the transmission loss increasing slightly with rib number and rising at 9 - 10 dB / octave. Below $f_{c,u}$ the curves flatten as the rib numbers increase. In the 1 rib case, it is believed the rib acts only as a transmission path and an isotropic transmission loss characteristic is seen with a distinctive coincidence dip at $f_{c,u}$ (calculated as 2328 Hz).

Figure 6.2 shows the measured transmission loss of the two most reliable field measurements of diaphragm walls (details of which are given in chapter 8, section 8.2). $f_{c,l}$ and $f_{c,u}$ are approximately 24 Hz and 270 Hz, respectively, in both cases. A change of gradient occurs about $f_{c,u}$ for both walls. Above $f_{c,u}$ gradients are roughly 10 dB / octave. Below $f_{c,u}$ the plateau region is not as obvious as with the scale walls but the gradient decreases to between 3 - 4 dB / octave. Other in-situ wall measurements are described in sections 8.2 and 8.4.

Measurements indicate a significant change in bending stiffness of the diaphragm wall from that of the fin wall. In the case of the 1:8 scale fin wall, as more ribs are added $f_{c,l}$ falls and the plateau region extends down in frequency. For the diaphragm wall, $f_{c,l}$ remains essentially unchanged, at roughly 200 Hz. This is expected as the moment of inertia is dominated by the cavity width which is fixed. (See Appendix A.2 for calculations of moments of inertia for the fin and diaphragm walls). Table 8 shows the calculated values of $f_{c,l}$ for the 1:8 diaphragm walls. Included are the respective values for the fin walls given in table 6, for completeness.

Table 8: Lower Critical Frequencies of Model Diaphragm Walls

No. of ribs:	I_{xx} (m^4)	B ($Kg/m^2\ s^{-2}$)	Diaphragm $f_{c,l}$ (Hz)	Fin $f_{c,l}$ (Hz)
1	26.3e-6	134.4e+3	202	1073
3	26.6e-6	135.7e+3	201	687
7	27.1e-6	138.4e+3	199	490

For all the diaphragm walls $f_{c,l}$ is below the model frequency range and thus sub-critically only a plateau is seen. For a full scale diaphragm with ribs at 1.25 m centres, $f_{c,l} \approx 21$ Hz.

6.2.1 Vibration Level Difference between Leaves

A second important difference exists between the fin wall and diaphragm wall. For the fin walls an equivalent surface density was used, m_{eq}, which increases the transmission loss by a maximum of approximately 2 dB (see section 5.4.1). For the diaphragm walls, the effect of including the rib mass would be only to increase the transmission loss by approximately 1 dB. It is wrong to assume an equivalent mass at all frequencies for the diaphragm wall as this implies the leaves behave as a single wall. This is seen as not true in figure 6.3 for the scale walls and figure 6.4 for the in-

situ diaphragm walls. These show the measured vibration level difference between the leaves of the walls. The details of the measurement are described in chapter 8.

For the 1:8 scale wall measurements the vibrational level difference up to 200 Hz is less than 0.5 dB. It might therefore be assumed that the wall is like a single wall upto roughly $f_{c,u}$ and that the equivalent mass of the wall should be used in the sub-critical region. Above $f_{c,u}$ the gradient is roughly 2 dB / octave indicating each leaf begins to act independently. The 1:4 scale wall follows the same trend but gives slightly higher values. This may be due to imperfect bonding between rib and leaf, which was the problem with the first model wall built by Hung [18]. The large dips at the 1/3 octave centre frequencies of 500 Hz (1:4 scale) and 1 kHz (1:8 scale) may be due to the first cross-rib bending resonance frequencies of 582 Hz and 635 Hz respectively.

The measurements in figure 6.4 for the in-situ full scale walls, suggest a similar but slightly lower vibration level difference to that of the scale walls. The mean vibration level difference of the in-situ walls is shown. Individual measurements are shown in figure 8.25. Also shown is a measurement of a free standing post-tensioned diaphragm wall, discussed in chapter 8. Like the scale walls, where $f < f_{c,u}$ it can be assumed that the leaves act as a single wall. Above $f_{c,u}$ measurements tend to plateau, about 2-3 dB, then rise with a similar gradient as the scale walls. The free-standing wall gives slightly lower values of vibration level difference than the in-situ walls which may be explained by the stronger post-tensioned bonding of the leaves at foundation and capping beam.

6.3 PREDICTION OF TRANSMISSION LOSS

Figure 6.5 shows the difference between measured and predicted transmission loss for the 1:8 scale diaphragm walls, where prediction simply assumes the wall to be

isotropic with an equivalent mass. Agreement is poor below $f_{c,u}$ as no account of orthotropicity is included although above $f_{c,u}$ agreement for all curves is within 5 dB.

If we try to apply existing double bridged theory according to Sharp [41] as used for lightweight stud partitions (see equation 2.29) this also gives poor agreement with measurement. Figure 6.6 is for the 1:8 scale 7 rib diaphragm wall as an example. Theory includes both stud and cavity paths, but like single wall theory it assumes an isotropic radiation and over emphasises the coincidence dip with no plateau region. The agreement is good in the mass law region below $f_{c,l}$. Such theory is suitable for lightweight stud partitions by Sharp [41] and Gu & Wang [57]. The stud and panel are usually of different materials which will effect the calculation of I_{xx} (see Appendix A.3).

From the vibration level difference measurements of figures 6.3 & 6.4 it can be taken that, below the upper critical frequency, an equivalent mass can be assumed. Above this frequency the mass of the wall is assumed to be the sum of both leaves plus a constant to account for the vibration level difference. Figures 6.7 and 6.8 show the difference in transmission loss between measurement and prediction using the above assumptions for the scale walls and in-situ walls, respectively. For the scale models agreement improves with increased ribbing. However, agreement is at best only fair, within ± 5 dB at all but the highest frequency band. Figure 6.8 uses the same prediction for two full scale diaphragm walls. The discrepancy is of the same order as for the model walls, if slightly more encouraging in that one case is within ± 4 dB where $f < f_{c,u}$ and within ± 2 dB where $f > f_{c,u}$.

Extending the orthotropic fin wall approach by inclusion of a constant for the vibrational level difference between leaves is accurate to approximately ± 5 dB. In addition, this approach cannot account for sound transmission across the cavity, nor

can it include resonant transmission across the cross-ribs. It also cannot account for internal variations in material parameters between ribs and leaves, such as the surface density or thickness of the cross-rib, which will effect the transmission efficiency across the junction. Therefore it is only suited to the monolithic case, where all material elements are the same and the cavity transmission path is considered negligible. To include such parameters requires a more sophisticated approach described in detail in chapter 7.

6.4 SOUND TRANSMISSION VIA THE CROSS-RIBS - IMPEDANCE ANALYSIS

Up to this point the cross-rib as a transmission path has not been fully considered. The importance of the cross-rib as a path is clearly seen in figure 6.9 which shows the difference in measured transmission loss for a 1:8 scale isotropic double wall compared to the three diaphragm walls. The transmission loss is lower with the addition of ribs particularly below $f_{c,u}$ where orthotropicity is also important.

Transmission via the cross-rib of the diaphragm wall will be shown to be poorly described by existing theoretical models of double bridged walls for a number of reasons. The easiest model to consider involves the transmission of a non-resonant longitudinal force between two plates, via a bridge. Existing theories then sum the transmitted power via this path with that given by the wall unbridged, to give the total transmitted power. The effect of a high or low impedance cross-rib attached to a radiating surface has been partially discussed in chapter 5. Now let us examine the impedance relationship between bridge and leaf, and show how the diaphragm wall is considerably different to other double wall constructions and how existing impedance models for transmission between the leaves are inappropriate.

For a double bridged construction one of three bridging models will apply, a low, matched and high impedance ratio case between leaf and cross-rib, already discussed in chapter 5. The example of the cavity tie as a low impedance bridge can be described by an equivalent stiffness. Such cavity ties are considered by Wilson [52] and hold true as long as the bridge is short compared with its longitudinal wavelength. The high impedance bridge, such as a stud, can be assumed rigid and the vibration of the receiver leaf does not hinder the bridge which acts by its own inertia. The close impedance matching between bridge and leaf of the diaphragm wall produces optimum transmission between leaves and is therefore a poor design for sound insulation. Hence it is better to have a strong impedance mis-matching between bridge and leaves [39]. (In actuality most diaphragm walls will have a leaf which has a slightly different material density).

Let us consider this further by examining the transmission at a single junction between cross-rib and leaf. Primarily here we are interested in how the forces are transmitted over the bridge. The mechanical impedance of any material is given by:

$$Z_m = \frac{F}{v} \qquad (6.1)$$

This is the complex ratio of the alternating excitation force, F, and resulting particle velocity, v, in the excitation region. It depends on the method of excitation and the system excited. Ties and rods are represented by point impedances (equation 6.2) and a stud connection by a line force impedance (equation 2.32). The driving point impedance of a homogenous infinite plate is given by [39]:

$$Z = \frac{4}{\sqrt{3}} \rho_c c_L h^2 \qquad (6.2)$$

and for a tie of length, L, and cross-sectional area, S, [124]:

$$Z = \frac{SE}{\omega L} \tag{6.3}$$

For the diaphragm wall the mechanical impedance of leaf and cross-rib are virtually matched if both are excited into bending vibration.

Let us first examine the effect of wave transmission at a single cross-rib/leaf junction, purely in terms of impedance matching (see figure 6.10). A travelling wave of unit velocity on the first leaf incident at the junction generates a wave onto the cross-rib. The change in displacement or velocity across the junction depends on the impedance ratio of the two elements. Consider the continuity expressions:

$$v_i + v_r = v_t \tag{6.4}$$

$$F_i + F_r = F_t \tag{6.5}$$

where v is the velocity of the wave travelling across the junction and F is the force through the junction. Subscripts i, r and t are the incident, reflected and transmitted components. Substituting equation 6.1 into equation 6.5 and eliminating the reflected component gives:

$$Z_1 v_i + Z_1[v_t - v_i] = Z_B v_t \tag{6.6}$$

where subscripts 1 and B apply to the first leaf and bridge respectively. (Subscript 2 will relate to the second leaf). Rearranging the expression and replacing v_i and v_t with v_1 and v_B, respectively, gives the ratio of the cross-rib to leaf velocity at the junction:

$$\frac{v_B}{v_1} = \frac{2 Z_1}{Z_B + Z_1} \tag{6.7}$$

and rearranging again gives the ratio of the cross-rib to leaf impedance at the junction:

$$\frac{Z_B}{Z_1} = \frac{2v_1 - v_B}{v_B} \qquad (6.8)$$

By examination of equation 6.7, if the bridge impedance tends to infinity v_B/v_1 tends to zero and if the bridge impedance tends to zero $v_B/v_1 \rightarrow 2$. For the diaphragm wall $Z_B \approx Z_1 \approx Z_2$ therefore $v_B/v_1 \rightarrow 1$. Suffice to say that the transmission coefficient is greater across a junction of matched impedances compared with the mis-matched case. There will be some reduced transmission however due to the junction and the wave conversion between incident and generated waves.

6.4.1 Impedance Models for Bridged Double Walls

Previous work describing transmission across a double bridged wall [37, 41, 52, 124] predicts the transmission between the leaves across the bridge and across the cavity independently. Together they give the total transmission between leaves. Consider figure 6.10 again. The first leaf has a flexural wave of velocity v_0 at a distance from the bridge. This velocity will decrease at the bridge to v_1, producing a force, F:

$$F = (v_0 - v_1) Z_1 \qquad (6.9)$$

where Z_1 is the line impedance of the first leaf. The flexural wave will induce a longitudinal force along the bridge and produce a velocity v_2 on the second leaf which has a line impedance Z_2. Figure 6.11 shows this as an electrical analogy. The current, I, corresponds to the force, the voltage, V, corresponds to the velocity and the resistance, R, is given by the admittance or mobility, Y, (where Y=1/Z). The incident velocity gives rise to a force F where:

$$v_0 = \frac{F}{Y_1 + Y_2 + Y_B} \tag{6.10}$$

Y_B is the admittance of the bridge. As the force is constant through the circuit,

$$V_x = F Z_x \tag{6.11}$$

where x denotes the 1, 2 or B. Substituting equation 6.10 into equation 6.9 gives the velocity difference between leaves across the bridge:

$$\frac{v_2}{v_0} = \frac{Y_1 + Y_2 + Y_B}{Y_2} \tag{6.12}$$

Assuming both leaves are the same, equation 6.12 can be given by a level difference, as:

$$Ld_B = 20\log\left[\frac{2Y_L + Y_B}{Y_L}\right] \tag{6.13}$$

where Y_L is the line admittance of an infinite plate and is given by equation 2.32, and Ld_B is the vibration level difference between leaves across the bridge. Sharp [41] assumed that for stud partitions, the stud is both rigid and massless. On this basis $v_1 = v_2$ on either side of the stud, and the force on the second leaf becomes $F = v_1/Y_2$. Relating Sharp's assumptions to equation 6.13 means $Y_B = 0$, and $Ld_B = 6$ dB. The vibration level difference between leaves in the absence of sound bridges is a function of f^2 where $f_0 < f < f_1$ and f where $f > f_1$ (already discussed in chapter 2, section 2.5).

The bridge cannot always be assumed rigid or massless. Such as for metal studs which were assumed resilient by Gu and Wang [57], hence allowing a velocity difference across the bridge, and Fahy [37] who included the stud mass. Fahy

showed the plate impedance is generally much greater than the stud impedance at all but the highest frequencies where the rigid stud analogy assumption is inappropriate.

The analysis of both Sharp and Fahy applies to the sub-critical region, where transmission via the bridge and via the air in the cavity are easier to distinguish. Above critical frequency full surface radiation occurs and the distinction of paths is less obvious.

As part of a statistical energy analysis Wilson [52] and Craik [124] defined coupling loss factors for sound transmission across the air cavity and along the ties of double walls and across dry lining battens. The tie was assumed massless and its impedance defined by its stiffness, given by equation 6.3. Thus a velocity drop occurs across the tie. The transmission between leaves across the tie is described in terms of coupling loss factor as:

$$\eta = \frac{r\,Y_2}{\omega m_1 \left[(Y_1 + Y_2)^2 + \left(\frac{\omega L}{ES}\right)^2 \right]} \qquad (6.14)$$

where r is the number of ties per square metre. Wilson predicts the coupling loss factor across the tie, by excluding the second bracketed denominator term when the tie is infinitely stiff and excluding the first bracketed denominator term when the tie is less stiff. The air path between leaves is also given in terms of a coupling loss factor where the second bracketed denominator term, the tie term, is replaced by an 'air tie' term $\left(\frac{\omega L}{SK}\right)^2$, where K is the bulk air modulus and L the cavity width. Also included in the coupling loss factor are cross-cavity resonances at high frequencies. Dry lining battens fixed to walls are assumed to be stiff, massless bridges. The leaf to leaf coupling loss factor η_{lw} is given by:

$$\eta_{lw} = \frac{h_{rib}\, Re\,(Y_{leaf})}{m_{leaf}\,\omega\,|\,Y_{leaf} + Y_{leaf} + Y_{rib}|^2} \qquad (6.15)$$

The mobility of the leaves, are given by Cremer [39] as beams parallel to the rib, where:

$$Y_{leaf} = [\,2.67\ m\ \sqrt{h\, c_L f}\,]^{-1} \qquad (6.16)$$

The mobility of the rib is given by :

$$Y_{rib} = \frac{j\,\omega\,d}{E\,h} \qquad (6.17)$$

where d is the width of the rib. This 'impedance model' applies well where the bridge is very short and stiff and resonances do not occur across the batten in the frequency range of interest.

6.4.2 Discussion

These approaches are not likely to apply well to the case of the diaphragm wall. The cross-rib is of significant mass compared with the rest of the wall (approximately 14% of total mass). It cannot be considered a massless path, as assumed by Sharp [41], nor its impedance small compared with leaf impedance, as suggested by Fahy [37]. There is a need to consider the effect of the large width of the cross-rib. For conventional double walls the bridge is a stiff tie or a masonry return closing the cavity. Hence they are non-resonant, as the cavity is usually no greater than 100 mm wide. The condition where the cross-rib will resonant is where the cavity width equals $\lambda_b/2$ or $\lambda_l/2$ (where λ_b and λ_l are the bending and longitudinal wavelengths) which does not occur until frequencies well above the range of interest. For a steel tie in longitudinal mode, the first resonance is around 30 kHz, and for the bending

mode across masonry, resonance is at about 11 kHz. For the diaphragm wall the cross-rib will have an internal width upto 0.46 m (2 bricks wide) where the first bending resonance will occur between 300 - 800 Hz, clearly within the frequency range of interest.

Therefore how best should the cross-rib be described? At low frequencies, below the first resonance, the cross-rib might simply be assumed as a rigid non-resonant link. This assumption is supported by measurement which has shown the vibration level difference between leaves to be close to zero. At mid and high frequencies the cross-rib cannot be assumed as a rigid non-resonant bridge rather it can be thought of as a separate resonant plate, where transmission across each junction is considered individually. At low-to-mid frequencies non-resonant longitudinal transmission assumes importance. At higher frequencies longitudinal motion becomes more important in the re-generation of bending motion on the second leaf. The analysis is further complicated by the need to consider the interaction of different wave types and their generation and re-generation at junctions, the possibility of standing waves across the cross-rib and resonances in the vertical direction of the cross-rib. As the wall is typically 8 m high, half wave bending resonance will exist at about 2 Hz. A different approach is therefore required to define the transmission between leaves of the diaphragm wall.

6.5 WAVE ANALYSIS

Consider a travelling wave analysis to describe the transmission between the leaves via the cross-rib in terms of the transmission coefficient, γ. Where γ is the ratio of the intensity of a transmitted wave to that incident. We shall define two transmission coefficients; firstly for transmission across one cross-rib/leaf junction, a T-junction, and secondly across both junctions, an I-junction. In terms of an SEA approach, the former case assumes the cross-rib to be a resonant sub-system and in that latter case

the cross-rib is only the transmission path. In chapter 7 a coupling loss factor will he expressed in terms of γ and applied in an SEA model of the diaphragm wall.

The transmission coefficient, γ, is dependant on the boundary conditions and wave types being considered. Obliquely incident waves must also be considered and an angle averaged or random incidence coefficient, $\bar{\gamma}$ derived. Longitudinal and transverse shear waves must also be included, often referred to in combination as in-plane waves. The question arises of what wave types and boundary conditions need to be considered and how should the structural path across the diaphragm wall be best described?

6.5.1 Review of Relevant Work

To give a better understanding of the problem a review is given of previous research on structure-borne transmission at junctions. Such research has many applications, including buildings, transportation vehicles, spacecraft, machinery etc.

Cremer (1948) [39] first derived the transmission coefficient at a junction of thin semi-infinite plates due to an oblique incidence bending wave. He included transmission across corners, cross and T-junctions. In 1965 Lyon and Scharton [125] examined a theoretical three element structure, plate-to-beam-to-plate, and found the energy transfer at junctions to be dependant predominantly on bending waves, and on torsional waves at high frequencies.

Crocker, Bhattacharya et al [126, 127] examined transmission between parallel plates connected by a tie beam and tie plate. With Mulholland [126] they calculated the transmission across the tie plate accounting for all bending and longitudinal waves. Calculations were for normal incidence only. They showed that flexural waves along the source plate will produce longitudinal waves on the tie plate which,

in turn produce flexural waves on the second plate. It was shown that due to the transportation of energy across to the second junction by these faster longitudinal waves a gain or loss in flexural wave amplitude could occur. Where the tie is long and thin compared with the plates, two single T-junction calculations give similar results to an I-junction model. Where the tie is short and similar in dimension to the plates, the physical parameters and the longitudinal waves become significant. Kihlman [123] included in-plane energy transfer in perpendicular plates but not on source or co-planar plates forming cross-junctions.

Craven & Gibbs [128] calculated mode coupling and energy intensity transmission across corner and cross junctions using thin plate theory. Their analytical model allowed for any incident wave type and at any angle of incidence and could produce results for bending, quasi-longitudinal and transverse shear waves. Average transmission coefficients were calculated and dissipative loss factors could be included. Their results support those of Kihlman for the symmetrical case in that no in-plane waves are generated on the cross walls. The assumption is shown not to be true for T-junctions. Transmission coefficients are given for all incident wave types against angle, across a corner and cross junction of the same material. It is seen that the transmission coefficients become zero at angles greater than that of total reflection.

Gibbs & Craven [129] presented a parametric survey for a concrete T-Junction with varying material parameters. Also, the frequency variation of angle averaged transmission loss for different incident waves is calculated. It is shown that bending rigidity and material density are of greater importance than plate thickness or material loss factor. An increase in material loss factor could also increase transmission by improving mode coupling between flexural and in-plane waves. Importantly it is indicated that in-plane vibrations attenuate slowly over many junctions and thus can create significant bending vibration at distance.

Wohle et al [130] examined transmission across the junction of finite concrete slabs for incident bending waves, producing flexural and in-plane wave types on the coupled slab. Angle average values of γ generally increased with frequency from 0 at 100 Hz to 0.2 at 3150 Hz for bending to in-plane wave transmission and 0.1 to 0.5 for bending to bending wave transmission. In a later paper [131] they considered an airborne excited slab which produces resonant transmission by free bending waves and the non-resonant transmission by forced bending waves. Non-resonant transmission is introduced in Chapter 7. They show that except for exceptionally high values of material loss factor ($\eta = 0.3$) the effect on non-resonant transmission is small at all frequencies.

Craik [132] re-expresses Cremer's [39] transmission coefficients for angle averaged bending waves only. Transmission loss charts for cross, corner and T-junctions are given for various material relationships and for ratios of plate thicknesses. He compares a theoretical model of in-plane and bending vibration with a model of bending vibration only [133]. Both are compared with measurement. It is shown that for buildings it is only at a significant distance (3 - 4 rooms from the source) that in-plane waves become important at all frequencies. The analysis is simplified by assuming that the longitudinal and transverse shear waves can be summed in proportion to their modal densities into a single in-plane coupling. Comparing this approach with the full model gives good agreement at low and mid-frequencies close to the source. Although far from the source and at higher frequencies errors become significant.

6.5.2 Wave Generation at a Junction

In considering the transmission of vibrational energy around a T-junction and I-junction it is not the intention of the author to give an exhaustive derivation of

transmission coefficients for all boundary conditions and wave types. Rather to describe the cases which exemplify the theory and the assumptions and definitions made; then to show the relevant expressions for the diaphragm case. For full detailed descriptions of expressions the reader is referred to [39, 124].

Consider the wave fields possible on a (ith) semi-infinite plate with a straight edge, which forms a junction with another, as yet unspecified, (rth) semi-infinite plate. Figure 6.12 shows the co-ordinate system and waves generated on one plate. The bending wave generated at an angle θ_i to the normal of the junction can be expressed in the form:

$$v_{z_i} = \left[t_i e^{-j k_i x \cos\theta_i} + t_{n_i} e^{+j k_{n_i} x \cos\theta_i} \right] e^{-j k_i y \sin\theta_i} e^{j\omega t} \qquad (6.18)$$

where t describes the transmitted wave generated at the junction. The first term in brackets is the travelling wave component and the second term is the evanescent near field component, with wave number:

$$k_{n_i} = k_i \sqrt{1 + \sin^2\theta_i} \qquad (6.19)$$

Where k_i is the travelling bending wavenumber. The first term outside the brackets is common to all such expressions and describes the trace wave component along the junction. The last term, $e^{j\omega t}$, is also common, describing the time dependency and is now omitted. A bending wave of unit amplitude, which excites the generated wave, is incident on the junction of the ith plate at angle θ_i, given as:

$$v_{z_{in}} = e^{j k_i x_i \cos\theta_i} e^{-j k_i y \sin\theta_i} \qquad (6.20)$$

In the same way, other generated wave fields on other plates joined to the ith plate are expressed as equation 6.20. To obtain the unknowns coefficients and hence the

transmission coefficients, we must consider the boundary conditions at the junction. The simplest junction is a corner junction between two plates, but we will consider a T-junction as it is relevant to the diaphragm wall. The T-junction between leaf and cross-rib consists of two co-planar plates, and a third cantilevered plate perpendicular to the co-planar plates (the cross-rib).

Consider the case of only bending waves incident and only bending waves generated. This corresponds to a boundary condition of zero displacement in the x and y direction. The angular velocities equate and the bending moments sum to zero. Thus equating slopes for any joined rth plate:

$$\left(\frac{dv_{z_i}}{dx_i}\right)_{x_i=0} = \left(\frac{dv_{z_r}}{dx_r}\right)_{x_r=0} \tag{6.21}$$

The sum of the moments is zero, for n plates, say:

$$\sum_{r=1}^{n} M_r = 0 \tag{6.22}$$

where;

$$M_r = - B_r \left[\frac{d^2 v_{z_r}}{dx_r^2} + \mu \frac{d^2 v_{z_r}}{dx_r\, dy_r}\right] \tag{6.23}$$

and B_r is the plate bending stiffness of the rth plate. For n connected plates, the above boundary conditions yield 2 n simultaneous equations and thus the solutions for the 2 n coefficients. The transmission coefficient is expressed in terms of intensities, as:

$$\gamma(\theta) = \frac{I_{b_i}(\theta_i)}{I_{in}(\theta_i)} \tag{6.24}$$

where, I_{in} is the incident bending wave and I_{bi} the transmitted bending wave. I_{in} is given by [39] as:

$$I_{in\,i} = \quad h_i \rho_i \frac{\omega^3}{K_i} \cos\theta_i \tag{6.25}$$

and I_{bi} by:

$$I_{b\,i} = \quad h_i \rho_i \frac{\omega^3}{K_i} |b_i|^2 \cos\theta_i \tag{6.26}$$

For normal incidence the transmission coefficient is simplified by Cremer [39] to:

$$\gamma_0 = \chi\varphi\, t_r^2 \tag{6.27}$$

where,

$$\chi = \sqrt{\frac{c_{L,i}\, h_i}{c_{L,r}\, h_r}} \tag{6.28}$$

and,

$$\varphi = = \frac{c_{L,r}\, h_r\, m_r}{c_{L,i}\, h_i\, m_i} \tag{6.29}$$

The transmission coefficient, γ_0, about a T-junction is further simplified [39] to:

$$\gamma_0 = \left[\sqrt{\frac{2\chi}{\varphi}} + \sqrt{\frac{\varphi}{2\chi}} \right]^{-2} \tag{6.30}$$

for energy transfer to and from cantilever to one co-planar plate, and γ_0 is:

$$\gamma_0 = \left[2 + \frac{2\varphi}{\chi} + \frac{1}{2}\left[\frac{\varphi}{\chi}\right]^2 \right]^{-1} \tag{6.31}$$

for energy transfer between co-planar plates. Without derivation the transmission coefficient for an oblique angle of incidence is obtained by [132]:

$$\gamma_{ir}(\theta) = \frac{4\varphi \sqrt{\chi^2 - \sin^2\theta}\, \cos\theta}{(2\varphi)^2 + 2\varphi\left\{\sqrt{\chi^2 + \sin^2\theta}\,\sqrt{1 + \sin^2\theta} + \sqrt{\chi^2 - \sin^2\theta}\,\sqrt{1 - \sin^2\theta}\right\} + \chi^2} \tag{6.32}$$

from cantilever to one co-planar plate, and:

$$\gamma_{ir}(\theta) = \frac{{}^1/_2\chi^2 \cos^2\theta}{\left(\frac{\varphi}{2}\right)^2 + \frac{\varphi}{2}\left\{\sqrt{\chi^2 + \sin^2\theta}\,\sqrt{1 + \sin^2\theta} + \sqrt{\chi^2 - \sin^2\theta}\,\sqrt{1 - \sin^2\theta}\right\} + \chi^2} \tag{6.33}$$

between co-planar plates. A condition of total reflection, given by Snell's law, occurs when:

$$K_i \sin\theta_i = K_r \sin\theta_i \tag{6.34}$$

Equation 6.32 applies below the angle of total reflection. Above it:

$$\gamma_{ir}(\theta) = \frac{\cos^2\theta}{2 + 2\left[\frac{\varphi/2}{\chi^2}\right]\left[\sqrt{\chi^2 + \sin^2\theta} + \sqrt{\sin^2\theta - \chi^2}\right] + \frac{[\varphi/2]^2\left[\sqrt{\chi^2 + \sin^2\theta} + \sqrt{\sin^2\theta - \chi^2}\right]}{\chi^4}} \tag{6.35}$$

The angle averaged (random incidence) transmission coefficient, $\bar{\gamma}$, is given in terms of intensities as:

$$\overline{\gamma_{ir}} = \frac{\int_0^{\frac{\pi}{2}} I_{b_r}(\theta_r)\cos\theta_r}{\int_0^{\frac{\pi}{2}} I_{in}(\theta_i)\cos\theta_i} \qquad (6.36)$$

The denominator is integrated to give [39]:

$$\overline{\gamma_{ir}} = \int_{\frac{\pi}{2}}^{-\frac{\pi}{2}} \gamma_{ir}(\theta)\cos\theta_r \, d\theta_r \qquad (6.37)$$

The above expressions are frequency independent and easy to employ at normal incidence. Generally at low frequencies they give good agreement with measurement where non-bending fields can be neglected.

6.5.3 In-plane Wave Fields

At higher frequencies and with increased distance from the sound source other waves contribute to the structure-borne transmission process. To include these the boundary conditions must allow translation at the junction. The incident bending will now also produce in-plane motion in the form of longitudinal and transverse shear waves. Hence, the expressions for the bending waves on the rth plate are now accompanied by that for a quasi-longitudinal wave, given by:

$$v_{lr} = t_{lr} e^{-jk_{lr} x \cos\theta_{lr}} e^{-jk_{lr} y \sin\theta_{lr}} \qquad (6.38)$$

and for a transverse shear wave, given by:

$$v_{sr} = t_{sr} e^{-jk_{sr} x \cos\theta_{sr}} e^{-jk_{sr} y \sin\theta_{sr}} \qquad (6.39)$$

where, k_{lr} and k_{sr} are the quasi-longitudinal and transverse shear wavenumbers, respectively. Additional boundary conditions are now required. The incident bending displacement caused before the junction must be equal to the component in-plane displacement in the same direction on the connected plate. For mutually perpendicular plates:

$$v_{z_i} = v_{lr} \cos\theta_{lr} + v_{sr} \sin\theta_{sr} \tag{6.40}$$

Also, forces must be equated where, for the ith plate:

$$F_{b_i} = -B_i \left[\frac{d^3 v_{z_i}}{dx_i^3} + (2-\mu_i) \frac{d^3 v_{z_i}}{dx_i^3 \, dy_i} \right] \tag{6.41}$$

for bending waves. For in-plane waves on the rth (perpendicular) plate, the force of the longitudinal component is:

$$F_{l_r} = \frac{Eh_r}{1-\mu_r} \left[\frac{dv_{lr}}{dx_r} \cos\theta_{lr} + \mu_r \frac{dv_{lr}}{dy} \sin\theta_{lr} \right] \tag{6.42}$$

and for the transverse shear component:

$$F_{s_r} = \frac{Eh_r}{2(1-\mu_r)} \left[\frac{dv_{sr}}{dx_r} \cos\theta_{sr} + \mu_r \frac{dv_{sr}}{dx_r} \sin\theta_{sr} \right] \tag{6.43}$$

Values for t, t_n, t_l and t_s follow for each plate by the solution of a set of simultaneous equations and hence the transmission coefficients.

Using Cremer's [39] simplifications, where $h_i = h_r$, $E_i = E_r$ and $\theta = 0$; for a corner joint the transmission and reflected efficiencies of bending and longitudinal waves can be calculated. Figure 6.13 shows the energy distribution of transmitted and

reflected, bending and longitudinal waves, for an incident bending wave. In this case the transmitted bending energy converted to longitudinal energy is equal to that converted to a bending wave above 400 Hz. Figure 6.14 shows the result for an incident longitudinal wave.

A full description of transmission across a junction must allow for all incident wave types and all generated wave types. Boundary conditions must allow rotational and translational displacement in all directions. To include all these waves required a significant computer program. Such a program was written initially by Craven and Gibbs for research previously published [128, 129] and was altered to calculate the required transmission coefficients for a T-junction of brickwork. Values of γ are produced for every wave combination, i.e. bending to longitudinal, bending to shear etc., and at all angles. At every angle the values of γ are summed for all wave combinations and the random incidence transmission coefficient, $\bar{\gamma}$, is derived for each frequency. At particular angles and above, total wave reflection occurs where the generated wave is faster than the incident wave and does not transmit to its coupled plate. This will occur for all wave combinations except the fastest, longitudinal waves. In the case of the diaphragm wall travelling bending waves on the first leaf can produce bending waves on the second leaf, not only by bending wave transmission across the cross-rib but also by longitudinal transmission as described by Crocker et al [126, 127]. Figures 6.15 and 6.16 show the difference in predicted transmission loss ($TL = 10\log(1/\bar{\gamma})$) between a prediction allowing only bending waves incident and transmitted, and a prediction allowing all wave types to be incident and transmitted. These shall be termed the 'bending wave' model and the 'all wave' model respectively. Figure 6.15 shows transmission from the cantilever plate to one co-planar plate, and figure 6.16 between two co-planar plates.

A range of thickness and material parameters are considered, from lightweight concrete block to brickwork to dense concrete block. Details are given below.

Lightweight Concrete	(LC)	$\rho c = 1300$ Kg/m^3	$c_L = 1700$ m/s
Typical brickwork	(TB)	$\rho c = 1850$ Kg/m^3	$c_L = 2375$ m/s
Dense Concrete	(DC)	$\rho c = 2300$ Kg/m^3	$c_L = 3360$ m/s

The cantilever plate is seen to correspond to the cross-ribs and the co-planar plates correspond to a leaf of the diaphragm wall. Figures 6.15 and 6.16 show results for various material combinations between the cross-rib and leaf. The thickness of all elements was fixed at 0.1 m. A doubling of the cross-rib thickness is also shown for a typical material leaf and cross-rib. Both figures show the difference between the 'all wave' model and the 'bending only' model to increase with frequency as the longitudinal wave transmission becomes more important. However for all these cases the discrepancy between the two models, whether transmission is to or from the cross-ribs, is less than 2 dB upto 3150 Hz. Therefore, in the statistical energy analysis of chapter 7, when the cross-rib is assumed a resonant sub-system, it was sufficient to consider only bending waves transmission when calculating $\bar{\gamma}$ at the cross-rib / leaf junction.

6.5.4 Variations in Transmission Coefficient

It is useful to examine the variations in the transmission coefficient which would be expected for all likely forms of the diaphragm wall construction. Equations 6.30 - 6.31 and 6.32 - 6.35 were used to calculate the normal incidence and random incidence transmission coefficients, respectively. Two cases are considered, a change in thickness of the cross-rib and change in the material constants.

Change in thickness ratio:

A different thickness of cross-rib from that of the leaf is not very common for presently built diaphragm walls. During field measurements only one such wall was

found. This was a free-standing pre-stressed wall where the cross-rib was twice the width of the leaf. Any practical changes in the cross-rib or leaf thickness would be in increments of 1/2 brick thickness. Any increase in thickness would realistically only be expected with respect to the cross-rib as an increase in the leaf thickness would significantly increase the cost of construction and partly negate one of the principle reasons for the diaphragm wall, that of a relatively lightweight tall single storey masonry structure.

Nevertheless, to include all possibilities, a range in thickness ratio between cross-rib and leaf of 1/4 and 4 times were chosen i.e. to include the unlikely case of 2 brick thick leaf connected to a 1/2 brick cross-rib. Figures 6.17 and 6.18 show the change in transmission loss at a T-junction for variations in the thickness ratio between cross-rib and leaf, for normal and random incidence, respectively, and where material constants are the same. According to Cremer [39] at normal incidence, the transmission loss from the cross-rib to leaf is equal to that from the leaf to cross-rib. For random incidence the transmission loss is higher for the latter case. The minimum transmission loss does not occur where the plates are of equal thickness, as in the case of the corner junction, but where $h_c/h_l = 1.32$. It is reasonable to assume, for practical purposes, that the minimum value will occur where all walls are the same thickness. Values are also given between co-planar plates of the leaf for completeness.

Change in material constants:

Most diaphragm walls use a slightly different density brick for one leaf compared with the cross-rib. Diaphragm walls are also built of concrete block and high density engineering bricks. Thus it is important to estimate the effect of a change in material parameters.

Figures 6.19 and 6.20 show the change in transmission loss, for variations in the materials parameters where the thickness of cross-rib and leaf is 0.1 m. The material density and longitudinal wavespeed are changed up to the limits given in section 6.5.3. The variations are shown in terms of χ and φ, given by equations 6.28 and 6.29, respectively. With equal thicknesses these expressions simplify to $\chi=\sqrt{(c_{Lc}/c_{Ll})}$ and $\varphi=(c_{Ll}m_l)/(c_{Lc}m_c)$ where subscript L and c are the leaf and cross-ribs respectively. Using the same limits given in section 6.5.3, curves are shown for φ for a range $0.25 < \varphi > 4$. Figures 6.19 and 6.20 show the predicted transmission loss from cross-rib to leaf and leaf to cross-rib respectively.

Considering the extreme cases in both figures for the incident wave on cross-rib and on the leaves; the improved transmission loss to be gained by a material mis-match at the junction, over the worst case scenario (where cross-rib and leaf are identical), is 6 dB and 4 dB respectively.

Interestingly, if we take the range of material constants for the measured in-situ diaphragm walls (see chapter 8) as typical for the walls built at present, then φ does not vary greater $\pm$ 0.5 (assuming c_L is fairly constant). Hence the transmission loss across the junction will not vary more than about 2 dB in either direction.

Overall therefore, for the majority of cases, the transmission coefficient across the junctions will not vary more than 2 dB due to changes in material constants and 1 dB due to a doubling of cross-rib thickness. It is only if extreme combinations of materials are used between cross-rib and leaf that any significant benefit is gained. Overall this implies that large improvements in the diaphragm walls structure-borne transmission of energy will be small.

6.5.5 Bending Wave Coupling across the Cross-rib

The transmission coefficients calculated so far have not included the effect of the finite width of the cross-rib. So far the reduction in transmitted energy from the first leaf to the cross-rib has been considered separately from that of the cross-rib to the second leaf. Here we shall allow both T-junctions to contribute to the bending wave fields and derive a single transmission coefficient for an I-junction between both leaves across the cross-rib. Considering bending wave transmission only - for the cross-ribs equation 6.17 becomes:

$$v_{z_i} = \left[t_i e^{-jk_i x \cos\theta_i} + t_{n_i} e^{+jk_{n_i} x} + t_{ir} e^{-jk_i x \cos\theta_i} + t_{n_{ir}} e^{+jk_{n_i} x} \right] e^{-jk_i y \sin\theta_i} \quad (6.44)$$

where t_{ir} and t_{nir} are the travelling wave and evanescent wave, respectively, returning from the second junction. The boundary conditions 6.20 and 6.21 apply at both junctions and a set of simultaneous equations result for solution as before.

Figures 6.21 and 6.22 show the predicted transmission loss (TL = 10 log(1/γ) at normal, oblique (45°) and random incidence, for a 0.5 m and 0.35 m wide cross-rib, respectively. At low and mid-frequencies both figures predict a smooth, fairly constant non-resonant transmission coefficient. In both cases random incidence is roughly 4 dB lower than normal incidence. At the higher frequencies significant resonances occur along the cross-rib, increasing the transmission loss by up to 10 dB. For the 0.5 m cross-rib, resonance occurs at 800 Hz and 2.4 kHz, and for the 0.35 m cross-rib only one resonance is seen between 1.6 - 2 kHz. These relate approximately to the $\lambda_b/2$ and λ_b resonant conditions. These resonant frequencies depend upon the bending stiffness of the wall so will vary with the material parameters set.

Figure 6.23 shows the normal and random incidence coupling loss factors, according to equation 6.44. The 4 dB difference between normal and random incidence values of transmission loss is now reduced to approximately 2 dB, but the resonances are still pronounced at the higher frequencies.

To illustrate the effect of resonant and non-resonant behaviour by the bending wave field on the cross-rib, figure 6.24 shows the predicted displacement normalised with respect to an input wave of unit amplitude for a 0.5 m cross-rib. Two resonant (800 Hz and 2400 Hz) and two non-resonant (100 and 1500 Hz) frequencies are indicated. At the junctions (x = 0 and 0.5 m) the displacements are zero and are represented as a sum of an equal and opposite displacement produced by the propagating and near field waves. The 800 Hz $\lambda_b/2$ and 2400 Hz λ_b resonance can be clearly seen, with amplitudes at roughly 2 times that of the incident wave. At non-resonance the vibration of the cross-rib is small; minimal below the first resonance, but more significant after the first resonance where partial resonance is observed. The effect of damping would be to incorporate a complex Young's modulus of the form $\bar{E} = E(1+j\eta)$ where η is the loss factor. Figure 6.25 shows the random incidence transmission losses of a 0.35 m cross-rib for a variable loss factor. It is seen that the effect is minimal for the analytical model, except at high frequencies and where the loss factor is much greater than a typical value for masonry. This variation in loss factor is seen in terms of normalised displacement across a 0.5 m cross-rib at 2.4 kHz in figure 6.26. Figures 6.27 and 6.28 show the normalised travelling and evanescent wave components.

Wilson [52] produced a wave model for a normally incident bending wave between two leaves, for short masonry bridges across traditional cavity walls, i.e. a 50 - 100 mm return closing the cavity at a window or door jamb. Comparing this directly with his impedance model for transmission across battens (equations 6.15 - 6.17) between a leaf and dry lining; he indicates a difference of only 1.5 dB. In Wilson's

case neither the batten nor the masonry return were of sufficient length to produce wave transmission and thus the bridge can be considered as a conservative transmission path rather than a separate element or sub-system.

Figure 6.29 shows normal incidence coupling loss factors, η, calculated for a typical masonry wall with a 0.35 m cross-rib. At frequencies below 400 Hz there is a discrepancy of 10 - 20 dB between Wilson's estimate, η_{Iw} (equation 6.14) and the wave model of the I-junction, η_I (calculated from equations 6.44 and 6.45); except at resonant frequencies. (η_T is for the T-junctions given by equation's 6.30 - 6.31, and 6.44). This suggests significant wave transmission not accounted for by Wilson's model. The reason for this large difference is unknown. The significance of these results will be made clear in the statistical energy analysis, described in chapter 7.

6.6 SUMMARY

The work in chapter 5 and chapter 6 is summarised at this point. Chapter 5 shows that existing theory can be used to predict well the transmission loss for single walls. Measurements for model fin walls and diaphragm walls indicate a flattening of the transmission loss curves below $f_{c,u}$ due to the orthotropic nature of the construction. By calculating a second lower critical frequency, $f_{c,l}$, based on the bending stiffness across the ribs, and interpolating transmission loss between $f_{c,l}$ and $f_{c,u}$, good agreement with fin wall measurements was obtained.

In this chapter, it is seen that diaphragm wall measurements exhibit stronger orthotropic behaviour than that of the fin walls and application of the orthotropic single wall theory gives poor agreement with measurement. Vibration level difference measurements between leaves on full scale and model walls show that at low frequencies, roughly up to $f_{c,u}$, the wall behaves as a single leaf wall of

equivalent mass. At higher frequencies, the leaves begin to act independently and the vibration level difference increases with increased frequency. Attempts to incorporate measured vibration level difference into existing theory were not successful and it was concluded a more sophisticated approach was required.

It is necessary to investigate in more detail the transmission of sound between the leaves, including structure-borne cross-rib transmission. A simple impedance model of transmission across the cross-rib as used for lightweight and short bridge length constructions was seen to be inadequate. A travelling wave analysis is used to calculate random incidence transmission coefficients; describing transmission across an individual cross-rib/leaf junction and across both junctions. A 'bending wave' only model was used as the difference compared to an 'all-wave' model for a T-junction was shown to be no greater than 2 dB. Examining practical variations in the geometry and material qualities between the cross-rib and leaf, showed differences in the transmission coefficient no greater than 4 dB and typically less than 2 dB. Hence, to predict the overall transmission loss of the diaphragm wall and to allow for further examination of the changes in geometric and material parameters, SEA is invoked in chapter 7. This approach describes the wall as a combination of separate sub-systems and defines how they are coupled together. Radiation efficiencies proposed in chapter 5 and transmission coefficients derived in this chapter will be converted into coupling loss factors and included within the SEA program.

6.7 CONCLUDING REMARKS

Chapter 6 has primarily examined the role of the cross-rib as a structure-borne transmission path. It has explained the difficulty in describing the bridge due to its length and resonant behaviour. A wave model is used to describe transmission across the cross-rib as two T-junctions or as one I-junction between the leaves. Both approaches will be explored further in the following chapter.

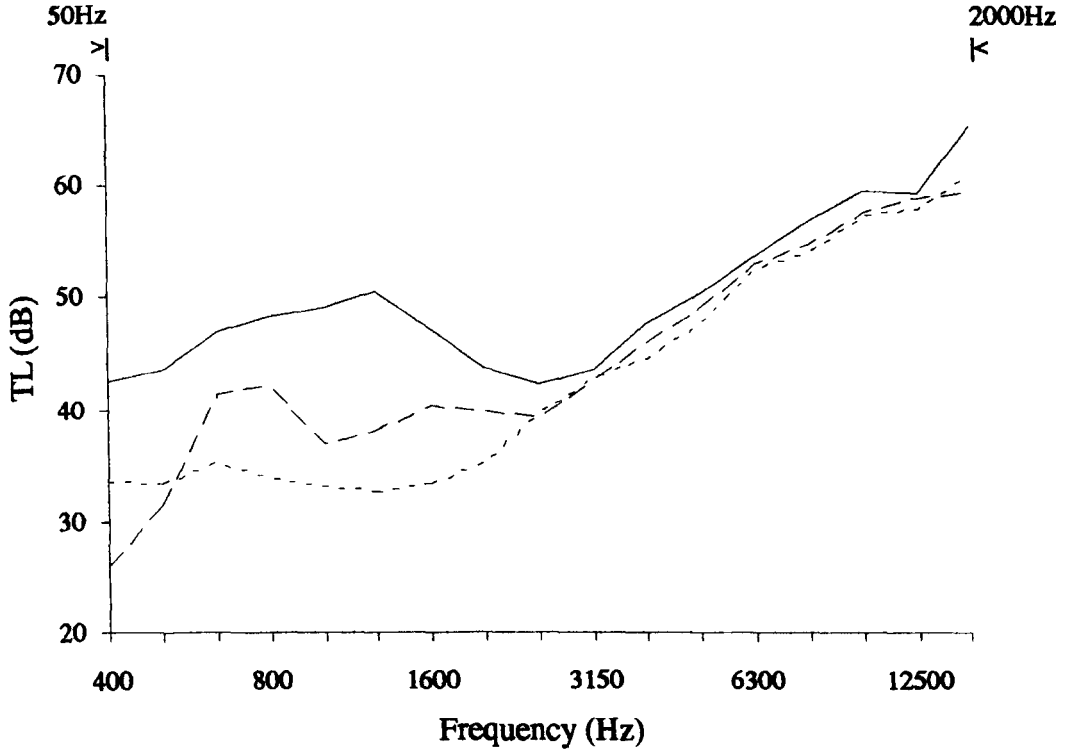

Figure 6.1: Measured transmission loss of 1:8 scale diaphragm walls

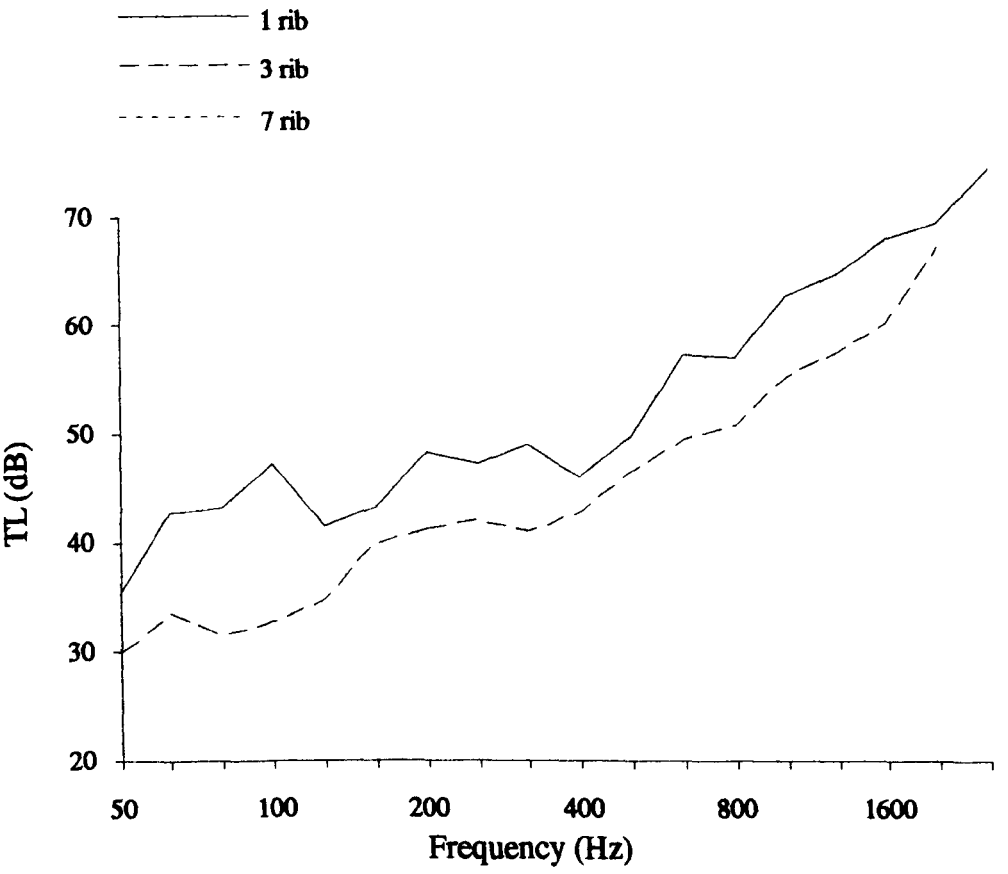

Figure 6.2: Measured transmission loss of two in-situ diaphragm walls

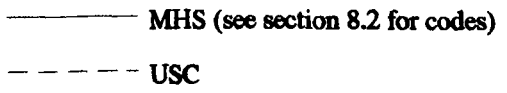

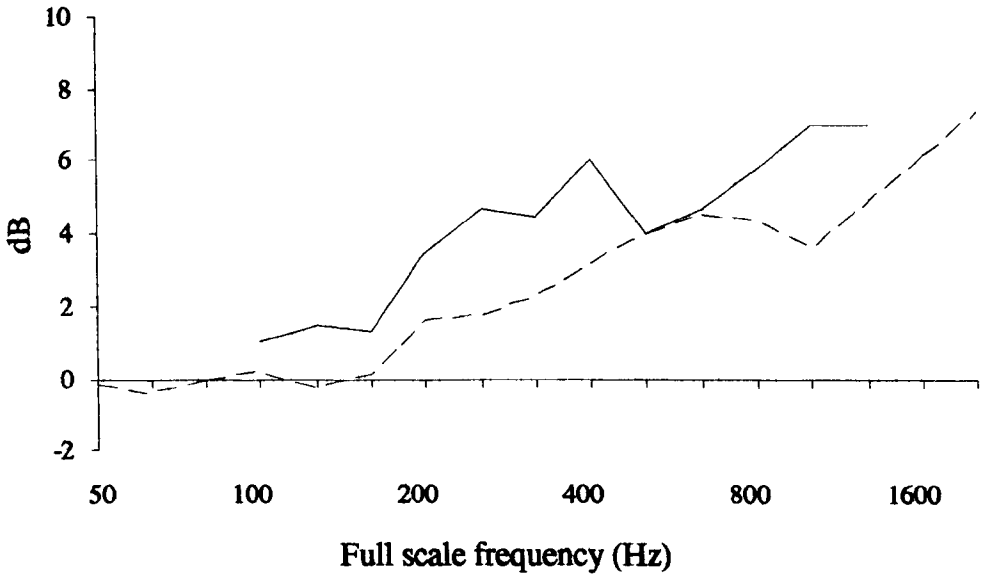

Figure 6.3: Measured vibration level difference between leaves of scale diaphragm walls

1:4 scale 7 rib wall

1:8 scale 7 rib wall

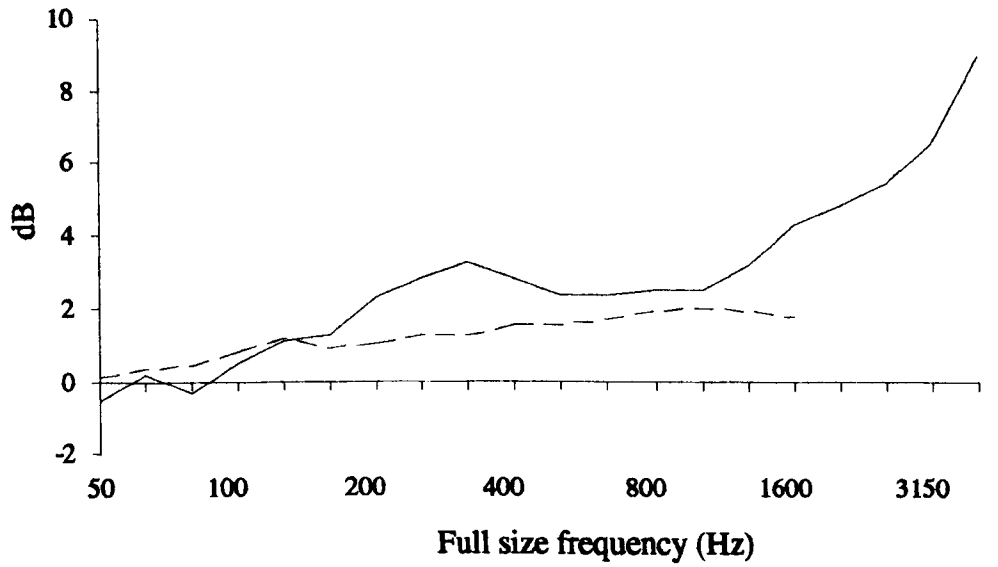

Figure 6.4: Measured vibration level difference between leaves of full scale diaphragm walls

Mean of in-situ measurements (see figure 8.25)

Diaphragm wall at Ceram Research

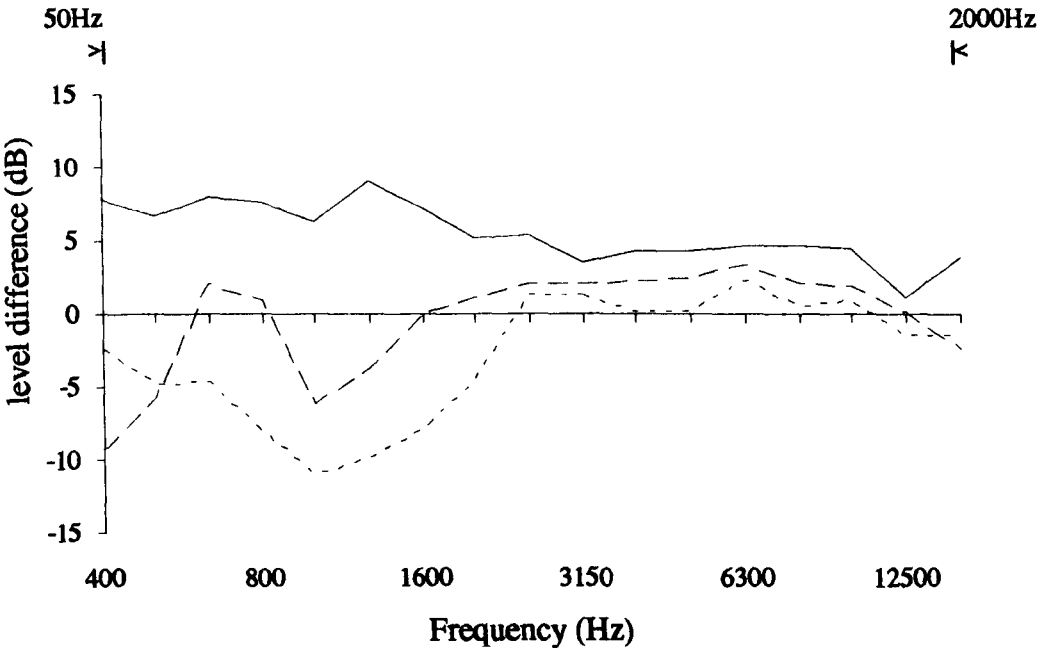

Figure 6.5: Difference in transmission loss between measurement and prediction
(prediction: isotropic radiation and equivalent mass)

1 rib wall
3 rib wall
7 rib wall

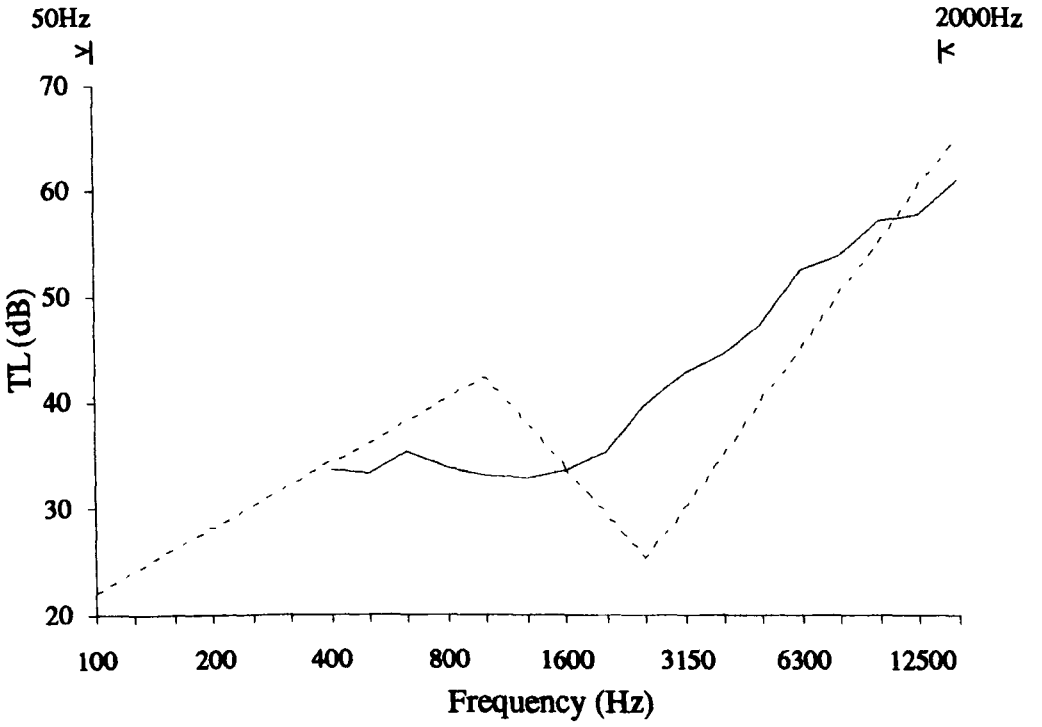

Figure 6.6: Predicted transmission loss of 1:8 scale 7 rib diaphragm wall

prediction [2.25]
measurement

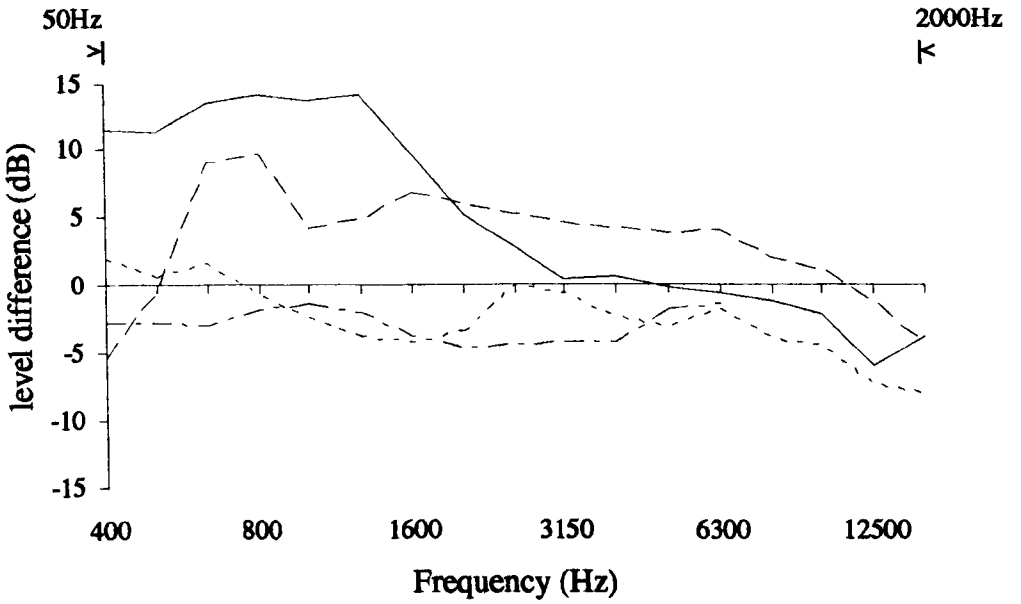

Figure 6.7: Difference in transmission loss between measurement and prediction for scale walls (prediction: orthotropic radiation plus constant)

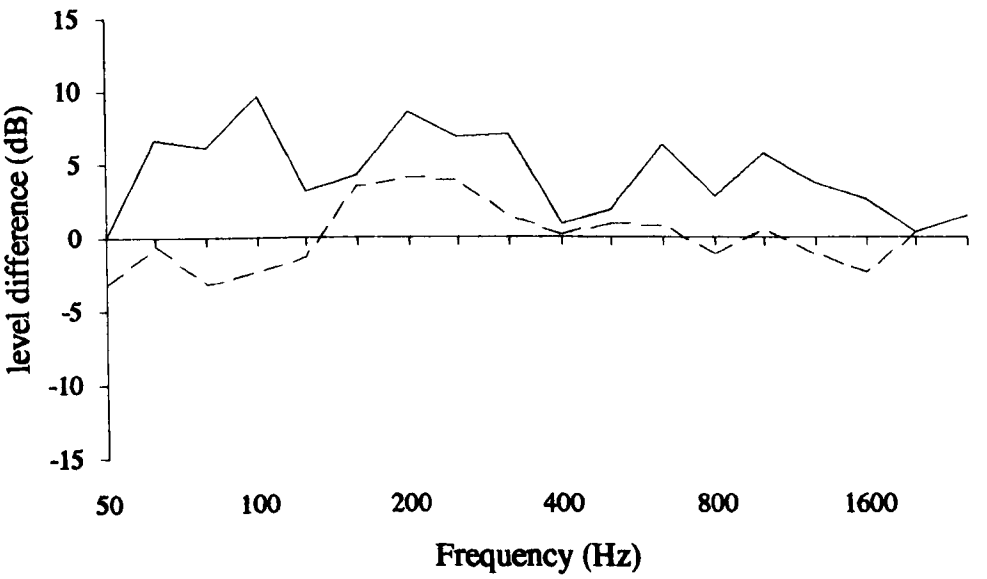

Figure 6.8: Difference in transmission loss between measurement and prediction for in-situ walls (prediction: orthotropic radiation plus constant)

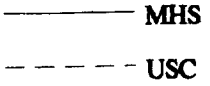

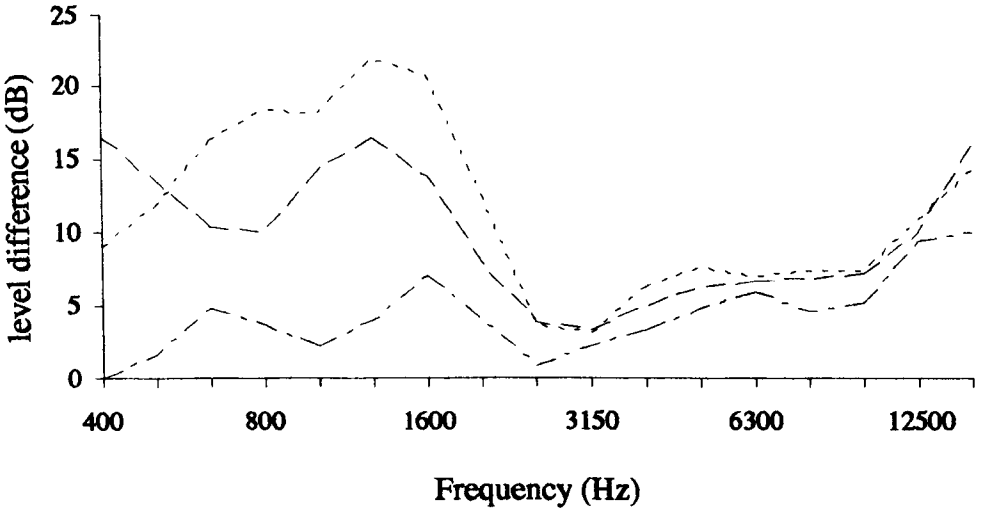

Figure 6.9: Difference in measured transmission loss between the double and 1:8 scale diaphragm walls

1 rib
3 rib
7 rib

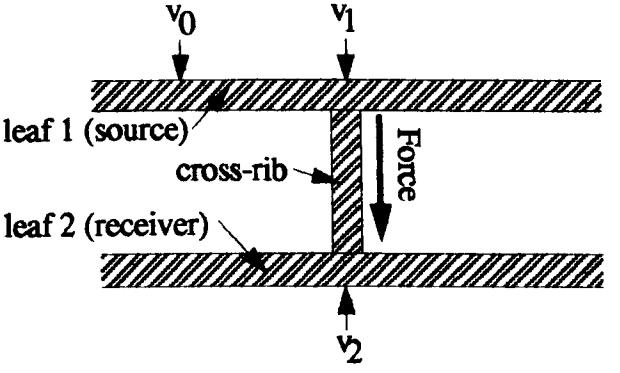

Figure 6.10: Two leaves coupled by a bridge

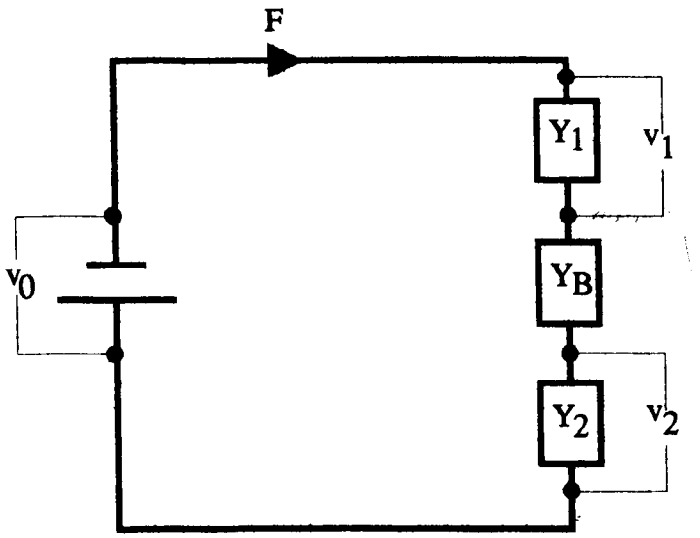

Figure 6.11: Electrical analogy of figure 6.10

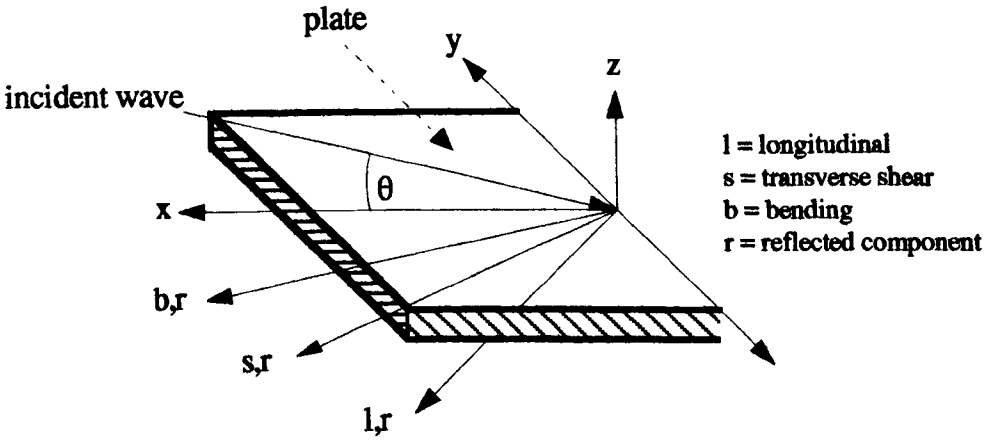

Figure 6.12: Waves generated on a plate

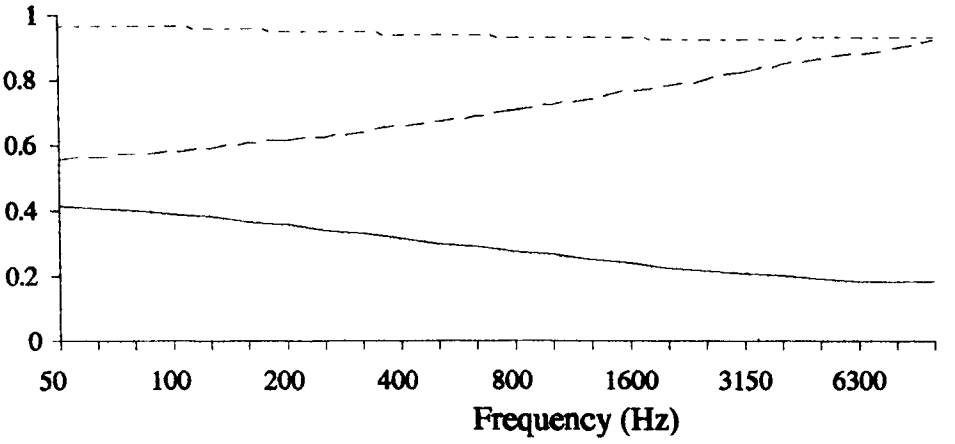

Figure 6.13: Transmitted & reflected efficiencies for an incident bending wave at a corner

transmitted bending wave only

transmitted bending wave and bending to longitudinal wave

transmitted and reflected bending waves and transmitted bending to longitudinal wave

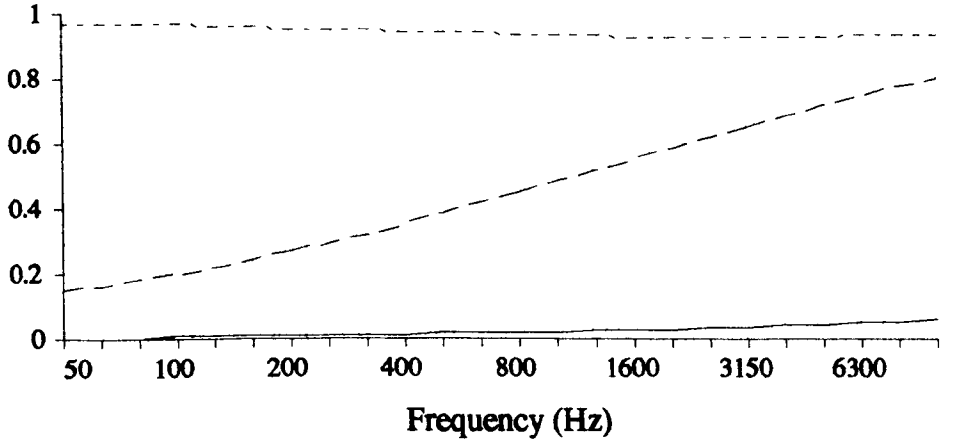

Figure 6.14: Transmitted & reflected efficiencies for an incident longitudinal wave at a corner

transmitted longitudinal wave only

transmitted longitudinal wave and longitudinal to bending wave

transmitted and reflected longitudinal waves and transmitted longitudinal to bending wave

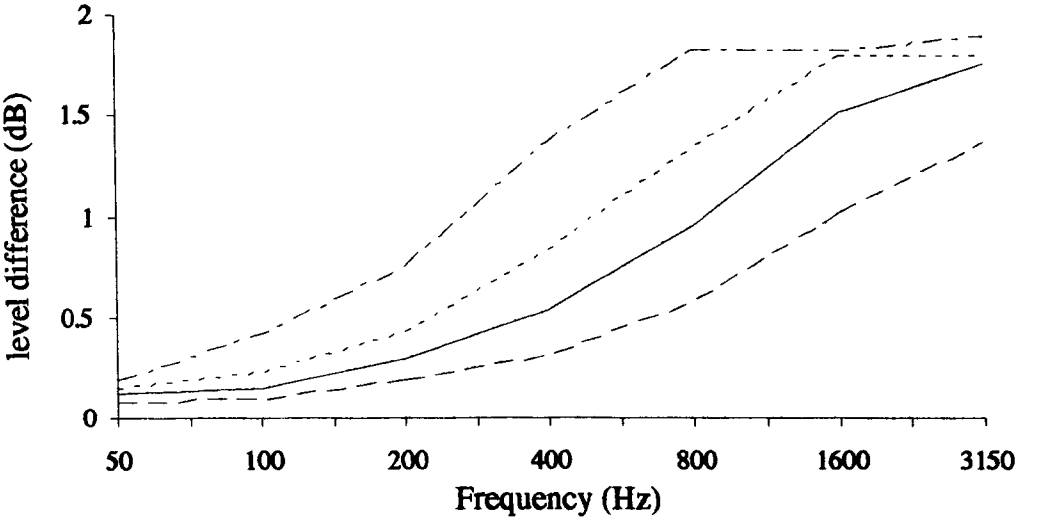

Figure 6.15: Predicted difference in transmission coefficient between 'bending only' and 'all waves' models - incident waves from cantilever

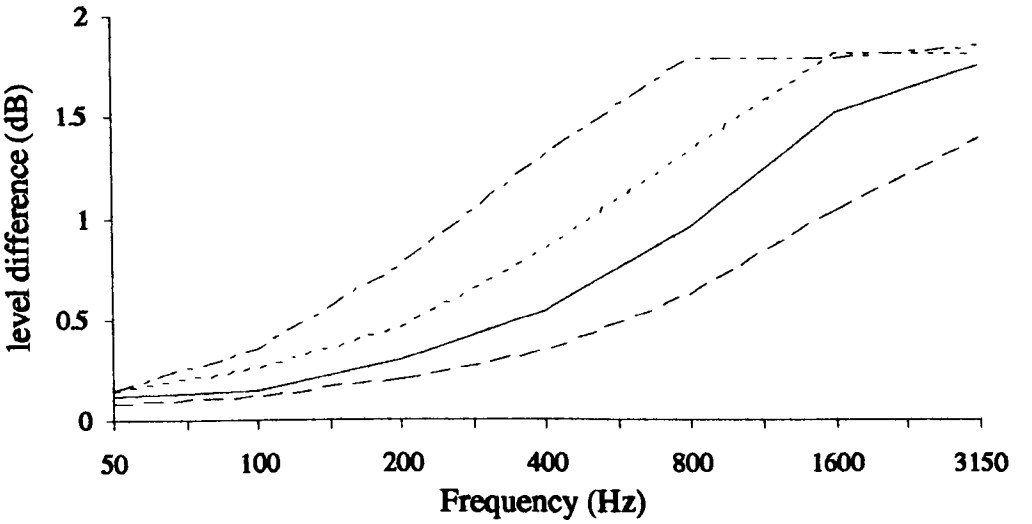

Figure 6.16: Predicted difference in transmission coefficient between 'bending only' and 'all waves' models - incident waves from co-planar plate

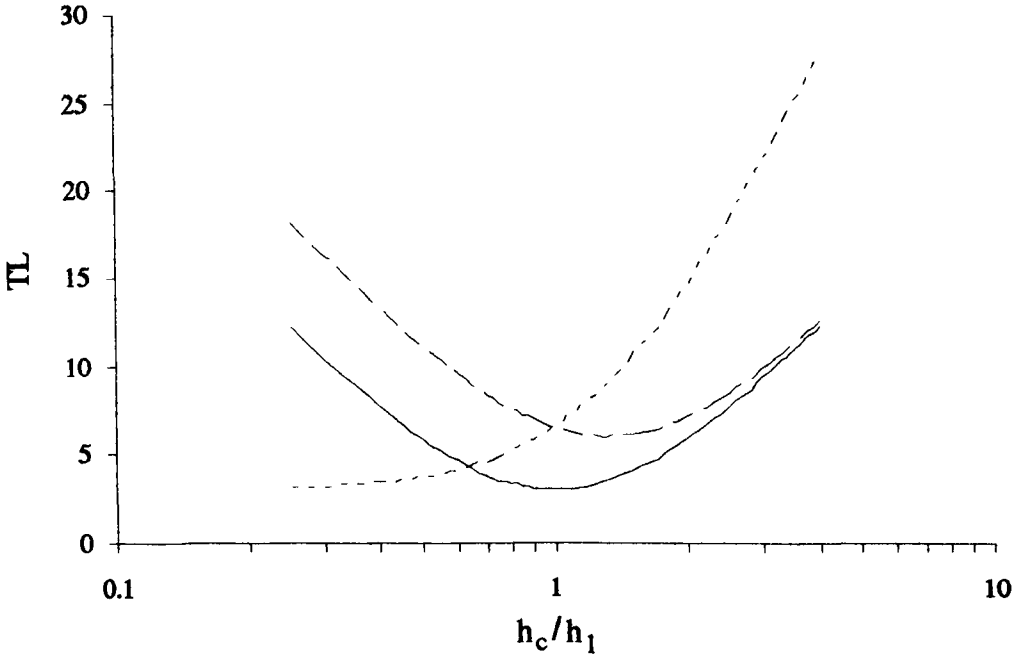

Figure 6.17: Predicted normal incidence transmission coefficient

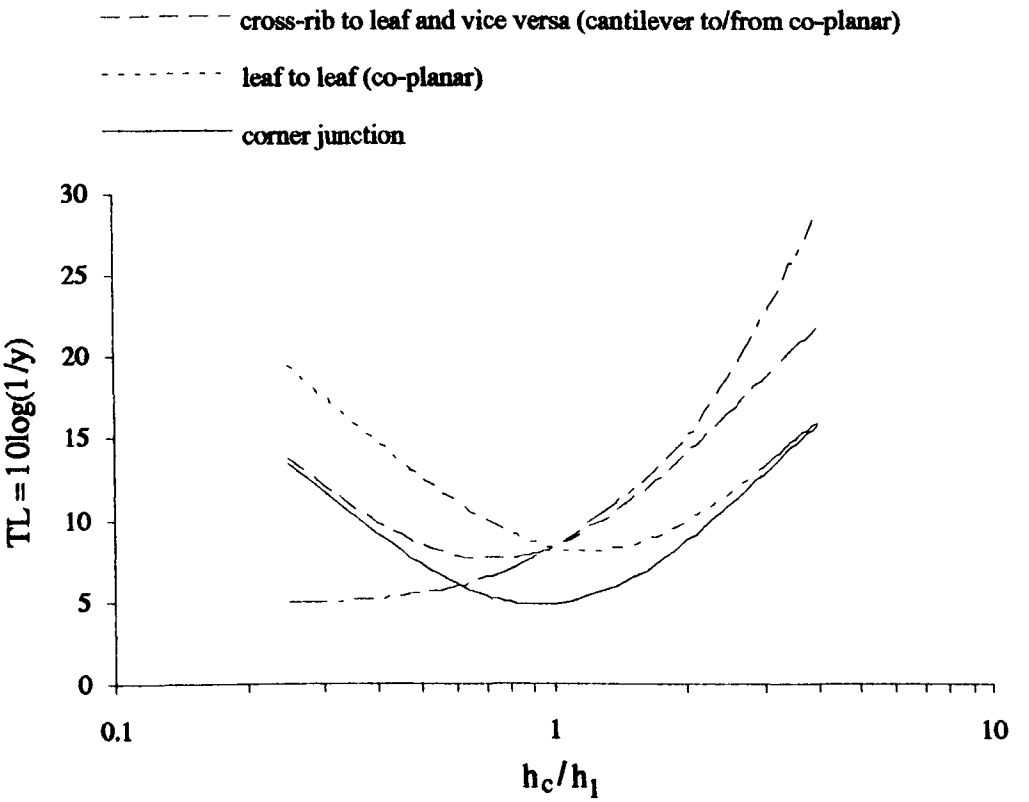

Figure 6.18: Predicted random incidence transmission coefficient for a T-junction - for different thickness ratios

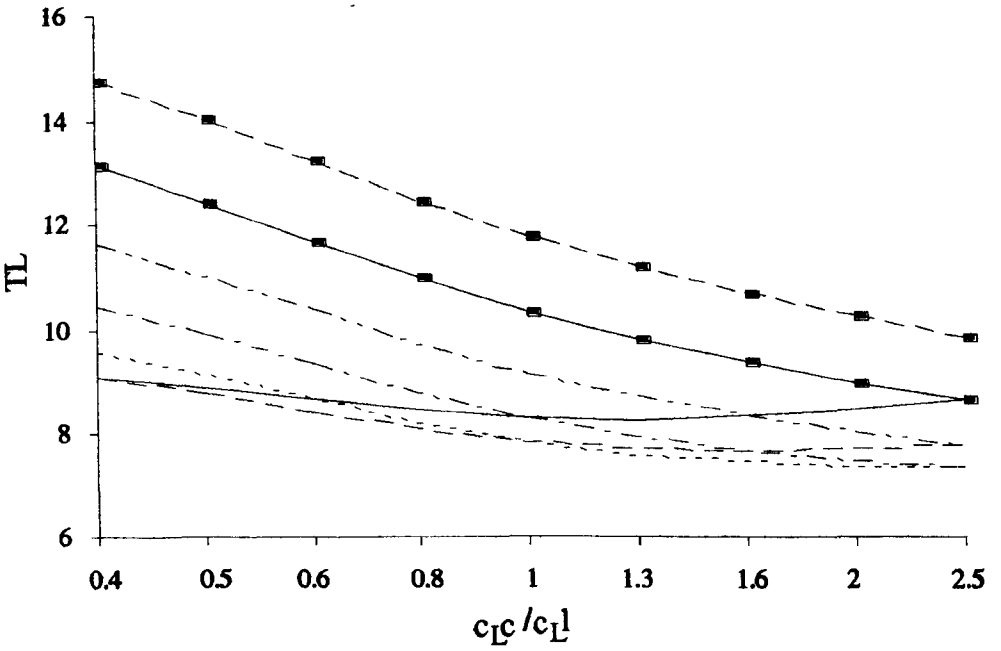

Figure 6.19: Predicted random incidence transmission coefficient - incident wave on cross-rib

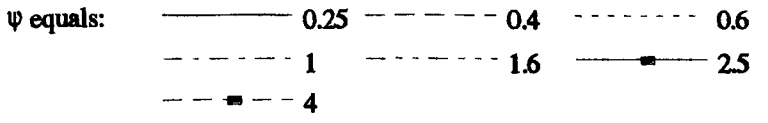

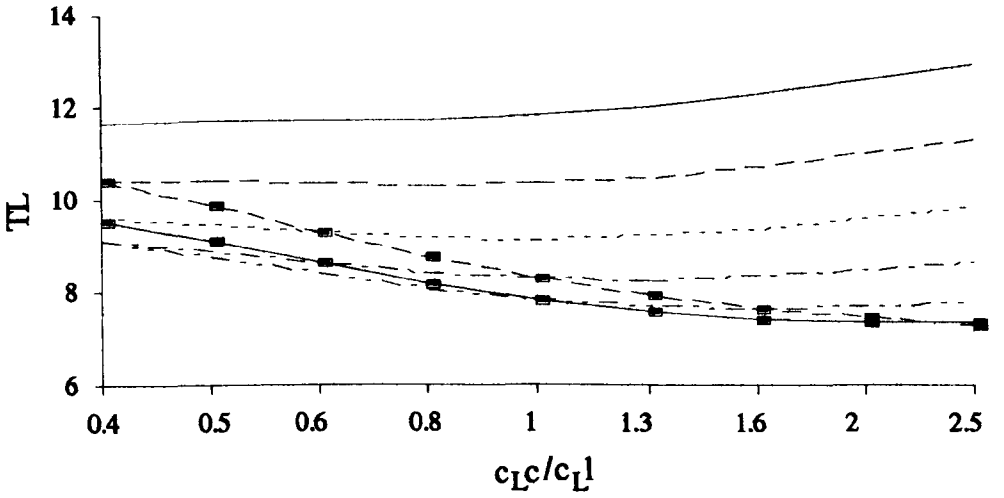

Figure 6.20: Predicted random incidence transmission coefficient - incident wave on leaf

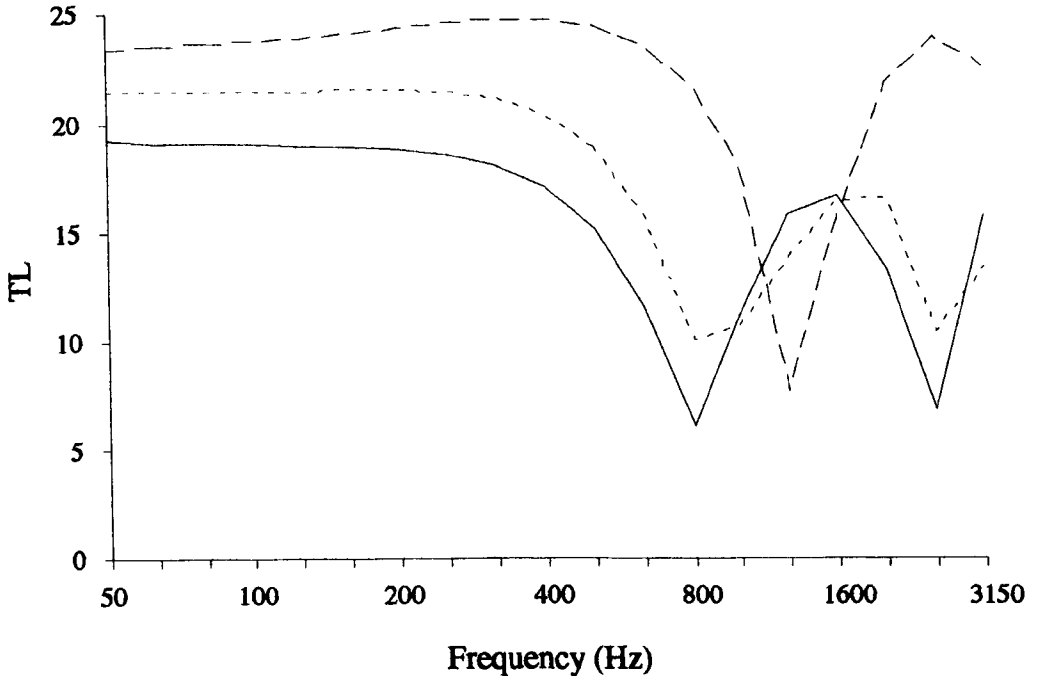

Figure 6.21: Predicted transmission coefficient across a 0.5 m cross-rib

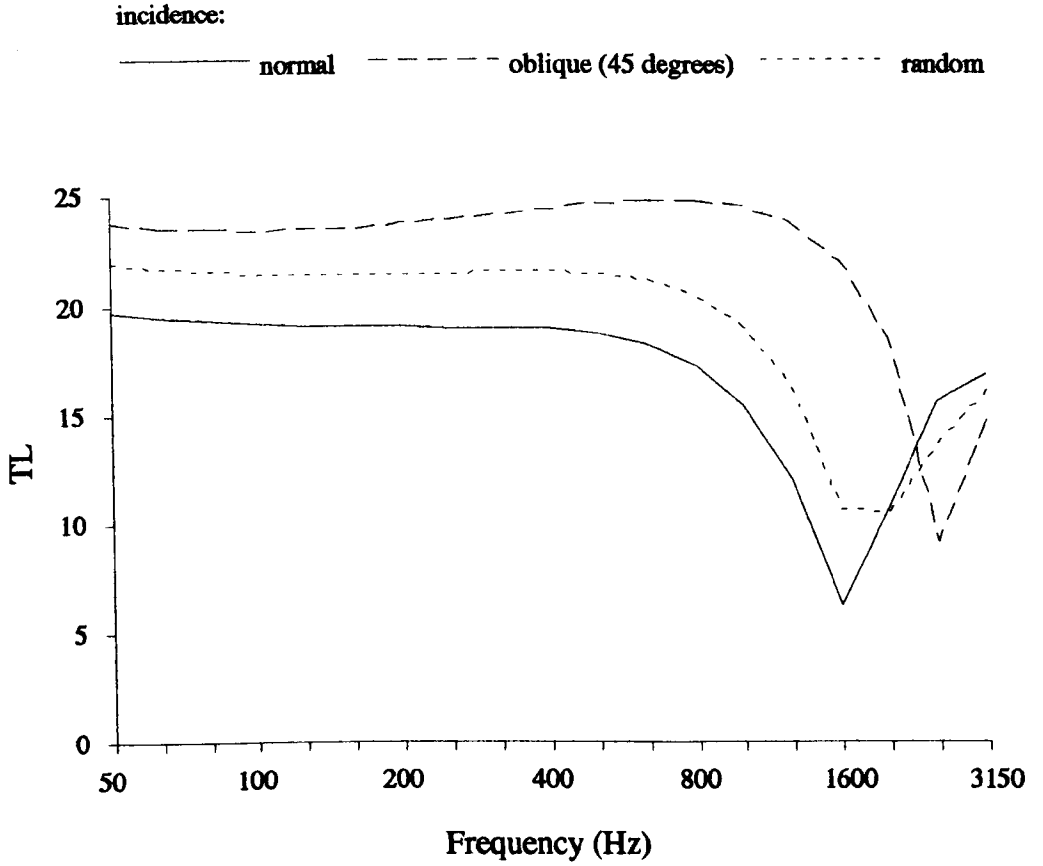

Figure 6.22: Predicted transmission coefficient across a 0.35 m cross-rib

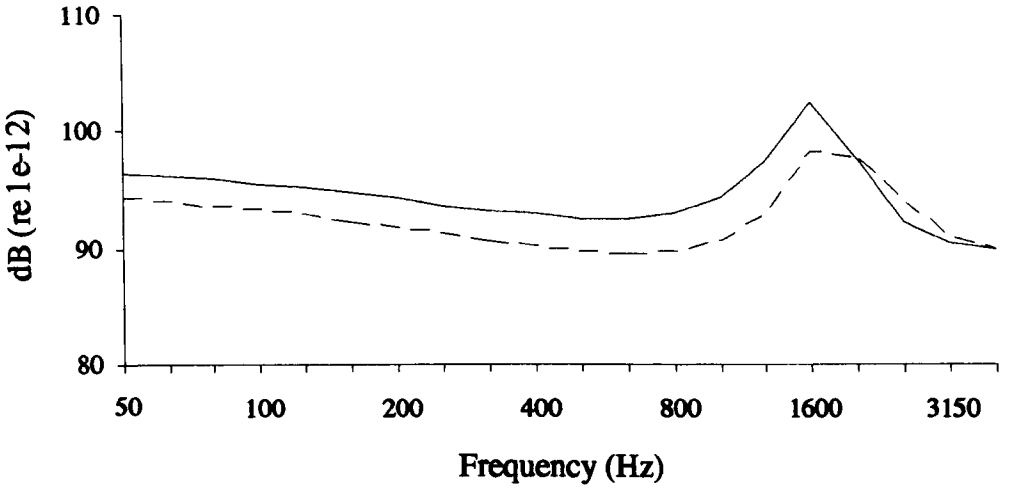

Figure 6.23: Predicted normal & random incidence coupling loss factor for an I-section

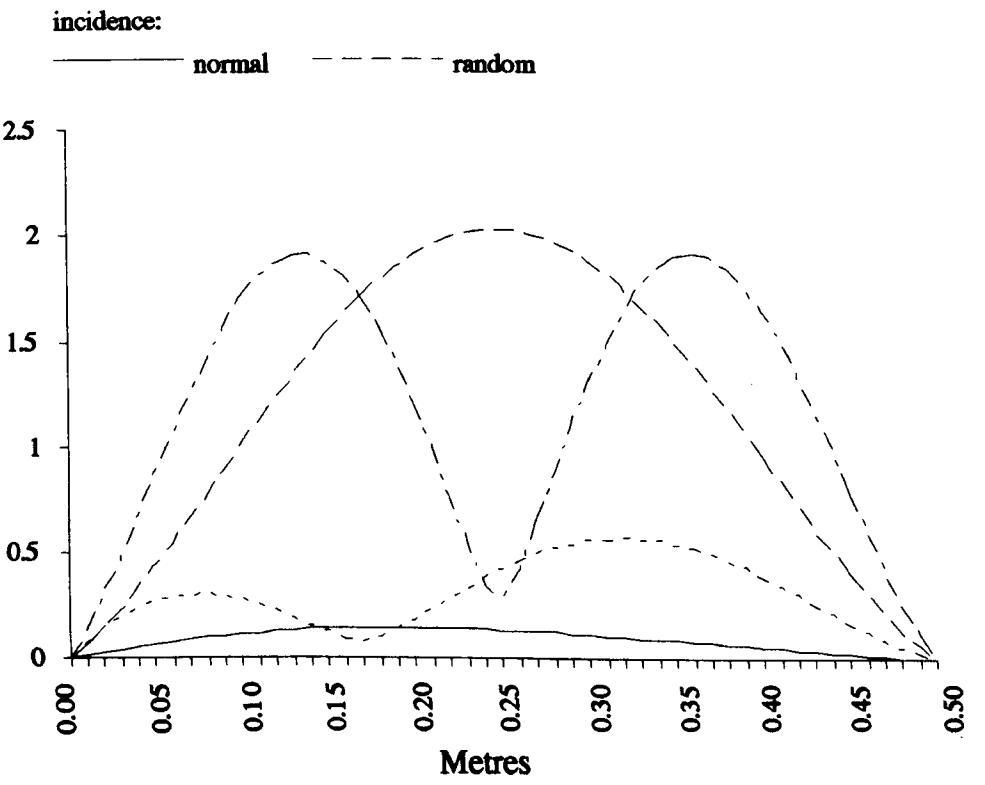

Figure 6.24: Predicted normalised displacement across a 0.5 m cross-rib

Selected frequencies:

non-resonant	resonant
100 Hz	800 Hz
1500 Hz	2400 Hz

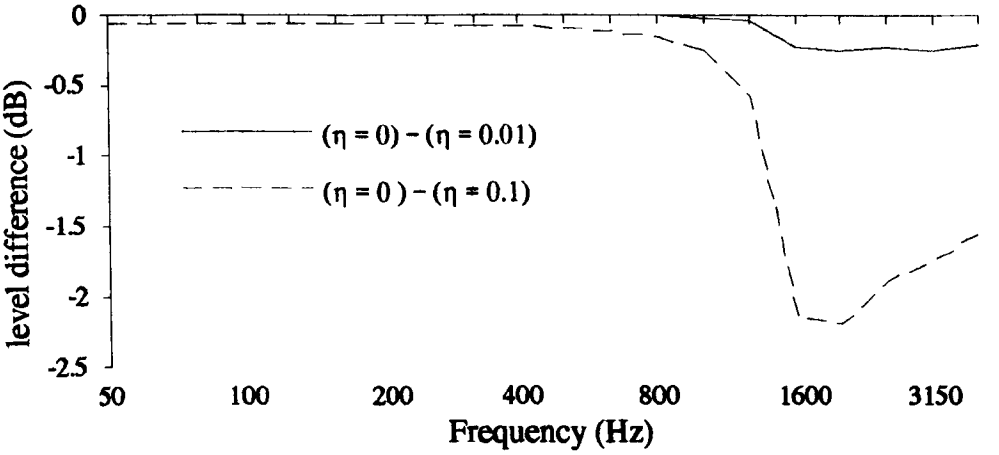

Figure 6.25: Difference in predicted transmission coefficient across a 0.35 m cross-rib due to changes in loss factor

Variation in loss factor for a 0.5 m cross-rib (figures 6.27 - 6.29)

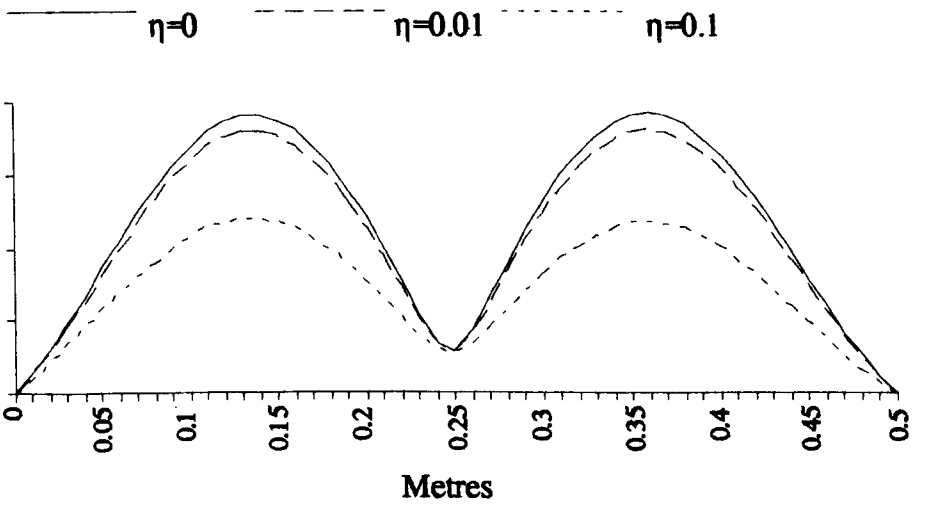

Figure 6.26: Predicted normalised displacement

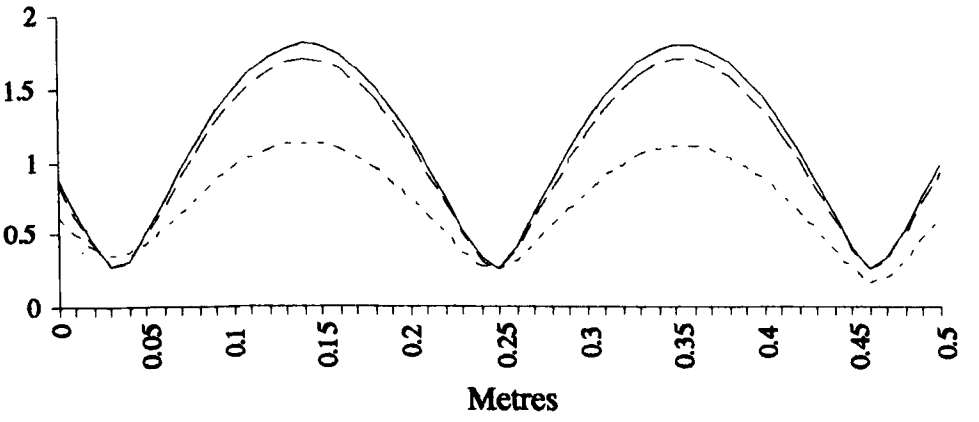

Figure 6.27: Predicted normalised travelling component

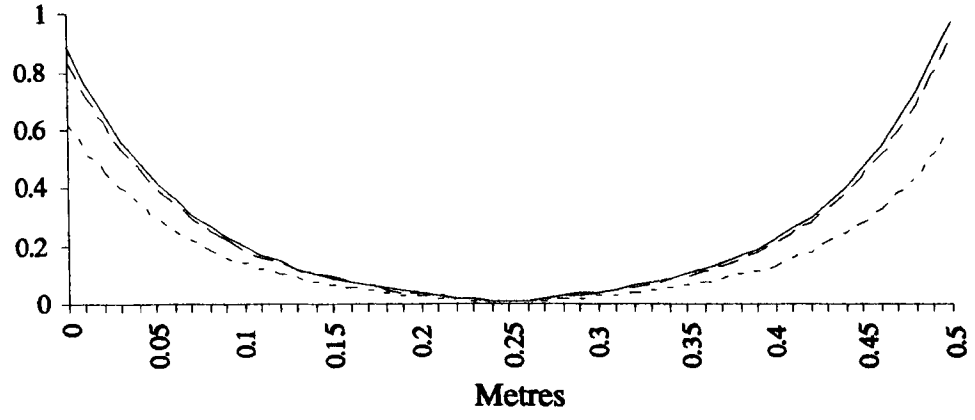

Figure 6.28: Predicted normalised evanescent component

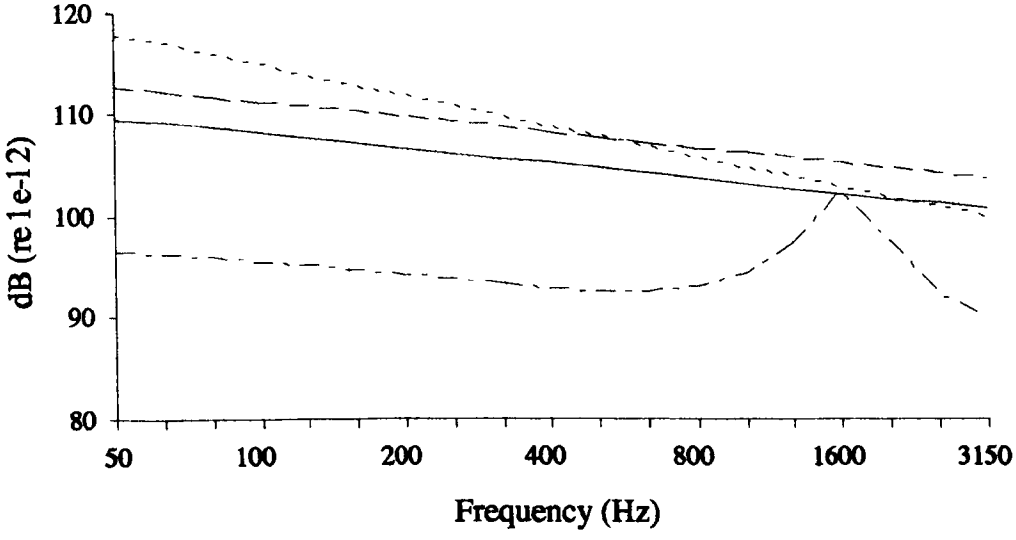

Figure 6.29: Predicted normal incidence coupling loss factor for T and I-junctions

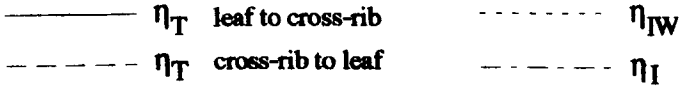

7 STATISTICAL ENERGY ANALYSIS

7.1 INTRODUCTION

The limitations of conventional bridged wall theory and modified single wall theory, to predict the transmission loss of the diaphragm wall, were identified in chapter 6. Such theories only considered the wall as a uniform element and could not properly account for internal mis-matches in impedances and wall thickness, between the cross-rib and leaves. Nor could they account for the transmission across the cavity or standing waves across the rib. Hence predictions of variations in sound insulation were only possible by altering the total mass and bending stiffness of the wall. To better predict the wall's sound insulation and account effectively for structural and geometric variations, there was a requirement for a more flexible analytical approach and so Statistical Energy Analysis (SEA) was invoked.

SEA was initially developed in the 1960's as part of a NASA programme and is considered more as a framework of analysis rather than a specific method. Conventional methods involve rigorous and detailed calculation using standard analytical methods, such as involving eigen functions and numerical approaches, like finite element analysis. These methods become intractable or excessively time consuming as the system under study increases in complexity and frequency. For example, the vibration analysis of one part of a machine may require consideration of numerous connected components, involving many source and transmission paths, while random excitation adds further complications.

SEA is statistical in its approach and involves spatial averages over structural elements and within acoustic spaces. These components are defined as energy storage systems with vibrational or acoustic power transmitted between them. SEA assumes that each component is resonant and is best applied where components

have a high modal density. Agreement between SEA prediction and measurement is generally good at high frequencies. Therefore, it may be argued that as a system increases in complexity, deterministic methods become less feasible and SEA more practically applicable [134].

What could be described as the bible of SEA was published by Lyon in 1975 [119]. This encapsulated work from the 1950's onwards by himself and others, significantly by Smith [135], Maidanik [115], Scharton [125] and Eichler [136], which established the fundamental principles of SEA. Most of the research was carried out for the aircraft and aerospace industries, and so, related directly to these types of structural elements, where thin plate theory was applicable. SEA was specifically applied to building acoustics through a number of papers beginning with Crocker and Price. These calculated the transmission loss for single [120] and double panels [137] and compared theory with measurement for the sound radiation from panels [118, 138]. A re-evaluation of their work is given by Brekke [139]. Structure-borne sound transmission theories for building structures were developed by Cremer [30], and extended by Kihlman [140] and Gibbs [113], which have already been discussed in Chapter 6. Craik [124] applied SEA to large buildings, measuring and predicting many parameters, the initial research providing a measurement data bank of information.

In this chapter, we shall first, describe the SEA approach and define its parameters, then apply this theory to single, fin and diaphragm walls.

7.2 PRINCIPLES AND THEORY

The canon of SEA is that defined by Lyon [119] as, "the power flow between a pair of coupled sub-systems is directly proportional to the difference in steady state or average energy between the sub-systems." A sub-system is an element which is

assumed to have a separately identifiable energy distribution to any connecting elements; and the excited energy within that sub-system must be resonant. Let us consider the simplest SEA model - a two sub-system model.

A thermal analogy is often used to explain the dynamic relationship between two sub-systems [134]. Figure 7.1 shows a 2 sub-system heat flow diagram. It is assumed that this is the whole 'system'. A system includes all the sub-systems which will significantly influence the energy levels of those sub-systems. The thermal bodies i and r have individual energies, defined by their temperatures, θ_i and θ_r, and are connected by a thermal link. If body i is heated, $\theta_i > \theta_r$, and heat will flow from i to r at rate proportional to the difference in temperature. The degree of heat transfer depends on the constant of proportionality or thermal conductivity, k. Heat is also lost from a body as surface radiation. Thus, if the conductivity is high the difference in temperature between sub-systems is small and if the heat loss is high from body i then less heat energy is available to be transferred to body r.

Figure 7.2 illustrates the equivalent SEA model, described as an 'energy flow' or 'power flow' diagram. The energy levels in sub-system i and r are given by E_i and E_r. It is assumed that the energy within a sub-system is purely resonant and there is equal energy in each mode within a frequency band, and these in turn are equal in their spatial distribution throughout a sub-system. $\Pi_{in,i}$ is the input power to sub-system i. η_{ir} and η_{ri} are the 'forward' and 'reverse' coupling loss factors between sub-systems i and r. η_i and η_r are the loss factors of each sub-system. For the whole system and each sub-system the power balance equation is:

$$\Pi_{in} = \Pi_{out} \qquad (7.1)$$

The power balance equation for sub-system i is,

$$\Pi_{in} + \Pi_{ri} = \Pi_{ir} + \Pi_i \qquad (7.2)$$

and for sub-system r,

$$\Pi_{ri} + \Pi_r = \Pi_{ir} \qquad (7.3)$$

where Π_{ir} and Π_{ri} are the powers between sub-systems, and Π_i and Π_r are the powers dissipated in those sub-systems.

7.2.1 Parameters

The energy within sub-systems, the power flows between them and their losses, are all parameters of the SEA model, which need to be defined in order to determine the transmission of energy between any two sub-systems.

The power $\prod_{ir}$, within a bandwidth $\Delta\omega$, can be written as [119]:

$$\Pi_{ir} = E_i \, \omega \, \eta_{ir} \qquad (7.4)$$

where ω is the angular frequency. For a room, E_i is given by [119]:

$$E_i = \frac{p^2_{rms} V}{\rho c^2} \qquad (7.5)$$

where V is the volume, p^2_{rms} is the mean square pressure, ρ is the density of air and c is the speed of sound in air. For an isotropic plate, E_i is the total bending wave energy in the sub-system and is given by [119],

$$E_i = m A_w v^2_{rms} \qquad (7.6)$$

where m is the surface density, A_w is the area of the wall and v^2_{rms} is the mean squared velocity of the surface.

If the coupling loss factor, η_{ir}, is structure-borne, it can be derived in terms of the transmission coefficient, γ_{ir}, as discussed in chapter 6. Where the common expression for the coupling loss factor between connected plates is given by Heckl [39], Lyon [119] et al, as:

$$\eta_{ir} = \frac{2}{\pi} \frac{L_{ir}}{A_i} \frac{1}{k_i} \gamma_{ir} \qquad (7.7)$$

where, A_i is the area of the ith source wall, L_i is the length of the junction between the ith and rth walls, and k_i is the wavenumber of the ith wall.

If η_{ir} is a structure to air coupling, such as from a wall into a room, it is termed the radiation loss factor, denoted η_{rad}. For a wall of finite area η_{rad} is given in terms of radiation resistance, $R^{2\pi}_{rad}$ into half-space, where:

$$\eta^{2\pi}_{rad} = \frac{R^{2\pi}_{rad}}{M_w \omega} \qquad (7.8)$$

and M_w is the total mass of the wall. The 'forward' coupling loss factor, between two sub-systems, can be related to the 'reverse' coupling loss factor, between the same two sub-systems, by using the reciprocal relationship given by Lyon and Scharton [125]:

$$\eta_{ir}\, n_i = \eta_{ri}\, n_r \qquad (7.9)$$

where n_i is the modal density of the ith sub-system. Hence, the radiation loss factor, η_{rw}, from a room to a wall, can be given by:

$$\eta_{rw} = \eta_{wr} \frac{n_w}{n_r} \qquad (7.10)$$

where η_{wr} is the wall-to-room radiation loss factor, and n_r and n_w are the modal densities of the room and the wall, respectively.

The modal density is the number of modes per hertz within a sub-system. For an isotropic plate in bending vibration it is given by [119]:

$$n_w = \frac{\sqrt{3}\, A_w}{h\, c_L} \qquad (7.11)$$

and is frequency independent. The modal density for a rectangular enclosure is given by Dah-You Maa as [142]:

$$n_r = \frac{4\pi f^2 V}{c_0^3} + \frac{\pi f A}{2c_0^2} + \frac{L}{8c_0} \qquad (7.12)$$

where V, A and L are the room volume, area and perimeter, respectively. The second and third terms of the RHS apply where the wavelength is of the order of the room dimensions. Equation 7.12 is often simplified to the first term for mid and high frequencies. As the first term is a function of f^2, the number of modes rises rapidly with frequency. At high frequencies there may be many thousands of modes, while at low frequencies only a few modes may occur and n_r is commonly less than one. Here it is often useful to know the exact number of modes within a bandwidth.

For a space to be acoustically 'three dimensional' it must have at least half an acoustic wavelength ($\lambda_a/2$) across its shortest dimension. Below this cut-off frequency the space can be considered 'two dimensional'. Again, at a lower cut-off frequency the same condition will occur along the next shortest dimension, and the

space is considered 'one dimensional.' The modal density for one and two dimensional spaces are given [119] below:

$$n_{r\,(1\ dim.)} = \frac{c}{2L} \tag{7.13}$$

$$n_{r\,(2\ dim.)} = \frac{2\pi f A}{c^2} + \frac{P}{c} \tag{7.14}$$

where, L is the length in the longest room dimension, A is the surface area and P is the perimeter of that area.

The final SEA parameter required is the internal loss factor of a sub-system, which describes that energy which is dissipated as heat. The internal loss factor, η_i, or damping, of a wall was discussed in chapter 5. For the 1:8 scale walls, a value of 0.02 was measured, and for the full scale masonry walls, a typical value of 0.015 is used for all predictions. Internal loss factors can often be assumed independent of frequency.

The total loss factor of the room is given by:

$$\eta_{room} = \frac{2.2}{fT} \tag{7.15}$$

where T is the measured reverberation time. The sound decay within the room depends both on the internal room loss factor and the coupling loss factor to other sub-systems. However the former is often assumed to dominate.

7.2.2 Solving SEA Models

Returning to the 2 sub-system model and equations 7.2 and 7.3, these may be re-written, including equation 7.4, as:

$$\Pi_{in} = E_i\omega\eta_{ir} - E_r\omega\eta_{ri} + E_i\omega\eta_i \quad (7.16)$$

$$0 = -E_i\omega\eta_{ir} + E_r\omega\eta_{ri} + E_r\omega\eta_r \quad (7.17)$$

If the reciprocity relationship, equation 7.9, is invoked then,

$$E_i\omega\eta_{ir} - E_r\omega\eta_{ri} = \omega\,\eta_{ir}\,n_i\left[\frac{E_i}{n_i} - \frac{E_r}{n_r}\right] \quad (7.18)$$

Equation 7.16 cannot be solved without knowing the input power, but the energy ratio between the two sub-systems can be obtained from equation 7.17, as:

$$\frac{E_i}{E_r} = \frac{\eta_{ri} + \eta_r}{\eta_{ir}} \quad (7.19)$$

where ω is common to all terms and is omitted. This can be expressed in terms of level difference, as $10\log(E_i / E_r)$.

Where there is only one power flow path, or where one path is of interest, the energy level difference between two sub-systems is easily obtained. For a series of n sub-systems, where each sub-system is connected to a maximum of two sub-systems then the energy ratio between the nth and first sub-system is given by;

$$\frac{E_1}{E_n} = \frac{E_1}{E_2}\,\frac{E_2}{E_3} \cdots \frac{E_{n-1}}{E_n} \quad (7.20)$$

Intermediate energy ratios such E_{n-1}/E_n are also obtained.

In more complex systems the modal energy of a sub-system may result from many transmission paths. Where no simplifying assumptions can be made, the set of

simultaneous equations becomes large and are best expressed and solved in a matrix form. For n sub-systems,

$$\begin{bmatrix} \eta_1 & -\eta_{21} & \cdots & -\eta_{n1} \\ -\eta_{12} & \eta_2 & \cdots & -\eta_{n2} \\ \cdots & \cdots & \cdots & \cdots \\ -\eta_{1n} & -\eta_{2n} & \cdots & \eta_n \end{bmatrix} \begin{bmatrix} E_1 \\ E_2 \\ \cdots \\ E_n \end{bmatrix} = \begin{bmatrix} \Pi_1 \\ \Pi_2 \\ \cdots \\ \Pi_n \end{bmatrix} \qquad (7.21)$$

If the first sub-system only is directly excited, then the solution in the form E_i/E_1, is:

$$\begin{bmatrix} -\eta_{12} & \eta_2 & \cdots & -\eta_{n2} \\ \cdots & \cdots & \cdots & \cdots \\ -\eta_{1n} & -\eta_{2n} & \cdots & \eta_n \end{bmatrix} \begin{bmatrix} E_2/E_1 \\ \cdots \\ E_n/E_1 \end{bmatrix} = \begin{bmatrix} 0 \\ \cdots \\ 0 \end{bmatrix} \qquad (7.22)$$

The versatility of the SEA approach is clear. As all field variables can be converted to energies any relationship can be made, such as between mean pressure of a room and the mean bending vibration of a wall.

It remains to apply SEA to the systems of interest. Other important aspects of SEA will be discussed as they become relevant to the analysis.

7.3 SINGLE WALLS

As in chapter 5, we shall consider the single wall case first, before applying it to the more complicated fin and diaphragm walls.

A single wall between two rooms is considered with a 3 sub-system model, shown in figure 7.3, where E_1, E_2 and E_3 are the energies of the source room, single wall and receiver room, respectively. An input power, $\Pi_{in,1}$, is produced in the source room from a loudspeaker, and all three sub-systems are assumed to be resonant in the frequency bands of interest. No other sub-systems or paths are required as

flanking is assumed minimal in a test transmission suite. The same model is given by various authors [120, 139].

The power balance equations for each sub-system are given by,

$$\Pi_{in,1} = -\Pi_{21} + \Pi_{12} + \Pi_1 \quad (7.23)$$

$$0 = -\Pi_{12} - \Pi_{32} + \Pi_{21} + \Pi_{23} + \Pi_2 \quad (7.24)$$

$$0 = -\Pi_{23} + \Pi_{32} + \Pi_3 \quad (7.25)$$

From equation 7.4, equations 7.24 and 7.25 become,

$$0 = -E_1\eta_{12} - E_3\eta_{32} + E_2(\eta_{21} + \eta_{23} + \eta_2) \quad (7.26)$$

$$0 = -E_2\eta_{23} + E_3(\eta_{32} + \eta_3) \quad (7.27)$$

From which, the level difference between the rooms is:

$$\frac{E_1}{E_3} = \frac{(\eta_{32} + \eta_3)(\eta_{21} + \eta_{23} + \eta_2) - \eta_{23}\,\eta_{32}}{\eta_{23}\,\eta_{12}} \quad (7.28)$$

Crocker [120] assumes $E_1/n_1 \gg E_3/n_3$ (except at low frequencies), therefore η_{32} can be assumed negligible. If $\eta_{21} \approx \eta_{23}$ then:

$$\frac{E_1}{E_3} = \frac{\eta_3(2\eta_{21} + \eta_2)\,n_1}{\eta_{21}^2\,n_2} \quad (7.29)$$

Figure 7.4 shows the predicted and measured energy level difference between source room and wall for the 1:8 scale single wall. Agreement is good below f_c, and surprisingly so below 400 Hz. Figure 7.5 shows energy level difference between the wall and receiver room. Prediction agrees with measurement to within 1 - 3 dB, with a maximum error of 5 dB at coincidence. The negative difference implies the 'total energy', within each bandwidth, is greater in the receiver room than in the wall. This is not surprising as there are a greater number of modes in a room compared with a small plate in bending vibration. The net power is controlled not by the total energies of sub-systems but rather by their modal energies, which are greater in the wall than in the receiver room. Figure 7.6 shows the associated modal energies for these sub-systems and a clear decrease from sub-system 1 to 3 is indicated at all frequencies.

The SEA approach predicts energy level difference between sub-systems, but here predictions are given in terms of transmission loss as most field measurements were made using the sound intensity technique which gives a direct measure of the transmission loss (see chapter 8). For continuity, transmission loss is calculated and compared in most cases. When both rooms are the same size the transmission loss is

$$TL = 10 \log\left[\frac{E_i}{E_r}\right] + 10 \log\left[\frac{A_w T}{0.163 V}\right] \qquad (7.30)$$

T is the measured reverberation time of the receiver room, V is the volume of the receiver room and A_w is the area of the aperture under consideration.

Measured and predicted transmission loss are given in figures 7.7, 7.8 and 7.9, for the 1:8 scale wall, the 1:4 scale wall, and the 120 mm large transmission suite wall, respectively. So far the predictions have been for resonant transmission only. In two cases agreement between prediction and measurement above critical frequency is within 0 - 3 dB. For the full scale wall above 1600 Hz an increasingly poor signal to

noise ratio and high reactivity index resulted in questionable measured intensity levels. About the critical frequencies the discrepancy is between 5 and 20 dB. This is due to an incorrect estimate of damping and surface radiation in this region and is universally observed in such predictions. At frequencies below f_c, prediction is always higher than measurement by up to 10 dB in figure 7.7. This suggests that another sound transmission path is occurring, not accounted for by the SEA approach so far.

7.4 LOW FREQUENCIES AND NON-RESONANT TRANSMISSION

7.4.1 Low Frequencies

SEA is a statistical approach which is best applied where many resonant modes exist within a frequency bandwidth. Problems occur at low frequencies and simple systems where modal densities can be low. For rooms this is rarely the case in the building acoustics frequency range where thousands of modes can exist. Problems may well occur for small cavities or plates/beams where there may be only a handful of modes. SEA should not be applied where no resonant modes exist. Hence there is a transition region where only a few resonant modes occur and the applicability of SEA might be expected to break down. Therefore it is important to have some idea of a lower limiting frequency for SEA. This can be considered from the viewpoint of, whether there a minimum number of modes required within a frequency bandwidth to adequately characterise a sub-system? Recent work by Craik et al. [144 - 146] attempts to answer a related question by examining the discrepancy between predicted and measured coupling loss factors, for coupled walls of different sizes (and therefore different mode counts). It is shown that it is the modal response of the receiver sub-system which is important when defining a limiting frequency. Results showed that reliable values of η_{ir} can be obtained where there is, at least, 1 or 2 modes per frequency band. For the 1:8 scale walls, one mode

occurs, on average, in each 1/3 octave band above 80 Hz. For a typical diaphragm wall there is approximately 10 - 20 modes in the 50 Hz 1/3 octave band. At very low frequencies statistical averaging is difficult and agreement is possible only at actual mode frequencies.

A better indicator is the modal overlap, defined by equation 3.3, which includes the influence of damping within a sub-system. Higher modal overlaps produce a more even energy density distribution with fewer modes. A minimum modal overlap of 0.2 is offered by Craik [144]. The fundamental mode occurs at approximately 2 Hz and, hence, the modal overlap is approximately 17 at 50 Hz, assuming a 10 Hz bandwidth. Therefore in the frequencies region of interest, 50 Hz - 3.15 kHz, and its scaled equivalents, there is said to be an even distribution of energy throughout the sub-system and SEA is assumed applicable. Note that, at very low frequencies the modal density of the wall will be equal to, or even greater than that of the connected room. However as indicated in figure 7.6, this does not effect the net power flow in our case until below 400 Hz (1:8 scale) i.e. 50 Hz full scale.

At low frequencies bending wavelengths become comparable with the smallest wall dimension. A correction for the wall size is given by Donato [55] and re-written by Elmallawany, as a correction to transmission loss [147] and is given below,

$$TL_{corr} = 5\left[\frac{\omega r}{2.3\,c}\right]^{-0.72} \qquad (7.31)$$

where r is half the smallest wall dimension. The smaller the panel, the greater the correction. For the diaphragm wall this will add approximately 2 dB at 100 Hz and 0.5 dB at 500 Hz. For the 1:8 scale wall this gives a correction of 3.6 dB at 400 Hz, falling to 1 dB at 2 kHz. These corrections may partially account for some of the discrepancy between measurement and prediction, but a further and probable

explanation is due to the exclusion of the non-resonant transmission path from the SEA model, (referred to as this by [120, 137 - 139]).

7.4.2 Non-resonant Transmission

Non-resonant transmission is that caused by 'forced' bending waves. If a wave impinges on a wall at any angle the speed of the forced wave, c_p, will always be greater than the incident wave in air, $c_p > c$; and under excitation from diffuse broadband sound field the wall will be excited at all angles equally and at all frequencies. These waves are described by Lyon [119] as "...the non-resonant excitation of modes that have resonant frequencies above Δf ", where Δf is the measurement bandwidth. The forced waves will be reflected at boundaries and return as free bending waves, only becoming modes where their resonant frequencies are within the band Δf.

The transmission purely by forced waves can only occur on infinite plates, and is described by mass law. As SEA is a resonant approach to finite systems it can be argued that the inclusion of non-resonant transmission path is, at worst, heretical to the principles of SEA or at best is creating a non or pseudo-SEA model. Alternatively, if the model is incomplete without this non-resonant path, then should it not be included? The author finds no clear discussion on this subject in the literature and thus believes it useful to include some discussion here.

Consider a single wall between two rooms. Theoretically energy can be transferred between the two rooms in two ways: through forced excitation and through resonant excitation of the wall. The forced excitation of the wall is defined by mass law. The forced bending waves along the wall are always supersonic and the energy transfer is purely a function of mass and frequency. The resonant excitation of the wall is due to standing waves or modes, the number of which depends on the size and

dimensions of the wall and will increase with frequency, although the bending modal density of thin plates is frequency invariant. A resonant mode will be of much larger amplitude than a non-resonant mode, and will carry far more energy even where there are only a few modes compared with the non-resonant waves. Therefore it is argued that when estimating the response of a system only the resonant modes need be considered. Yet, to impart their energy these modes must be supersonic which only occurs above coincidence. Below coincidence resonant energy radiation is dependent upon the dimensions of the wall and energy will only be imparted at corner and edges (see figure 5.20), since over the majority of the surface dipole and quadrapole cancellation occur. Thus the wall is a poor radiator of resonant modes in this frequency region.

Therefore, below coincidence it is possible for the cumulative energy in a bandwidth from low amplitude supersonic forced waves to be greater than, or at least comparable with, the subsonic radiative energy from the edge and corner modes; particularly if the wall is heavily damped, which exists with masonry constructions. Generally it is found that non-resonant transmission dominates where $f \ll f_c$, but reduces rapidly as the resonant transmission increases with frequency. At very high frequencies, the transmission loss (recovery) curve converges with an extended non-resonant mass law curve. Hence it might be argued that the non-resonant path again becomes significant as the amplitude of the resonant waves will be very small and damped due to the high transmission loss of the wall, and, at such frequencies, the wall would be more like an infinite plate, meeting the mass law criteria [136].

For SEA purposes the forced wave transmission is given as a non-resonant coupling loss factor, η_{nr}, and is a function of the transmission coefficient of the wall, τ [119], given by,

$$\tau = \frac{\Pi_{trans}}{\Pi_{incid}} = \Pi_{trans} \frac{4\rho c}{p^2 A_w} \qquad (7.32)$$

where A_w is the wall area, Π_{trans} is the transmitted sound power and Π_{incid} is the incident sound power, which equals $p^2 A_w / 4\rho c$. Substituting equation 7.5 into equation 7.4 to obtain Π_{trans} and rearranging the equation in terms of η_{nr} gives:

$$\eta_{nr} = \frac{A_w c}{4 \omega V_1} \tau \qquad (7.33)$$

Where, V_1 is the volume of the source room, and τ for normal incidence, τ_n, is given by equation 2.5:

$$\tau_n = \left[1 + \left[\frac{\omega m}{2 \rho c}\right]^2\right]^{-1} \qquad (7.34)$$

For coupling between two rooms Crocker [138] assumes a random incidence mass law transmission, τ_r, where:

$$\tau_r = 0.23 \, \tau_n \left[10 \log\left(\frac{1}{\tau_n}\right)\right] \qquad (7.35)$$

For this study the field incidence transmission coefficient, τ_f, is used for the non-resonant path, so as to ensure continuity with the same assumption in chapters 5 and 6 [136] where,

$$\tau_f = \tau_n \, 10^{0.5} \qquad (7.36)$$

The non-resonant path between two rooms, separated by a single wall, is shown schematically by the dashed line in figure 7.3, and other figures. The energy balance matrix for the single wall between two rooms, including the non-resonant path, is given as:

$$\begin{bmatrix} \eta_{21} + \eta_{23} + \eta_2 & -\eta_{32} \\ -\eta_{23} & \eta_{31} + \eta_{32} + \eta_3 \end{bmatrix} \begin{bmatrix} E_2/E_1 \\ E_3/E_1 \end{bmatrix} = \begin{bmatrix} \eta_{12} \\ \eta_{13} \end{bmatrix} \quad (7.37)$$

A solution for the resonant path only has already been given in equation 7.28. For the non-resonant path only the energy ratio is given by:

$$\frac{E_1}{E_3} = \frac{\eta_{31} + \eta_3}{\eta_{13}} \quad (7.38)$$

The combined effect of the resonant and non-resonant paths is given as the addition of two energies [139] where,

$$\left[\frac{E_3}{E_1}\right]_{\text{total}} = \left[\frac{E_3}{E_1}\right]_{\text{resonant}} + \left[\frac{E_3}{E_1}\right]_{\text{non-resonant}} \quad (7.39)$$

The ratio for both paths is thus given as:

$$\frac{E_1}{E_3} = \frac{[\eta_{21} + \eta_{23} + \eta_2][\eta_{31} + \eta_{32} + \eta_3] - \eta_{23}\eta_{32}}{[\eta_{21} + \eta_{23} + \eta_2]\eta_{13} + \eta_{12}\eta_{23}} \quad (7.40)$$

Figures 7.7, 7.8 and 7.9 also show the predicted transmission loss for the three single walls where a 'non-resonant only' path is allowed. As this is directly a function of mass law, it produces a straight line rising at 6 dB/octave. A combined prediction of both resonant and non-resonant paths is also shown, termed the 'all paths' model.

In figure 7.7, at mid and high frequencies, the 'non-resonant only' path does not influence the 'all paths' prediction, except at the very high frequencies, where it is within 10 dB of the 'resonant only' path. At low frequencies, the non-resonant path clearly fits much more closely with measurement than the 'resonant only' path and dominates the 'all paths' transmission loss. The agreement in this region is much

improved and the overall prediction is within 2 - 3 dB, except about coincidence. For the 1/4 scale wall in figure 7.8, above f_c, the 'all paths' prediction agrees with measurement within 1 dB up to 8 kHz. Non-resonant transmission is again seen to improve agreement at frequencies around 400 Hz. Figure 7.9 shows the 'all paths' prediction is generally within 1 - 2 dB except at the extreme frequencies and about f_c. The non-resonant path improves agreement between measurement and prediction, compared with the 'resonant only' path by approximately 2 dB at low frequencies.

In summary, good prediction of the transmission loss for single isotropic walls is given using the SEA approach. This is improved particularly in the lower frequency regions by the inclusion of the non-resonant transmission path. From here we can now consider the inclusion of orthotropicity in the SEA approach.

7.5 FIN WALLS

In chapter 5 the effect of the orthotropicity of fin walls was theoretically modelled by adaptation of existing single wall theory. A second bending stiffness is included which accounts for the stiffness along the rib and produces a lower critical frequency, $f_{c,l}$. The upper critical frequency, $f_{c,u}$, is determined by the bending stiffness across the ribs and is the same as that of the single isotropic wall. The transmission loss between these two critical frequencies is obtained by interpolation and produces a plateau region whose length is determined by $f_{c,l}$. This orthotropicity influences the surface radiation character of the wall and chapter 5 proposed ways of recalculating the radiation efficiency to account for this (see figure 5.22). Using equations 5.19 and 7.8 these are converted to radiation loss factors and included in an SEA approach so that their effect on the overall airborne transmission loss can now be predicted and compared with measurement.

Before applying these changes to the radiation loss factor let us place it in context of other loss factors. Figure 7.10 shows the predicted and assumed loss factors for the 1:8 scale single wall. Many of the coupling loss factors are seen to overlap as the source and receiver rooms dimensions are almost identical. It is seen that the largest loss factors are the internal loss factors of the wall η_2, and room, η_3, and the radiation loss factors η_{21} and η_{23}. The non-resonant coupling loss factors, η_{13} and η_{31}, are influential at low frequencies, becoming less important with increased frequency, as is seen in the transmission loss results. Radiation coupling loss factors exhibit a peak at coincidence, while those from the wall to the rooms, η_{21} and η_{23}, become increasingly larger than those from the rooms to the walls, η_{12} and η_{32}, as the modal density ratio n_w/n_r becomes smaller (see equation 7.10).

The SEA prediction for the fin wall assumes the wall to be a single wall but with an orthotropic radiation loss factor. Hence, the SEA energy balance matrix is the same as for the single wall, including both non-resonant and resonant paths, given by equation 7.37.

The proposed design curves for an orthotropic radiation resistance were fully described in Chapter 5 (section 5.6.1) and for ease of discussion these are briefly restated here.

i) to assume that the orthotropic radiation resistance, R_{ort}, is the same as an isotropic single wall, or

ii) as i) including an increased perimeter length for stiffened plates, or

iii) to combine the radiation resistances of the two bending stiffnesses according to parallel circuit theory (equations 5.20 and 5.21), or

iv) to calculate the geometric mean of the two radiation resistances (equation 5.22), or

v) to interpolate the radiation resistance between $f_{c,l}$ and $f_{c,u}$, and assume a unity radiation efficiency above $f_{c,u}$ (equation 5.23).

Transmission loss predictions are first compared with the measurements of the 1:8 scale 7 rib fin wall, using the intensity method. Then with the 1:4 scale fin wall, and 1, 3 and 7 rib 1:8 scale fin walls, measured using the ISO 140/3 method. Let us examine the five proposals:

i) Figure 7.11 includes no orthotropic behaviour and predicts the fin wall as an isotropic single wall. The lower curve assumes the surface density is that of the single wall and the upper curve assumes an equivalent surface density, which includes the additional mass of the fins. Both curves give poor agreement with measurement. The transmission loss is over predicted sub-critically and under-predicted about $f_{c,u}$. In terms of radiation efficiency (see curve (i) figure 5.22) σ_{rad} produces too steep a slope below f_c and a peak greater than unity at $f_{c,u}$. The effect of the increased surface density is small at mid and high frequencies and greatest at low frequencies where the non-resonant path is influential.

ii) Figure 7.12 shows the prediction where the radiation loss factor is assumed to have an isotropic surface radiation but includes Maidanik's [115] perimeter effect for stiffened plates. The effect is only sub-critical as above $f_{c,u}$ the wall's radiation efficiency tends towards unity, and is not determined by the perimeter length. Figure 5.22, curve ii) shows that this increase in perimeter length dramatically increases the radiation efficiency below $f_{c,u}$. The result in figure 7.12 is to under-predict the transmission loss by 5 - 10 dB. There is still a significant dip at $f_{c,u}$ as the theory is designed for isotropic stiffened plates rather than orthotropic plates. The inclusion of an equivalent mass would increase the transmission loss by the same 1 - 2 dB, as found in figure 7.11, but does not improve agreement significantly.

iii) & iv) Figure 7.13 predicts the transmission loss using parallel circuit theory and a geometric mean to combine the radiation resistances. For the parallel circuit approach the radiation efficiency obtained is actually slightly steeper than that for the isotropic case i) below $f_{c,u}$ (see curve iii) figure 5.22). Above $f_{c,u}$ the radiation efficiency is assumed to return to unity. A distance of one 1/1 octave was chosen where R_{ort} is interpolated after $f_{c,u}$ from equation 5.20 to 5.21 so that no step in the transmission loss is produced. The prediction gives good agreement with measurement at and above $f_{c,u}$, but does not plateau below $f_{c,u}$ to account for the orthotropicity.

R_{ort} calculated by taking the geometric mean of the radiation resistances, iv), is shown in figure 5.22. It follows Maidanik's perimeter effect at low frequencies but gives emphasis to both $f_{c,l}$ and $f_{c,u}$ where peaks are seen. In figure 7.13 the overall prediction under-estimates the transmission loss at all but the highest frequencies; emphasising both critical frequencies.

v) Up to this point no prediction fits well over the whole frequency range. The best agreement is given by the parallel circuit approach, but this still does not agree particularly well with measurement below $f_{c,l}$. None of the approaches could produce a plateau between $f_{c,l}$ and $f_{c,u}$. Therefore proposal v) interpolates the radiation resistance in the region between the two critical frequencies to give a logarithmic straight line, as shown in figure 5.22. This is a similar approach to that used for the transmission loss of fin walls described in chapter 5. Above $f_{c,u}$ a unit radiation efficiency is assumed.

Figure 7.14 shows agreement to be improved at all but the lowest and highest frequencies, generally within 1-2 dB of measurement. Measurements above 12 kHz were obtained using a non-standard 3mm intensity probe spacer, and must be treated with caution. In figure 7.15, results for the 1:4 scale fin wall give a similarly

good fit over the whole frequency range. Using the same prediction, figure 7.16 shows the difference between measurement and prediction for the 1, 3 & 7 rib 1: 8 walls measured using the ISO 140 method. Prediction is best for the 7 rib case which varies about measurement by ± 2 dB. For the 1 and 3 rib cases measurement is slightly less than prediction by 1 - 4 dB below 1kHz, which is due to flanking transmission reducing the measured transmission loss.

From these results for the fin walls it was decided that the interpolated radiation resistance approach, proposal v), would be used for all future predictions to account for the orthotropicity in the transmission loss measurements.

7.5.1 Heavyweight Walls

It remains to consider the radiation characteristics of diaphragm walls. The masonry diaphragm wall is an orthotropic heavyweight wall, but it may be that its orthotropic nature is not particularly distinguishable in a measured transmission loss curve compared with that of an isotropic wall of similar mass. The critical frequency for heavyweight walls made of masonry or concrete lies between 150 and 300 Hz, therefore the region $f < f_c$ is relatively small but nevertheless important as it is the region of poorest sound insulation. As the lower limits of a reliable measurement range are around 100 Hz and such heavyweight constructions are highly damped, transmission loss curves rarely produce a strong dip at critical frequencies and are preceded often by a fairly flat curve.

Wilson [52] produces a radiation resistance for a single isotropic masonry wall, based on work by Wallace [148], finding good agreement between measured and predicted transmission loss about and below f_c. Wallace derived radiation resistance expressions for natural modes shapes at low frequencies. A particular mode occurs when it is excited at its natural resonance frequency, but a surface can theoretically

be forced into any particular mode shape and vibrated at any frequency, and hence a radiation efficiency curve can be produced for an individual mode as a function of frequency.

Wallace gives asymptotic solutions to calculate the σ_{rad} curves for any mode, at frequencies well below f_c. This is extended by numerical integration producing a coincidence region with an asymptote of unity. Wilson assumes only the 1/1 mode dominates below critical frequency and calculations were for a square wall. Using the parallel circuit analogy between this mode, and a unity line, good agreement was found with measurement. The author admits some unease with this approach, as it is not clear why a 1/1 mode should be chosen over any other mode value. Wallace shows each mode has a different shape, but distinctive transition regions are lost with a wide band approximation. Generally the higher the mode number the steeper the gradient of σ_{rad} below f_c.

An approximation according to Wallace is given in figure 7.17, for the 1:8 scale 7 rib fin wall. The parallel circuit analogy is used to calculate the total radiation efficiency of the total number of modes whose natural frequencies are below $f_{c,u}$. The expressions for all mode combinations (odd and even) are given by Wallace. For the 1:8 scale walls this is 140 modes, and for a typical full scale diaphragm wall, this is 35 modes where f_c = 270 Hz. The curve fits well super-critically but falls to 10 dB below measurement at 400 Hz, although the shape of the predicted curve exhibits no change at critical frequency. Also shown is the simple devise of constructing a straight horizontal line below $f_{c,u}$ for the predicted transmission loss which fits reasonably well with measurement in all cases and was used originally by Gibbs [17], but has no analytical basis.

Now that the SEA approach has been shown to predict the transmission loss of the single and fin walls sufficiently well and an orthotropic radiation loss factor has been assigned, we can now predict the transmission loss of the diaphragm wall.

7.6 DIAPHRAGM WALLS

The first concern with any SEA model is to specify how the physical test object should be defined in terms of sub-systems, to which there is usually no single answer and is more difficult as the test object becomes complicated. Hence, it is necessary to consider what sub-systems must be defined to model the vibrational and radiation characteristics of the diaphragm wall with sufficient accuracy.

7.6.1 System Definition

Consider figure 7.18 which shows a cross-section through the diaphragm wall. Due to the repeatability of the structure it can be thought of as a series of connected I-sections. The wall could also be thought of as a series of hollow box sections but this would necessitate the cross-rib being split along its axis introducing difficulties in sub-system definition. The net energy flow across the leaves at a junction between any two I-sections is assumed to be zero. The transfer of energy through the wall, between leaves, is principally via two direct paths, over the cross-rib and across the cavity.

When we are only concerned with the internal energy transfer between the leaves, one I-section is taken to describe the whole wall. Hence the total transmission between the leaves is n times the transmission across one I-section, where n is the number of cross-ribs. Any change in wall dimensions can also be accounted for by one I-section. This I-section is separated into 7 sub-systems (see figure 7.18) where

2,3,7 and 8 are the leaf sub-systems, 5 is the cross-rib and 4 & 6 are each half of the air cavity.

When we are concerned with the transfer of energy into a room, the whole wall must be described as the modal density of radiating surface is a function of area. The complete SEA model is depicted in figure 7.19. As sub-systems 2 = 3, 4 = 6, and 7 = 8 these are simplified to 2, 4 and 7. The surfaces radiating into the rooms, based on the whole wall area, are denoted 2' and 7'. Sub-systems 1 and 9 are the source and receiver room sub-systems, respectively. By assuming an I-section the cavity is split into two sub-systems, but the modal density is taken to be that of the whole cavity. The total coupling loss factor from all the cross-ribs to the second leaf, $\eta_{57',T}$, is equal to $2n\eta_{57}$ where n is the number of cross-ribs.

The leaves of a diaphragm wall are of extremely large area (typically on sports hall between 100 - 400 m^2 per wall) and it might be questioned if such a large area could be defined as a single sub-system. If the wall flanked a series of rooms and was excited by one room, attenuation would occur over the area of the wall. Such a problem was thought unlikely as most diaphragm walls presently built, (and all those measured in chapter 8) are for sports centres or similar buildings where only one acoustic space faced the wall. For the inner leaf, the excitation of the room with loudspeakers was believed to produce a diffuse sound field of even energy distribution on the wall. While the large number of cross-ribs evenly spaced between leaves ensured an equal energy flow to the outer leaf. Any part of the wall is thus considered to be part of an infinite wall, with no energy flow between sections. The only disruption to this being at the corners which are analysed in chapter 8.

The transmission between the leaves was modelled in the following ways.

i) A 6 sub-system model, with the following sub-systems: source room, source wall, cross-ribs, cavities, receiver wall, receiver room. This includes both the cavities and cross-ribs as separate sub-systems. Figures 7.20 and 7.21 show the sub-system definition and the energy flow diagram, respectively. The energy balance equations are given below in matrix form.

$$\begin{bmatrix} \eta_{2'1} + 2n\eta_{25} + 2n\eta_{24} + \eta_2 & -2n\eta_{42} & -2n\eta_{52} & 0 & 0 \\ -2n\eta_{24} & 2n(\eta_{42} + \eta_{45} + \eta_{47} + \eta_{41} + \eta_{49} + \eta_4) & -2n\eta_{54} & -2n\eta_{74} & -2n\eta_{94} \\ -2n\eta_{25} & -2n\eta_{45} & n(2n\eta_{52} + 2n\eta_{54} + 2n\eta_{57} + \eta_5) & -2n\eta_{75} & 0 \\ 0 & -2n\eta_{47} & -2n\eta_{57} & \eta_{79} + 2n\eta_{74} + 2n\eta_{75} + \eta_7 & -\eta_{97} \\ 0 & -2n\eta_{49} & 0 & -\eta_{79} & 2n\eta_{94} + \eta_{97} + \eta_{91} + \eta_9 \end{bmatrix} \begin{bmatrix} E_2/E_1 \\ E_4/E_1 \\ E_5/E_1 \\ E_7/E_1 \\ E_9/E_1 \end{bmatrix} = \begin{bmatrix} \eta_{12'} \\ 2n\eta_{14} \\ 0 \\ 0 \\ \eta_{91} \end{bmatrix}$$

(7.41)

ii) A 5 sub-system model, with the following sub-systems: source room, source wall, cross-rib, receiver wall, receiver room. This model excludes the cavity and assumes the cross-rib to be a separate sub-system. Figures 7.22 and 7.23 show the sub-system definition and the energy flow diagram, respectively. The energy balance equations are given below:

$$\begin{bmatrix} 2n\eta_{25} + \eta_{2'1} + \eta_2 & -2n\eta_{52} & 0 & 0 \\ -2n\eta_{25} & n(2n\eta_{52} + 2n\eta_{57} + \eta_5) & -2n\eta_{75} & 0 \\ 0 & -2n\eta_{57} & 2n\eta_{75} + \eta_{79} + \eta_7 & -\eta_{97} \\ 0 & 0 & -\eta_{79} & \eta_{97} + \eta_9 + \eta_{91} \end{bmatrix} \begin{bmatrix} E_2/E_1 \\ E_5/E_1 \\ E_7/E_1 \\ E_9/E_1 \end{bmatrix} = \begin{bmatrix} \eta_{12'} \\ 0 \\ 0 \\ \eta_{19} \end{bmatrix}$$

(7.42)

iii) A 4 sub-system SEA model, with the following sub-systems: source room, source wall, receiver wall, receiver room. This model excludes the cavity and assumes the cross-rib not as a separate sub-system but rather as a direct coupling loss factor between the leaves. Figures 7.24 and 7.25 show the sub-system definition and the energy flow diagram, respectively. The energy balance equations are given below:

$$\begin{matrix} \eta_{2'1} + \eta_{2'7'} + \eta_{2'} & -\eta_{72'} & 0 & E_2/E_1 = \eta_{12'} \\ -\eta_{2'7'} & \eta_{72'} + \eta_{79} + \eta_{7'} & -\eta_{97'} & E_7/E_1 = 0 \\ 0 & -\eta_{79} & \eta_{97'} + \eta_9 + \eta_{91} & E_9/E_1 = \eta_{19} \end{matrix} \quad (7.43)$$

7.6.2 Influence of the Cavity

By comparing the 6 and 5 sub-system models the importance of the cavity is assessed.

Prediction using existing theory in chapter 6 has shown that reasonable agreement with measurement can be obtained by assuming the wall to be an orthotropic single wall of equivalent mass which indicates the cavity can be neglected. At mid-high frequencies an increasing vibrational level difference occurs between the leaves. This is due to the structure-borne transmission over the cross-rib and the air-borne transmission via the cavity. Equation 2.34 [37] estimated the ratio of the stud to air transmission coefficients between a line bridged double wall, which strongly suggested that, for a diaphragm construction, the cross-rib path will dominate, due to its large number of bridges and low critical frequency. This assumes a rigid non-resonant bridging which can only be applied in the low-mid frequencies for both cross-rib and cavity. At low frequencies the cavity acts more like a spring than a resonant air space and the degree to which the cavity resonates depends on whether modes can occur between surfaces. Cut-off frequencies can be defined depending on whether the space is resonant in one, two, or three cavity dimensions. The cavity

of a diaphragm wall is a long vertical air column closed at the top and bottom by a capping beam and foundation, respectively. A half wavelength will occur in the vertical axis at typically 20 Hz. The first half wavelength between the cross-ribs occurs at approximately 110 - 170 Hz and the cavity is resonant in all three dimensions between 400 - 800 Hz. By comparison a cavity wall will not resonate across the cavity until 1.7 - 3.15 kHz. The modal densities for one, two and three dimensional spaces are given in equations 7.12 - 7.14, and are included in the SEA prediction, with the appropriate cut-off frequencies. In table 10 dimensions and cut-off frequencies are given of all the air spaces, rooms and cavities encountered during the research. The laboratory test suite rooms act as three dimensional spaces, above 100 Hz and all the sports halls, above 20 Hz.

For the 6 sub-system model the internal loss factor of the cavity needs to be defined. For a traditional double wall cavity the internal loss factor is given by [137],

$$\eta_{cavity} = \frac{c S \bar{\alpha}}{V \pi \omega} \qquad f \leq f_d \qquad (7.44)$$

$$\eta_{cavity} = \frac{c S \bar{\alpha}}{V 4 \omega} \qquad f \geq f_d \qquad (7.45)$$

where $f_d = c/2d$ and d is the width of the cavity; V is the volume and $\bar{\alpha}$ is the angled averaged absorption coefficient. Equation 7.45 is the same as equation 7.15 (the loss factor for a room), except that the absorption area, S, is only for the edges of the cavity. Crocker & Price [120, 137] included edge absorption which reduced lateral resonances and aided replication to a theoretical infinite double wall. The internal loss factor of the cavity for diaphragm wall was predicted according to equation 7.45, including the total surface area and estimating $\bar{\alpha}$ for unplastered brickwork.

The inclusion of a cavity also increases the number of possible non-resonant transmission paths. If we consider an uncoupled double wall, the energy flow

diagram is given by figure 7.26. Sub-systems are denoted the same as the diaphragm wall. Non-resonant paths described by the coupling loss factors η_{14} and η_{49} were included by Crocker & Price [137]. Brekke [139] includes the path across the cavity, described by η_{27}, where $f < f_d$ and the air is non-resonant and stiffness controlled. Wilson [52] includes a two part expression for the coupling loss factor where $f < f_d$, and $f > f_d$ which includes cross-cavity resonances. A further non-resonant path described by η_{19}, occurs at very low frequencies below the mass-spring-mass frequency of the cavity, where the whole wall acts as a single wall. This will be below 50 Hz for normal masonry walls and 10 Hz for diaphragm walls. Thus the path has been omitted from the energy balance equations as it is outside of the frequency range of interest. Other combinations of non-resonant paths exist where the leaves are of different density or thickness, as noted by Wilson [52]. These paths also have been omitted here as the leaves of diaphragm walls are normally built with bricks of very similar density.

The energy balance equations for the double wall, including all non-resonant paths, are given as,

$$\begin{bmatrix} \eta_{21} + \eta_{24} + \eta_{27} + \eta_2 & -\eta_{42} & -\eta_{72} & 0 \\ -\eta_{24} & \eta_{41} + \eta_{42} + \eta_{47} + \eta_{49} + \eta_4 & -\eta_{74} & [-\eta_{94}] \\ -\eta_{27} & -\eta_{47} & \eta_{79} + \eta_{74} + \eta_{72} + \eta_7 & -\eta_{97} \\ 0 & -\eta_{49} & -\eta_{79} & \eta_{97} + \eta_{94} + \eta_{91} + \eta_9 \end{bmatrix} \begin{bmatrix} E_2/E_1 \\ E_4/E_1 \\ E_7/E_1 \\ E_9/E_1 \end{bmatrix} = \begin{bmatrix} \eta_{12} \\ \eta_{14} \\ 0 \\ \eta_{19} \end{bmatrix} \quad (7.46)$$

Figure 7.27 gives the measured and predicted transmission loss of the 0.06m cavity wall (see figure 4.25d). 'Resonant only', 'non-resonant only' and 'all paths' transmission are shown, f_c equals 2328 Hz. Prediction gives variable agreement with measurement over the frequency range. The resonant path significantly over-

predicts below approximately 0.5 f_c and under-predicts at f_c. Above f_c prediction is good but less so at high frequencies. Like the single wall case, the non-resonant path dominates prediction below 0.5 f_c but under-predicts, in this case, up to 1 kHz. The strong dip about f_c may be just due to coincidence or possibly its joint effect with the first cross-over frequency (2867 Hz). The all-path prediction gives reasonable agreement overall, varying between 1 - 5 dB. This is believed due to inaccuracies in predicting the cavity loss factor and questionable measurements at the high frequencies due to the measured intensity levels being very close to background levels in the receiver room.

Three estimates of loss factor, η_4, were considered for the cavities of the diaphragm wall. $\bar{\alpha}$ was estimated from brickwork absorption coefficients and the calculated values of η_4 fell between the extremes of 0 - 0.1 from high to low frequencies. Thus the three estimates were:

$\eta_4 = 0.1$ - as a low frequency approximation

$\eta_4 = 0$ - as a high frequency approximation

η_4 - estimated from typical values of $\bar{\alpha}$

Predictions of vibration level difference between leaves (figure 7.28) and airborne transmission loss (figure 7.29) were made for a typical diaphragm wall using the 6 sub-system analytical model compared with prediction using the 5 sub-system model, where the cavity is excluded.

Figures 7.28 and 7.29 show the level difference between the 5 and 6 sub-system predictions for three values of η_4. Positive values represent a lower, and negative a higher, value of vibration level difference or transmission loss due to the cavity. Where the cavity loss factor, η_4, equals zero, there is no loss of energy from the sub-system, thus all that has been introduced is an extra transmission path.

Therefore the energy level difference between leaves and transmission should be less than the 5 sub-system case, which is seen to be true in both figures. Where the cavity loss factor is non-zero, an increase in level difference occurs mainly at the higher frequencies as surface absorption becomes more influential. At the low frequencies the non-resonant path tends to dominate and there is little difference between the models. Figure 7.28 shows a difference of less than 1 dB up to 400 Hz for all values of η_4. For $\eta_4 = 0.1$, agreement is within 1 dB up to 400 Hz, before increasing to a maximum of 4.5 dB at 1600 Hz. For η_4, estimated from surface absorption, the discrepancy is a maximum of 2 dB at 4 kHz.

When considering transmission loss in figure 7.29, the effect of the cavity is more apparent. The discrepancy is about 2 dB for $\eta_4 = 0$. Where the estimated loss factor is included, the level difference is less than 2 dB up to 630 Hz and a maximum of 5 dB at 4 kHz. Between 125 - 400 Hz where the non-resonant path dominates the difference is almost zero. The extreme case, where $\eta_4 = 0.1$, yields a maximum discrepancy of 10 dB at 1250 Hz. However this case is unrealistic and can be discounted. The reduction at highest frequencies is caused by the non-resonant paths again influencing the overall value.

Assuming the internal loss factor from estimated absorption is the most likely case, the comparison suggests the exclusion of the cavity will be small over the low and mid frequencies. As will be seen in chapter 8, field measurement of full scale diaphragm walls became difficult above 1250 Hz, and the difference of including the cavity up to this frequency is 0.5 dB in vibration level difference. The suggests that over the low and mid-frequencies the dominant path is that of the cross-rib, but at high frequencies energy loss due to the cavity will become more important.

It was decided that the 5 sub-system model would be sufficient to predict the diaphragm wall unless prediction with measurement was very poor or was required

to higher frequencies. All SEA parameters and energy balance equations have been established and predictions of energy level differences are now compared with measurement.

7.6.3 Vibration Level Difference between Leaves

All the SEA predictions use the 5 sub-system power flow model and assume angle averaged bending only transmission at junctions. The prediction of the vibration level difference between leaves is shown in figure 7.30 for a typical diaphragm wall. Here the 4, 5 and 6 sub-system models are shown. For the former case the cross-rib is a transmission path, defined by the coupling loss factor, η_{27}, where resonances are allowed. For the latter cases the cross-rib is assumed resonant and there are two coupling loss factors, η_{25} and η_{57}. The three curves are in close agreement and rise with frequency from 0.4 dB at 50 Hz to approximately 1.2 dB at 800 Hz. Above 800 Hz the 4 sub-system model dips close to zero at 1.6 - 2 kHz, which corresponds to the first $\lambda_b/2$ resonance across the cross-rib before rising again toward the 5 sub-system prediction. The 6 sub-system prediction rises to 1.7 dB above the 5 sub-system prediction at 4 kHz.

Measured and predicted vibration level differences between leaves for the 1:8 and 1:4 scale 7 rib walls using the 5 and 4 sub-system models are shown in figures 7.31 and 7.32, respectively. There is little difference between the predictions, but the measured values rise above the predictions by between 3 - 6 dB at 1250 Hz. The first cross-rib resonance occurs at 635 Hz and 582 Hz for the 1:8 and 1:4 scale walls respectively, which matches the dip in the 1:4 scale wall. Agreement is better between prediction and in-situ measurements of four full size diaphragm walls shown in figure 7.33. At low and mid frequencies agreement is within ± 3 dB. Above 800 Hz discrepancies increase with frequency. The agreement at high

frequencies would not have been improved significantly by including the cavity until the highest measured octave.

One possible reason why prediction is lower than measurement at the highest frequencies is that, when measuring the source side acceleration of a wall the accelerometer might begin to act like a microphone due to the high signal levels. This would produce a higher source side acceleration and hence a larger measured vibration level difference between the leaves. It should be emphasised that no evidence is given for this except if we consider figure 7.34. This shows the measured and predicted vibration level difference between the leaves of the free-standing post-tensioned wall, where an impact source is used, hence excluding this effect. The measured values are produced by taking the frequency response between accelerations levels on either leaf. Agreement is seen to be very good between the curves, within 0.5 dB. Measurement rises from 0 - 1.5 dB at 1600 Hz and there is no sign of resonances or a more rapid increase at higher frequencies.

Overall, the results show that prediction gives reasonable agreement with measurement at low frequencies, and less so at the highest frequencies. Comparison with measurement of full scale walls gives better agreement over most of the frequency range. Details and statistical analysis of the measured vibration level differences are described in chapter 8.

7.6.4 Prediction of Transmission Loss

Predicted values of transmission loss are presented using the 5 and 4 sub-system models and existing theory given in chapter 6. The latter assumes the diaphragm wall to be an orthotropic single wall. At frequencies where the vibration level difference between the leaves is close to zero an equivalent mass is assumed based

on both leaves and the cross-ribs. At higher frequencies the equivalent mass is that of the two leaves and a measured vibration level difference is added.

Before comparing prediction and measurement, it is interesting to note the predicted modal energy drops between two rooms across a diaphragm wall, shown in figure 7.35 at 100 Hz and 1 kHz. (The 100 Hz curves are shifted down 50 dB). Curves show the modal energies in each room and on each leaf of the diaphragm wall. The modal energy drop between the leaves is almost identical which ever analytical model is used, as was seen in figure 7.30 up to 1.6 kHz. Yet the drop in modal energy between source and receiver rooms is different for each case. This occurs because of a difference in the drop between the source room and the first leaf, which is largest with the 4 sub-system model and which does not vary significantly if the loss factor is included for the cross-rib (even though it is not a sub-system). This difference in predicted transmission loss from 5 sub-system model is 8 dB at 1 kHz and 6 dB at 100 Hz. The 6 sub-system model agrees closer, within 3 dB at 1 kHz and 1 dB at 100 Hz.

Hence each analytical model will produce a similar vibration level difference between the leaves but a different room to room transmission loss, particularly in the case of the 4 sub-system model. As the 6 sub-system model has already been put aside to simplify the analysis we shall compare the 4 and 5 sub-system models in figures 7.36 and 7.37. These show results for the 1:8 and 1:4 scale diaphragm walls, respectively. For the former, the 5 sub-system model agrees best with measurement being within 1 - 2 dB above $f_{c,u}$ and below 1 kHz, and in the plateau region agreement is at worst 3 dB. The existing theory predicts only as well as the 5 sub-system model below 1 kHz and between $f_{c,u}$ and 6300 Hz. Overall it over-predicts by between 1 - 5 dB. The 4 sub-system SEA prediction is approximately 5 dB below measurement above $f_{c,u}$ and overall under-predicts.

In the case of the 1:4 scale wall all predictions exceed measurement by between 2 - 5 dB, except at the highest frequencies. As it is impossible to check the validity of the diaphragm measurements by Ma [19] this discrepancy cannot be satisfactorily explained. The relationship between the three prediction curves is like that of the 1:8 scale wall. The 4 sub-system model predicts between 2 - 6 dB lower than the 5 sub-system model.

Up to this point the author would argue the 5 sub-system model satisfactorily predicts the single, and fin walls. To confirm this for the diaphragm wall it was necessary to attempt to measure a series of full scale diaphragm walls. Although some in-situ measurements have already been shown in chapter 6 a full description will be given in chapter 8, so as to explain the method of measurement and show the statistical analysis of the results obtained.

7.6.5 Non-resonant Transmission

It is interesting to assess the influence of the non-resonant path, described by the coupling loss factor, η_{19}, on the total airborne transmission loss of a diaphragm wall. Using the 5 sub-system model, the difference in transmission loss is predicted with and without this path. Figure 7.38 shows results for the 1:8 scale and 1:4 scale walls and two in-situ full size walls. The frequency axis is shifted for the scaled walls to match the full size walls, and the ordinate is the level difference between the prediction with and without the non-resonant path.

At low frequencies the non-resonant path 'pulls down' the transmission loss of the diaphragm wall. Over mid and high frequencies the effect of the path is less than 1 dB and at high frequencies it again influences the overall transmission loss, but to a lesser degree. Whether a non-resonant path should be allowed to continue over the whole frequency range is questionable, but when the leaves begin to act separately

the wall clearly cannot be described in terms of a single wall and therefore the direct non-resonant path between the rooms is inapplicable.

7.7 CONCLUDING REMARKS

Overall the SEA approach has provided a useful tool for examining the diaphragm wall. Predictions of level differences and transmission loss for single and fin walls have been successfully modelled.

Orthotropicity has been included in the radiation loss factor to produce a plateau region between the upper and lower critical frequencies, and the influence of the cavity as a significant transmission path has been shown to be small compared with the structure-borne cross-rib path up to roughly 1250 Hz. As will be seen in chapter 8 the field measurements were generally limited to this frequency range and because one of the aims of the work was to produce as simple a predictive model as necessary to adequately characterise the diaphragm wall, the 6 sub-system model was discounted from further analysis.

Prediction of vibration level difference between the leaves significantly under-estimated measurement at all but the low frequencies for the scale walls. Better agreement was found for the full scale walls and particularly for the free-standing wall. Scale walls measurements of transmission loss were not felt enough to validate the prediction, so it was decided to compare prediction with further field measurements. Due to the difficulties involved in this, the method of measurement will first be discussed in chapter 8.

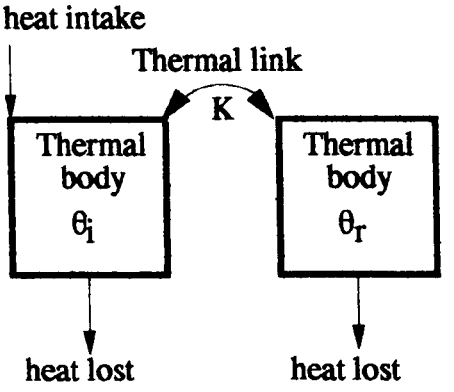

Figure 7.1: Heat flow model

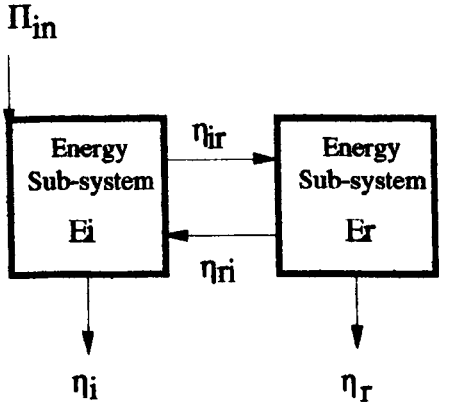

Figure 7.2: 2 Sub-system universal SEA model

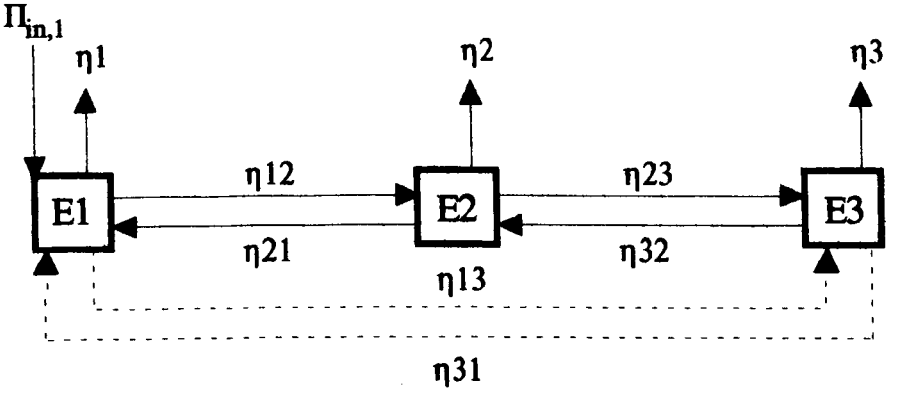

Figure 7.3: 3 sub-system energy flow for a single wall

E1 = source room E2 = wall E3 = receiver room

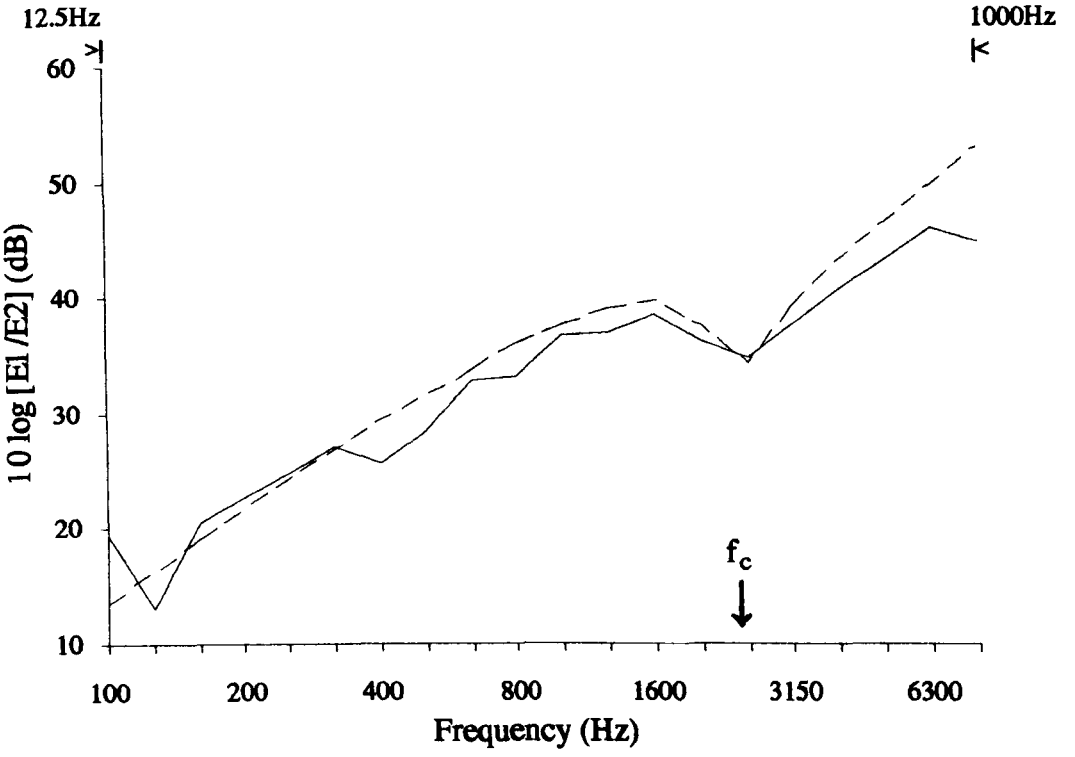

Figure 7.4: Energy level difference between source room and wall

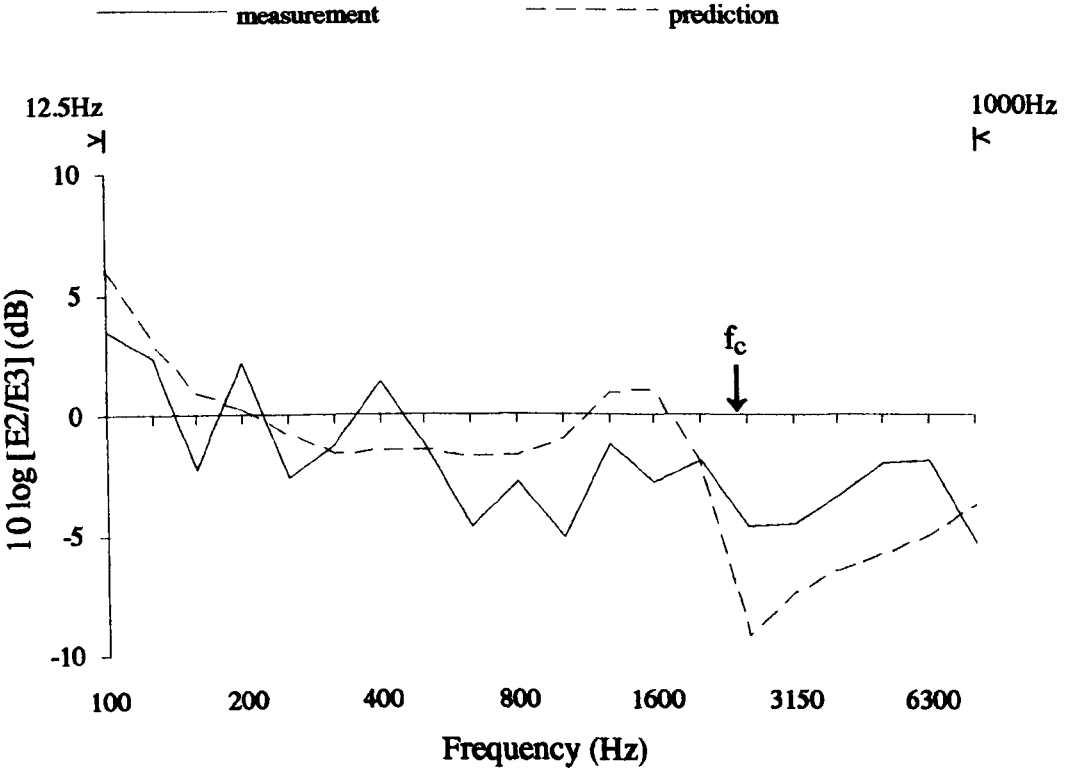

Figure 7.5: Energy level difference between wall and receiver room

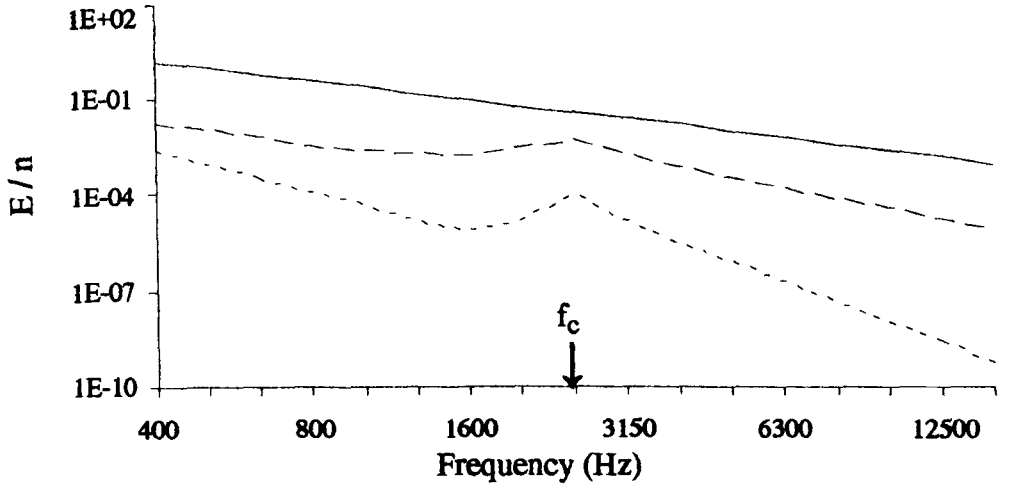

Figure 7.6: Predicted modal energies for the 1:8 scale single wall

source room wall receiver room

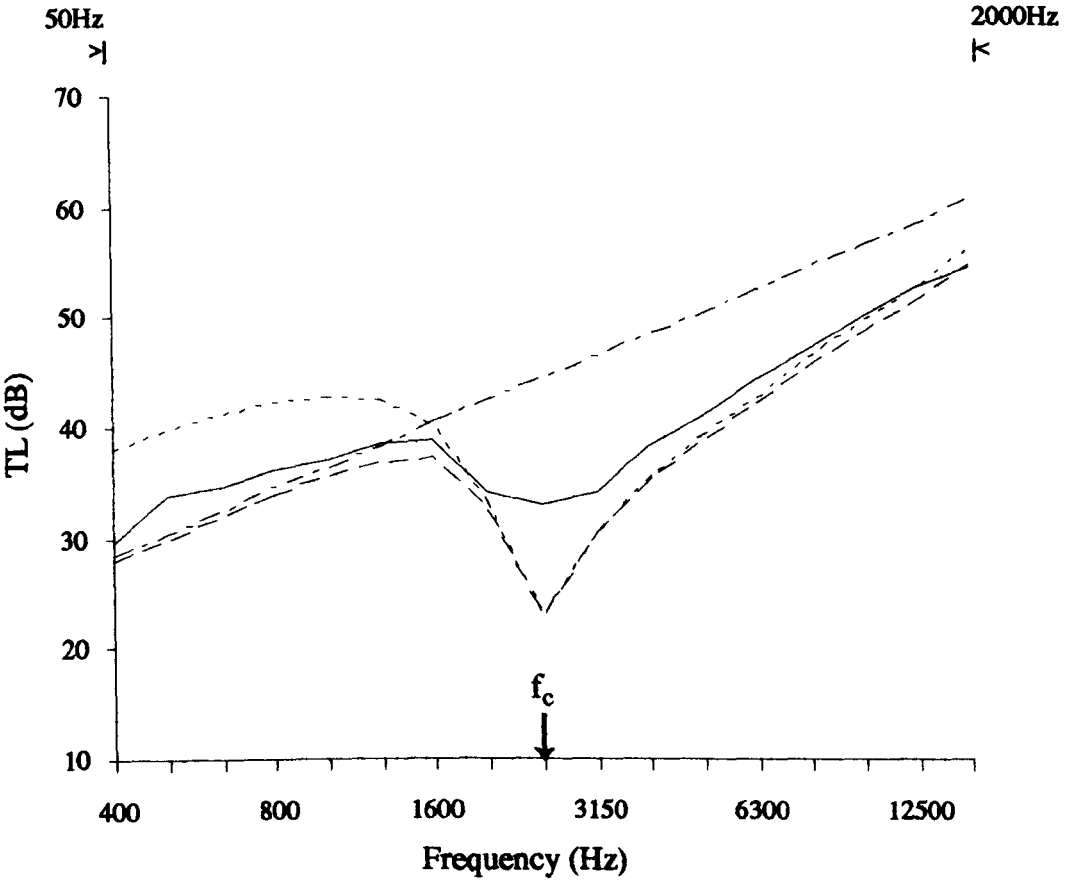

Figure 7.7: Transmission loss of 1:8 scale single wall

measurement prediction:

'all' paths

'resonant only' path

'non-resonant only' path

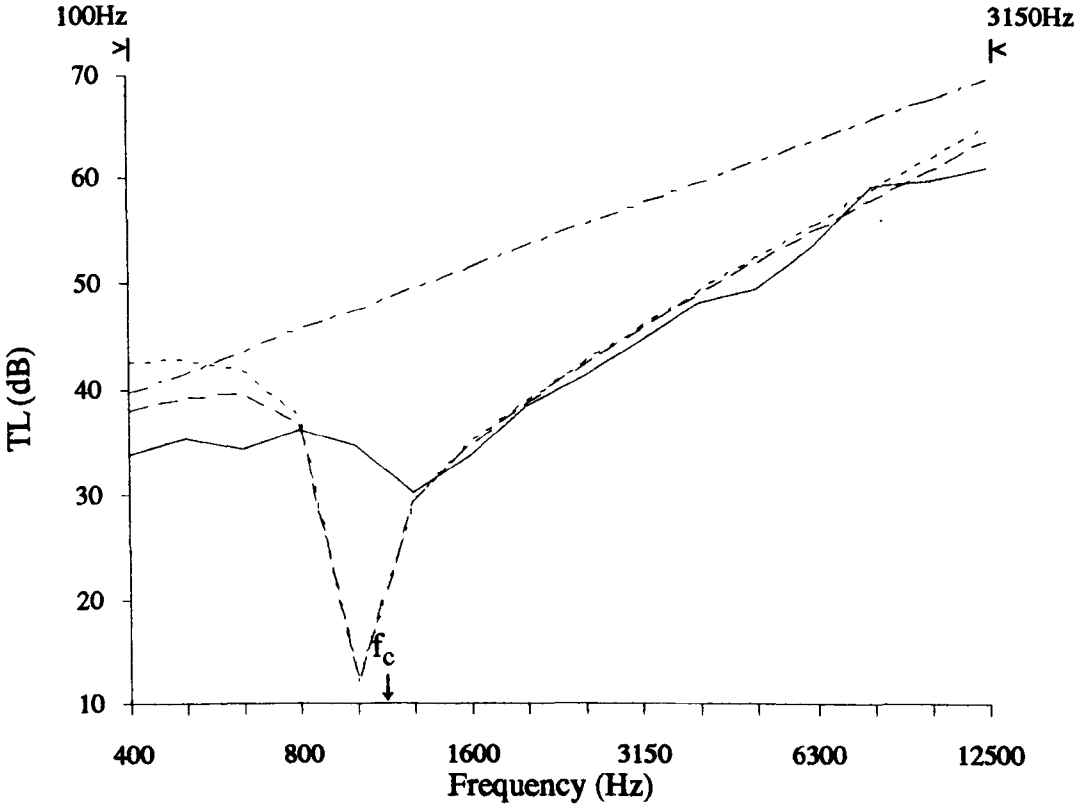

Figure 7.8: Transmission loss of 1/4 scale single wall

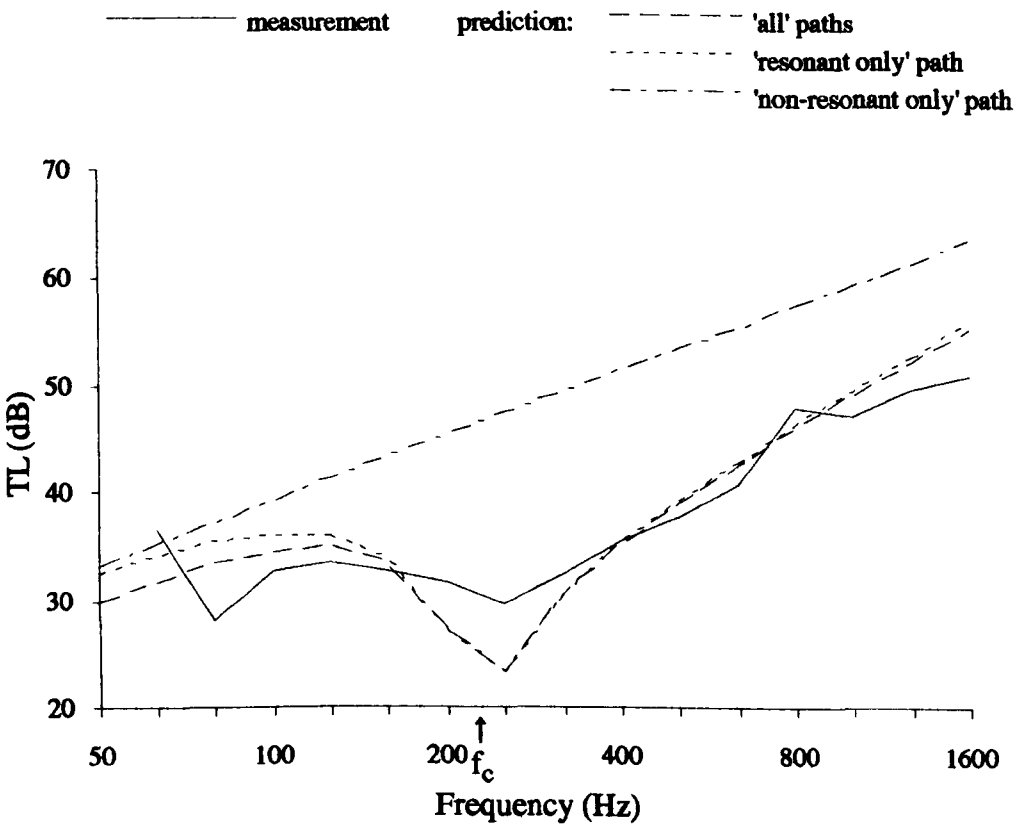

Figure 7.9: Transmission loss of the large transmission suite single wall

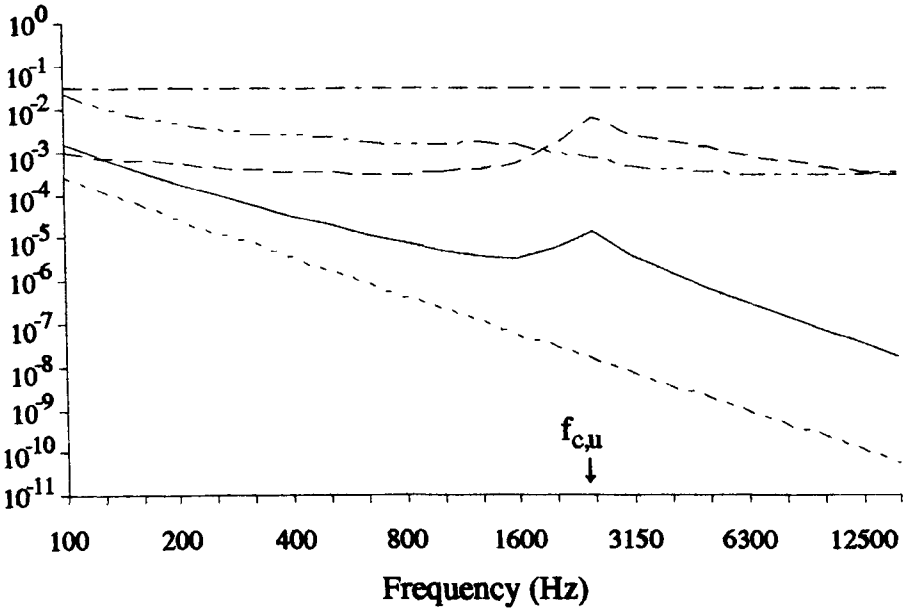

Figure 7.10: Predicted loss factors

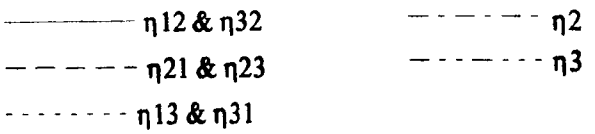

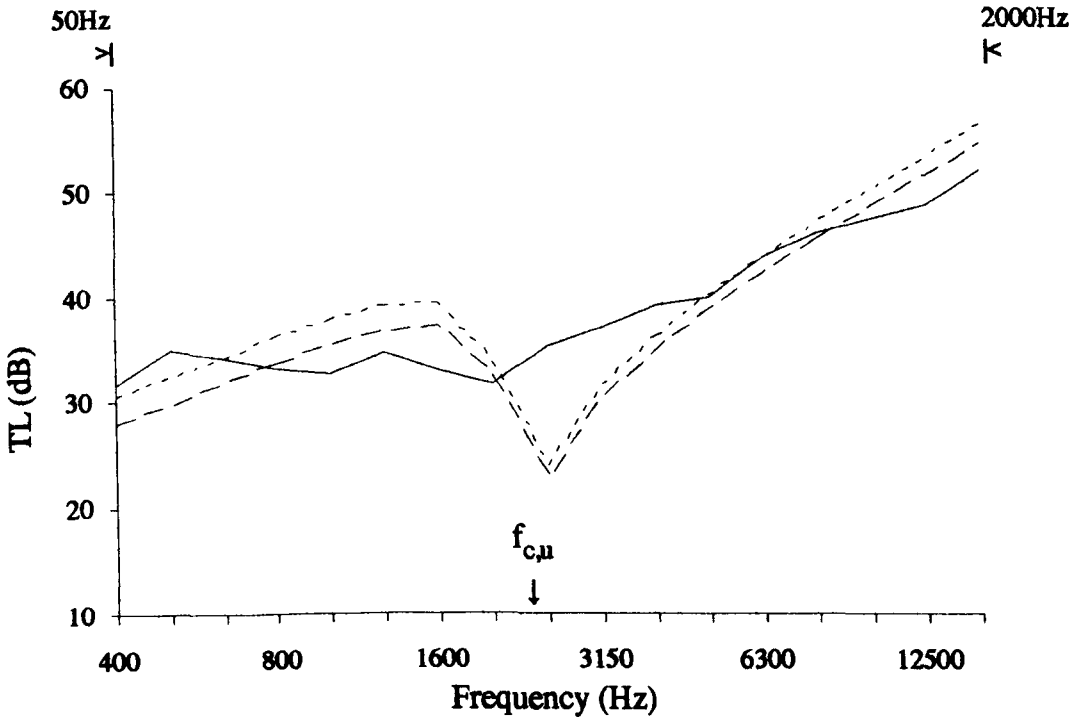

Figure 7.11: Transmission loss of 7 rib fin wall
- assuming an isotropic radiation resistance (i)

measurement

prediction: (i)

prediction: (i) plus the equivalent mass of the whole wall

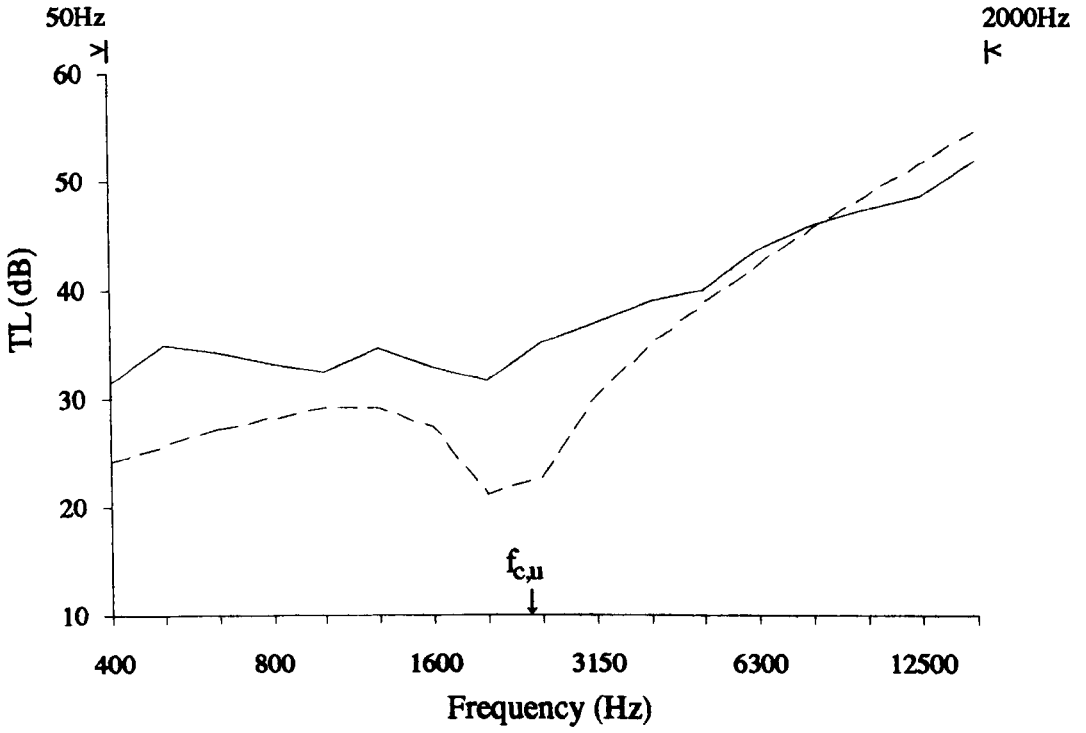

Figure 7.12: Transmission loss of 7 rib fin wall
- assumes a stiffened isotropic radiation resistance (ii)

measurement prediction: (ii)

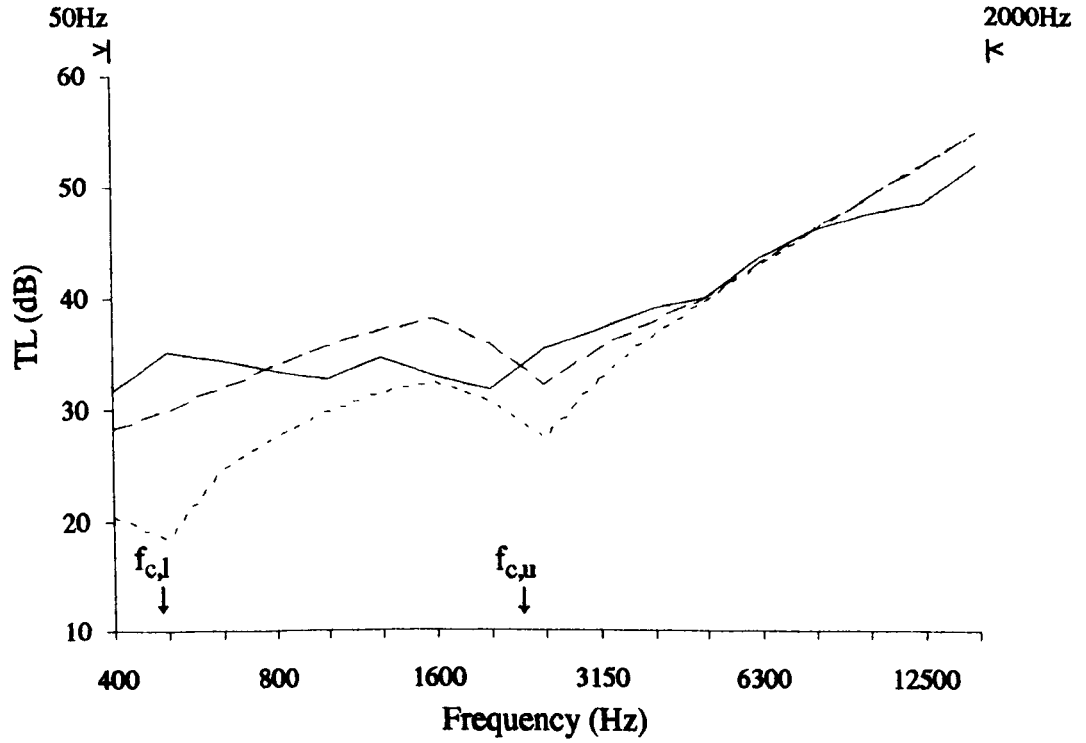

Figure 7.13: Transmission loss of 7 rib fin wall
- calculates an orthotropic radiation resistance (iii) & (iv)

measurement prediction: (iii) prediction: (iv)

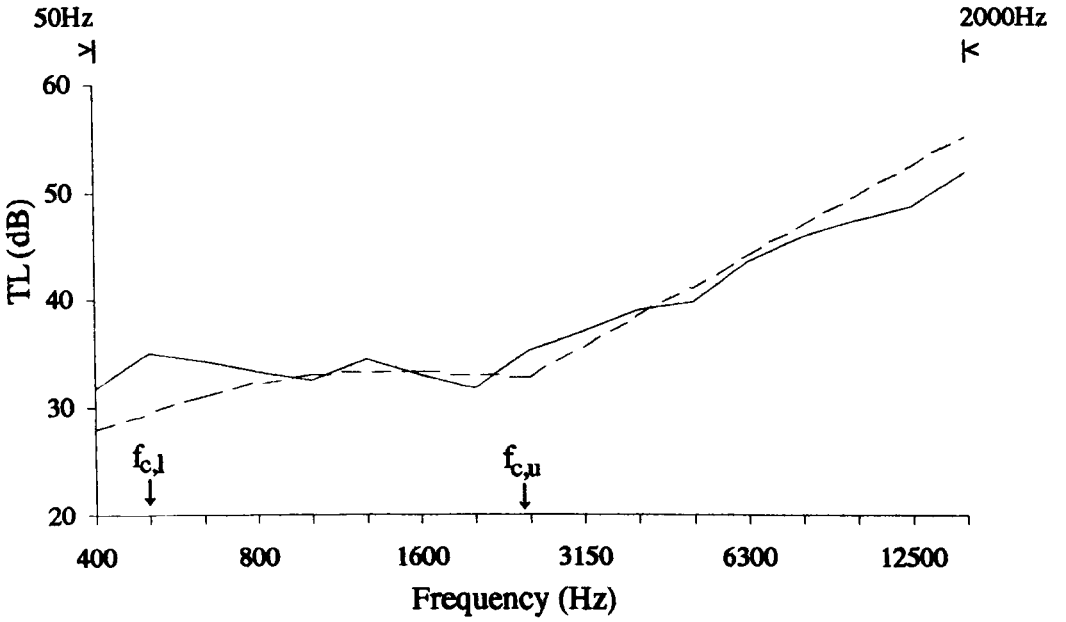

Figure 7.14: Transmission loss of 7 rib fin wall
- calculates an orthotropic radiation resistance (v)

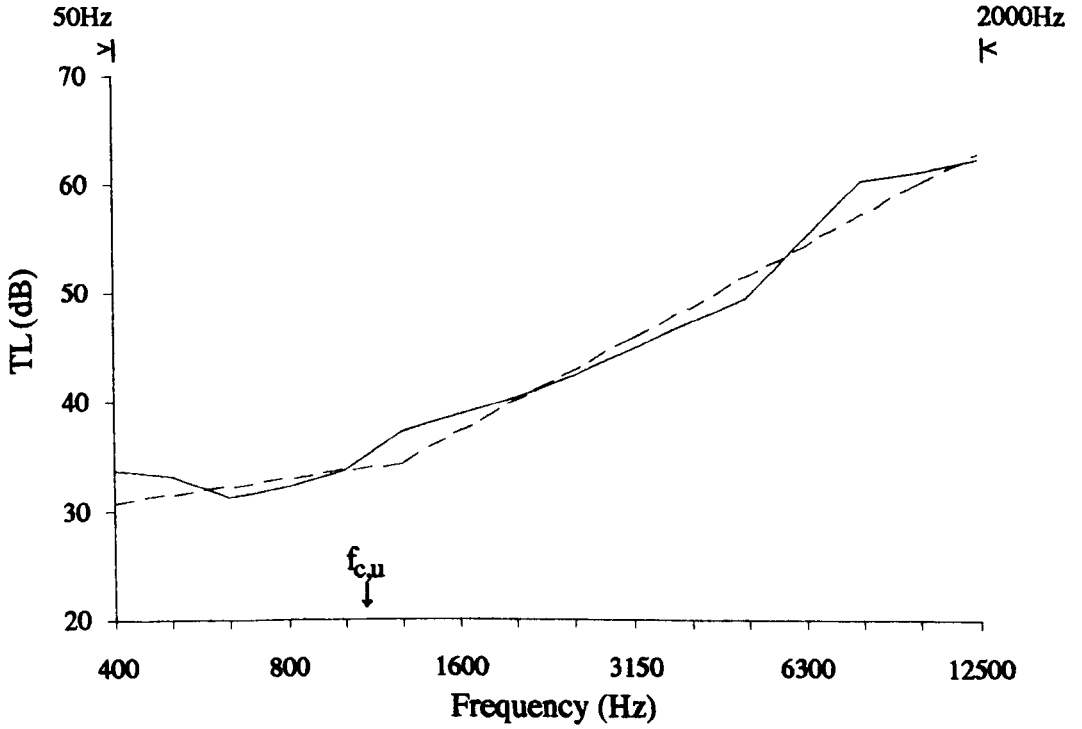

Figure 7.15: Transmission loss of 1/4 scale fin wall

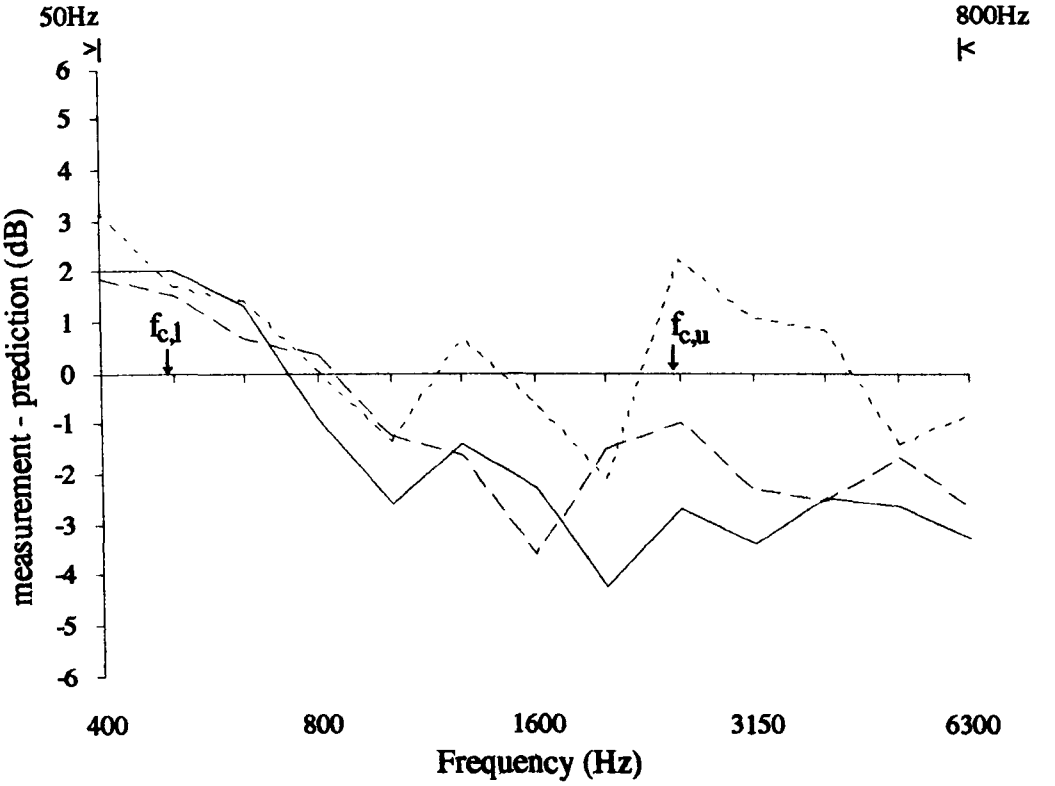

Figure 7.16: Difference in transmission loss between prediction and pressure measurements

——— 1 rib – – – – 3 rib ····· 7 rib

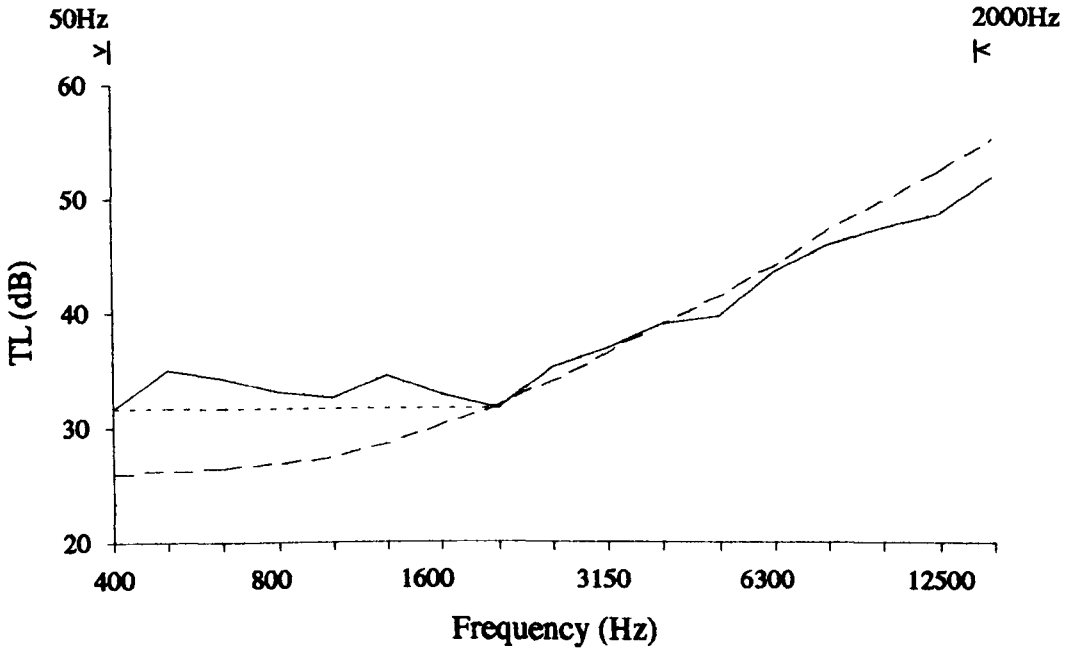

Figure 7.17: Transmission loss of 7 rib 1:8 scale fin wall

——— measurement – – – – – prediction: Wallace curves

····· simple prediction with horizontal line

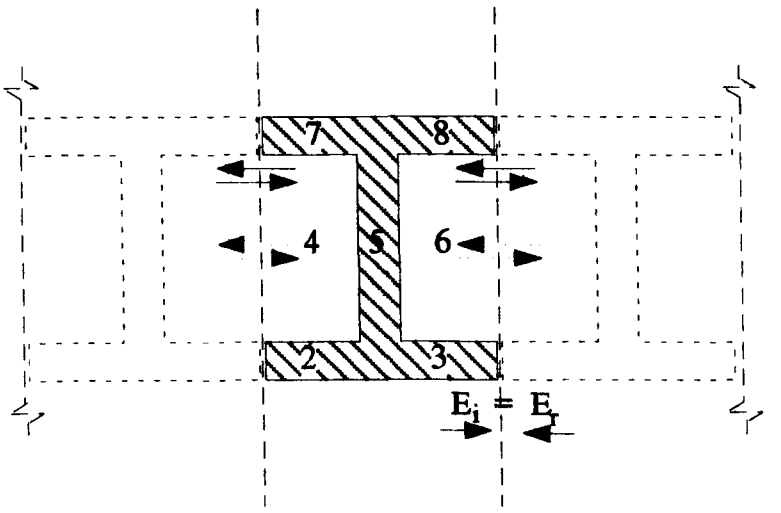

Figure7.18: Energy transfer a diaphragm wall

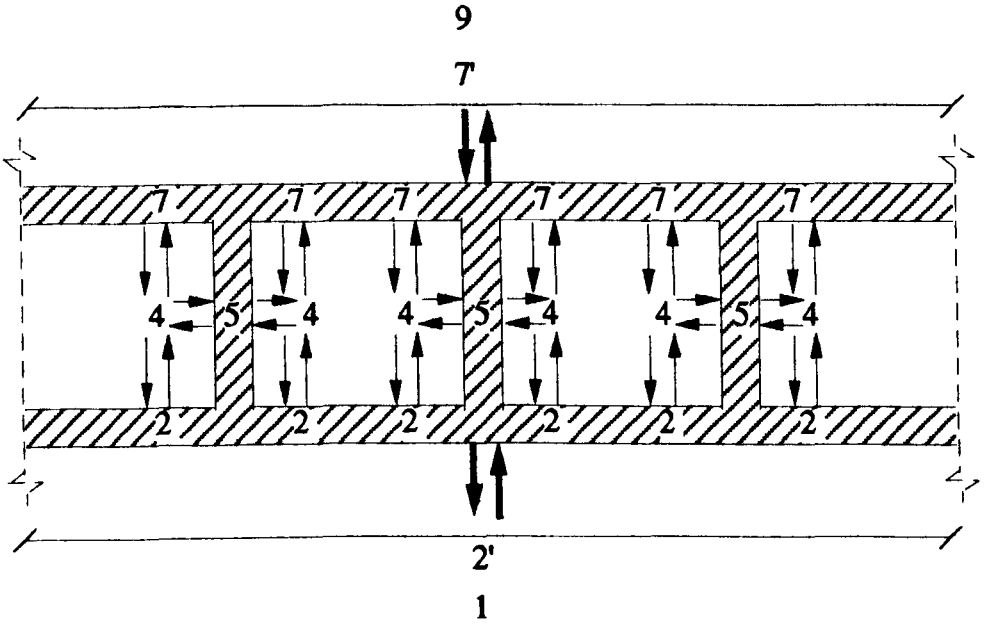

Figure 7.19: Complete SEA sub-system definition

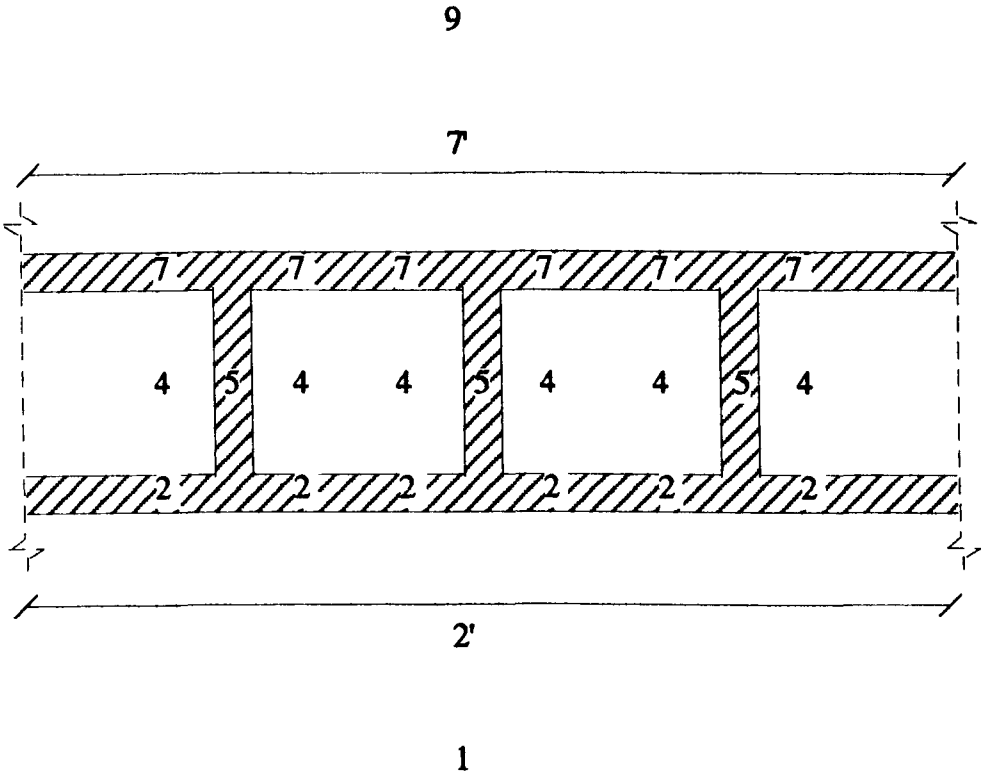

Figure 7.20: 6 sub-system model

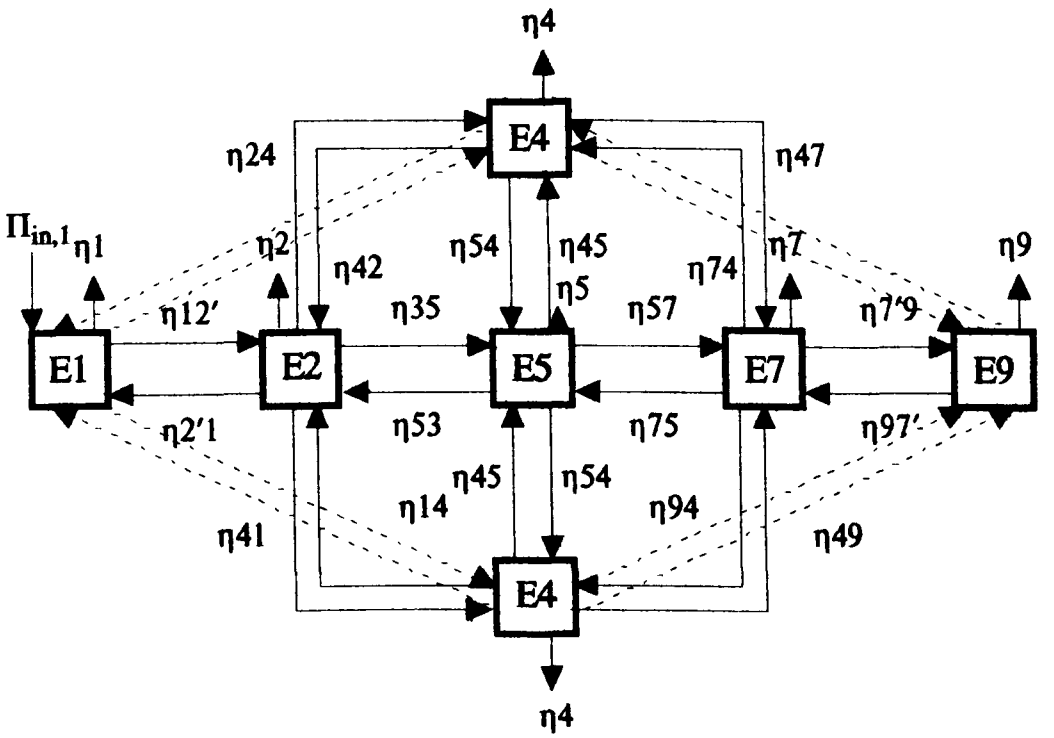

Figure 7.21: 6 sub-system energy flow

E1 = Source room E4 = Cavity E7 = Receiver wall
E2 = Source wall E5 = Cross-rib E9 = Receiver room

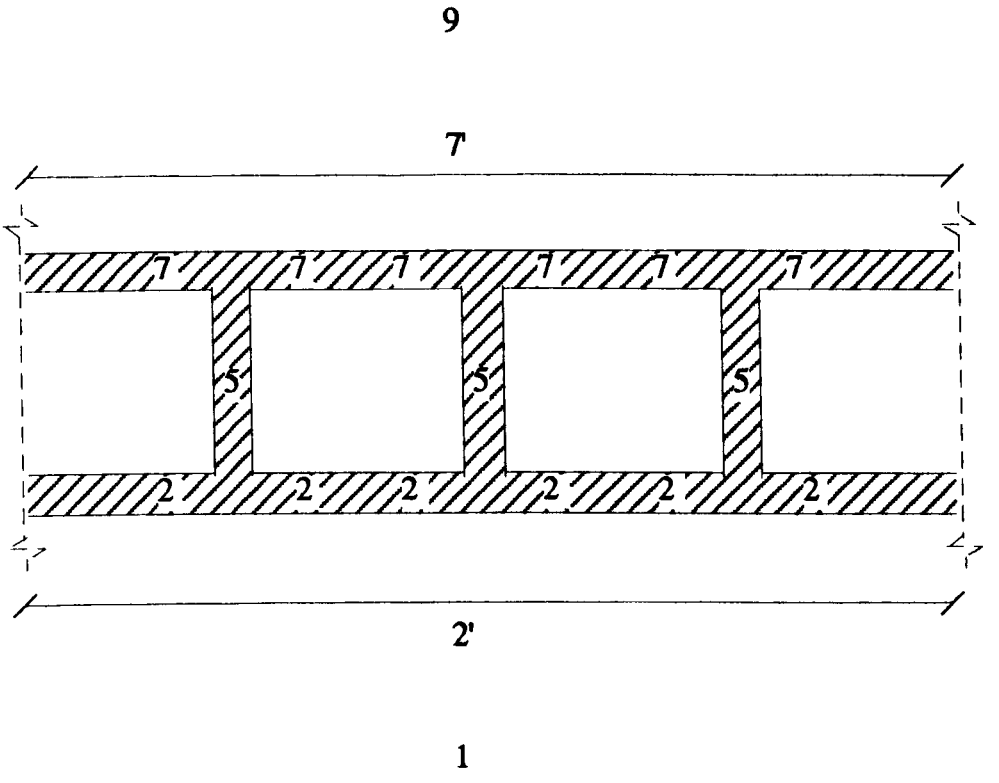

Figure 7.22: 5 sub-system model

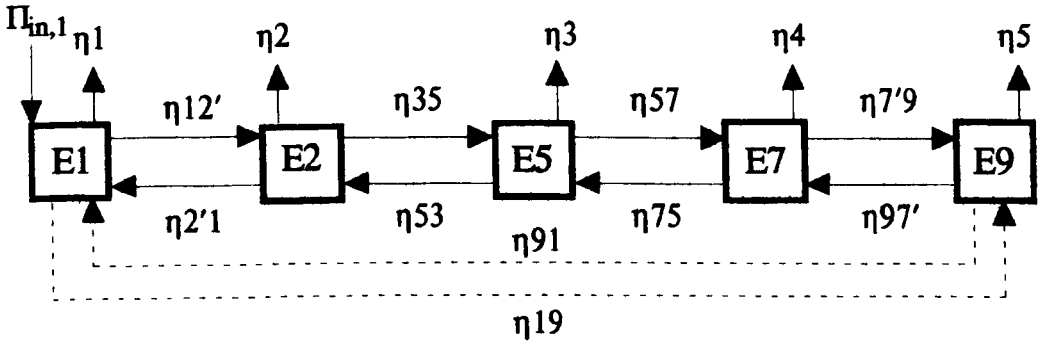

Figure 7.23: 5 sub-system energy flow

E1 = source room
E2 = source wall
E5 = cross-rib
E7 = receiver wall
E9 = receiver room

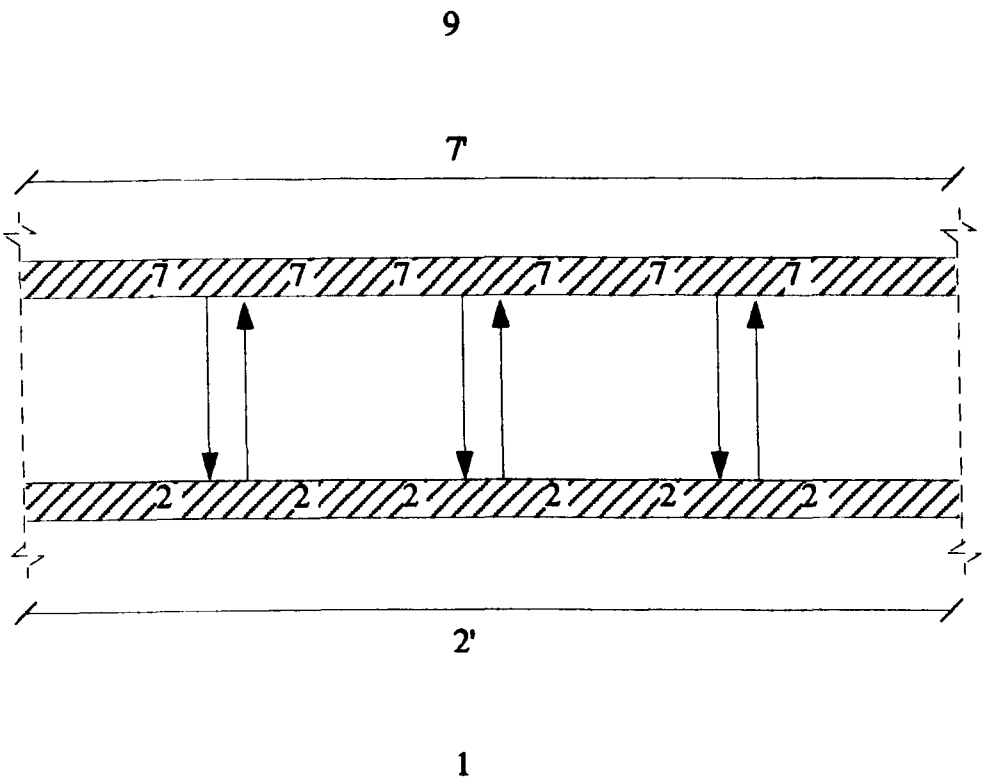

Figure 7.24: 4 sub-system model

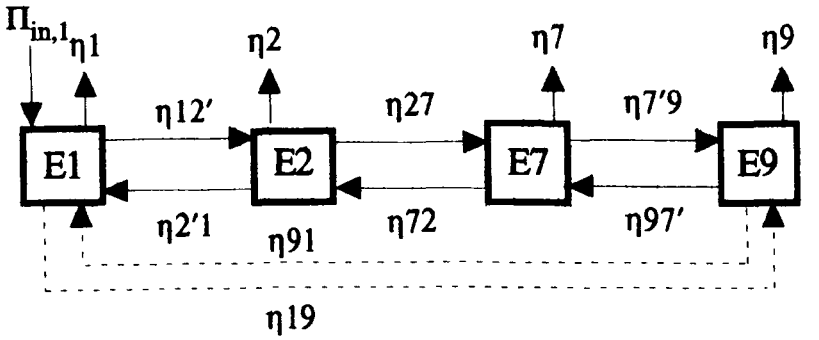

Figure 7.25: 4 sub-system energy flow

E1 = source room E7 = receiver wall
E2 = source wall E9 = receiver room

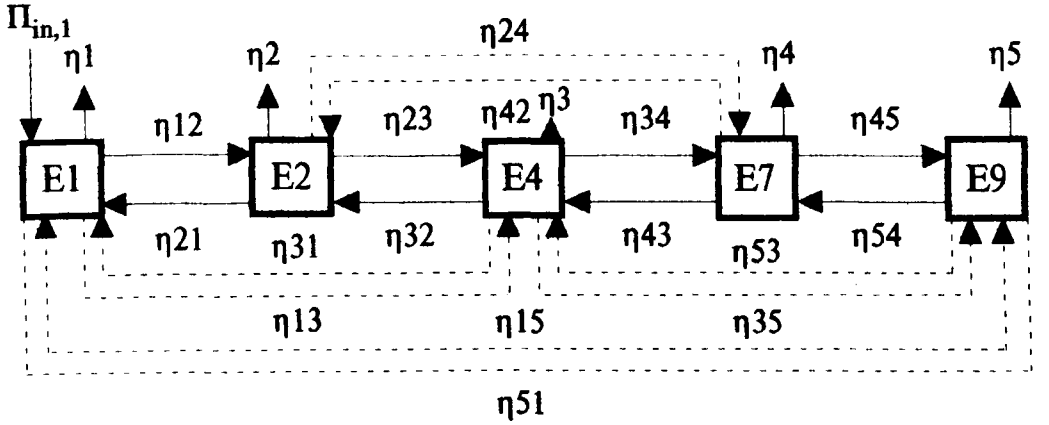

Figure 7.26: Energy flow for a double wall

E1 = source room
E2 = source wall
E4 = cavity
E7 = receiver wall
E9 = receiver room

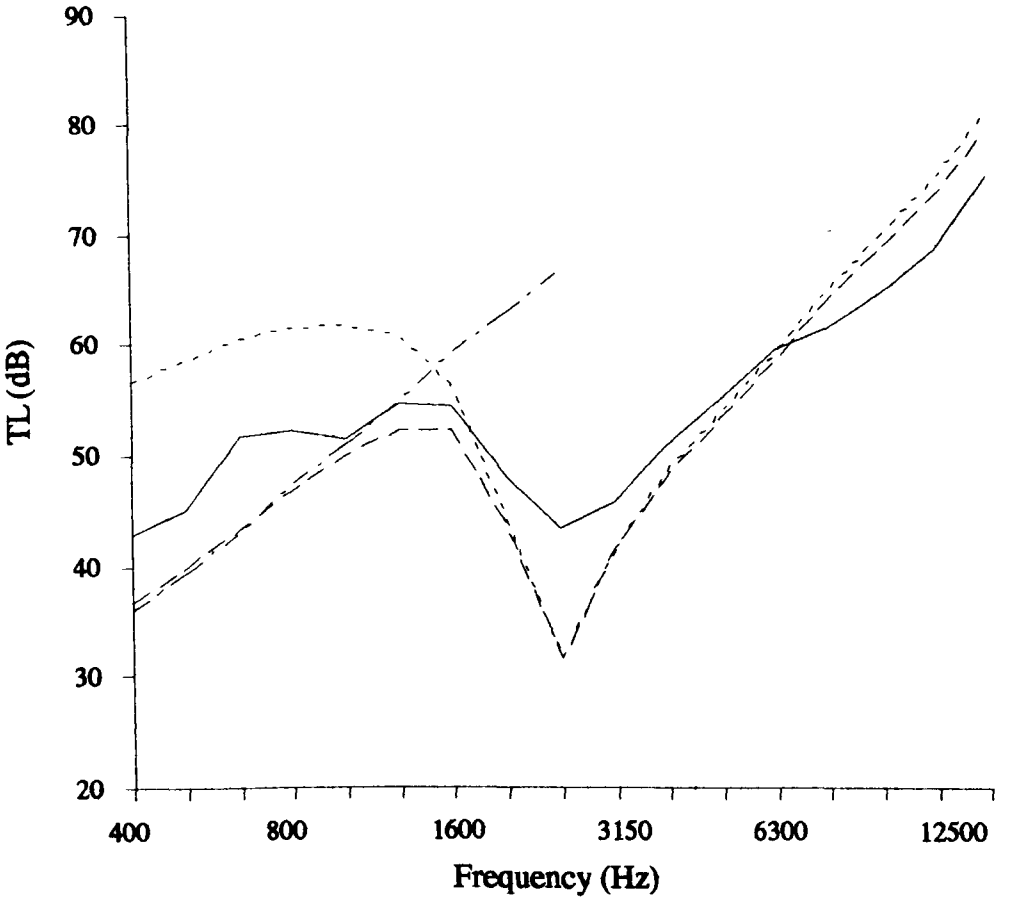

Figure 7.27: Transmission loss of double wall (0.06 m cavity)

measurement
prediction: 'all' paths
'resonant only' paths
'non-resonant only' path

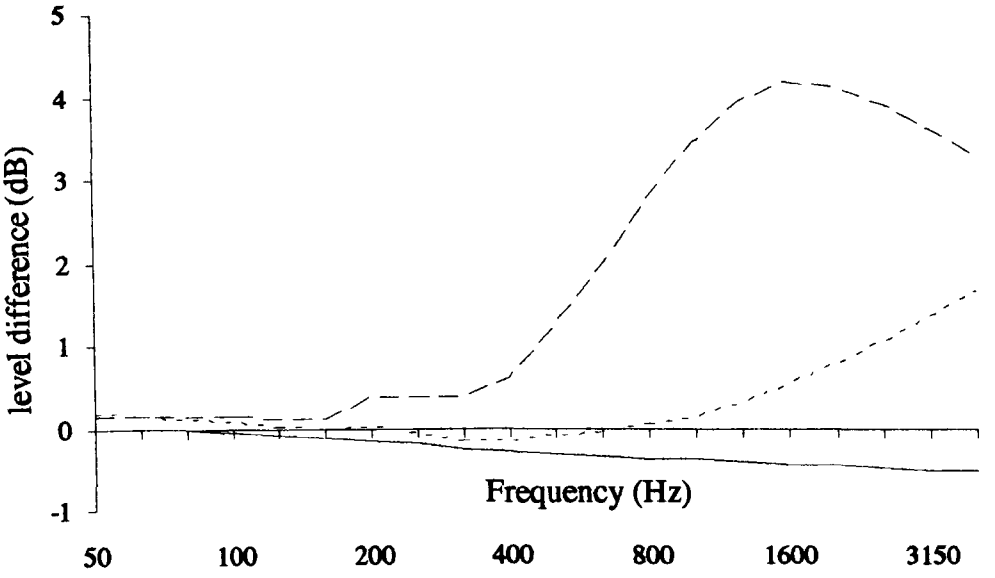

Figure 7.28: Difference in vibrational level difference between the 6 and 5 sub-system models

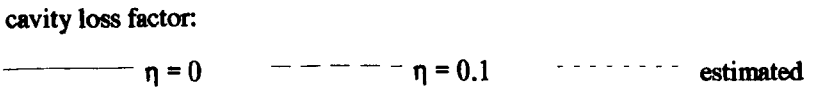

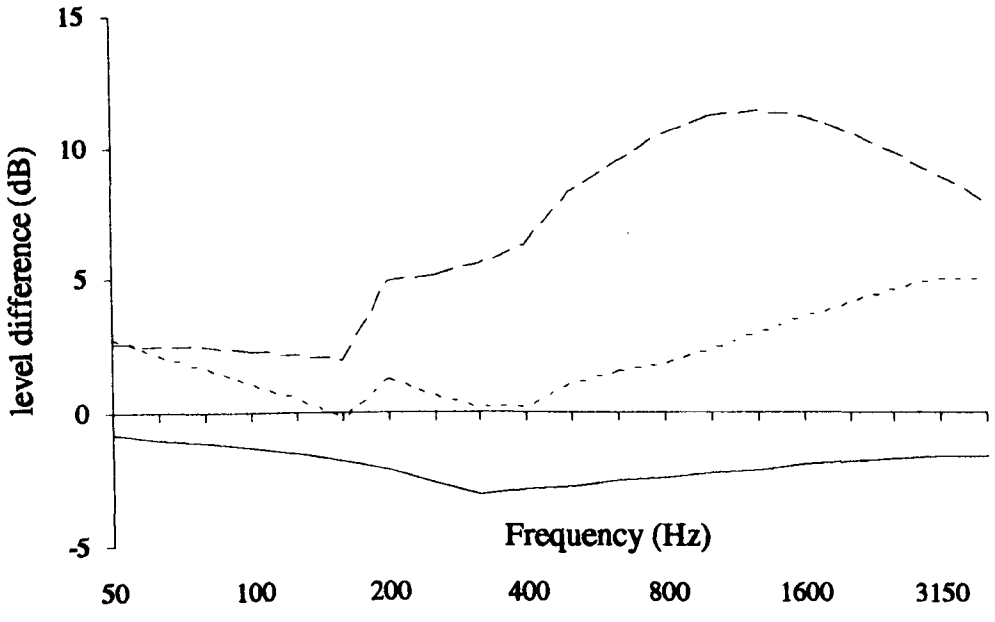

Figure 7.29: Difference in transmission loss between 6 and 5 sub-system models

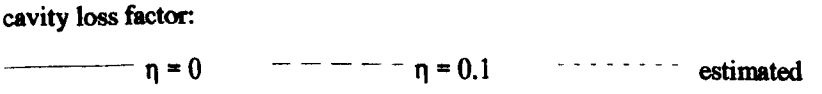

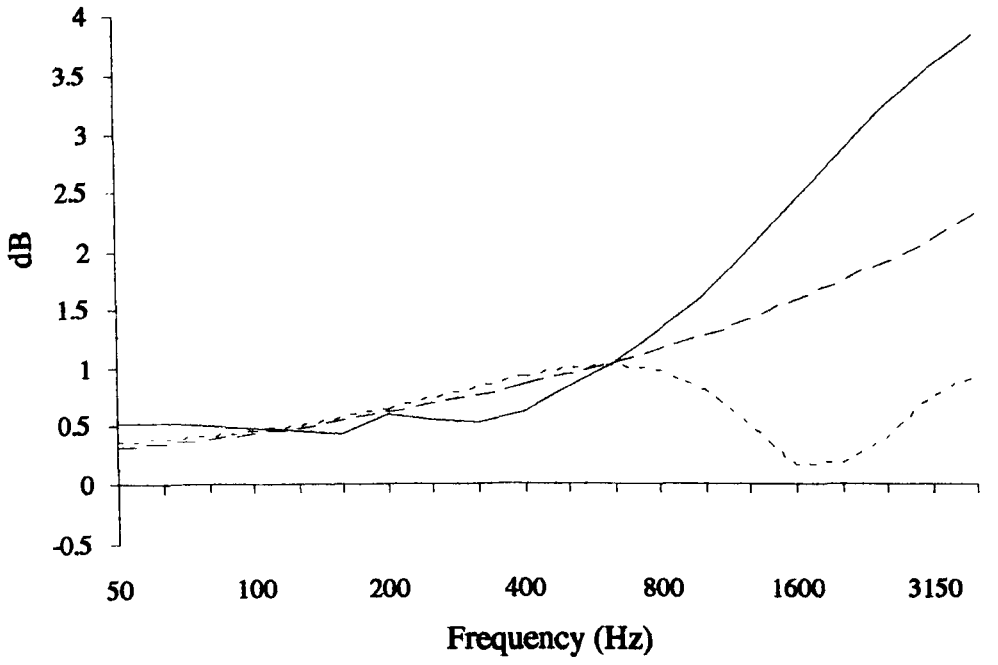

Figure 7.30: Predicted vibrational level difference for a typical full size diaphragm wall

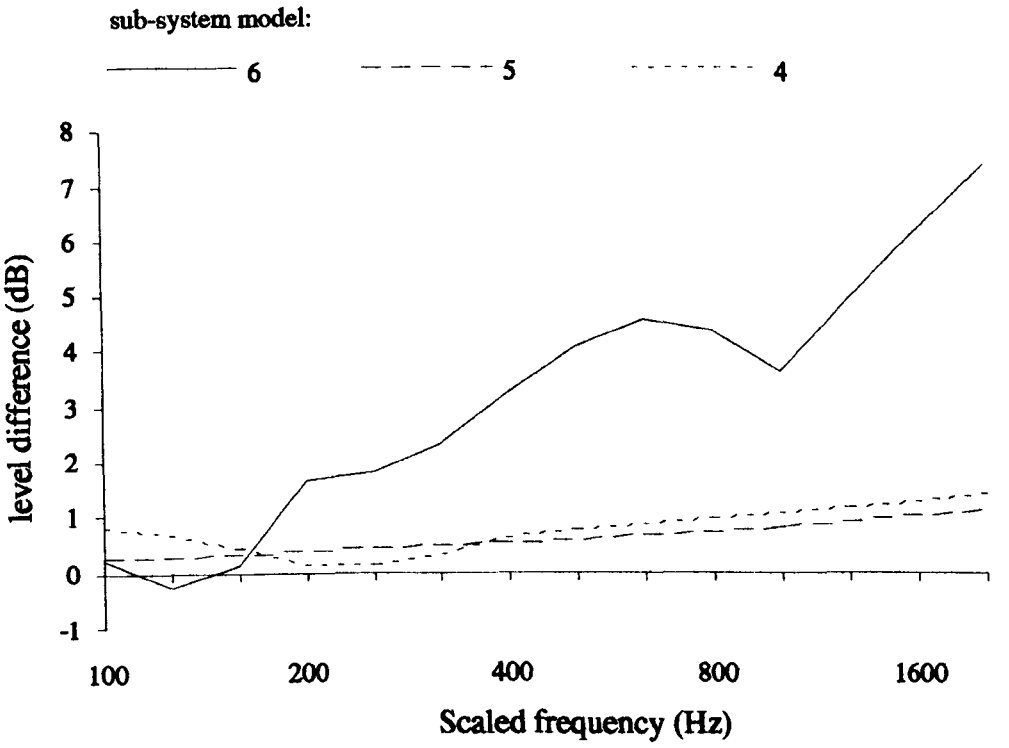

Figure 7.31: Vibrational level difference between leaves of the 1:8 scale 7 rib diaphragm wall

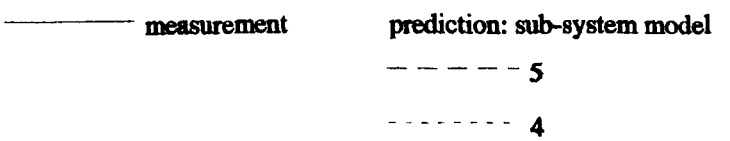

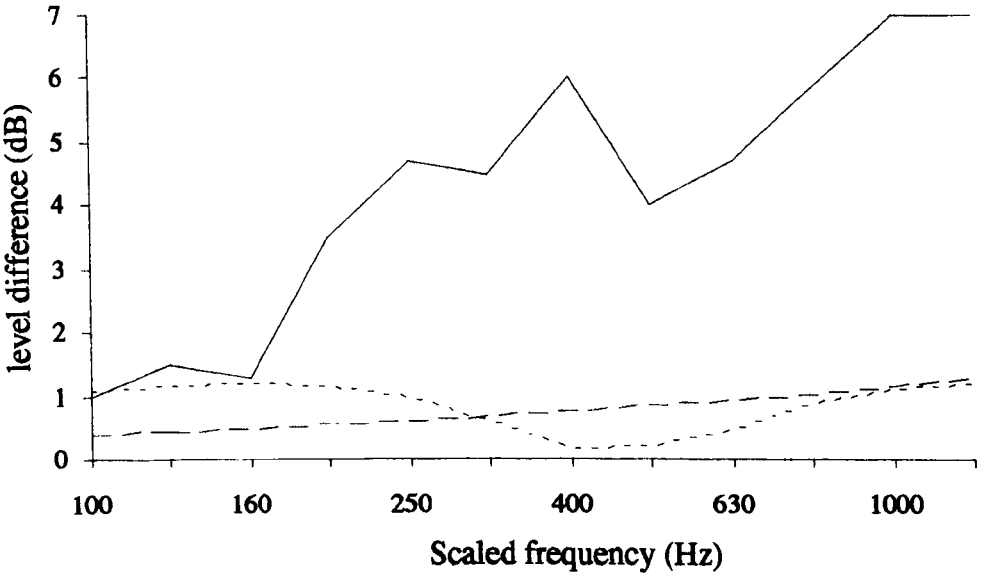

Figure 7.32: Vibrational level difference between leaves of the 1:4 scale diaphragm wall

measurement

prediction: sub-system model

5

4

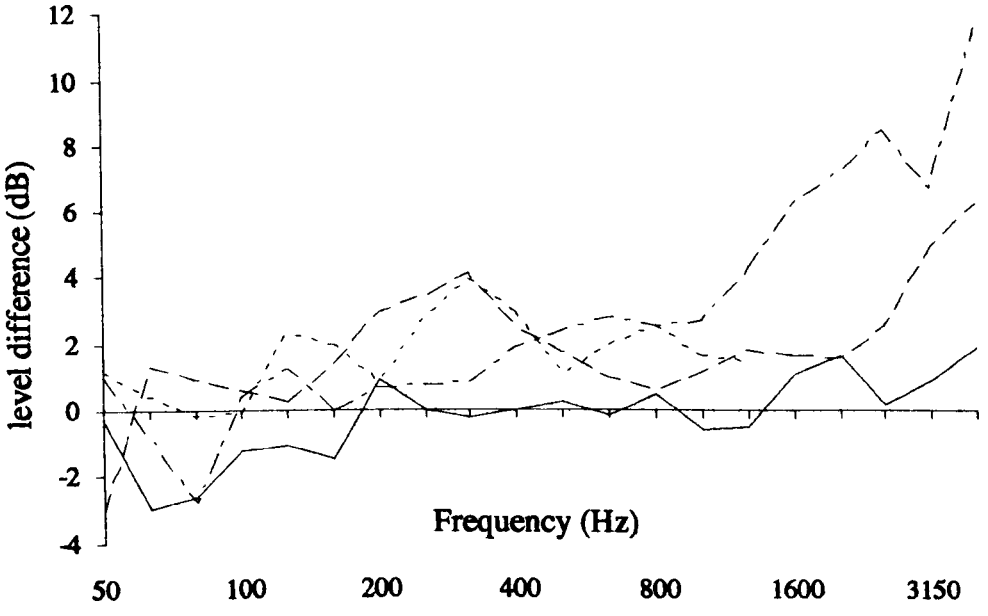

Figure 7.33: Vibration level difference of 4 in-situ diaphragm walls: measurement minus prediction

USC

UGS

MHS

AHS

(see chapter 8 for reference codes)

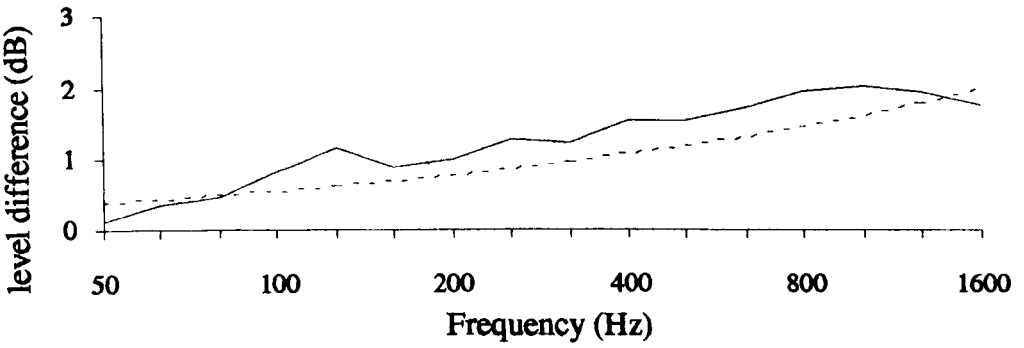

Figure 7.34: Vibrational level difference between leaves of a post-tensioned diaphragm wall

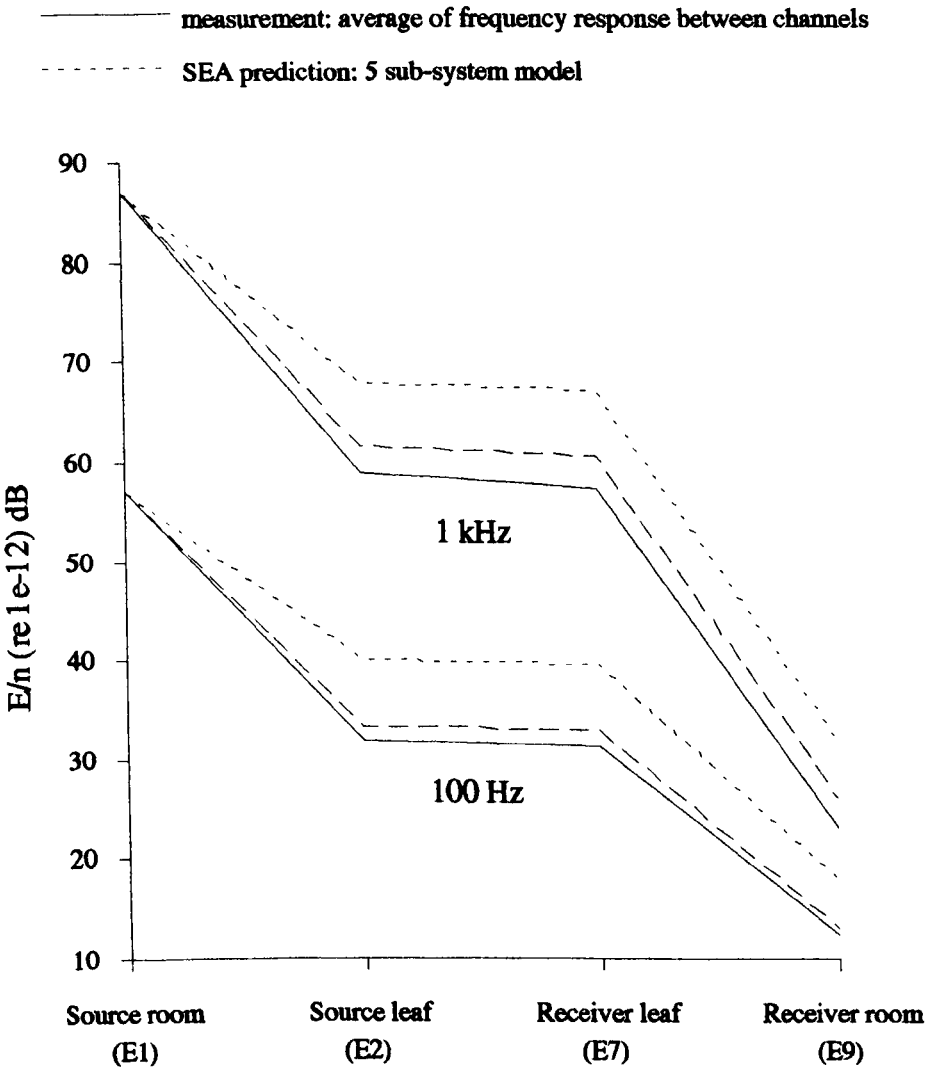

Figure 7.35: Modal energies across a diaphragm wall

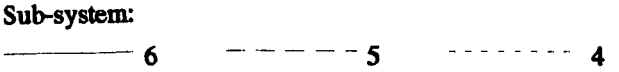

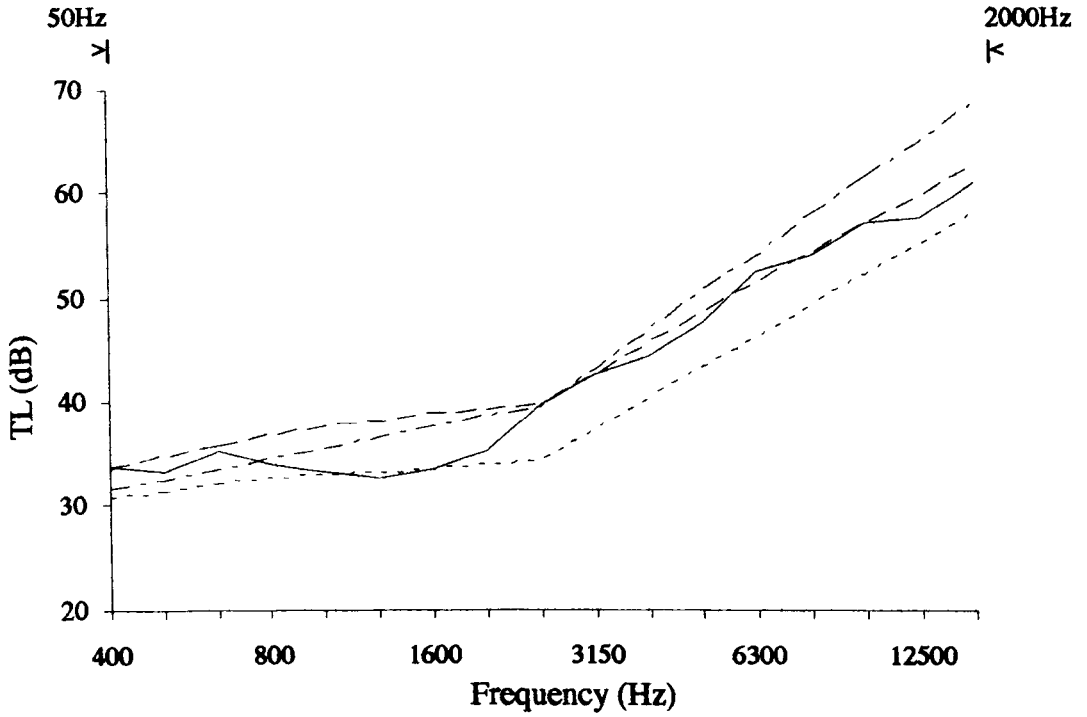

Figure 7.36: Transmission loss of the 1:8 scale 7 rib diaphragm wall

measurement prediction: SEA : 5 sub-system model
SEA : 4 sub-system model
adapted existing theory

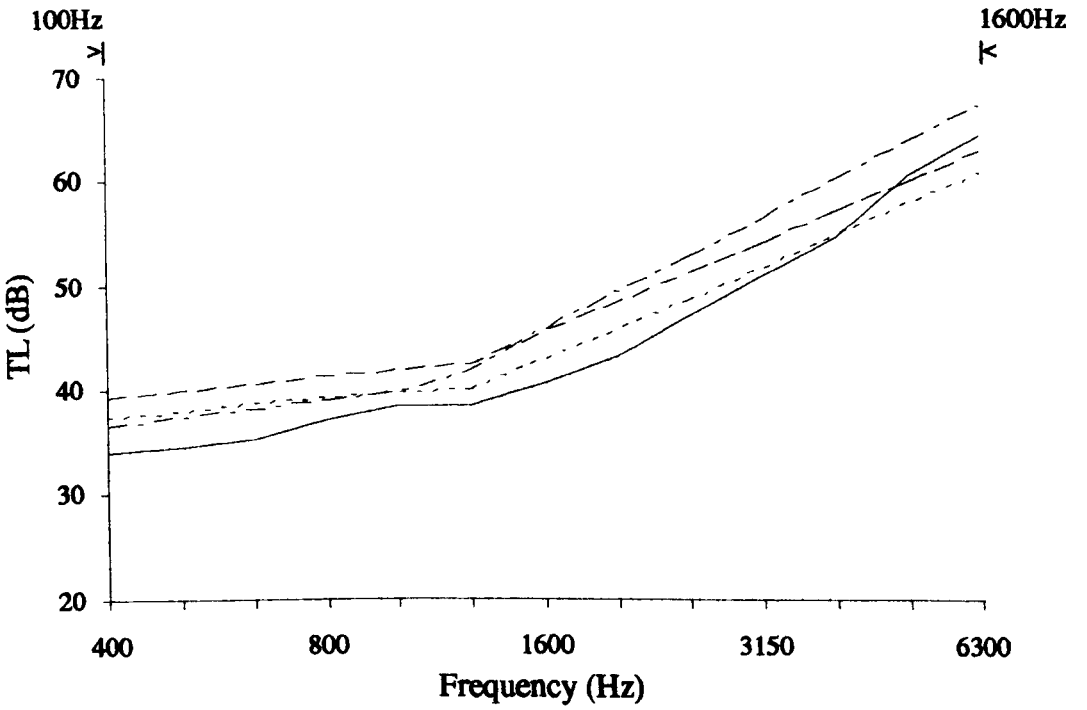

Figure 7.37: Transmission loss of the 1:4 scale diaphragm wall

measurement prediction: SEA : 5 sub-system model
SEA : 4 sub-system model
adapted existing theory

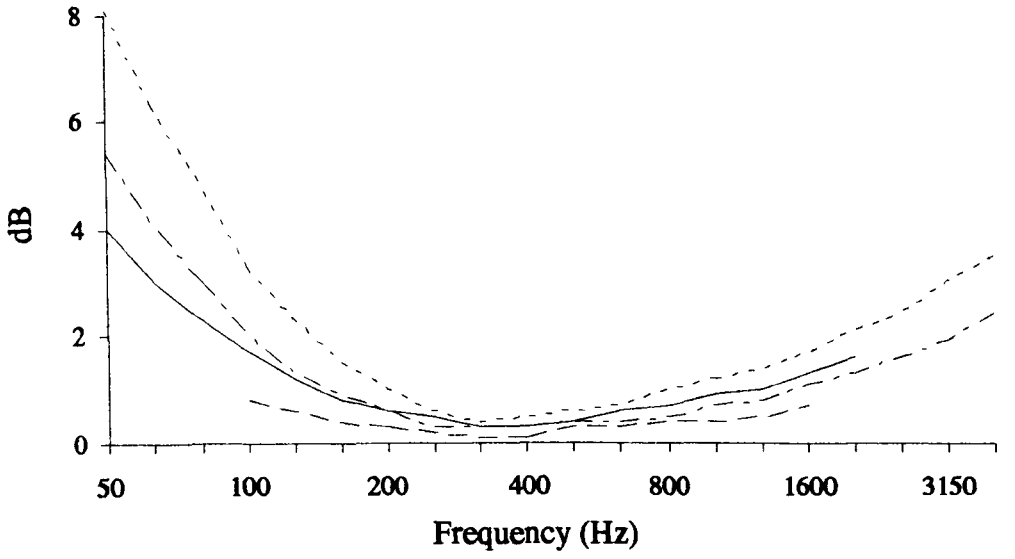

Figure 7.38: Difference in transmission loss with and without non-resonant path

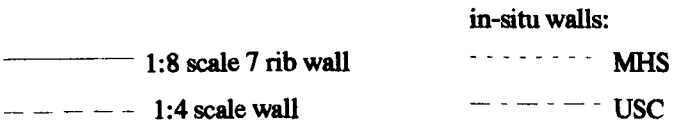

8 FIELD MEASUREMENT

8.1 INTRODUCTION

This chapter examines the in-situ measurement, by intensimetry, of a selected group of diaphragm walls found in the North West region of the U.K. To the author's knowledge there has been no previous attempt to measure the sound insulation of a full scale diaphragm wall, nor to use sound intensimetry for the measurement of such heavyweight constructions.

The field measurements had a threefold purpose: to acquire reliable sound insulation data for this wall type, to validate transmission loss prediction discussed in chapter 7, and to explore the use of sound intensimetry as a measurement tool for in-situ heavyweight facades. Two measurements were obtained from the sites visited; the airborne transmission loss of the wall and the vibration level difference between the leaves. Some of the measured results have already been incorporated in chapters 6 and 7 without a full description of method.

The field measurement of high insulation facades has always posed acoustical problems such as poor signal-to-noise ratios and flanking noise, as well as practical problems such as a site's location and the portability of instrumentation. The standard recommended method, ISO 140/5 [106], requires a loudspeaker or nearby traffic as a source, and is only suitable for the sound insulation measurement of lightweight elements, such as windows or doors. It is not suitable for high insulation constructions as neighbouring elements of lower sound insulation result in flanking transmission, and an external noise source is often disturbing to local residences. Following the successful use of the intensimetry, under laboratory conditions in chapter 4 and by other authors [96 - 101], it was seen to offer the potential for the field measurement of high insulation elements under in-situ conditions.

To date there has been little study of the uses of sound intensimetry for the field measurement of transmission loss. Emmanuel [149] compared measurements of transmission loss by the standard method [106] and the intensity method for single and double glazed facades using both loudspeaker and traffic noise sources. Agreement was within 1 - 2 dB at almost all frequencies, but the window was clearly the strongest transmission path and the measurements did not suffer from problems of a high reactivity index, background or flanking noise.

Sperling [150] attempted measurement of a composite wall with corrugated external cladding panels, which formed part of a large power plant boiler house. Measurement was over a limited frequency range, 125 Hz - 2 kHz, in 1/1 octaves using an unconventional sound intensity approach. The source sound pressure level was measured close to the internal facade, adjacent to the external measurement surface, with a loudspeaker directed at the test surface from inside the boiler house. The transmission loss, TL, was given by:

$$TL = L_p - L_i - 12 \qquad (8.1)$$

Where L_p is the spatial and time averaged sound pressure level close to the internal wall surface and L_i is the spatial and time averaged intensity level over the external measurement area. The theory was questionable since it assumed free field conditions inside the boiler house.

Lai & Burgess [104] used both pressure and intensity methods to measure the transmission loss of an external door, louvre, internal door and wall, which formed an enclosure. Various spacers and scanning distances were used. The close proximity of the lower insertion loss elements is seen to dominate both methods of measurement, although this is not stated by the authors. With respect to the

measurement of the diaphragm walls in the present study, it was hoped that a 'closed scan' and a greater distance from flanking elements would reduce or eliminate this effect.

8.2 IN-SITU DIAPHRAGM WALLS

Sites were found either via contact with consultants known for the construction of diaphragm walls or simply through casual observation and conversation. In total nine sites were visited and six sites were selected. The selected sites are listed below with their short-hand notation which will be used for brevity.

Urmston Grammar School	UGS
Urmston Sports Centre	USC
Plessington R.C. High School	PHS
Bebbington Sports Centre	BSC
St. Augustines R.C. High School	AHS
Mount St. Josephs R.C. High School	MHS

All were sports halls, four were attached to schools and two were at sports centres. USC was visited twice, for repeatability measurement purposes [81] and for an ISO 140/3 [73] measurement. The problems of flanking transmission and high background noise levels were primary concerns before taking measurements and for this reason a preliminary visit was made to assess the site and measure background pressure levels. A prime consideration for the acceptability of a site was a sufficiently large area of wall which was unbroken by acoustically weak links such as doors, windows or ventilation openings. All the chosen sites were at least 50 m from any residential areas, and most considerably greater. Access to most sites was difficult and all, except MHS and PHS, had to be measured in the early morning between 7 - 10 am, before opening hours. A minimum time of 3 hours was

required, without weather or instrumentation problems, for one measurement set. Inevitably on some sites less time was available as problems occurred and tests were shortened. The instrumentation would be best described as 'transportable' rather than 'portable' and required at least two people to set up and carry out the tests.

The sites that could not be used were; at Accrington Brickworks where site noise levels were too high, at Sutton High School where the room volume was too large to be driven to a sufficiently high sound pressure level, and at George Tomlinson High School where there were an excessive number of flanking paths from ventilation grills and doors. Appendix A.5 gives general details of all the sites visited and the present contacts for any future study.

Figure 8.1 shows schematically the six field measurement sites visited. The heavy line denotes the diaphragm wall and faint lines adjoining rooms and corridors. The heavy short lines indicate measurement locations. These diagrams are roughly to a 1 : 570 scale. Table 9 gives details of the wall constructions. In some cases it was not possible to obtain details of older walls due to drawings and specifications having been destroyed. All these walls had tied cross-ribs, hence where details were not available it was necessary to estimate cross-ribs centres. The wall at Ceramics Research, Stoke-on-Trent (CERAM), was the only wall with bonded cross-ribs and is discussed later. Table 10 gives measurement details of all the rooms and diaphragm cavities for both the scale and full size walls. Also included are their one, two and three dimensional space cut-off frequencies determined by the first half wavelength between parallel surfaces, denoted f_1, f_2 and f_3 respectively. All the halls were calculated to be sufficiently diffuse above 30 Hz, from equation 3.3 and assuming a minimum modal overlap of one-third.

8.3 CORNER AS AN ENERGY SINK

Many diaphragm walls completely surround a space, such as with the sports halls measured, and therefore have corners. Yet, in both prediction and measurement, assumptions are made based on the principle of an 'equi-partition of energy' throughout a sub-system. For predictive purposes the diaphragm wall has been assumed to be an infinite wall consisting of a repeatable series of I-Sections. Thus it is taken that there is no net flow of energy between each sub-system of the internal leaf and between those of the external leaf. This is true until the wall forms a corner. By assuming equal energy distribution across the wall surface we need only measure a sample area of the wall to adequately represent the transmission loss of the whole wall. This also assumes an equal excitation of the wall. Therefore before measuring the diaphragm walls it was necessary to check the assumption that these corners do not act as energy sinks, or if they do, to what degree do they influence the assumption of an equi-partition of energy over the wall's surface?

Figure 8.2 shows the typical corner of a diaphragm wall. If we compare a corner to a straight wall there is: an increase in external surface length relative to the internal surface length in the former, the structure-borne transmission paths between the leaves are altered, and the cross-ribs are closer together. Hence there will be a greater energy transmission between leaves at the corner than at the centre of the wall and thus an energy flow towards the corners. If this energy draw is significant it will negate the assumption of an even energy distribution over a leaf.

To examine this an SEA model was produced according to the energy sub-systems shown in figure 8.2 and compared with an SEA model of an infinitely long diaphragm wall which can be represented by a single I-section. A comparison is made between them in terms of the vibrational level difference between the leaves.

For both analytical models it is assumed that sound transmission between the leaves is via the cross-ribs only and the radiated energy from the external wall travels into free space.

Figure 8.3 shows the difference between the two cases as a function of the number of bays (I-Sections) from the corner. With each additional bay the influence of the corner reduces and results converge quickly and exponentially to the infinite wall case. The level difference between SEA models is 0.7 dB when only the first bay is considered. The side of a typical diaphragm wall may have 20 bays and therefore at the centre of the wall, where measurements were normally made, the error due to the corners from an infinite wall assumption is only 0.1 dB. Hence the effect of the corners was considered negligible.

As an aside, one or two construction joints are usually found over the length of a diaphragm wall. Typically they are 10 mm wide between two facing cross-ribs filled with sealant to a depth of approximately 100 mm on either face. As this is a break in the wall any incident wave travelling along the wall will be attenuated across the joint. This is not a problem when measuring the transmission loss of the wall when it is excited equally over its surface. However in some cases the wall will be excited locally by an adjacent room. The attenuation across a typical joint was measured as a level difference on the diaphragm wall at MHS. The wall on one side of a construction joint was excited by a diffuse sound field produced in an adjoining changing room. Airborne flanking paths, which would excite the other side of the joint, were reduced by a separating 1/2 brick plastered wall and a long corridor with closed doors between the changing room and hall. Spatial averaged acceleration levels were measured on either side of the joint at a minimum distance of 1.5 m. Figure 8.4 shows the level difference rises from close to zero at below 63 Hz by 5 - 6 dB / octave up to 400 Hz, dipping only at coincidence. Above 400 Hz the

difference is constant at approximately 20 dB, which is probably due to airborne flanking transmission in the receiver room exciting both leaves equally.

8.4 MEASUREMENT OF TRANSMISSION LOSS

For the field measurement of facade and facade elements, ISO 104/5 [106] requires a receiver room and a sound source external to the facade. As the sound intensity technique only requires a source room a large sound level can be generated without disturbing the neighbourhood. Most building facades will be interrupted by low sound insulation flanking elements such as vents, doors, windows etc. The standard method [106] cannot distinguish between sound transmitted through more than one element as only the pressure level is measured. Hence it is only suitable where the element of interest is the whole facade, or by far the largest transmission path such that transmission via the other elements can be assumed negligible. Thus the method excludes the field measurement of elements which are comparable or higher in sound insulation than their neighbouring elements. It was hoped that the sound intensimetry technique would allow measurement of the diaphragm wall while in the presence of distant flanking paths.

Before attempting to measure an in-situ diaphragm wall, the measurement procedure was tested on a large single leaf wall which formed part of the transmission suite in the Acoustics Research Unit, at Liverpool University. As this was within the laboratory, the measurements benefited from low background levels and did not suffer from flanking transmission (as the test suite door was measured and predicted to give a transmission loss greater than the wall). Plate A.7.4 shows the sound intensity through the wall being measured. The measured transmission loss of the wall has been shown previously, see figures 5.5 and 7.9. The wall was scanned twice using a probe configuration of two 1/2" microphones at 50 mm or 12 mm spacing. Figure 8.5 shows as a level difference, the dynamic range of the

instrument, ($L_{k,0}$ - 7 dB), minus the field reactivity index, L_k, for both spacers. A positive value is required for the field reactivity to be within the instrument range. For the 50 mm spacer L_k is within the dynamic range of the instrument at all but one frequency, while the 12 mm spacer is only within the range above 800 Hz. L_k varied between 10 - 15 dB for both spacers which, as will be seen, was higher than for the diaphragm wall measurements. This is probably due to the receiving space being a corridor while for the diaphragm walls this space was either of greater volume (a sports hall) or an open field.

8.4.1 Field Measurement Procedure

The measurement set-up is given in figure 8.6 and appendix A.4 gives details of the instrumentation used. Plate A.7.5 shows the diaphragm wall at AHS under measurement.

The source room was always a sports hall, except for measurements at USC and one measurement at MHS, where it was a changing room. Mean room sound pressure levels were measured using a 1/2" condenser microphone on a revolving boom positioned slightly off-centre in the room - see plate A.7.6. The sound was generated by a multi-sine wave signal band-limited between 12 Hz - 5 kHz. Two 15Ω loudspeakers were positioned facing into the far corners of the hall driven with a stereo amplifier, giving approximately 300 W per channel. This produced mean sound pressure levels, $L_{p,s}$, for all the sites of between 80 - 105 dB over the frequency range of 50 Hz -4 kHz. Where it was possible to use a changing room as a source room an increase in $L_{p,s}$ between 3 - 7 dB was attainable due to the reduced volume of the space. A hand held 1/1 octave sound level meter was used to estimate the diffusivity of the sound field in each frequency band. The level varied no more than ± 1 dB above 250 Hz and ± 2 dB below 250 Hz. Hence it was assumed that a diffuse sound field was striking the wall and that only one revolving

boom position was necessary. Reverberation times were measured at three locations in the source rooms using the B&K Building Acoustics Analyser (Type 4418) for ease and speed of measurement. The mean reverberation times are given in figure 8.7 and were used within the transmission loss predictions to calculate the room absorption and total loss factor. Between 100 Hz - 2 kHz all reverberation times were between 4 - 7 seconds, then falling by approximately 1 sec/octave.

All intensity measurements, except for those at USC and one measurement at MHS, were on external facades - see plate A.7.7. The measurements were recorded over the frequency range from 50 Hz to 4 kHz in 1/3 octaves. The measurement area was scanned according to ISO/DIS 9614-2 [91] resulting in a single figure surface average intensity level, L_i. A 3 m^2 area of the wall was scanned: which was 3 m long, 1 m high, and 1 m from ground level, positioned furthest from any flanking paths, usually in the centre of the wall and never across a construction joint. The length of the measurement area was chosen so that at least two cross-ribs would be scanned and the height was chosen so no scaffolding would be required. The measurement area was separated into a grid of 75 boxes, each 200 x 200 mm. The probe was scanned over the measurement area at 100 mm from the wall surface giving a total measurement surface area, including the perimeter, of 3.8 m^2. A total of 258 averages were taken 204 normal and 54 adjacent to the wall. A scanning speed of approximately 0.15 m/s was used. Two scans, one vertical and one horizontal, were made and the average of the two taken. The measurement average was 'paused' after the 'open scan' and mean L_p and L_i values recorded. Measurement was then completed around the perimeter of the box and the 'closed scan' values of L_p and L_i were recorded. This allowed measurement of the flanking power through the side of the 'box'. ISO/DIS 9614-2 [91] recommends the pausing of measurement to allow readjustment and the recording of data over a particular measurement segment. The probe was always held to the side and at arms length to minimise the operators influence on the results. By holding the probe by hand there is inevitably

some degree of shaking while traversing the wall. So as not to lose a measurement at each perimeter corner the average was paused to allow the operator to reposition himself. Further, measurements were only taken when the wind speed was less then 2 m/s as recommended by ISO/DIS 9614-2, and a windscreen was always used to reduce wind noise and protect the microphones.

At two sites, USC and MHS, room to room transmission loss measurements were possible as the wall separated a hall and a changing room. The procedure was the same as above, but these measurements had a number of advantages over those of the external facade. Background levels were significantly lower in the receiver room compared with outside, higher source room levels were obtained by using the changing rooms, and wind noise, weather problems etc. were eliminated.

8.4.2 Discussion of Measurements

Although measurements were recorded between 50 Hz - 4 kHz the frequency range over which readings were valid was limited by the microphone configuration, the dynamic capability of the instrument and the reactivity of the field. Figure 8.8 shows the dynamic capability of the instrument and the mean 'closed box' reactivity index ± 1 standard deviation, given by equation 4.22. The reactivity index is approximately 10 dB which increases the low frequency limit to 100 Hz while the upper limit is unchanged at 1.25 kHz. In this region $L_k < (L_{k,0} - 7\ dB)$ and thus does not further limit the measurement frequency range.

Measurements of the external facade suffered from insufficient signal above background noise, and flanking transmission via the roof and fire doors. Figure 8.9 shows typical background intensity levels at the measurement area for both internal and external wall measurements. The levels at external facades were approximately 5 - 20 dB higher than those for internal wall measurements up to 1 kHz. At low

frequencies, the external background intensity levels were between 45 - 55 dB and the source pressure levels were between 80 - 90 dB, hence the transmission loss of the diaphragm wall in this frequency region was difficult to measure. Figure 8.10 shows as an example, the mean measured intensity level above the background intensity level for the internal and external measurements at MHS. External wall intensity levels were never more than 10 dB above background levels, except about $f_{c,u}$. Indeed below 100 Hz intensity level is measured less than the background level. Internal wall measurements were always greater than 10 dB above background, except below 63 Hz, where the level was still greater than background. Hence, for the internal wall measurements at USC and MHS, the higher source room pressure levels and lower background intensity levels allowed the transmission loss to be measured with confidence. The external measurements suffered from high background levels, due to wind noise and flanking transmission, and lower source room levels due to large source room volumes. It was considered whether to double the sound power to the halls by adding an extra two speakers driven by a second amplifier, but this would have increased the room sound pressure level by only 3 dB and thus was not attempted.

It was of concern that internal and external wall transmission loss measurements might be effected by flanking transmission. With respect to the internal measurements at USC and MHS, in both cases the only flanking path was a corridor of roughly 20 - 25 m with three equally spaced closed doors. This was thought sufficient to reduce the contribution of this path on the measured intensity to a negligible level. At USC the transmission loss was also measured by the standard ISO 140/3 method. The mean level difference in transmission loss between the methods is shown in figure 8.11 to be between 0 - 4 dB.

For the external measurements, two flanking paths were identified, the fire doors and the roof. In most cases double fire doors were positioned at either end of the

facades, normally between 10 - 16 m away from the measurement area; a typical door and frame was measured and calculated to have an R_w = 26 dB. The roof was usually of a lightweight steel decking, in some cases insulated and often with roof lights. It was clear that these paths would radiate a much greater sound energy from the building envelope than the diaphragm wall, but would this influence the intensity level measured over the sample area?

Investigating this further: none of the surface averages produced any negative net power flow, either for 'open' and 'closed box' or scans, indicating no significant extraneous noise. Hence, the predominant intensity was from the wall and was not influenced sufficiently by the flanking paths to change any intensity vectors. In figure 8.12 is shown the mean reactivity indices of all the 'closed box ' scans, $L_{k(\text{closed box})}$, compared with the mean of the 'open box' scans, the 'closed box'$_{(\text{external walls only})}$ scans and 'closed box'$_{(\text{internal walls only})}$ scans. In the figure zero on the y-axis is mean $L_{k\ (\text{closed box})}$. The reactivity index of the 'open box' measurements varies by no more than 1 dB and thus little energy is lost through the perimeter, hence flanking transmission entering the measurement area via this path is minimal. The mean L_k for the external walls only, is lower than the overall mean by 1 dB in the measurement range and by up to 3 dB below 100 Hz and above 1250 Hz. The mean L_k (internal walls only) is higher than the overall mean L_k, by between 1 - 4 dB. This would be expected as the enclosed hall would produce a diffuse sound field and have a greater value of L_k than under external free field conditions. The standard deviation in the values of L_k is shown in figure 8.13 and varies little between these categories, being less than 4 dB between 100 - 630 Hz, rising to 8 - 10 dB.

From these results it was concluded that the internal wall measurements were reliable between 100 Hz and 1.25 kHz, as the measured signal in the receiver room was sufficiently above background levels, the field reactivity was within the

capability of the instrument and flanking transmission was considered minimal. The external wall measurements were not considered as reliable, due to high flanking transmission and a poor signal to background noise ratio. The strong flanking transmission did not directly influence the measurement so as to produce a negative net flow of intensity from the wall, but did add to the background noise levels. So that any increase in the source room levels would not have improved the signal-to-noise ratio as this would in turn increase the total background level.

8.4.3 Analysis of Results

Although the external wall transmission loss measurements cannot be considered reliable for the reasons discussed above, let us examine the raw data from all the in-situ diaphragm walls as if presented with no prior knowledge. Figure 8.14 shows the transmission loss of all the walls between the frequencies 100 Hz - 1.25 kHz. The walls lie within a band of approximately 15 dB and all curves are characterised by two distinct slopes across the frequency range: a flatter slope where $f < f_{c,u}$ and a steeper slope where $f > f_{c,u}$. The two highest curves are the internal wall measurements at USC and MHS. Below $f_{c,u}$ the external wall measurements tend to lie within a band of 5 dB, lower than the internal walls measurements. Above $f_{c,u}$ the curves tend to converge. The poorest results were those for BSC which show no particular transmission loss shape and were not considered further. The results shown for USC are the mean of two visits to be discussed.

The material density, ρ_c, for all the walls is estimated (from the known data) to vary from the mean by ± 12 %. If we first assume that all the walls are a sample from the same normally distributed population, then the overall mean transmission loss and 95 % upper and lower confidence limits can be obtained. These are given in figure 8.15. The 95 % confidence limits are given by:

$$\bar{x} \pm \frac{\sigma}{\sqrt{n}} t_c \qquad (8.1)$$

where σ is the known standard deviation, n is the sample size at each frequency and t_c is the T-test factor. For large samples $t_c = 1.96$, but for small samples (< 30) t_c increases, and widens the confidence range. At 500 Hz the mean transmission loss equals 46 dB with the confidence limits roughly ± 5 dB. These limits are closest at low frequencies where there were a greater number of results. Considering the internal measurements at USC and MHS as the most reliable results, the mean of these is plotted in figure 8.16 against the mean of the external wall measurements. Plotted with these curves are their best fit regression lines for the two slopes of each curve. The internal transmission loss measurements are higher than the external measurements by between 7 dB at the lowest frequencies and 1 dB the highest frequencies. Due to a smaller sample number the upper curve is more variable.

At the most promising measurement location, USC, an ISO 140/2 [81] test of measurement confidence was made when returning to the site and repeating the intensity measurement. Although the test does not strictly apply to field measurements, the difference in transmission loss between the two visits are compared with the recommended maximum values given by the standard in figure 8.17. The results should lie between the two limits to be 95 % confident of the measured result. This is true up to 500 Hz, above this frequency the excessive discrepancy is believed due to an intrusive signal from an air-conditioning unit in the corridor outside the hall which was not running during the first visit and could not be stopped during the second visit.

The external wall measurements of transmission loss have been shown to suffer particular at low frequencies from an increased background level due to wind and flanking transmission. Consider the external measurement at UGS, assuming the 'true' transmission loss of the wall is the same as the mean transmission loss of the

internal walls. Then the underestimate of transmission loss due to background noise levels, before the source is turned on, and flanking transmission, after the source is turned on, can be roughly estimated. If we deduct the measured background intensity level from the measured intensity level, the transmission loss will increase and the region left between these new values and the estimated 'true' values gives the predicted effect of the flanking transmission. This is shown in figure 8.18. The lower line shows the estimated transmission loss that is lost due to existing background noise. The upper line is a summation of the lower line and the transmission loss lost via flanking transmission, which clearly dominates over most of the frequency range. (As the 'true' transmission loss is only estimated, at the highest frequencies the upper curve falls below the lower curve, which would not occur with the true value). Generally therefore external measurements have suffered greatly from flanking transmission by lifting the overall background level during measurement. Hence results would be much more favourable at external sites where flanking transmission is eliminated.

The author appreciates that as the sample population of field measurements is small, the estimates made will have wide confidence limits. Therefore only the internal wall measurements at USC and MHS have been, and will be, used to compare with predictions of transmission loss. Further, intensimetry is shown to be limited as a method in the field measurement of transmission loss where excessive flanking transmission occurs. Although it does offer an approach that is suitable where the standard method can presently be used and in cases of limited flanking transmission.

8.5 MEASUREMENT OF VIBRATION LEVEL DIFFERENCE

As well as measuring the airborne transmission loss of the diaphragm wall it was useful to measure the vibration level difference between the leaves. In general this

was easier to measure and provided useful data with which to compare with theory, already shown in chapter 6. The difficulty was how to measure a wall such that a sufficiently large number of modes could be excited within the frequency range of interest, so that when a sample area was spatially averaged it characterised that wall.

The average level difference between the two leaves can be measured in two ways. If the inner leaf vibration level is constant, such as in the case for loudspeaker sources used in the intensimetry measurement, the average acceleration level of each surface can be measured and the 'difference of the averages', L.d, can be calculated:

$$L.d = \overline{L_1} - \overline{L_2} \qquad (8.2)$$

where $\overline{L_1}$ and $\overline{L_2}$ are the average surface acceleration levels of the first and second leaves respectively. For impulsive noise sources, such as spatially averaged hammer blows then, according to Craik [151] , the level difference is best represented as an average of the level differences, where:

$$L.d = \overline{L_1 - L_2} \qquad (8.3)$$

It is a relatively simple matter to measure the second case by means of a dual channel FFT analyser, where the level difference is obtained as an average transfer function. This approach is discussed with respect to the free-standing wall measurements ahead.

8.5.1 Measurement of a Free-standing Wall

The vibration level difference was measured between the leaves of a free standing post-tensioned wall, at CERAM Research. (The wall was built with Accrington

Class A engineering bricks, with a brick compressive strength of 166 N/mm^2 and a brickwork compressive strength of 36 N/mm^2). Here the wall could not be excited by a airborne source as both leaves were coupled by the same acoustic space. Therefore to excite a large number of modes simultaneously required a different approach. Input power to the wall was considered via either a series of broadband drivers connected to the wall or by using a single hammer source striking the wall at a number of random points. The former has certain advantages being a broadband source of constant and repeatable amplitude and when more than one is used a large number of modes can be excited. This method though, was not considered usable, as it would have required a frame system to support the drivers. Thus the latter method was adopted for its portability and speed.

When exciting a wall with a hammer at a single point few modes are excited and the wall is never more than semi-diffuse, although the significant modal overlap of such walls will improve this. Therefore a large number of hammer positions should be used to excite as many modes as possible and a large array of points should be measured to obtain a mean surface acceleration. For impulse sources equation 8.3 is used. Each hammer strike will have a different input level and so is considered as a single event of infinitely short time duration. Craik [151] has shown this impulse source method to give good agreement with a continuous source (a tapping machine or driver), whether using a few source positions and many measurement positions or vice versa.

The 4.1 x 5.6 m wall was free standing on a large concrete pad aside a similar sized fin wall in a large warehouse space - see plate A.7.8. Access to the centre of one face of the wall was impossible due to the closeness of the fin wall, and access to the cavities was also impossible due to a capping beam. The cross-ribs were one brick wide connected to 1/2 brick leaves, and the wall was post-tensioned between foundation and capping beam by two 20 mm diameter rods per cavity. Acceleration

levels were measured on either leaf using two 12 g accelerometers positioned randomly. A rubber tipped hammer imparted the source signal on one leaf 8 times at 16 randomly chosen positions. The measurement positions were changed randomly after each series of strikes. Acceleration signals were input to a dual channel F.F.T. analyser and two level differences were obtained: the difference of the spectrum averages on each leaf - as equation 8.2; and the average frequency response between leaves - as equation 8.3. Figure 8.19 shows the vibration level difference by both methods. The difference in spectrum average produces no particular pattern with frequency, varying significantly about zero, and thus shows the inapplicability of the equation 8.2 to a varying input level. Yet the vibration level difference calculated according to equation 8.3 rises smoothly with frequency, and has been previously shown to agree within 0.5 dB of prediction, (see figure 7.34).

8.5.2 Measurement of In-situ Walls

Here, the walls were excited with a steady-state signal from two broadband loudspeakers placed in the far corners of the room relative to the wall to be measured. Hence a large number of modes were excited simultaneously and randomly over the wall such that equation 8.2 applied. An accelerometer was fixed to each wall face with beeswax. Where the bricks were rustic facing, regular re-coating was required due to poor surface adhesion. 16 positions were randomly selected on each surface and 8 averages taken at each. The mean acceleration level above background noise is shown in figure 8.20 for the internal and external wall measurements. There is little difference, except at mid-high frequencies where the external level falls by 5 dB. The signal-to-noise ratio is greater than 10 dB at all frequencies above 125 Hz.

Figure 8.21 shows the measured vibration level difference between the leaves, from 50 Hz - 4 kHz, for all sites but one. The wall at PHS is excluded as receiver wall

measurements were carried out in an adjacent corridor to the hall. It is believed that the corridor was a significant flanking path which resonated at low-mid frequencies producing higher levels on the receiver side than the source side. Generally values lie within a band of 5 dB, giving closest agreement at mid frequencies and poorest at high frequencies. Below 160 Hz the level difference is approximately zero, from 160 Hz - 1.25 kHz the difference is between 1 - 4 dB, then rises rapidly. This variation at low frequencies may be caused by random errors incurred due to the finite number of random measurement positions, and a low mode count. Figure 8.22 shows the mean level difference and the 95 % confidence limits. Up to 1.6 kHz the limits are between 1 - 3 dB either side of the mean. At high frequencies the confidence interval is wider due to the small sample numbers and the possibility of the source side accelerometer acting like a microphone, producing larger level differences which also would vary depending on each site. The figure also shows a regression line through the results assuming no change in slope.

From these measurements the author is confident in the results between 100 Hz and 1.25 kHz, which is the same range as the transmission loss measurements. Below 100 Hz measurements are within 10 dB of background levels, but still agree closely with those of the scale model walls. If any account were taken for background levels this would affect both leaves equally, due to their strong bonding, and hence not change the vibration level difference.

8.6 CONCLUDING REMARKS

Chapter 8 has been concerned with presenting and analysing the measured field data. Difficulties of measurement and the limitations of the results have been discussed. The author would have wished to measure more sites, to reduce random error and confidence limits, but also believes these measurements are indicative of typical diaphragm constructions and a greater number of field measurements would

not have dramatically changed the final analysis. Wall specifications and drawings were obtained wherever possible, but in some cases estimates have had to be made. It is worth noting here some other sources of error which have not been considered. Variations in transmission loss between apparently similar walls are likely due to variation in workmanship. Craik & Evans [152] ascribed an error of roughly 2 dB due to variable workmanship above experimental error for a series of 'identical' walls. Here workmanship variability could not be explored properly, as visual inspection of cross-rib / leaf connections is impossible after construction of the diaphragm walls. Further, additional or thickened cross-ribs at doors or construction joints are extra transmission paths which have been assumed to have minimal effect compared with the large number of cross-ribs, and would vary from site to site. Finally, the sound insulation of the wall may degrade with time. On one face of the diaphragm wall at AHS the positioning of vertical rainwater pipes over the construction joints was causing degradation of the joint filler producing access to the inner leaf and a localised reduction of sound insulation performance.

Walls:	UGS	USC	PHS	AHS	MHS	BSC	CR
Rib centres	1.05	1.42	1.24	*	*	1.08	0.69
Number of ribs	34	12	13	*	*	23	6
Rib width (int)	0.348	0.348	0.348	0.348	0.348	0.46	0.585
Length of wall	36	17	16.7	22.5	25.2	24.3	4.1
Height of wall	8.3	7.5	6.68	7.73	7.65	9.25	5.63
Area of wall	298.8	127.5	111.6	173.9	192.8	225.1	23.1
p_c (wet) int.	1670	1521	1678	*	*	*	2160
p_c (wet) ext.	1811	1406	2009	*	*	*	"
p_c (wet) rib	1811	1406	2009	*	*	*	"
p_c (dry) int.	1650	1800	1660	*	*	*	"
p_c (dry) ext.	1820	1660	2060	*	*	*	"
I_{xx}	11.1e-3	10.9e-3	11e-3	10.9e-3*	10.9e-3*	18.4e-3	30.4e-3

Table 9: Details of in-situ diaphragm walls

int. and ext. are internal and external leaves, respectively. Dry and wet are include and exclude mortar, respectively. * denotes estimated values where data is not available.

Air space	Volume	Max. Height	Width	Length	1	2	3
1 : 8 Models							
Diaphragm wall: 7 rib cavity	0.006	0.05	0.125	1	17	1376	3440
3 rib cavity	0.013	0.05	0.25	1	17	688	3440
1 rib cavity	0.025	0.05	0.5	1	17	344	3440
Double wall cavity	0.05	0.05	1	1	17	3440	3440
Source & Receiver Rooms	12.97	1.82	2.48	2.88	60	69	95
1 : 4 Model							
Diaphragm wall cavity	0.047	0.11	0.283	1.5	115	608	1564
T. Suite Source Room	121.2	4.3	4.9	5.75	30	35	40
T. Suite Receiver Room	75.4	3.05	4.3	5.75	30	40	56
Field Measurement							
Typical diaphragm wall cavity	3.5	0.35	1.25	8	22	138	491
Urmston Grammer School Hall	5447	9.5	17	36	5	10	18
Urmston Sports Centre Hall	6273	12	17	36	5	10	14
& Male Changing Room	83	2.4	4.1	8.4	20	42	72
Bebbington Sports Centre	7951	9.3	24.3	35.3	5	7	19
Plessington School Hall	3797	10.8	16.7	26.1	7	10	16
St. Augustines School Hall	4045	11.9	18.4	22.5	8	9	15
Mount St. Josephs School Hall	3840	10.6	18.4	25.2	7	7	16
& Male Changing Rooms	48.5	2.1 *	2.7 *	8.7 *	20	65	83

Table 10: Rooms & cavities

1,2 and 3 denote the cross cavity/room modes. * Not a rectangular room.

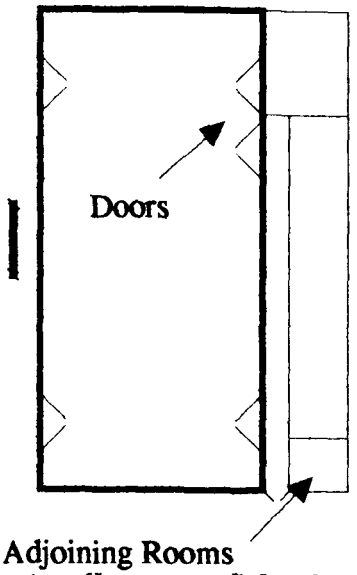

Urmston Grammer School Hall

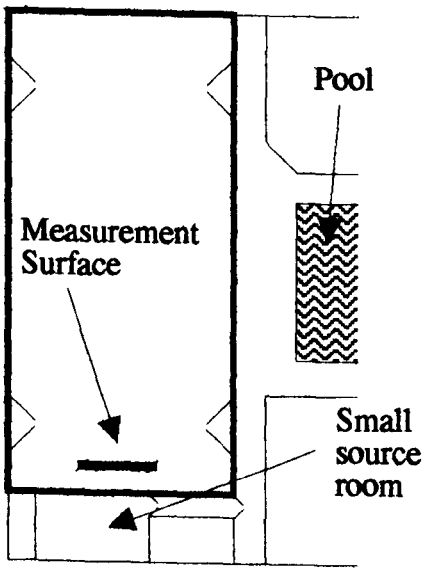

Urmston Sports Centre

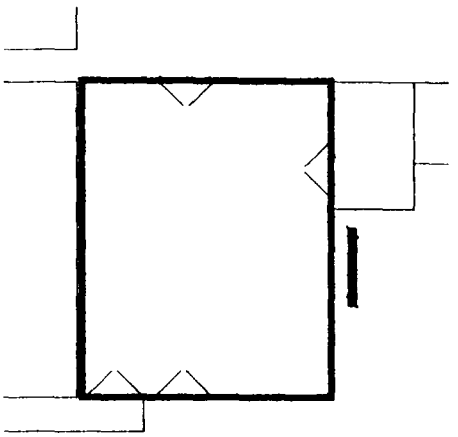

St. Augustines R.C. High School

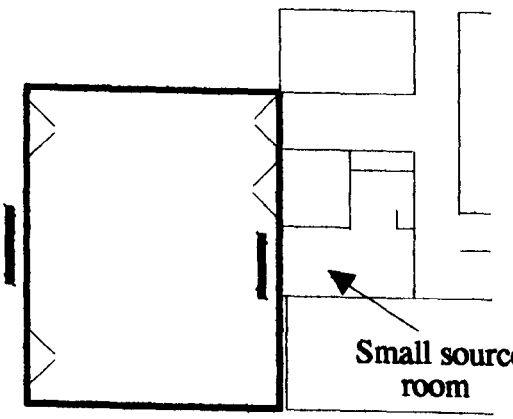

Mount St. Joseph R.C. High School

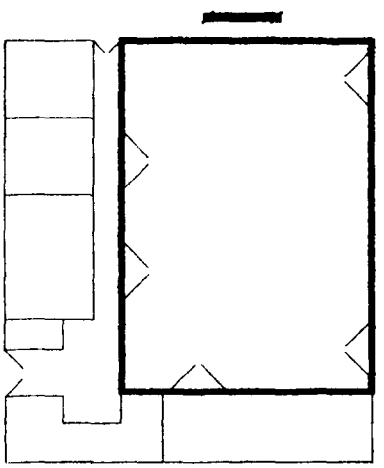

Plessington R.C. High School

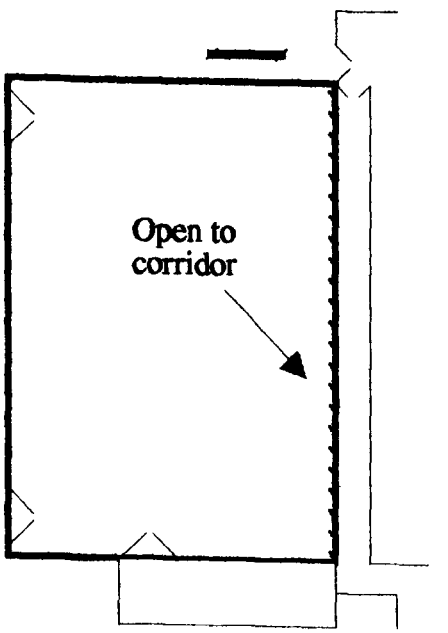

Bebbington Sports Centre

Figure 8.1: Schematic of Field Measurement Sites

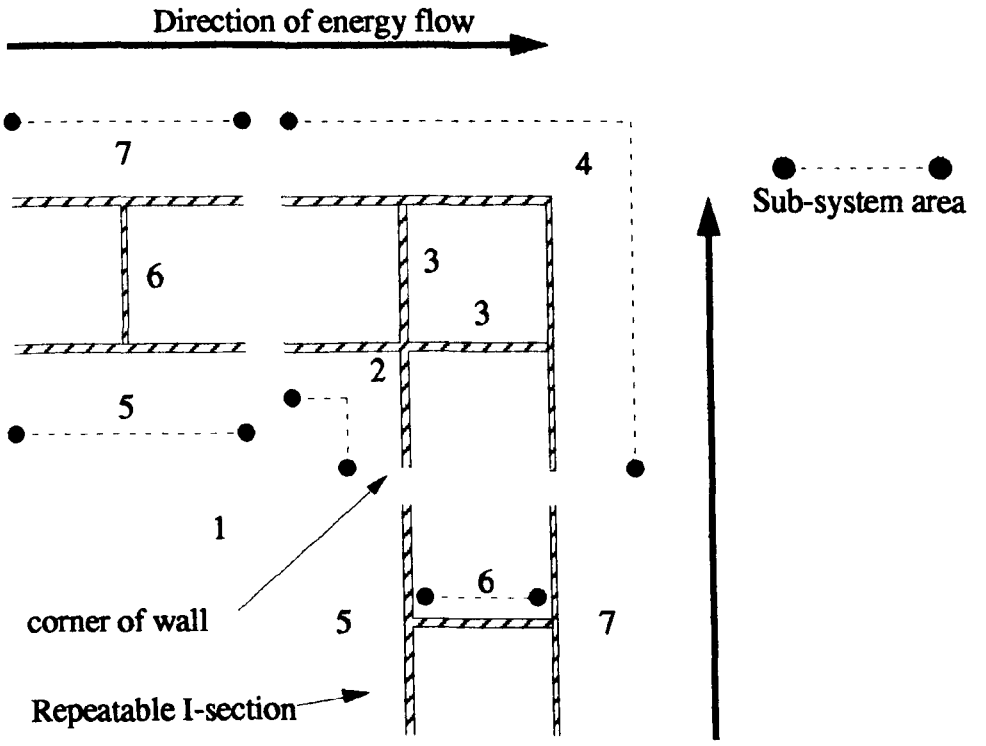

Figure 8.2: Diagram of a corner as an energy sink

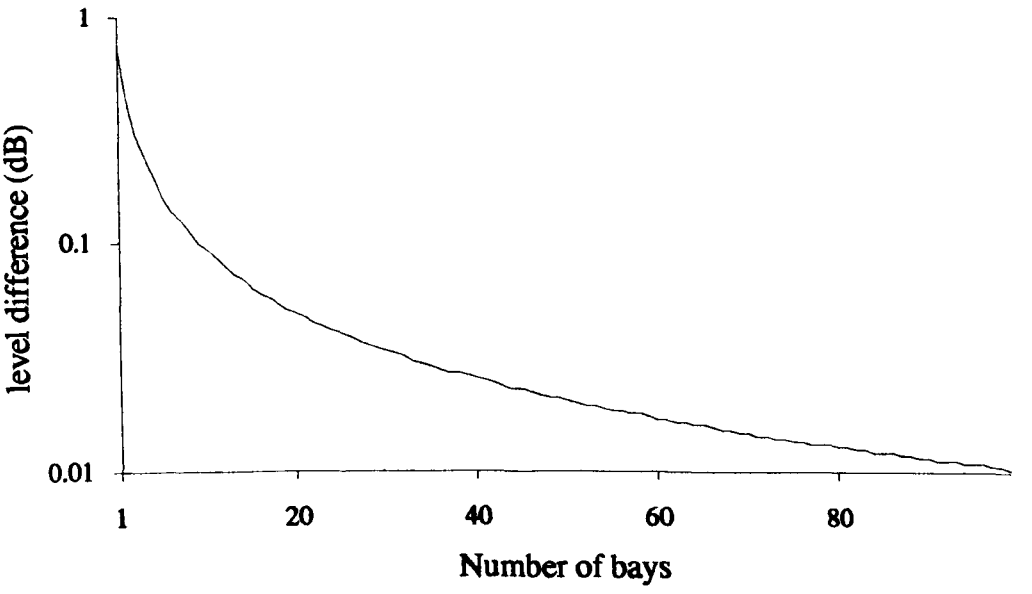

Figure 8.3: Effect of corner on vibrational level difference

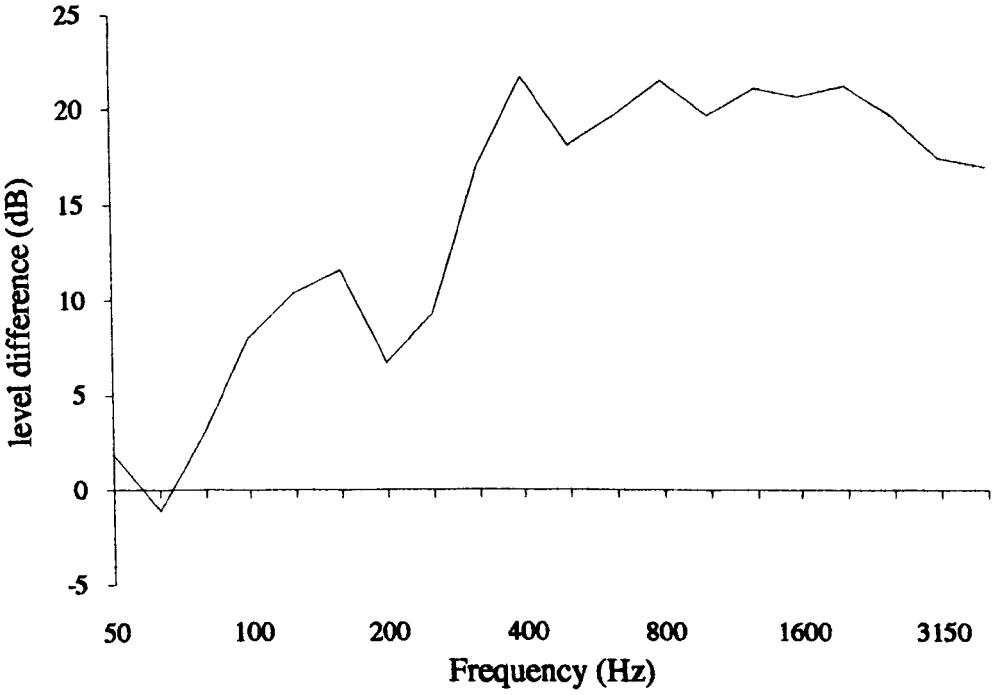

Figure 8.4: Vibrational level difference across a construction joint

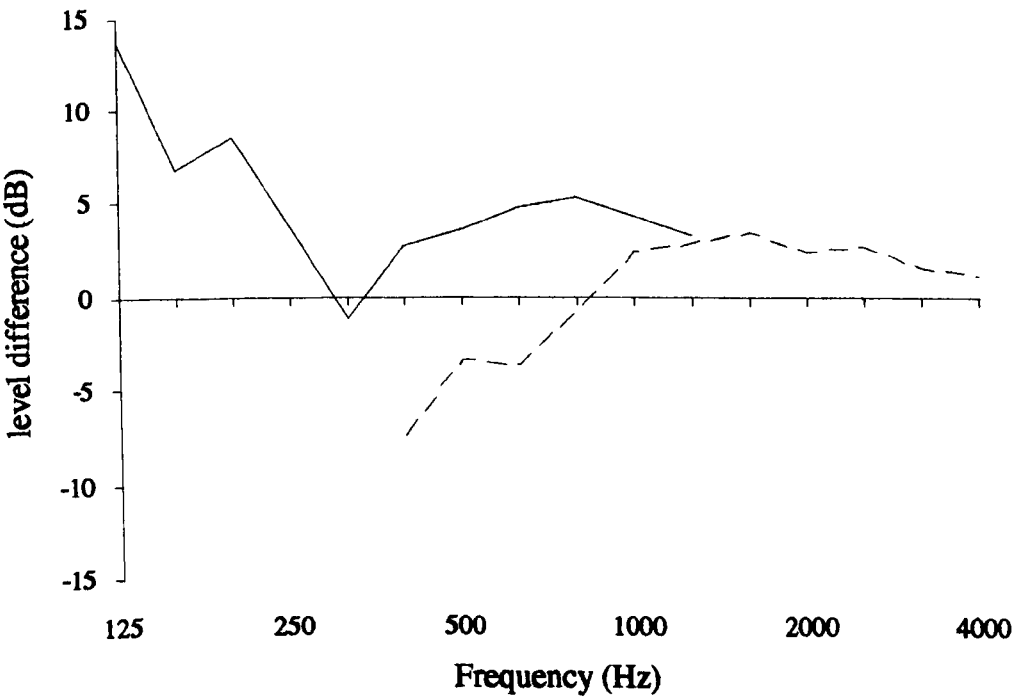

Figure 8.5: Difference between dynamic capability and reactivity index

50mm 12mm

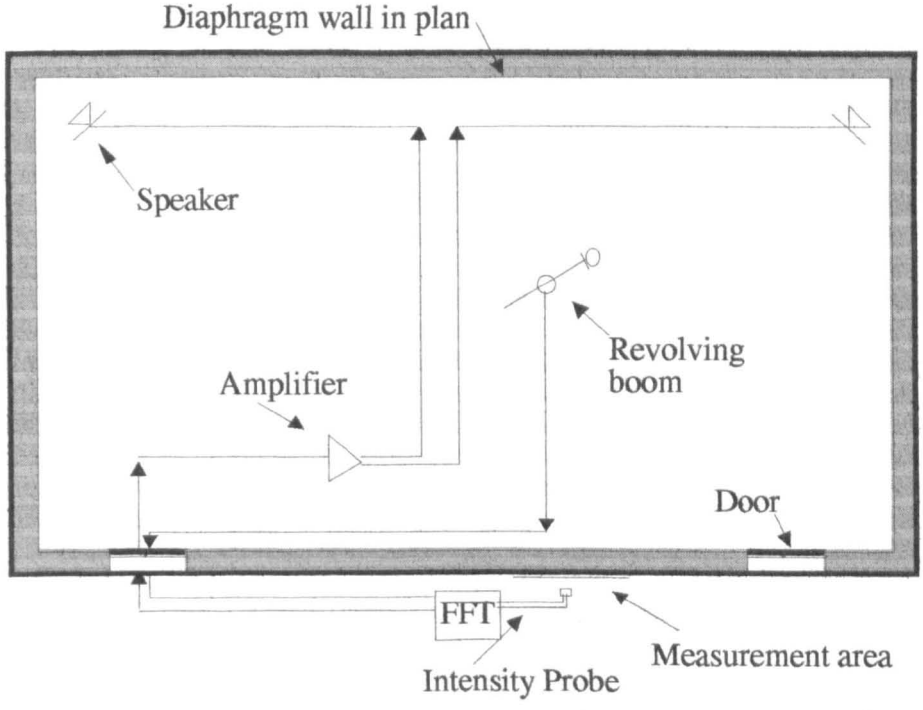

Figure 8.6: Transmission loss measurement set-up

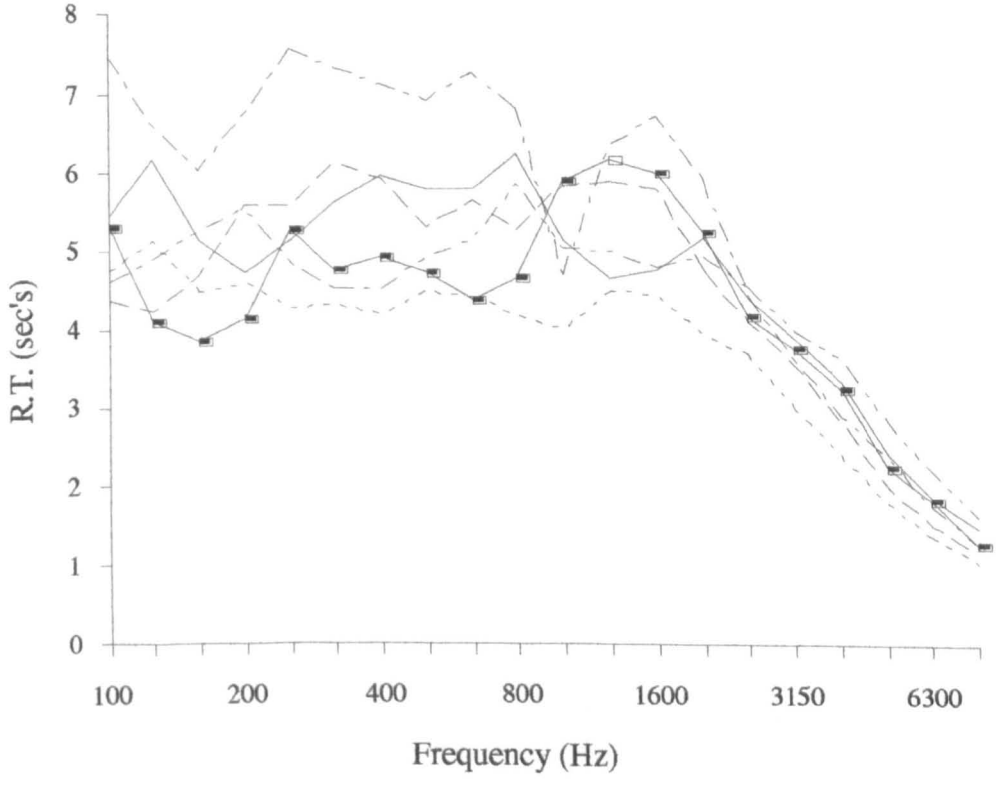

Figure 8.7: Reverberation times of source rooms

MHS UGS USC
PHS AHS BSC

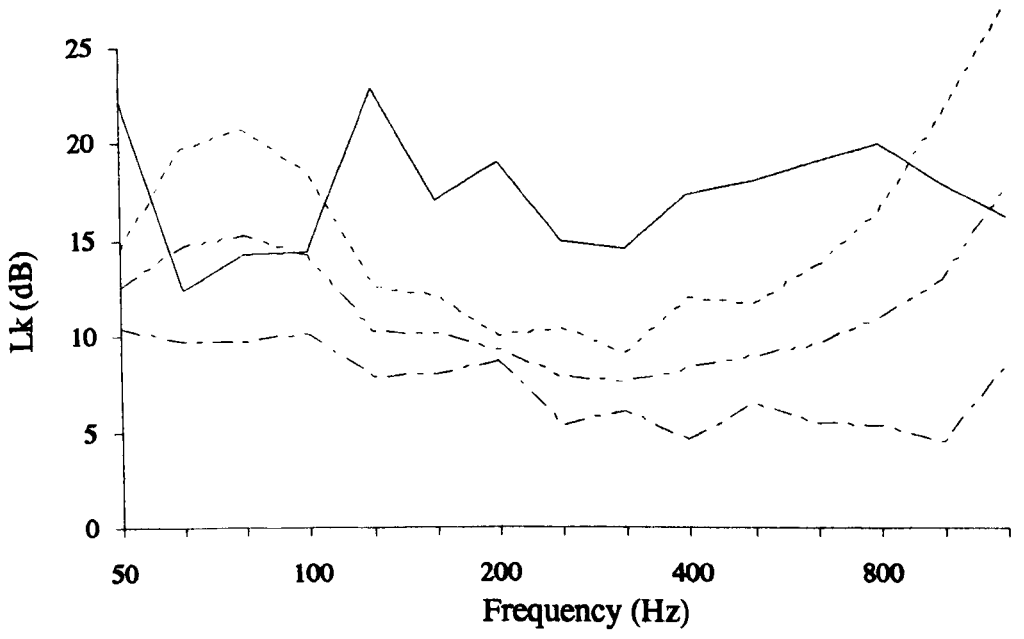

Figure 8.8: Reactivity indices of field measurements

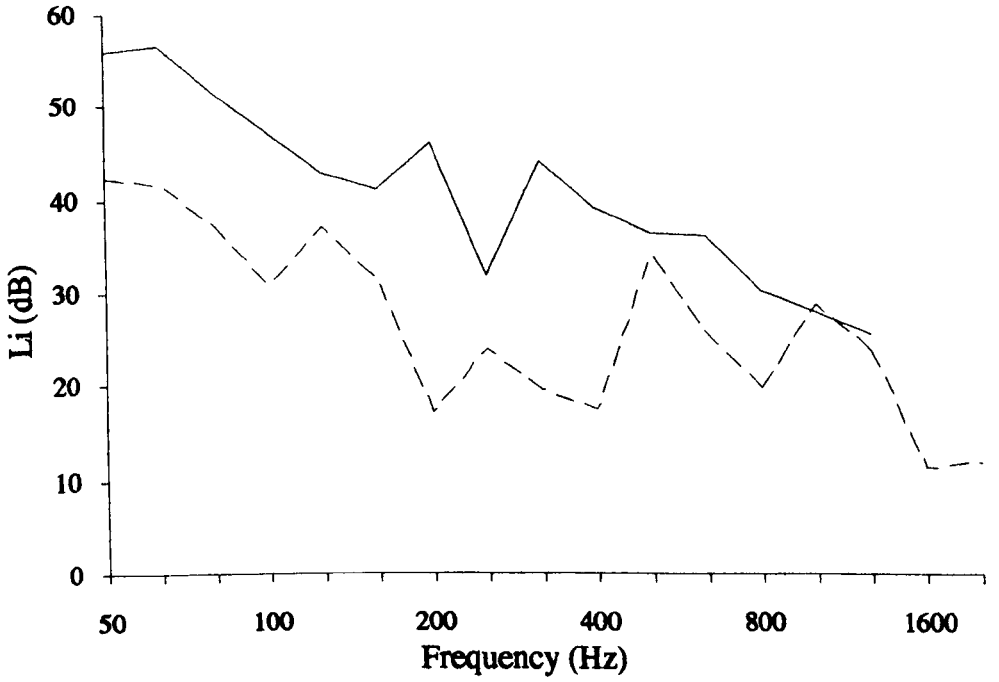

Figure 8.9: Typical background intensity levels.

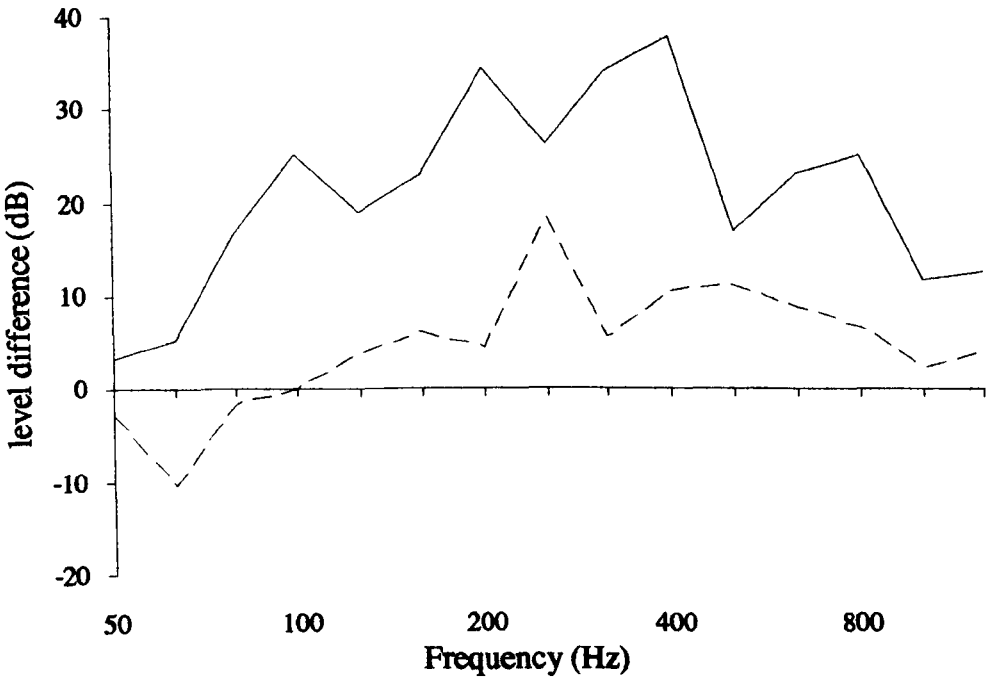

Figure 8.10: Measured intensity levels above background

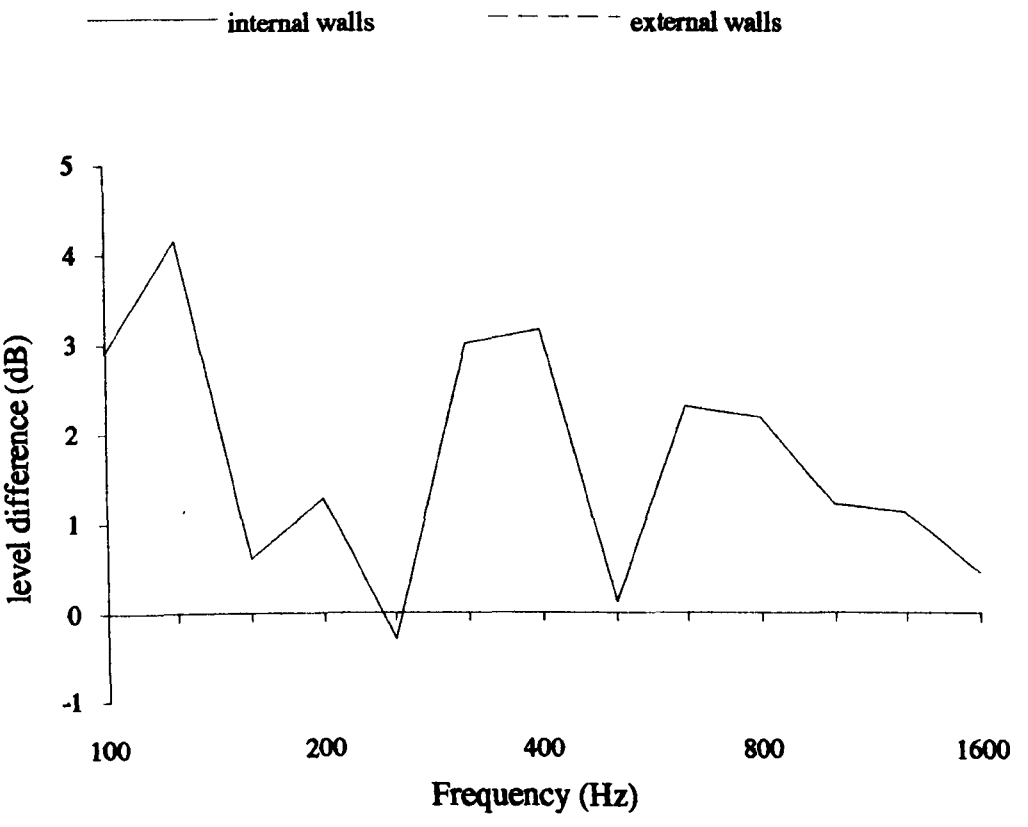

Figure 8.11: Difference in transmission loss between ISO 140/3 and intensimetry methods at USC

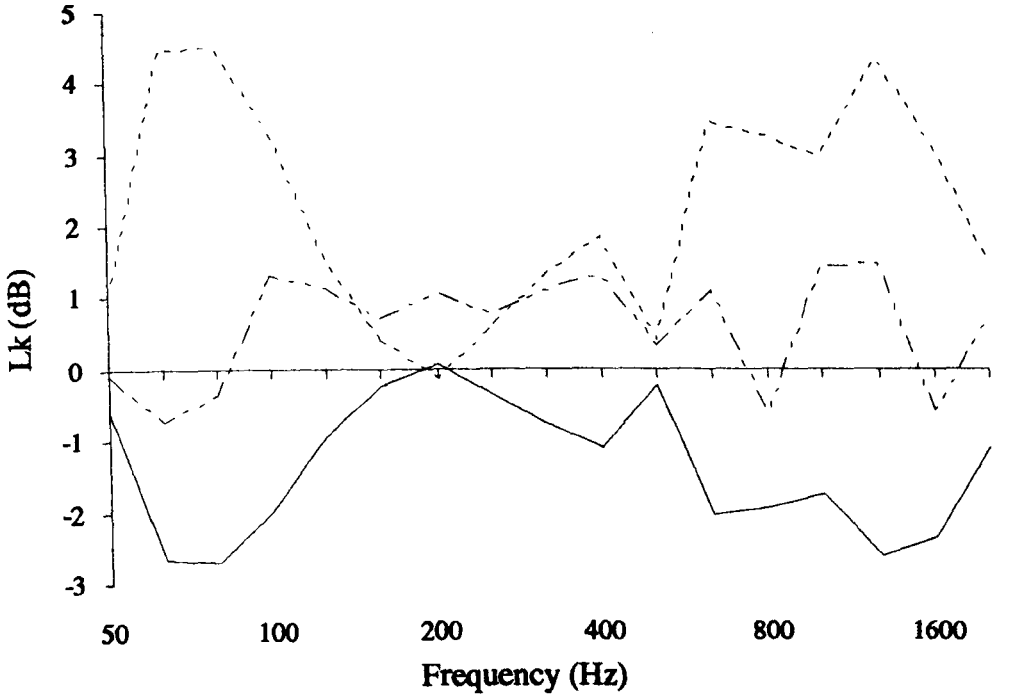

Figure 8.12: Difference in reactivity indices

closed box minus:
- open box
- closed box (external walls only)
- closed box (internal walls only)

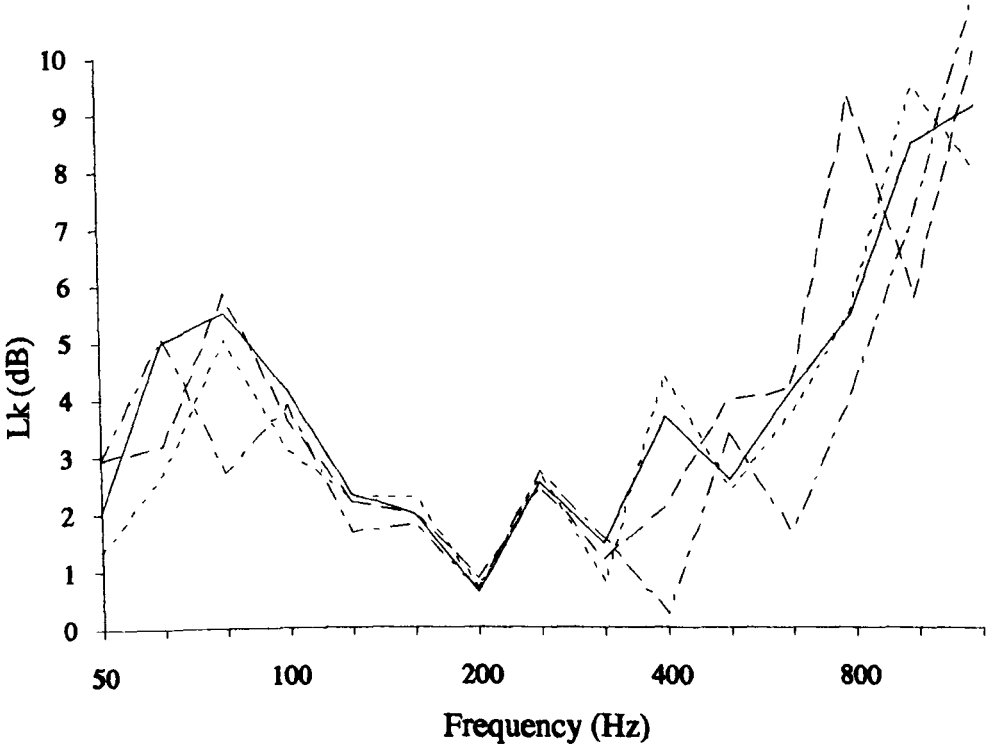

Figure 8.13: Standard deviation of reactivity indices

- open box
- closed box: all walls
- external walls only
- internal walls only

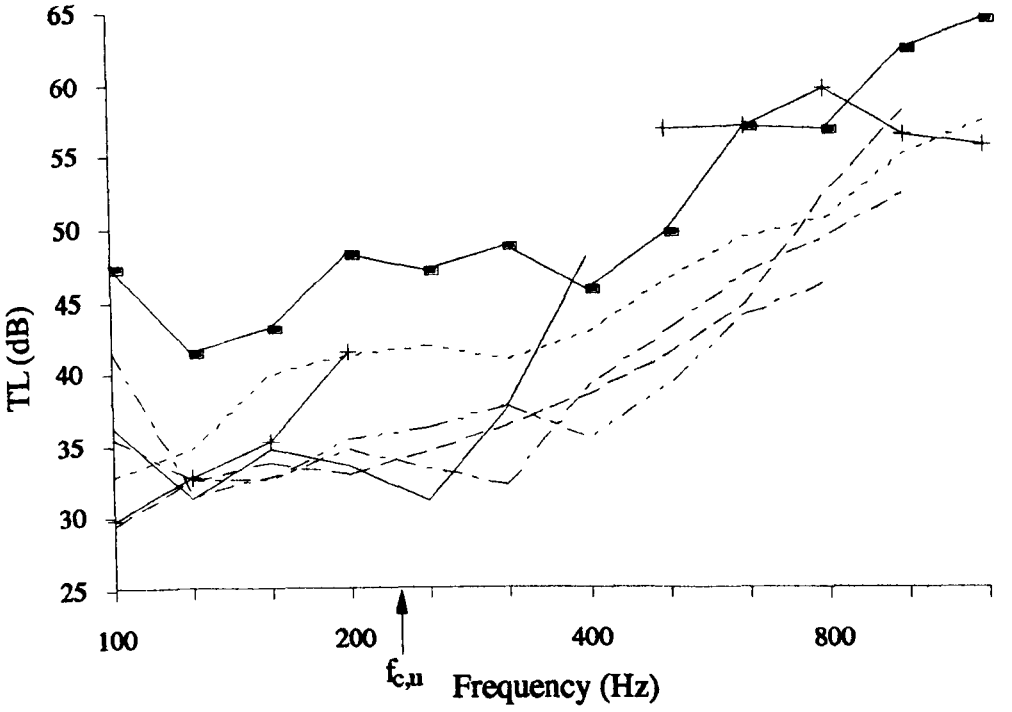

Figure 8.14: Transmission loss measurements of the in-situ diaphragm walls

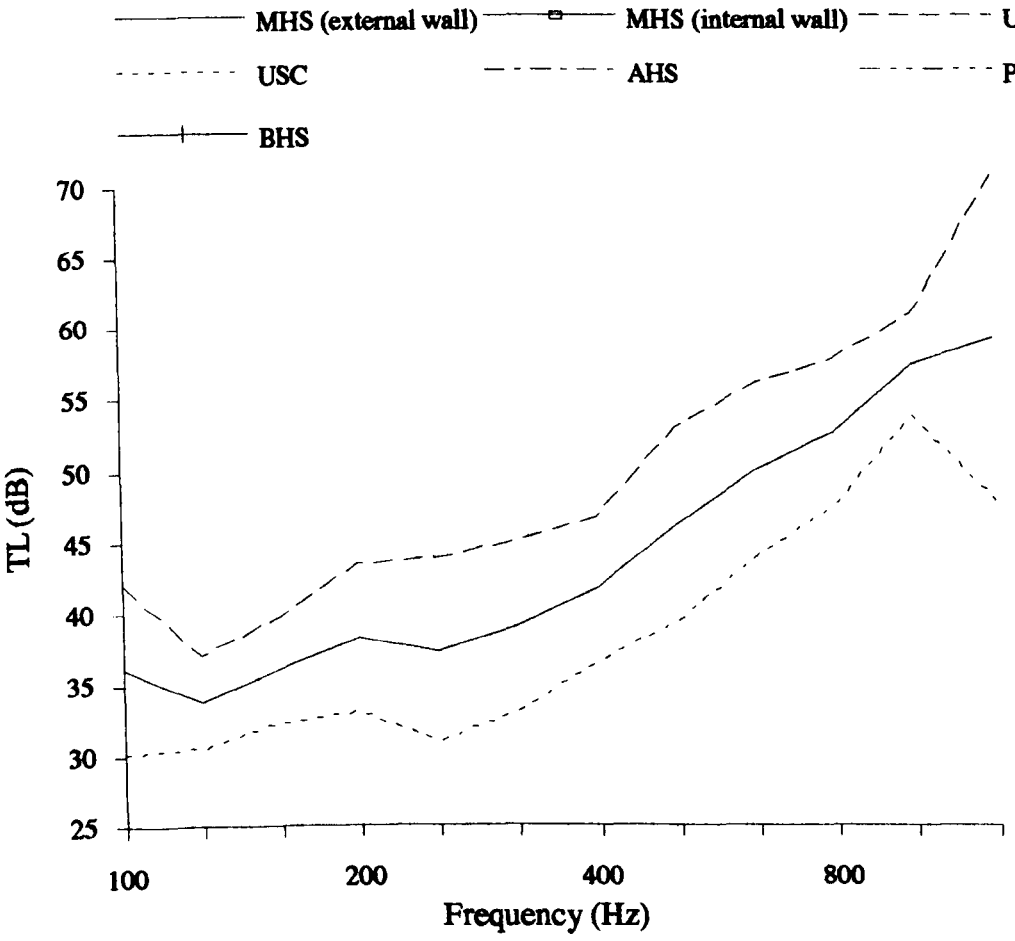

Figure 8.15: Mean and 95% confidence limits

Mean Upper 95% C.L. Lower 95% C.L.

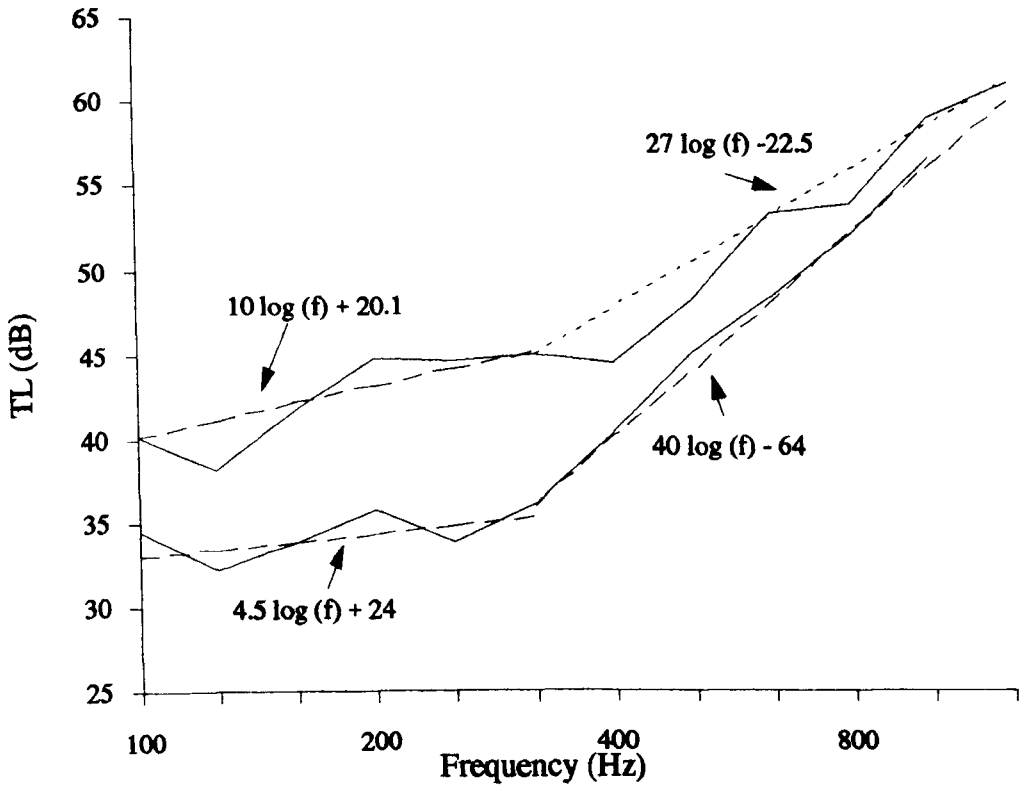

Figure 8.16: Transmission loss regression lines

Upper line: mean of internal walls
Lower line: mean of external walls

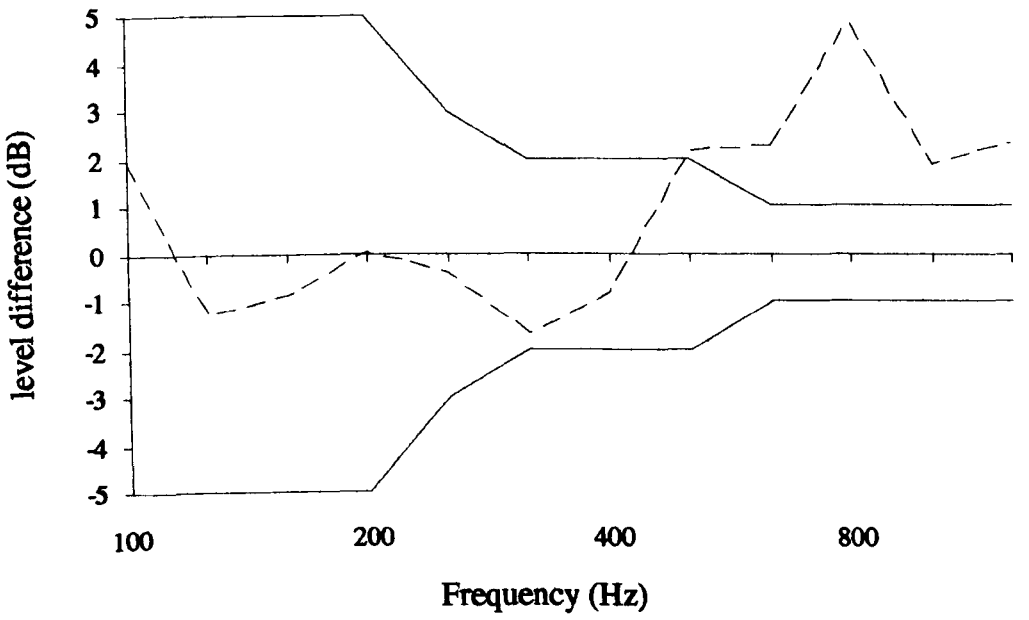

Figure 8.17: ISO 140/2 test for repeatability of measurement

– – – – – level difference ——— repeatability factor: r

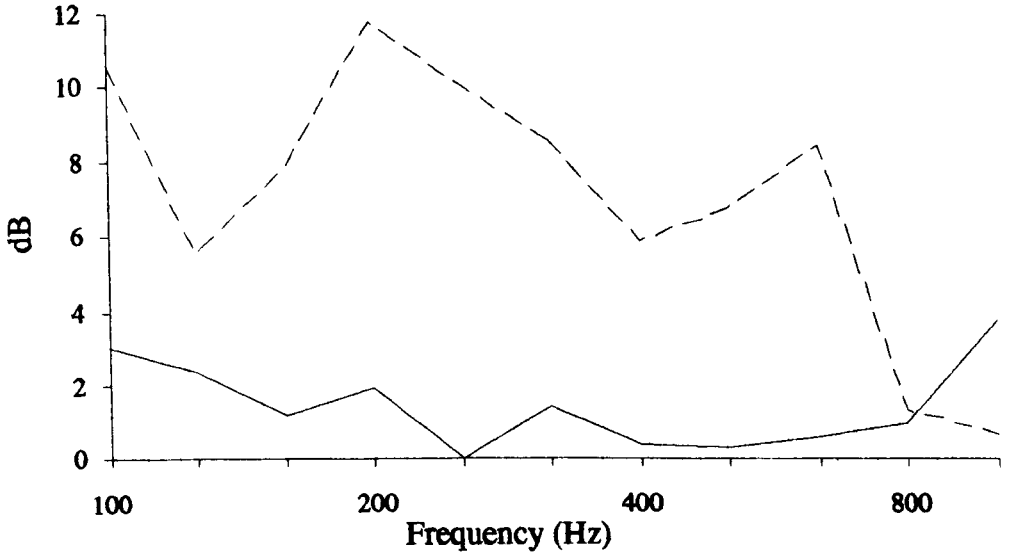

Figure 8.18: Predicted flanking and background noise levels at UGS

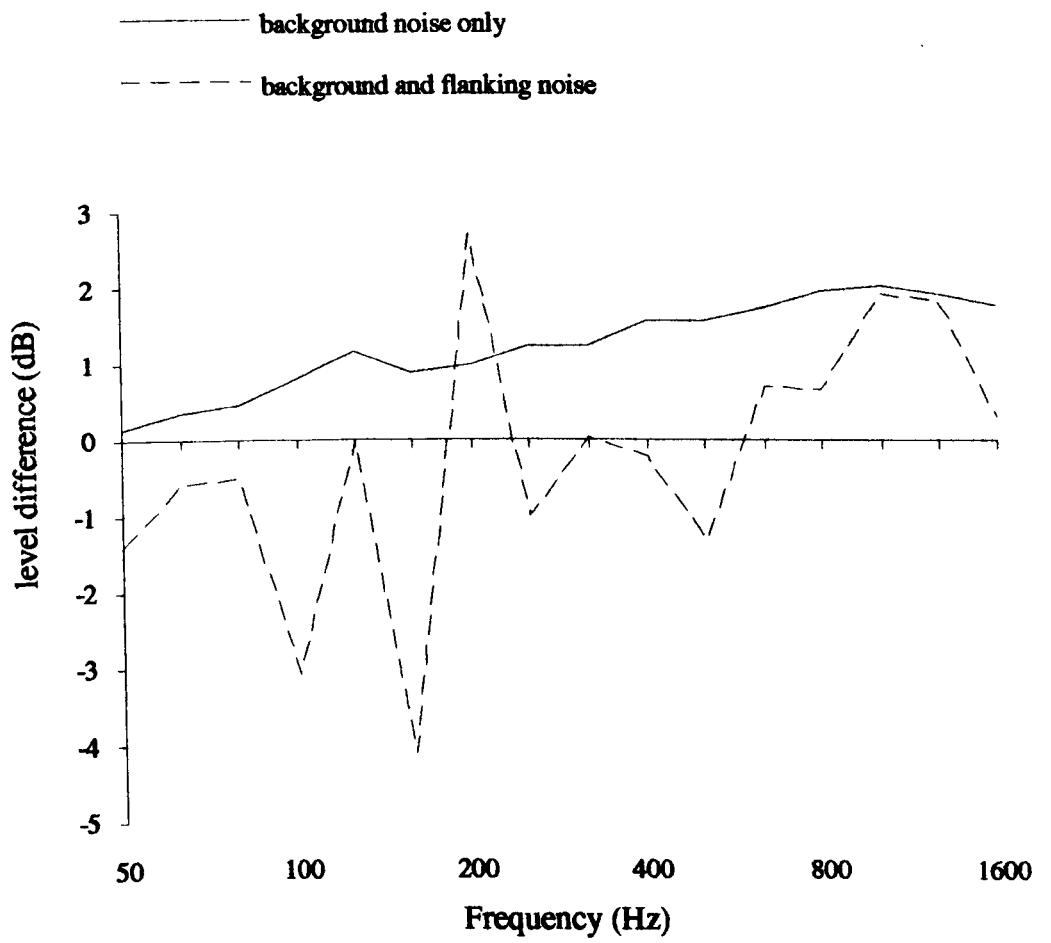

Figure 8.19: Vibrational level difference between leaves of the post-tensioned diaphragm wall

mean of differences (equation 8.3)

difference of means (equation 8.2)

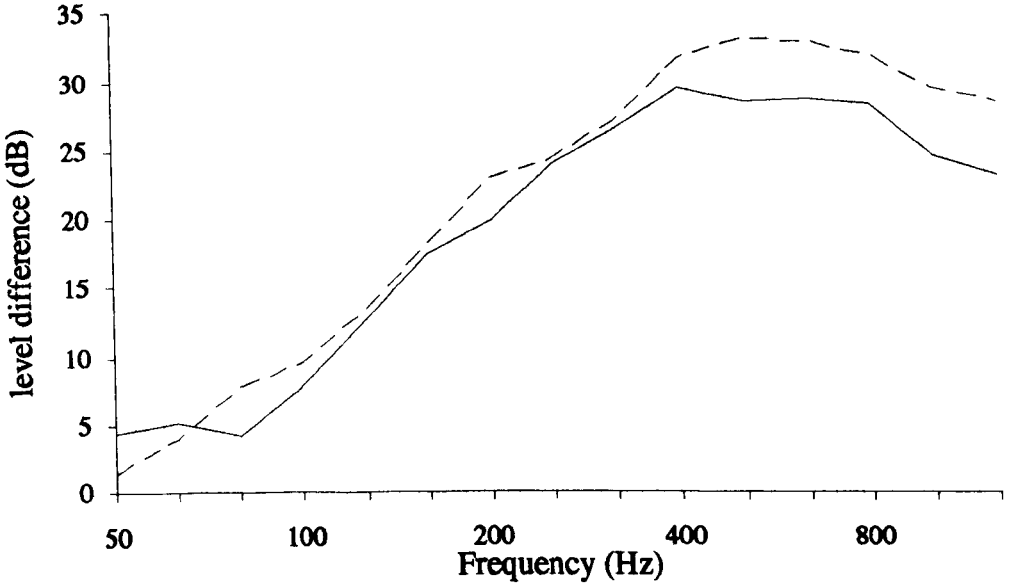

Figure 8.20: Measured acceleration levels above background level

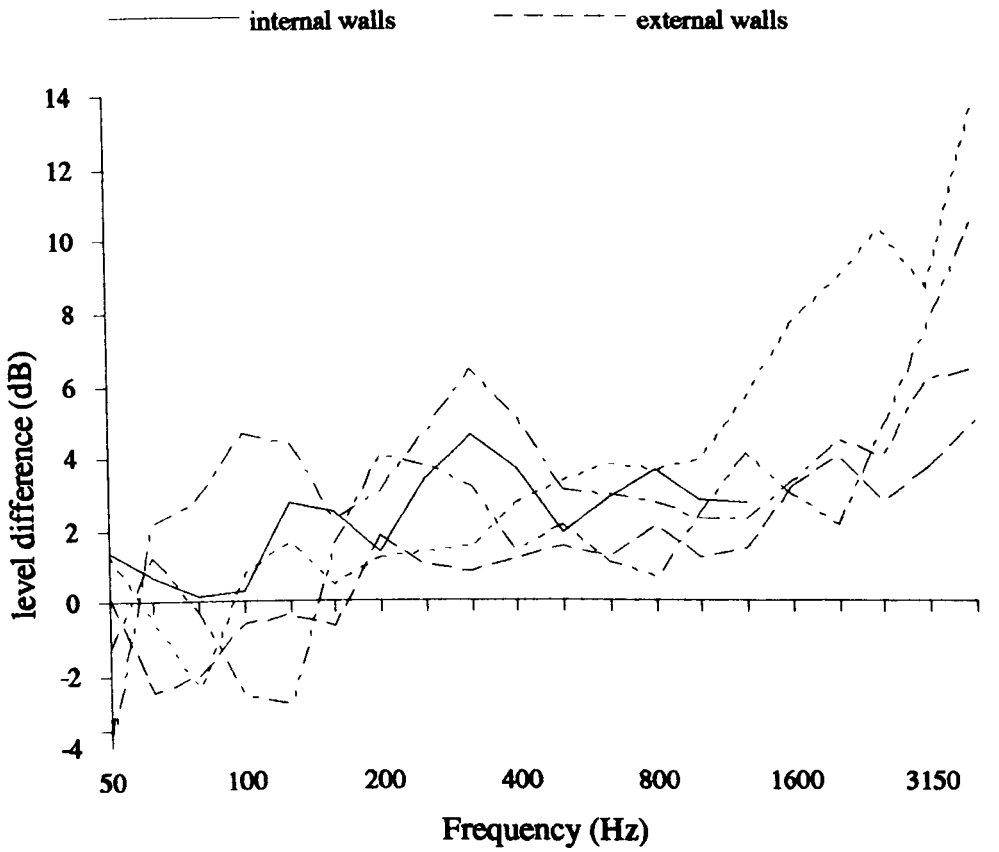

Figure 8.21: Field measurements of vibrational level difference between leaves

UGS
USC
AHS
MHS (external wall)
MHS (internal wall)

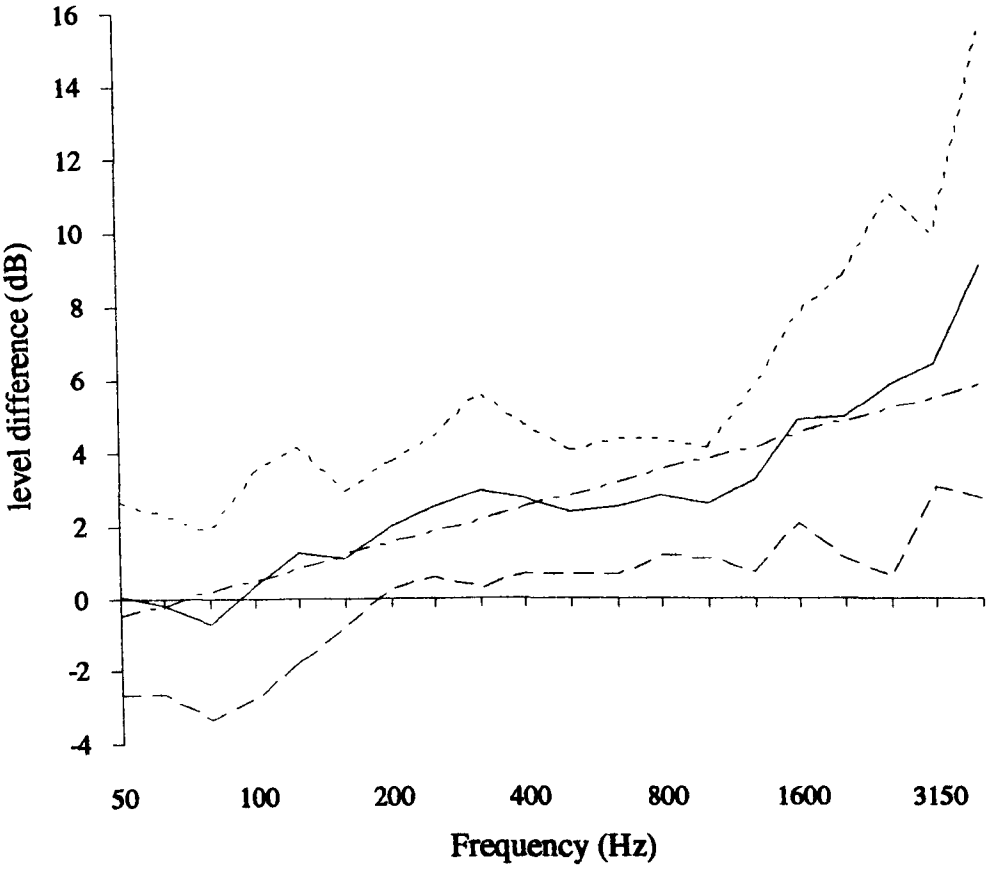

Figure 8.22: In-situ vibration level difference between leaves: mean and confidence limits

Upper 95% C.L.
Mean
Lower 95% C.L.
Regression line: 3.3log(f) -6.2

9 PREDICTION AND OPTIMISATION OF TRANSMISSION LOSS

9.1 INTRODUCTION

In chapter 7 the 5 sub-system SEA model was shown to give good agreement with the measured scale diaphragm walls. In this chapter the transmission loss is predicted for the reliable field measurements, identified in chapter 8, to further validate the SEA model. The analytical model is then applied, through a parametric survey, to estimate the variation in transmission loss likely within the present range of geometries and materials used for this construction. In addition, the associated range of single figure ratings is calculated. Finally, the effect on transmission loss of de-coupling one leaf is predicted as a method of further optimising diaphragm wall performance.

9.2 PREDICTION OF TRANSMISSION LOSS

In order to predict the transmission loss of full scale diaphragm walls, using SEA, the characteristics of a source and receiver room must be defined. Let us assume that the diaphragm wall is positioned between two identical halls with the same dimensions and reverberation times as the measured hall. To predict the sound level difference between the rooms the SEA model requires the loss factor of the receiver room. This was assumed to be that measured in the source room calculated from its reverberation time given by equation 7.15. The transmission loss is calculated according to the equation 3.11. An estimation of the longitudinal wavespeed through the masonry was also required. As masonry is a composite construction the effect of both brick and mortar must be included. Craik [153] observed that longitudinal wave speeds across a masonry wall were greater in the horizontal direction than the vertical direction for all types of brick and block walls

investigated. This maybe due to the larger mortar/brick ratio in the vertical direction.

Figures 9.1 and 9.2 show the measured transmission loss of the USC and MHS diaphragm walls, respectively, compared with the prediction by the 5 sub-system SEA model and the simple orthotropic theory given in chapter 6. The frequency range is limited to that valid for the intensity measurement. For the USC wall, agreement with SEA prediction is within 1 dB above 160 Hz. The simple theory gives values lower than the SEA prediction, but still agrees with measurement within 1 dB above 400 Hz. Below 400 Hz the simple theory gives an under-estimate of about 5 dB. For the MHS wall, there is a greater fluctuation in measurement. However the SEA prediction lies within 3 dB of measurement, while simple theory gives an under-estimate of between 3 - 7 dB. From these two cases the SEA prediction clearly gives the best fit, indicating that the more sophisticated model is required, particularly at low and mid frequencies.

9.3 PARAMETRIC SURVEY

If we accept from all the results presented so far that the SEA model gives the most accurate predictive tool, then it can now be used to estimate the transmission loss of proposed fictive diaphragm walls. Let us consider the likely values of transmission loss that could be obtained for a diaphragm wall by changes in its geometric and material parameters. Earlier indications with respect to transmission coefficients across junctions, in Chapter 6, suggest only small variations of 1 - 2 dB might be expected.

Results are presented as transmission loss normalised with respect to a typical value for a monolithic diaphragm wall, with material parameters in the middle of the range. The wall is of dimensions 20 m x 8 m, with ribs at 1.25 m centres and 0.35 m

wide: ρ_c = 1850 Kg/m^3 and c_L = 2350 m/s. Figures 9.3 - 9.7 show normalised level differences; a positive value indicates a larger transmission loss and vice versa.

Figure 9.3 shows the predicted change due to variation of the cross-rib width between 0.2 m and 0.5 m. The x-axis denotes the 0.35 m case. The transmission loss varies by no more than ± 2 dB; the longer the cross-rib, the greater is the transmission loss due to the increase in wall mass. However at frequencies between $f_{c,l}$ and $f_{c,u}$ this variation is much smaller, only effected by the changing slope of the plateau as $f_{c,l}$ alters.

Figure 9.4 shows the predicted changes in transmission loss due to variations in cross-rib centres. The x-axis is for 1.25 m spacing and the variation is between 1 m and 1.5 m. Values of transmission loss are within ± 1.5 dB, with maxima at $f_{c,u}$. A higher transmission loss occurs with smaller rib centres due to the increase in overall mass. Between $f_{c,l}$ and $f_{c,u}$ the variation is slightly less for the same reason as given for the previous figure. This is less significant than in figure 9.3, as a change in the rib numbers does not influence the moment of inertia as much as a change in the wall width.

A variation in material parameters was also considered. The normalising wall was ρ_c = 1850 Kg/m^3 and c_L = 2350 m/s. Two practical extremes were considered; a lightweight concrete wall and a dense brick wall. Figure 9.5 shows the variation by altering the material qualities of one leaf only. The results unsurprisingly show an increased transmission loss with a heavier leaf, due to both the greater mass and change in the structure-borne transmission coefficient across the junctions. Variations lie between -3 dB and +2 dB and can be considered as frequency invariant. In figure 9.6 both leaves are altered producing a slightly greater variation in transmission loss, between ± 3 dB.

It has been shown that variations in the geometric and material characteristics of the diaphragm wall, within present constructional limits, will offer improvements in transmission loss of the order of 3 dB for material changes and 2 dB for geometric changes. A doubling of the cross-rib width has little effect, changing the transmission loss by less than 0.6 dB.

9.4 RATING & PRACTICAL EXTREMES

To simplify the representation of possible improvements or otherwise in diaphragm configurations, the single figure rating R_w was used, given by ISO 717/3 [154]. A wall performance is rated by shifting a reference curve onto the measurement curve until the mean unfavourable deviation is less than 2 dB. An unfavourable deviation at any frequency occurs when the measurement value is less than the reference value. When this criteria is met the rating curve value at 500 Hz is R_w. Before considering rating values it should be realised that the method has limitations in its use since it is greatly influenced by a large discrepancy at any one frequency, giving a misleading representation of a material's sound insulation. Table 11, below, shows the measured and predicted ratings for all the full size diaphragm walls. For the measured transmission loss, where a value was unable to be measured at a particular frequency an estimate was made. In the plateau region interpolation was used, below the first measured frequency a flat transmission loss is assumed, and above the last measured frequency a 10 dB/octave rise is assumed.

Table 11: R_w values for full size diaphragm walls

Wall	Measurement	SEA prediction	Simple prediction
USC	51	52	49
USC (ISO 140)	54	52	49
MHS (internal wall)	56	56	52
MHS (external wall)	50	56	52

AHS (external wall)	46	55	52
UGS (external wall)	46	56	51
PHS (external wall)	46	53	50
BSC (external wall)	54	56	52

The reliable measurements at USC and MHS give an R_w of 51 - 54 dB and 56 dB respectively, while the other in-situ wall measurements, which suffered from flanking and background noise problems, rate lower, between 46 - 54 dB. As would be expected, the SEA predicted rating is within 2 dB of the reliable measured values. Hence, using the SEA prediction as a 'true' rating of the other in-situ walls these now lie between 52 - 56 dB. If we assume that the in-situ walls measured are atypical of this construction, then we can estimate that a typical wall will lie within this same range. The simple orthotropic theory is seen to predict R_w at 3 - 4 dB below reliable measurements and therefore is not considered further.

From the parametric survey two practical extreme conditions of transmission loss can be estimated theoretically: a lightweight concrete wall with a 0.2 m cross-rib at 1.5 m centres, and a heavyweight masonry wall with 0.5m cross-rib at 1 m centres. The transmission loss of these two walls is given in figure 9.7. The lightweight wall is rated 49 dB and the heavyweight as 58 dB. Above $f_{c,u}$ the predicted transmission loss differs by approximately 9 dB. This is the practical scope of transmission loss probable for a diaphragm wall, which is due partially to the variation in mass but more significantly to the shift in the critical frequency due to the change in estimated longitudinal wavespeed. The change in $f_{c,l}$ and $f_{c,u}$ of these two walls, for two geometric configurations, is given in table 12. These configurations show the widest range in critical frequencies that could be expected.

Table 12: $f_{c,l}$ and $f_{c,u}$ for two wall configurations

Critical frequency	Lightweight concrete	Heavyweight masonry
$f_{c,u}$ (Hz)	370	200
cross-rib width and centres		
$f_{c,l}$: (Hz) 0.2 m 1.5 m i)	53	27
$f_{c,l}$: (Hz) 0.5 m 1 m ii)	27	14

Figure 9.8 shows the difference between the two extreme geometric cases for both the heavy and lightweight walls. Except for the shift in $f_{c,u}$, due to the change in longitudinal wavespeed, the same pattern is seen in both cases. For the same construction a higher transmission loss is produced where a lower value of $f_{c,l}$ occurs. Above $f_{c,u}$ the difference in transmission loss is simply due to change in mass. Around $f_{c,l}$, agreement between geometries is within 1.5 dB. The slightly falling slopes being due to the transmission loss gradient of the wall with the lower $f_{c,l}$ being less than that of the wall with a higher $f_{c,l}$.

To summarise, the R_w value for a diaphragm wall would typically be expected to lie between 52 - 56 dB with a potential maximum of 58 dB if a heavyweight masonry wall is built with 0.5 m cross ribs, centred every 1 m. Compare this with a series of unplastered traditional walls [25], a single 1/2 brick wall, R_w = 45 dB; a 1 and a 1/2 brick wall, R_w = 51 dB; or a traditional cavity wall R_w = 53 dB. Note that these values can vary significantly and will increase if plastered.

9.5 STRUCTURAL DE-COUPLING AT JUNCTIONS

It was shown in chapter 5, through model measurement that structural de-coupling of one leaf from the cross-ribs would significantly improve the transmission loss of a diaphragm wall. In addition it has been shown that the cross-ribs should not be broken at their centre as both leaves would still radiate orthotropically and the

plateau in transmission loss would remain (see figure 5.25). It was shown to be better to de-couple the diaphragm wall at one cross-rib/leaf junction, as this would create one orthotropic and one isotropic leaf. This eliminated the plateau region, due to the dominance of the isotropic radiation resistance.

We can examine the potential improvements in transmission loss by such de-coupling using the SEA model. The 6 sub-system model is required as energy transmission via the cavity path will now become more important. The wall is theoretically de-coupled by changing the transmission coefficient, γ, between the wall leaves and thus the structural coupling loss factor, given by equation 7.7. Let us first assume a total de-coupling of the one leaf from the rest of the wall. Thus $\gamma = 0$, so energy can only be transmitted across the wall via the cavity path. This represents the theoretical maximum optimisation possible for the wall by this method, although it's impossible to construct as the single isotropic leaf is structurally unstable, with a slenderness ratio > 100. The de-coupled leaf radiates isotropically and the coupled leaf still radiates orthotropically. Also, the non-resonant path between the rooms based on the mass of the whole wall, described by η_{19}, does not occur as the wall is now two separate constructions. Strictly, the non-resonant coupling between room and cavity for each leaf [137] and the cross-cavity non-resonant path [139] will become more important and should be included. Yet the inclusion of such non-resonant paths, as has been seen previously in figures 7.7 - 7.9, sets a maximum value on the transmission loss.

Figure 9.9 shows the predicted level difference between the transmission loss obtained for a typical monolithic coupled diaphragm wall (with 0.35 m ribs at 1.25 m centres) and the transmission loss from two de-coupled diaphragm walls, where $\gamma = 0$. Two cases are; where the separation is at one cross-rib/leaf junction and for two interlocking fin walls with ribs at 1.25 m centres (see figure 5.24). The de-coupling produces an increase in transmission loss, except about coincidence,

where there is a reduction of between 1 - 3 dB. The large increase at low frequencies is due to changes in radiation resistance. This is greater for the single leaf due to its isotropic leaf. The increase at higher frequencies is due to the exclusion of the non-resonant coupling loss factor, η_{19}.

Partial de-coupling may be possible but some connection will always be required between leaf and cross-rib to ensure structural stability. The possibility of leaving, for example, a 10 mm gap between leaf and cross-rib connected only by ties, would probably require shear ties on all courses [155]. Let us consider three values of γ, 0.1, 0.01, 0.001, the monolithic case being where $\gamma = 0.15$ (see section 6.5.2). Note that the degree of de-coupling will influence the iso/ortho-tropicity of the un-coupled leaf, and also determine the degree of structural non-resonant transmission at low frequencies. The change in transmission loss with respect to the monolithic case is shown in figures 9.10 and 9.11, for variations in γ. Figure 9.10 shows the case of the partial de-coupling of an orthotropic leaf including the non-resonant path, and figure 9.11 shows the partial de-coupling of an isotropic leaf excluding the non-resonant path.

In figure 9.10 it is surprising to see that a decrease in transmission coefficient produces a lower transmission loss, but only by 1.3 dB, in the low and mid frequencies. This is difficult to explain, though the modal energy of the cross-rib will rise with the reduction in the value of γ, and so increase the energy coupling to the cavity and then to the outer leaf. The variation is small suggesting that the type of cross-rib link could vary significantly and not influence the overall transmission loss greatly, assuming a non-resonant transmission across the wall and no change in its orthotropic character.

In figure 9.11 the isotropic character of the partially de-coupled leaf dominates, and as in figure 9.9, produces a large increase in transmission loss at low frequencies.

Above $f_{c,u}$, the radiation resistance is not different to the monolithic case and thus the increase in transmission loss is due to the increased importance of the cavity path, as the cross-rib path reduces. However, it is only at the highest frequencies that the cavity path can be said to dominate transmission. This would not have been seen if the non-resonant path between rooms had been included. The difference between the values when $\gamma = 0$ in figure 9.9, and $\gamma = 0.001$ here is less than $\pm$ 0.1 dB, and the variation between the curves for $0.001 > \gamma > 0.1$ is less than 1 dB upto 2 kHz; indicating that it is not the cross-rib transmission coefficient that is important but rather the leaf radiation character. The reduction in transmission loss at coincidence is due to change in the isotropic R_{rad} curve.

For all these cases the rated values vary by only 2 dB as the greatest increases in transmission loss are below or above the rating frequency range of 100 Hz - 3.15 kHz.

Finally let us consider if the 5 sub-system SEA model, which excludes the cavity, is suitable for non-monolithic constructions. From the results of figures 7.28 and 7.29 earlier, it was concluded that the 5 sub-system model was acceptable for practical, existing diaphragm wall constructions. The 5 sub-system model yielded predicted values of leaf to leaf vibration level difference within 0 - 1 dB and transmission losses within 2 - 3 dB of values obtained by the 6 sub-system model. Figures 9.12 and 9.13 show the level difference between the 6 and 5 sub-system SEA models for vibration level difference between leaves and transmission loss, respectively, with three values of γ. Figure 9.12 shows the 6 sub-system model produces a lower vibration level difference by up to 1.5 dB at 400 Hz than the 5 sub-system model, as γ decreases, indicating the importance of the cavity path. In terms of transmission loss, in figure 9.13, the difference can be up to 5 dB. Where $\gamma = 0.001$ this actually produces a lower transmission loss using the 6 sub-system model. It is therefore

concluded that for non-monolithic designs it is better to include the cavity transmission path as it becomes increasingly important.

9.6 CONCLUDING REMARKS

Reliable field measurements of diaphragm walls have been compared with theoretical prediction, agreeing best with the SEA approach. The SEA 5 sub-system model has been shown to be sufficient for prediction of presently built diaphragm constructions.

The parametric survey showed that possible changes in material and geometric parameters will result in variations in transmission loss of the order of 2 or 3 dB.

The rated performance of diaphragm walls is between 51 and 56 dB, with a potential maximum of 58 dB using a dense masonry construction with 0.5 m wide ribs at 1 m centres.

The effect of partial de-coupling one leaf of the diaphragm wall is difficult to assess and requires assumptions on how the leaf will radiate. If isotropic radiation can be assumed for the de-coupled leaf, potential improvements of 5 - 15 dB are theoretically possible in the frequency region 50 - 200 Hz and of 5 - 10 dB at high frequencies. If the wall is assumed strongly coupled up to $\gamma = 0.001$ and orthotropic in character, then there is little change possible, 1 dB at mid-frequencies. The author is inclined to think that the actual transmission loss will lie between the two cases. As the leaf is increasingly de-coupled it will become more isotropic in character, but at the same time, the cavity will become more important as an energy transfer path.

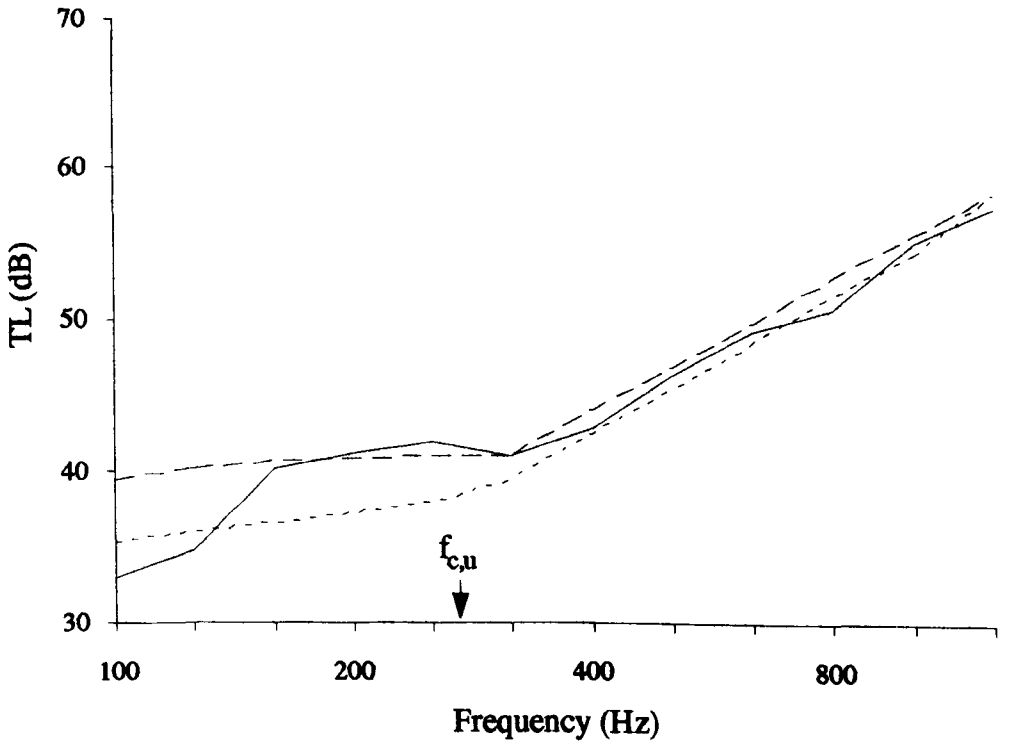

Figure 9.1: Transmission loss of USC

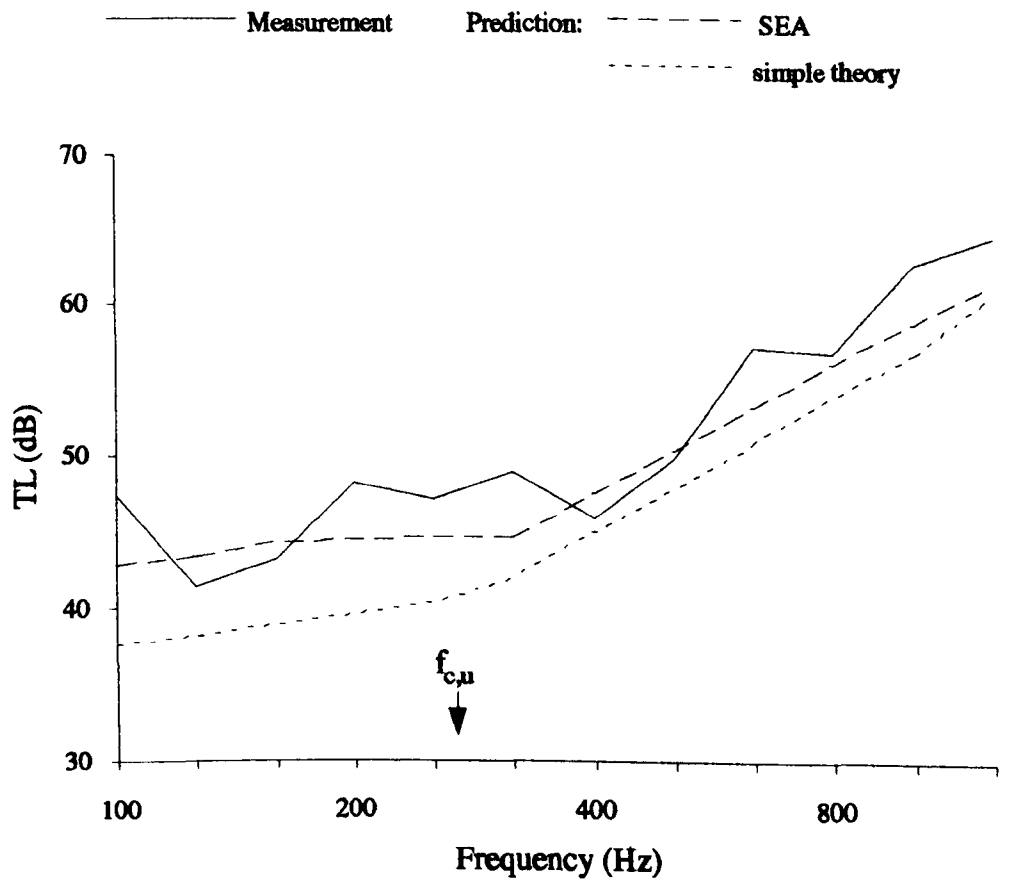

Figure 9.2: Transmission loss of MHS

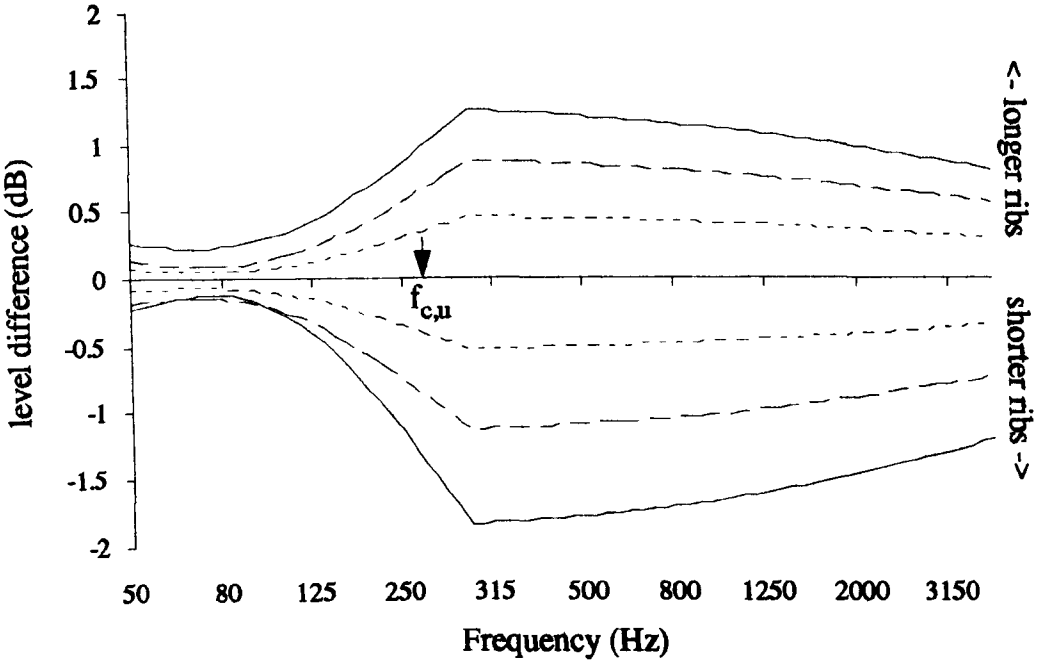

Figure 9.3: Change in transmission loss with variation in cross-rib width

0.35 m cross-rib ± :

——— 0.15 m - - - - - 0.1 m ····· 0.05 m

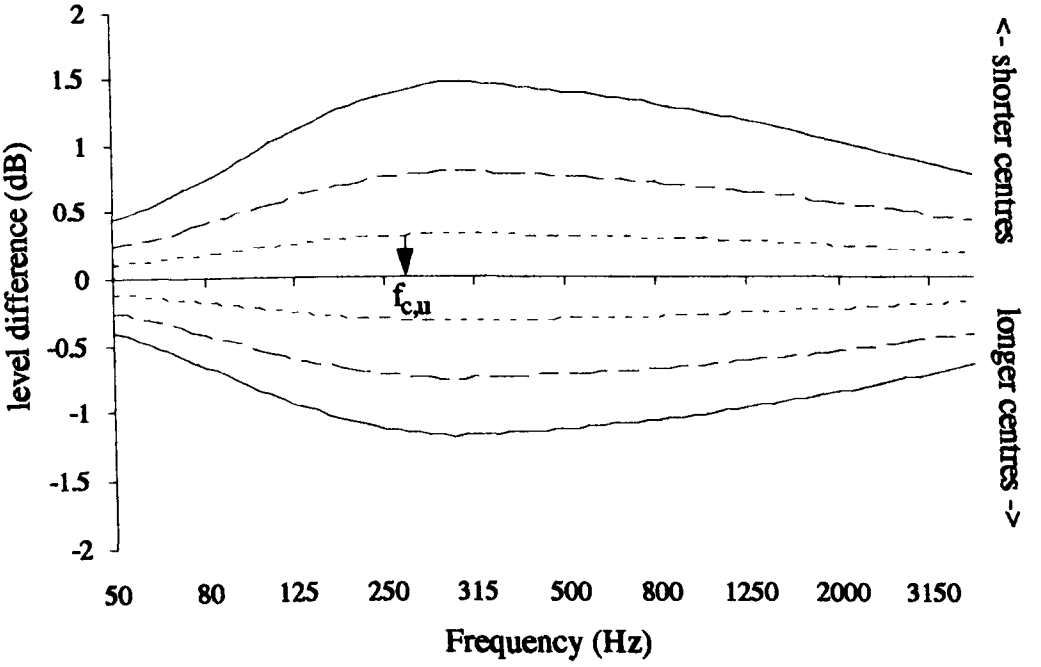

Figure 9.4: Change in transmission loss with variation in cross-rib centres

1.25 m rib centres ± :

——— 0.25 m - - - - - 0.15 m ····· 0.05 m

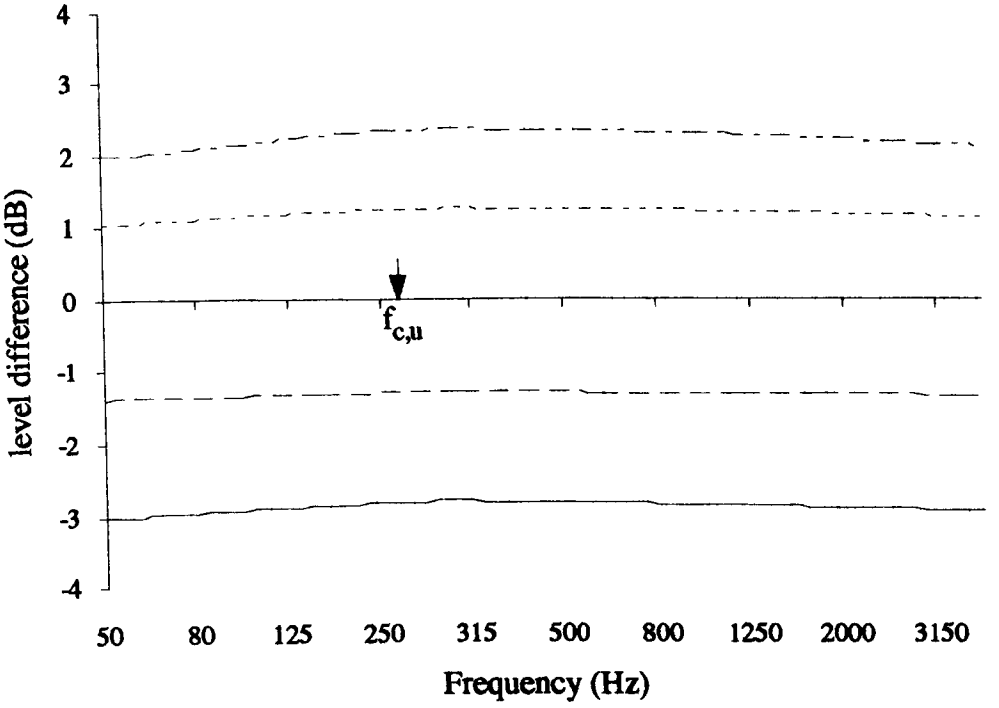

Figure 9.5: Change in transmission loss with variation in material parameters to one leaf

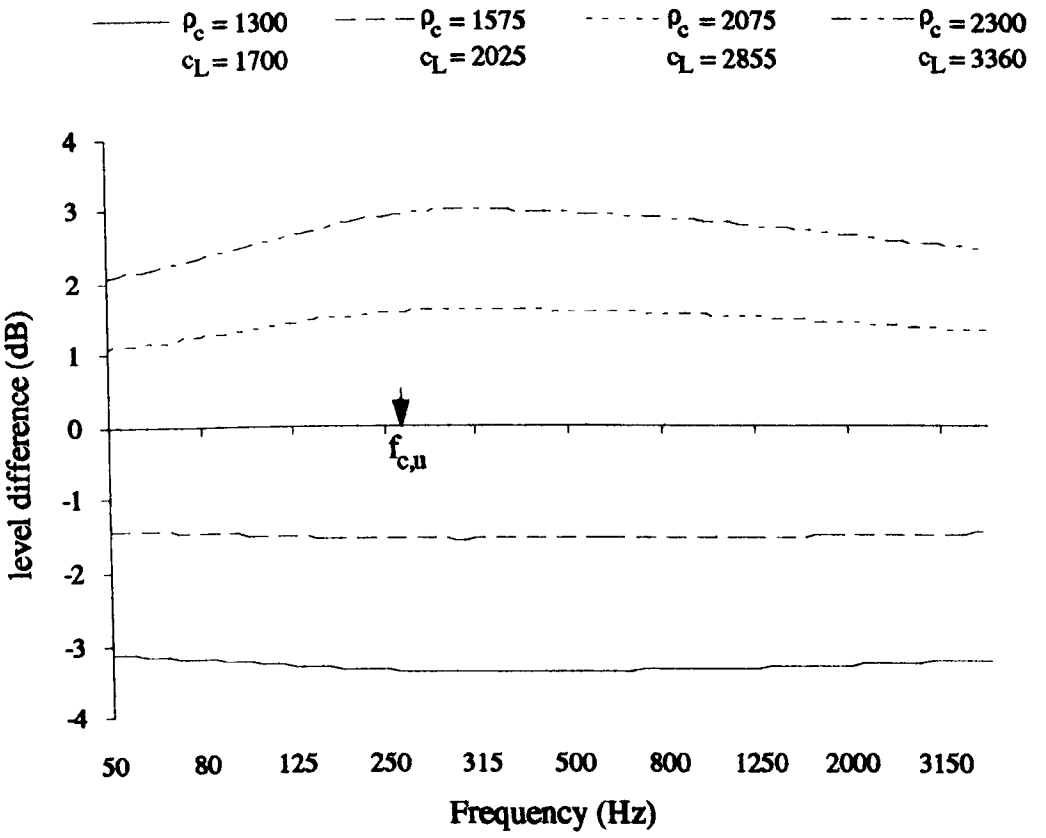

Figure 9.6: Change in transmission loss with variation in material parameters to both leaves

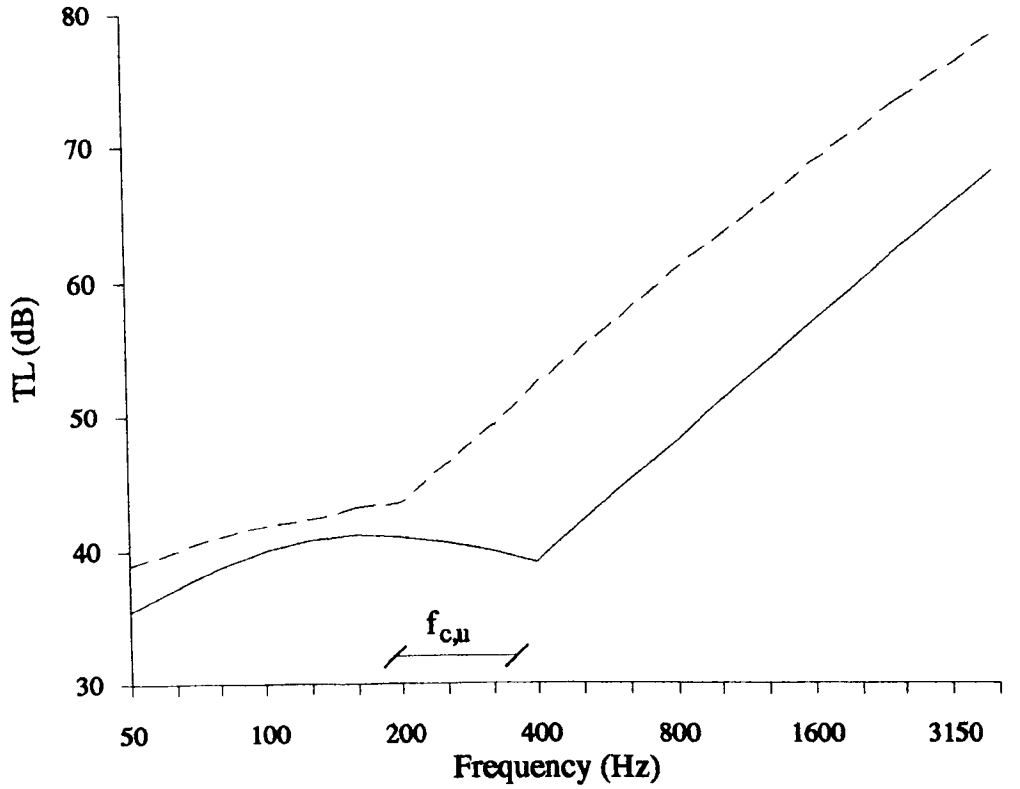

Figure 9.7: Predicted range of practical transmission losses

Lightwight concrete: Rw=49 dB Heavyweight masonry: Rw=58 dB

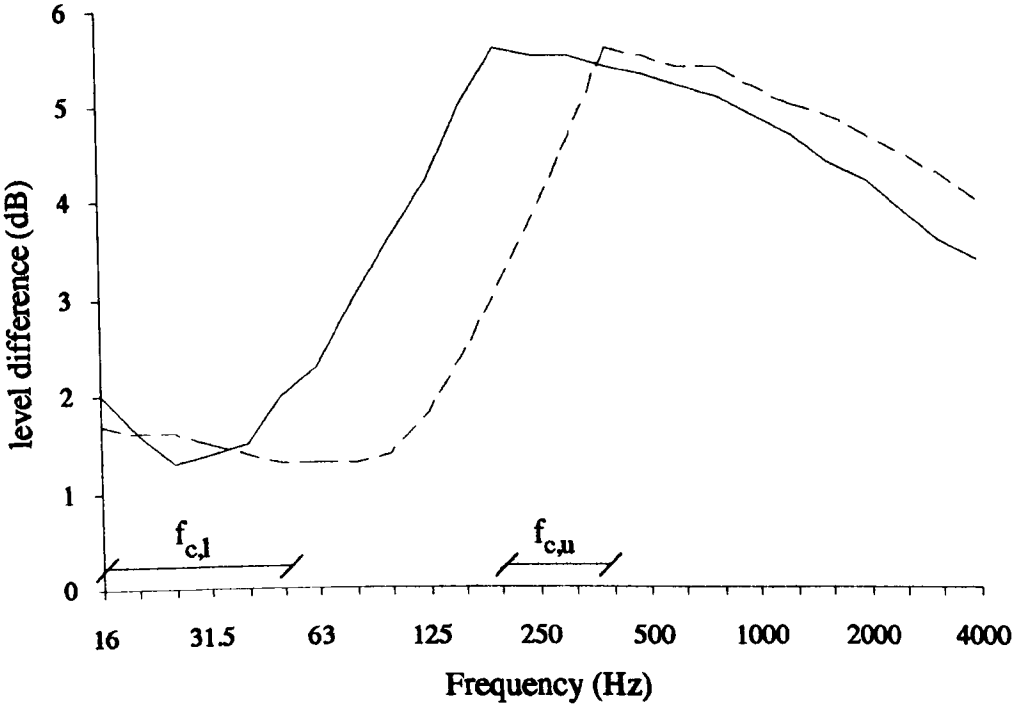

Figure 9.8: Difference in transmission loss between two geometric extremes (ii - i)

Lightweight concrete Heavyweight masonry

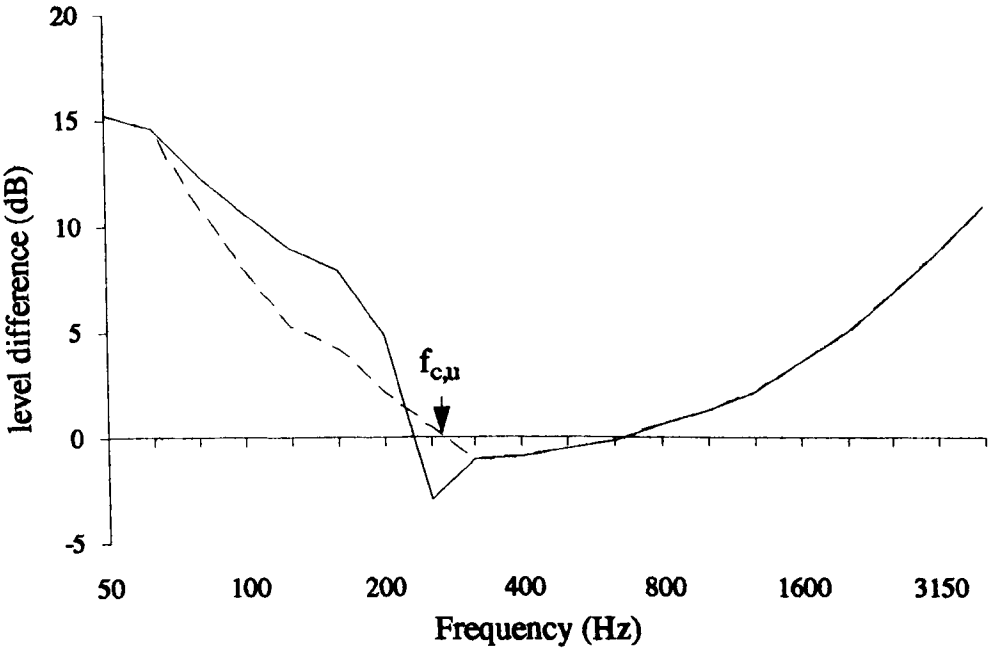

Figure 9.9: Difference in transmission loss between a monolithic coupled wall and two de-coupled walls

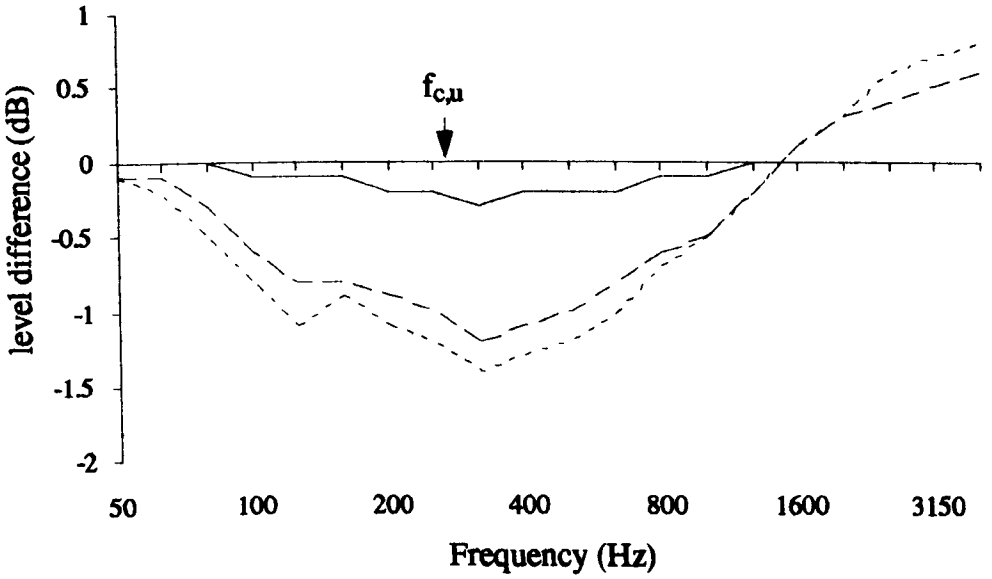

Figure 9.10: Difference in transmission loss between a monolithic coupled wall and a de-coupled wall - radiating orthotropically

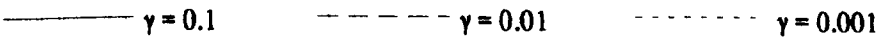

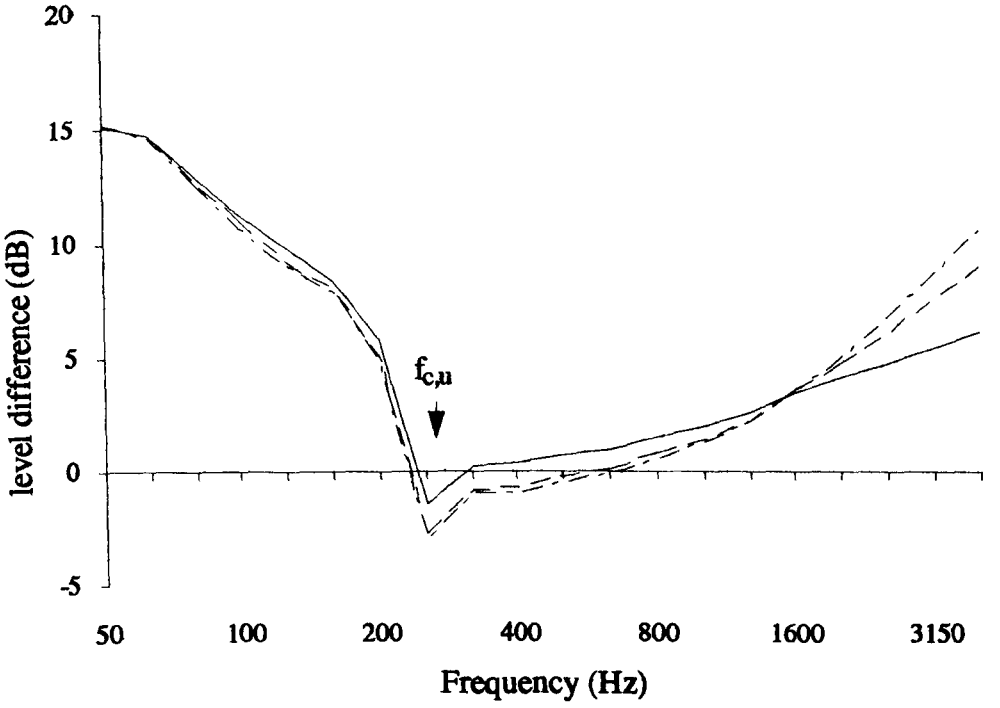

Figure 9.11: Difference in transmission loss between monolithic coupled wall and a de-coupled wall - radiating isotropically

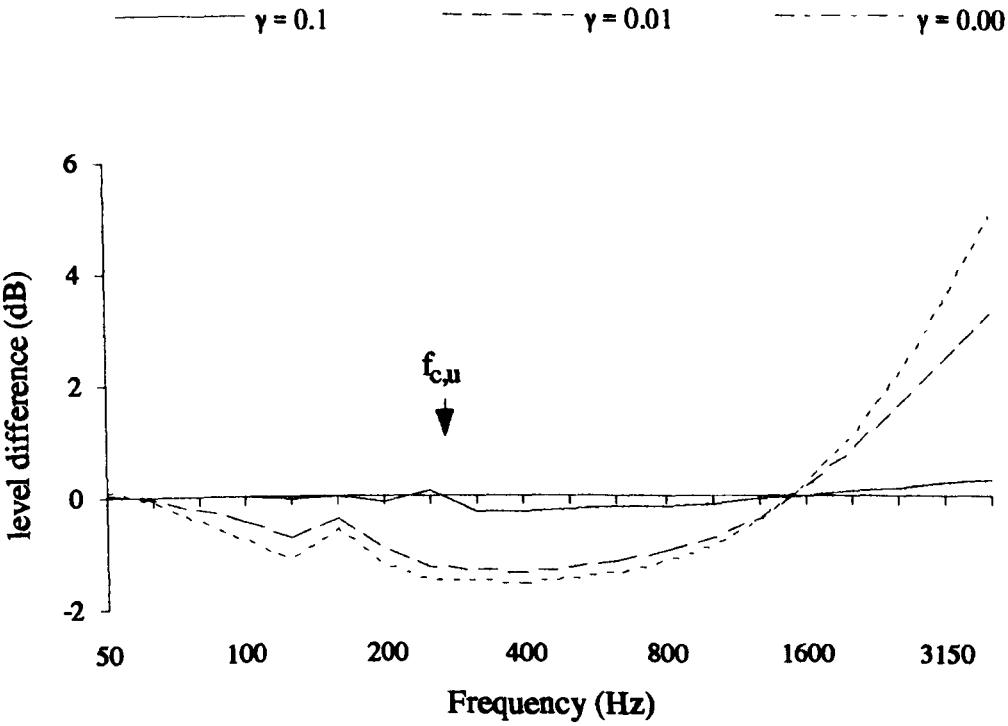

Figure 9.12: Difference in vibration level difference between 5 and 6 sub-system models

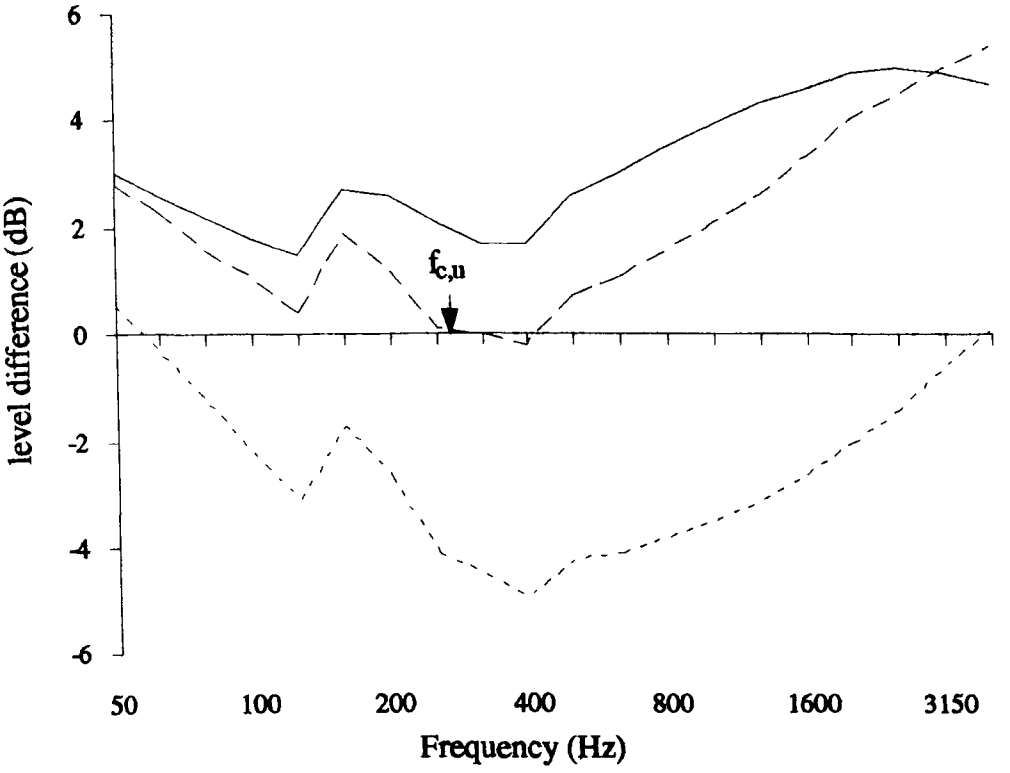

Figure 9.13: Difference in transmission loss between 5 and 6 sub-system models

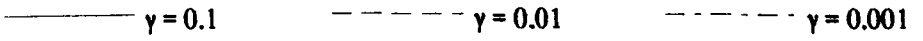

10 CONCLUDING REMARKS

10.1 INTRODUCTION

As an increasingly popular design for large single storey buildings, the diaphragm wall has been carefully studied in terms of its structural, environmental and aesthetic aspects but, previous to this research, little attention had been given to its acoustic properties and sound insulation characteristics. Hence this study has been concerned with the mechanisms of sound insulation of the wall, and with estimating the likely range of transmission loss.

As no existing theory directly relates to the transmission loss of this wall type it was necessary to measure the construction. As it is inherently difficult to measure full size heavyweight facades in-situ, geometric models were built and measured in a small transmission suite. Initial standard ISO 140/3 measurements of transmission loss suffered from poor signal to noise and flanking transmission. For this and other reasons sound intensimetry was adopted, which improved the test suite measurements. The technique was later applied with limited success to the field measurement of a selection of full size diaphragm walls.

Prediction of the transmission loss was initially by adaptation of existing single wall theory to account for the orthotropicity of the wall. This gave good agreement with measurement for fin walls, within 1 - 2 dB, but poorer agreement for diaphragm walls. Applying Statistical Energy Analysis (SEA) allowed a larger examination of the diaphragm wall including the vibration level differences between leaves, and the individual importance of the cross-rib and cavity transmission paths. SEA predicted the transmission loss of model and full size walls within 1 - 3 dB of measurement. Once validated, the approach was used to estimate, through parametric analysis, the

range of possible transmission losses and the effect of partially de-coupling one leaf. From this research the following conclusions can be drawn.

10.2 CONCLUSIONS

1. The transmission path via the capping beam and foundation of the diaphragm wall was estimated as negligible due to the large cross-rib coupling, and was neglected early in this study.

2. The addition of cross-ribs to an isotropic wall produces a reduction in transmission loss in the region between the upper critical frequency, $f_{c,u}$, based on the bending stiffness across the ribs (i.e. of the isotropic wall) and the lower critical frequency, $f_{c,l}$, based on the bending stiffness along the ribs. This region is generally flat, and hence termed the 'plateau region.'

3. As both fin and diaphragm walls have two bending stiffnesses they can be described as 'orthotropic' in their transmission loss or sound radiation characteristics.

4. The addition of cross-ribs to a wall increases the bending stiffness across the ribs causing $f_{c,l}$ to decrease, thereby increasing the width of the plateau region. For the model fin walls this decrease was typically one 1/3 octave with each halving of the distance between rib centres. For a diaphragm wall $f_{c,l}$ changes by only a few hertz as neither the centroidal axis nor width of the wall is greatly altered.

5. For single leaf orthotropic walls, such as fin walls, their transmission loss can be predicted by modifying Sharp's [41] isotropic single wall theory, such

that $f_c/2$ is replaced by $f_{c,l}$, and the region between the two critical frequencies is interpolated, replicating the measured plateau region.

6. The orthotropicity of the radiating surface also depends upon the impedance mis-match between rib and leaf and the spacing of those ribs. For the monolithic or near monolithic cases such as diaphragm walls and stud partitions, it is estimated that the distance between ribs should be at least $2\lambda_b$ to consider them independent of each other and the area between them to be isotropic in radiation character.

7. The radiation resistance of an orthotropic wall is best predicted by interpolating R_{rad} between $f_{c,l}$ and $f_{c,u}$, producing a logarithmic straight line. The radiation resistance for a stiffened thin plate is unsuitable as this still assumes an isotropic radiation efficiency and reduces the radiating area, neither of which hold for an orthotropic wall.

8. The transmission loss of a double wall where both leaves are orthotropic will still produce a plateau region. Where one of the leaves is isotropic, its radiation resistance dominates such that the plateau of the transmission loss curve disappears and the sound insulation in this region is regained.

9. From both model and field measurements, the vibration level difference between the leaves of the diaphragm wall is approximately 1 dB up to approximately 250 Hz (full size) then slowly increases with frequency. There is little increase above 250 Hz to 2 dB at 1600 Hz. This shows that at low and mid frequencies both leaves are strongly coupled, indicating the diaphragm wall acts much like a single wall.

10. The strong leaf coupling is due foremost to the large number of structural cross-rib links. With present types of diaphragm walls this transmission path dominates the cavity path for most of the building acoustics frequency range.

11. For typical diaphragm walls, the inclusion of the cavity transmission path is predicted not to influence transmission loss by more than 2 dB up to 1250 Hz. So at low and mid frequencies only the structural cross-rib path need be considered.

12. Unlike other bridging elements, such as studs, ties or masonry returns, the cross-rib is wide enough such that bending resonances can occur within the frequency range of interest, between 300 Hz - 800 Hz. Thus the cross-rib can be, and has been best described as, a resonant sub-system. Theoretically standing waves can exist between the leaves, but they were not observed in 1/3 octave bandwidth measurement.

13. At high frequencies or when the transmission coefficient between leaf and cross-rib is < 0.1, then the cavity path should be included in the SEA model.

14. The application of sound intensimetry to the field measurement of high insulation facades has been shown to suffer particularly from flanking transmission. Not through its direct influence on the radiated sound power from the measurement area, but by increasing the overall background level.

15. For field measurements, sound intensimetry is a quick and versatile tool and under suitable conditions can give reliable measurements of high insulation elements in-situ. (i.e., where there is a suitable signal to noise ratio and low flanking transmission).

16. The corners of the diaphragm wall were shown to have negligible influence on the equi-partition of energy over the facade. Hence, when choosing the measurement area on the facade and when modelling the system, physically or theoretically, the corners of the wall need not be included.

17. Masonry diaphragm walls will typically rate between R_w = 52 - 56 dB depending on construction details.

18. The anticipated variations in transmission loss for the present possible range of diaphragm wall constructions are predicted to be less than 3 dB through material changes and 2 dB through geometric changes. The optimum geometry for the highest sound insulation within present limits is 0.5 m cross-ribs at 1 m centres, which essentially increases the overall mass of the wall per unit length. Using a dense masonry brick (ρ_c = 2300 kg/m^3, c_L = 3360 m/s) the wall will rate at R_w = 58 dB.

10.3 TOPICS OF FURTHER RESEARCH

1 A major restriction to the improvement of the sound insulation of diaphragm walls is the requirement for a strong bond between leaves and cross-ribs. Research is required on how the cross-rib and leaf can be vibrationally de-coupled while preserving a strong static link. It is not clear to what degree partial de-coupling of one leaf from the rest of the wall will improve its transmission loss. Low frequencies transmission loss would be improved if one leaf could radiate isotropically, but as the wall is de-coupled the cavity path becomes a more important transmission path and must be included in the analysis.

2. All but one of the diaphragm walls measured in-situ had tied cross-ribs. It would be useful to measure further diaphragm walls, particularly with bonded cross-ribs, to increase the database of reliable measurements.

3. With respect to the external measurements, the options of increasing the source room level and using partial screens would be of little benefit in improving the received intensity signal. One approach would be to use 'selective intensity' [156]. This method cross-correlates the input signal from the source speaker with the pressure signals of the intensity probe. The technique has the potential to be particularly useful for facade measurements, using a multi-sine excitation signal under high background noise levels.

4. Further field measurements of sound intensimetry would be useful under different conditions of flanking transmission, particularly where these could be validated against standard ISO methods. From the in-situ measurements the inclusion of the measurement surface parallel to the wall was found to be negligible. This was believed to be due to the significant distance between measurement surface and flanking paths; but further research is necessary to quantify this observation.

5. Further validation is required of the 3 mm spacer for sound intensimetry as this would offer a wider measurement frequency range above 10 kHz.

6. Investigation into the distinction between the characteristics of stiffened and orthotropic building elements could produce design changes to improve their sound insulation.

7. Benefits in low frequency sound insulation might be possible by ensuring an isotropic inner skin next to the orthotropic outer skin of many present cladding systems.

8. A re-analysis of the diaphragm wall, in terms of thick plate theory, would be useful in investigating the transmission of an orthotropic pattern between both sides of a single leaf.

A APPENDICES

A.1-3 STRUCTURAL CRITERIA FOR DIAPHRAGM WALLS

The I-section of a diaphragm wall has a greater radius of gyration than a normal cavity wall, due mainly to its width. This gives it greater resistance, in particular to lateral loadings normally due to wind pressure. To ensure the safe structural design of a construction, both horizontal and vertical loadings must be considered.

A.1 SLENDERNESS RATIO

When defining an acceptable axial loading of single storey walls the 'Slenderness ratio' is a practical guide. This is the ratio of the effective height, h_{eff}, to the effective thickness, t_{eff}. The upper limit is usually 27. The effective height is not definitive. Standard figures are given by BS 5628 based on Euler's buckling theory and often adjusted for individual cases. A diaphragm wall is assumed to be a propped cantilever and h_{eff} equals 0.75 of the actual height, although the action of wind pressure and roof suction can produce a value closer to the actual height. t_{eff} of a single leaf wall is usually taken as the thickness, while for a cavity wall it is 2/3 of the sum of both leaves. For a single 102.5 mm wall the maximum height is between 2.77 - 3.69 m and for a cavity wall the maximum height is between 3.69 - 4.92 m. Diaphragm walls are commonly built between 7 - 9 m high. It is asserted by authors such as Curtin [1.4] that the slenderness ratio cannot be effectively applied to complicated structures such as diaphragm or fin walls. Rather, all walls should be redefined on the basis of their radius of gyration. The radius of gyration, 'r', is given by:

$$r = \sqrt{\frac{I_{xx}}{A}} \qquad (A.1)$$

Where I_{xx} is the moment of inertia, and A is the cross-sectional area of the solid wall per unit length (1 x h), h is the wall thickness. Rearranging equation A.1, (using equation A.4 ahead) gives an effective thickness of:

$$h_{eff} = r\sqrt{12} \qquad (A.2)$$

Using this approach, a typical diaphragm wall of width 0.665 m, has an effective thickness equivalent to a 0.917 m solid wall.

A.2 MOMENT OF INERTIA, I_{xx}

The 'moment of inertia' or 'second moment of area' is an important concept, both structurally and acoustically. It is the property of a profile which defines its ability to resist bending. The parameter does not consider any material properties, simply its geometry. There are standard formula given in many texts [1.11, 1.12], which are restated briefly here for the diaphragm and fin walls.

The moment of inertia is calculated with respect to its centroidal axis. For a symmetrical construction this is the same as the wall's symmetrical axis, as in the case of the diaphragm wall. The key centroidal axis is x-x, that of weakest bending resistance. For the fin wall the cross-section is not symmetrical and its position is calculated as a distance above a baseline, and is given by:

$$x\text{-}x_{distance} = \frac{\sum[(b_1.d_1).y_1 + (b_2.d_2).y_2 + \ldots]}{\sum[(b_1.d_1) + (b_2.d_2) + \ldots]} \qquad (A.3)$$

Where b and d are the width and depth, respectively, of the wall's sub-elements (denoted by subscripts 1, 2 etc.). For a diaphragm wall, and any wall of symmetrical cross-section, the centroidal axis will never change. For the fin wall, it will

continually change with any geometric alteration, thereby affecting the bending stiffness and critical frequency.

The moment of inertia is calculated by separating the wall into sub-elements. For those sub-elements symmetrical about the centroidal axis, i.e. the cross-ribs, I_{xx} is given by:

$$I_{xx} = \frac{bd^3}{12} \qquad (A.4)$$

I_{xx} is determined per unit length, therefore b is equal to unity. For a sub-element that is not symmetrical about the centroidal axis, such as a leaf:

$$I_{xx\ (\text{not on axis})} = \frac{bd^3}{12} + A\,y^2 \qquad (A.5)$$

where A is the area of the sub-element and y is the distance from the centre of the sub-element to the centroidal axis. For the diaphragm wall, considered as a repeated I-section of two leaves and a rib, the total moment of inertia is given by:

$$I_{xx\ (\text{total})} = 2(I_{xx\ (\text{flange or leaf})}) + I_{xx\ (\text{rib})} \qquad (A.6)$$

If the distance between rib centres is not equal to unity then $I_{xx(\text{total})}$ should be divided by this distance. The I-section has a low slenderness ratio and high moment of inertia and therefore the diaphragm wall is able to carry axial and lateral loading greater than that of a single wall of the same width.

A.3 MODULAR RATIO

In the calculation of $I_{xx(\text{total})}$, the sub-elements are all assumed to be of the same material. Where a sub-element of a wall is of a different material to the rest of the

wall, such as wooden stud between two plasterboard leaves, its depth is changed to an equivalent depth as if it were of the same material. This is calculated from the modular ratio, given by

$$\text{Modular ratio} = \frac{E_{stud}}{E_{leaf}} \qquad (A.7)$$

where E is the Young's modulus. The equivalent depth of the stud equals the modular ratio times the actual depth, d.

A.4: INSTRUMENTATION

F.F.T. Analyser	: ZONIC-AND 3524 Dual Channel Fast Fourier Transform
Sound Level Meter	: B & K Type 2218 Precision Integrating Type 1
Filter Set	: B & K Type 1616 1/3 octave
	: B & K Type 1613 1/1 octave
Random Noise Generator	: B & K Type 1402
High Pass Filter	: Kemo Dual Variable Filter Type VBF/14
Amplifier	: V800 MOS-FET Power Amplifier
Microphone Power Supply	: B & K Type 2801
	: B & K Type 2807 Dual Channel
Digital Power Module	: Environmental Equipments Ltd Type 2022
Digital Charge Amplifier	: Environmental Equipments Ltd Type 2021
Rotating Microphone Boom	: B & K Type 3923
Microphone Preamplifier	: B & K Type 2618
Microphones	: B & K Type 4135 1/4" Pressure
	: B & K Type 4165 1/2" Pressure
Intensity Microphones	: B & K Type 4178 phase-matched pair [2 x Type 4135]
Intensity Probe	: B & K Type 3519
Intensity Calibrator Set	: B & K Type 3541
	: B & K Type 4228 Pistonphone
	: B & K Type 3541 Intensity Coupler UA 0914
	: B & K Pink Noise Source ZI 0055
Sound Intensity Analyser	: B & K Type 4433
Lousdspeakers	: 2 No. 12" diameter 300W
	: High frequency 5 tweeter omni-directional speaker
Building Acoustics Analyser	: B & K Type 4418
Accelerometers	: 12g B & K Type 4471

: 4.8g miniature DJB A23E

Post-processing:

Computers : Macintosh Classic 4/40

: PC Viglen 33 MHz 486

Software : Excel 4.0, Word 5.0., Mini-cad 4.0,

Cricket Graph 2.1

: Mac Pascal 2.1, Salford Fortran 77

A.5 SITES VISITED

List of schools, leisure facilities, groups contacted and sites measured. Their help was gratefully appreciated.

Diaphragm walls:

1) Urmston Grammar School, Urmston. 1 visit

Access was allowed on the morning only, weather conditions were dry with little wind. One scan was lost through disturbance by visitors. There was a 2m high wall three metres from facade and major road 100m from facade. Flanking paths on the measured facade were two fire doors and the roof.

Contact: Chris Rudol (school P.E. teacher)

2) Urmston Sports Centre, Urmston. 2 visits

Access from 7.00-9.30 am. Both internal measurements were on the internal wall between hall and changing room. The swimming pool open from 8am. Fan noise was present in adjacent corridor which was not present on first visit.

Contacts: Chris Davy (Manager), Mrs Brown (Flixton Girls School)

3) Bebbington Sports Centre, Bebbington. 1 visit

Access between 7.00-9.30 am. Weather conditions were poor: raining and high winds. Only one scan could be completed and no vibrational level difference measurements were possible.

Contacts: Mr. Prescot (Manager)

4) Plessington R.C. High School, Bebbington. 1 visit

Access between 9.00-12.00 am. Weather conditions fair, dry but gusting with increasing wind speed during the second scan.

Contact: Mr Cook (Teacher)

5) Mount St Joseph R.C. High School, Bolton. 2 visits

Access from 9.00am-4.00 pm

First visit: Measurements of vibration level difference of external facade and room reverberation times .

Second visit: Weather fair and dry. Measurements on external and internal walls of transmission loss and vibrational level difference. Also measurements of the vibration drop across a construction joint.

Contacts: Sister Barbara (Head Mistress), Miss Janet Kvill (Teacher)

6) St Augustines R.C. High School, St Helens 1 visit

Access from 9.00 - 12.00 pm. Close to housing (30 m), flanking paths included two small 200 mm^2 vents and glass facade on side wall.

Contact: Ian Davis (Teacher)

7) CERAM Research (British Ceramic Research Limited) 2 visits

Penkhull, Stoke-on-Trent

Contact: Mr William Templeton (Section Leader, Structural Research Group, Building Materials Division)

<u>Information bodies:</u>

Architects Department, Metropolitan Borough of Trafford

Contacts: Les Birchall, Steve Bull - details for 1) & 2)

Ernest Williams Partnership (consulting engineers)

Contacts: Mr C. Martin, Mr Colin Spencer - details for 4) & 5)

Taylor Maxwell (Material Supplies and Specifications) - details for 4)

Other walls examined, but not used:

Sutton High School, St Helens.

George Tomlinson High School, Kearsley.

Accrington Brickworks, Accrington.

A.6 SAMPLE SEA PROGRAM

The program calculates the energies within each sub-system, by either 4, 5 and 6 sub-system matrices. It is given with extra notation, read and write statements to simplify input of data. fcxx and fc refer to $f_{c,l}$ and $f_{c,u}$, respectively, in chapter text.

```
program Diaphragm (input, output);
type
   response = (yes, y, no, n);
const
   po = 1.19;
   co = 344;
   v = 0.3;
   cocubed = 40707584;
   abso = 0.05;
   impediance = 410;
   pi4 = 97.40909103;

var
   a : text;
   answer : response;
   freq : integer;
   f : array[-9..20] of real;
   rt1 : array[-9..20] of real;
   rt9 : array[-9..20] of real;
   tca : array[-4..20] of real;
   lc : array[-4..20] of real;
   Rrad, clf27, clf72, tc27, tc72, lclf27, lclf72 : real;
   fc2, cl2, h2, pc2, b2, b2x, y2, ixx, ixxf, fc2x, fcxx, m2, n1, n9, n4, n2, n5, n7, w : real;
   ilf2, ilf4, ilf5, ilf7, ilf9, ilf1, TL : real;
   E2, E4, E5, E7, E9, m1e, m2e, m4e, m5e, m7e, m9e : real;
   fc5, fc7, m5, m7, pc5, pc7, h5, h7, cl5, cl7 : real;
   Plen2, PHt2, Plen5, PHt5, Plen7, PHt7 : real;
   A1, V1, A9, V9, a2, P2, a5, P5, a7, P7 : real;
   nclf14, nclf41, nclf94, nclf49, nclf19, nclf91, meff : real;
   rlf79, rlf97, rlf12, rlf21, rlf24, rlf42, rlf47, rlf74 : real;
   clf25, clf52, clf57, clf75, rlf54, rlf45, tc25, tc52, tc57, tc75, tc : real; RibC, z, CavH, CavW,
   CavD, Dim1, Dim2, Dim3, cavA, cavV : real;
   s : array[-9..20] of real;
   wavecrit, waveacoust, g1, g2, g2bottom, g2bottoms, alpha, calc : real;
   sqralpha, wak, logg, restart, reend, diffs, diff, add : real;

{rating variables}
   devsum, sum16 : real;
   R : array[4..19] of real;
   T : array[-4..20] of real;
   deviation : array[4..19] of real;

procedure rating_curve; {Rw standard curve}
begin
   R[4] := 77;
   R[5] := 80;
   R[6] := 83;
   R[7] := 86;
   R[8] := 89;
   R[9] := 92;
   R[10] := 95;
   R[11] := 96;
```

```
    R[12] := 97;
    R[13] := 98;
    R[14] := 99;
    R[15] := 100;
    R[16] := 100;
    R[17] := 100;
    R[18] := 100;
    R[19] := 100;
end;

procedure datacollect; {stores calculated orthotropic radiation resistances}
begin
    s[freq] := rrad;
    writeln(f[freq] : 2 : 1, ' : ', rrad : 2 : 3);
    rrad := 0;
end;

function log (x : real) : real; {logarithmic calculation}
    const
      ln10 = 0.434294481;
begin
    log := ln10 * ln(x);
end;

procedure critfreq; {critical frequencies}
begin
    fc2 := (sqr(Co) * sqrt(3)) / (pi * h2 * CL2); fc5 := (sqr(Co) * sqrt(3)) / (pi * h5 * CL5);
    fc7 := (sqr(Co) * sqrt(3)) / (pi * h7 * CL7); Y2 := sqr(CL2) * pc2 * (1 - sqr(v));
    B2 := (Y2 * Ixx);
    fc2x := ((sqr(Co)) / (2 * pi)) * (sqrt(m2 / B2));
    B2x := (Y2 * Ixxf);
    fcxx := ((sqr(Co)) / (2 * pi)) * (sqrt(m2 / B2x));
    writeln('B = ', B2 : 2 : 3, ' : Y = ', Y2);
    writeln('Fc2 = ', fc2 : 2 : 1, ': Fc5 = ', fc5 : 2 : 1, ' : Fc7 = ', fc7 : 2 : 1, ' : Fc2x = ', fc2x : 2 : 1,    ':
Fcxx = ', fcxx : 2 : 1);
end;

procedure init_freq; {frequencies}
begin
    f[-9] := 5;
    f[-8] := 6.3;
    f[-7] := 8;
    f[-6] := 10;
    f[-5] := 12.5;
    f[-4] := 16;
    f[-3] := 20;
    f[-2] := 25;
    f[-1] := 31.5;
    f[0] := 40;
    f[1] := 50;
    f[2] := 63;
    f[3] := 80;
    f[4] := 100;
    f[5] := 125;
    f[6] := 160;
    f[7] := 200;
    f[8] := 250;
    f[9] := 315;
    f[10] := 400;
    f[11] := 500;
    f[12] := 630;
    f[13] := 800;
    f[14] := 1000;
```

```
    f[15] := 1250;
    f[16] := 1600;
    f[17] := 2000;
    f[18] := 2500;
    f[19] := 3150;
    f[20] := 4000;
end;
```

{receiver room reverebration times rt9[1] to rt9[20] read from input file}

```
procedure inputs; {input values of rooms and panels}
    var
      len1, wid1, ht1, len9, wid9, ht9 : real;
begin
    writeln;
    writeln('_Inputs Parameters_'); writeln;
    writeln('* Source room (E1)*');
    write('Length > ');
    readln(Len1):
    write('Width > ');
    readln(wid1);
    write('Height > ');
    readln(ht1);
    v1 := Len1 * wid1 * ht1;
    A1 := (2 * len1 * wid1) + (2 * wid1 * ht1) + (2 * ht1 * len1);
    writeln('Volume = ', v1 : 2 : 3, ' : Surface Area = ', A1 : 2 : 3);
    writeln;
    writeln('* Receiver room (E9)*');
    write('Length > ');
    readln(Len9);
    write('Width > ');
    readln(wid9);
    write('Height > ');
    readln(ht9);
    v9 := Len9 * wid9 * ht9;
    A9 := (2 * wid9 * len9) + (2 * wid9 * ht9) + (2 * ht9 * len9);
    writeln('Volume = ', v9 : 2 : 3, ' : Surface Area = ', A9 : 2 : 3);
    writeln;
    writeln('* Source leaf (E2) *');
    write('length > ');
    readln(PLen2);
    write('height > ');
    readln(Pht2);
    A2 := PLen2 * PHt2;
    P2 := (2 * PLen2) + (PHt2 * 2);
    write('material density > ');
    readln(pc2);
    write('thickness > ');
    readln(h2);
    m2 := pc2 * h2;
    write('longitudinal wavespeed > ');
    readln(Cl2);
    writeln('Length = ', PLen2 : 2 : 1, ' : Height = ', PHt2 : 2 : 1, ' : Area = ', A2 : 2 : 1, ' :  Perimeter
= ', P2 : 2 : 1);
    writeln('pc2 = ', pc2 : 2 : 1, ' : m2 = ', m2 : 2 : 2, ' : h2 =', h2 : 2 : 1, ' : Cl2 = ', cl2 : 2 : 1);
    writeln;
    writeln('* Cross-rib (E5) *');
    write('length > ');
    readln(PLen5);
    write('height > ');
    readln(PHt5);
    A5 := PLen5 * PHt5;
    P5 := (2 * PLen5) + (PHt5 * 2);
```

```
    write('material density > ');
    readln((pc5);
    write('thickness > ');
    readln(h5);
    m5 := pc5 * h5;
    write('longitudinal wavespeed > ');
    readln(Cl5);
    writeln('Length = ', PLen5 : 2 : 3, ' : Height = ', PHt5 : 2 : 1, ' : Area = ', A5 : 2 : 3, ' : Perimeter =
    ', P5 : 2 : 1);
    writeln('pc5 = ', pc5 : 2 : 1, ' : m5 = ', m5 : 2 : 2, ' : h5 =', h5 : 2 : 1, ' : Cl5 = ', cl5 : 2 : 1);
    writeln;
    writeln('* Receiver leaf (E7) *');
    write('length > ');
    readln(PLen7);
    write('height > ');
    readln(PHt7);
    A7 := PLen7 * PHt7;
    P7 := (2 * PLen7) + (PHt7 * 2);
    write('material density > ');
    readln(pc7);
    write('height > ');
    readln(h7);
    m7 := pc7 * h7;
    write('longitudinal wavespeed > ');
    readln(Cl7);
    writeln('Length = ', PLen7 : 2 : 1, ' : Height = ', PHt7 : 2 : 1, ' : Area = ', A7 : 2 : 1, ' : Perimeter =
    ', P7 : 2 : 1);
    writeln('pc7 = ', pc7 : 2 : 1, ' : m7 = ', m7 : 2 : 2, ' : h7 =', h7 : 2 : 1, ' : Cl7 = ', cl7 : 2 : 1);
    writeln;
    writeln('* Ribs (E5) *');
    write('number of ribs > ');
    readln(z);
    write('rib centres > ');
    readln(RibC);
    meff := pc2 * (h2 + h7 + h5 * ((z * Plen5) / Plen2));
    writeln('Rib Centres = ', RibC : 2 : 3, ' : Number of ribs = ', z : 2 : 1, ' : Eff. mass = ', meff : 2 : 3);
    writeln;
    writeln('* Cavity (E4) *');
    write('height of cavity > ');
    readln(CavH);
    write('width of cavity . ');
    readln(CavW);
    writeln('Height = ', cavH : 2 : 1, ' : Width = ', cavW : 2 : 3, ' : Depth = ', CavD : 2 : 3);
    dim1 := (co / (2 * cavH));
    dim2 := (co / (2 * CavW));
    dim3 := (co / (2 * CavD));
    writeln('Dim1 =', dim1 : 2 : 1, ' : Dim2 = ', dim2 : 2 : 1, ' : Dim3 = ', dim3 : 2 : 1);
    writeln;
    Ixx := 8.974e-5;
    Ixxf := 19.2e-3;
    writeln('Ixx (whole) = ', Ixxf : 2 : 10, ' : Ixx (single leaf) = ', Ixx : 2 : 10);
end;

procedure n_room; {modal density of rooms}
    var
      co3 : real;
begin
    co3 := co * co * co;
    n1 := (v1 * 4 * pi * sqr(f[freq])) / co3;
    n9 := (v9 * 4 * pi * sqr(f[freq])) / co3;
end;

procedure n_cavity; (modal density of cavity}
```

```
    var
      n, Ap, Pcav2, Edge, ne1, ne2, ne3 : real;
begin
    if f[freq] < dim1 then
      begin
        CavA := (cavH * cavW * 2) + (CavH * CavD * 2) + (CavW * CavD * 2); Edge := (4 * CavH)
        + (4 * CavW) + (4 * CavD);
        Cavv := CavH * CavW * CavD;
        ne1 := (Cavv * 4 * pi * sqr(f[freq])) / cocubed; ne2 := (pi * f[freq] * CavA) / (2 * sqr(co)); ne3
        := Edge / (8 * co);
        n4 := ne1 + ne2 + ne3;
      end
    else if (f[freq] > dim1) and (f[freq] < dim2) then
      begin
        n := (2 * CavH) / co;
        n4 := n;
      end
    else if (f[freq] > dim2) and (f[freq] < dim3) then
      begin
        Ap := CavH * CavW;
        Pcav2 := (CavH * 2) + (cavW * 2);
        n := ((2 * pi * f[freq] * Ap) / (sqr(co))) + (Pcav2 / co);
        n4 := n;
      end
    else if f[freq] > dim3 then
      begin
        CavA := (cavH * cavW * 2) + (CavH * CavD * 2) + (CavW * CavD * 2); Edge := (4 * CavH)
        + (4 * CavW) + (4 * CavD);
        Cavv := CavH * CavW * CavD;
        ne1 := (Cavv * 4 * pi * sqr(f[freq])) / cocubed;
        ne2 := (pi * f[freq] * CavA) / (2 * sqr(co)); ne3 := Edge / (8 * co);
        n4 := ne1 + ne2 + ne3;
      end;
end;

procedure n_panel; {modal density of panel}
begin
    n2 := (A2 * sqrt(3)) / (h2 * cl2);
    n5 := (A5 * sqrt(3)) / (h5 * cl5);
    n7 := (A7 * sqrt(3)) / (h7 * cl7);
end;

procedure ilfs; {internal loss factors}
    var
      rt4 : real;
begin
    ilf2 := 0.015;
    ilf5 := 0.015;
    ilf7 := 0.015;
    ilf9 := 2.2 / (f[freq] * RT9[freq]);
    rt4 := (0.163 * CavV) / (cavA * abso);
    ilf4 := 2.2 / (f[freq] * RT4);
end;

function pow (z : real) : real; {ten to the power function}
begin
    pow := exp(z * ln(10));
end;

procedure non_resonant; {non-resonant transmission path}
    var
      tcoeff : real;
begin
```

```
    tcoeff := 1 / (1 + sqr((w * meff) / (2 * po * co)));
    nclf19 := ((co * A2 * pow(5 / 10)) / (4 * w * v1)) * tcoeff; {field incidence term is included}
    nclf91 := nclf91 * (n1 / n9);
end;
```

{Coupling loss factors and transmission coefficients for leaf to leaf coupling are read from files}

```
procedure clfsa; {coupling loss factor direct across rib}
    var
cb2, cb7, k2, k7, L27, L72, Aint, tccant, tctee : real;
begin
{Structure}
    Aint := (RibC * PHt2) / 2;
    cb2 := sqrt(1.8 * h2 * cl2 * f[freq]);
    cb7 := sqrt(1.8 * h7 * cl7 * f[freq]);
    K2 := w / cb2;
    K7 := w / cb7;
    L27 := Pht2;
    L72 := PHt2;

{tc := 1 / (pow(8.3 / 10));}
{tccant := 1 / (pow(9.67 / 10));}
{tctee := 1 / (pow(9.12 / 10));}
    tc := tca[freq];
    tc27 := tc;
    tc72 := tc;
    clf27 := (2 / pi) * (L27 / Aint) * (1 / K2) * tc27; clf72 := (2 / pi) * (L72 / Aint) * (1 / K7) * tc72;
    lclf27 := lc[freq];
    lclf72 := lclf27;

end;

procedure clfs; {coupling  loss factors from cross-rib to wall and vice versa}
    var
      cb2, cb5, cb7, k2, k5, k7, L25, L75, L57, L52, Aint, tccant, tctee : real;
begin
    Aint := (RibC * PHt2) / 2;
    cb2 := sqrt(1.8 * h2 * cl2 * f[freq]);
    cb5 := sqrt(1.8 * h5 * cl5 * f[freq]);
    cb7 := sqrt(1.8 * h7 * cl7 * f[freq]);
    K2 := w / cb2;
    K5 := w / cb5;
    K7 := w / cb7;
    L25 := Pht2;
    L75 := PHt2;
    L57 := Pht2;
    L52 := Pht2;
    tc := 1 / (pow(8.3 / 10));
    tctee := tc;
    tccant := tc;
    tc25 := tctee;
    tc52 := tccant;
    tc57 := tccant;
    tc75 := tctee;
    clf25 := (2 / pi) * (L25 / Aint) * (1 / K2) * tc25; clf75 := (2 / pi) * (L75 / Aint) * (1 / K7) * tc75;
    clf52 := (2 / pi) * (L52 / A5) * (1 / K5) * tc52; clf57 := (2 / pi) * (L57 / A5) * (1 / K5) * tc57;
end;

procedure S5imultsolve; {5 sub-system model}
    var
      a : array[1..4, 1..5] of real;
```

```
    r : array[1..4, 1..5] of real;
    b : array[1..4] of real;
    i, j, k, max, n : integer;
    t : real;

begin
  for i := 1 to 4 do
    for j := 1 to 5 do
      begin
        a[i, j] := 0;
        a[1, 1] := rlf21 + (2 * z * clf25) + ilf2;
        a[1, 2] := (-clf52 * 2 * z);
        a[1, 3] := 0;
        a[1, 4] := 0;
        a[1, 5] := rlf12;
        a[2, 1] := (-clf25 * 2 * z);
        a[2, 2] := z * ((clf52 * 2) + (clf57 * 2) + ilf5);
        a[2, 3] := (-clf75 * 2 * z);
        a[2, 4] := 0;
        a[2, 5] := 0;
        a[3, 1] := 0;
        a[3, 2] := (-clf57 * 2 * z);
        a[3, 3] := (clf75 * 2 * z) + rlf79 + ilf7;
        a[3, 4] := (-rlf97);
        a[3, 5] := 0;
        a[4, 1] := 0;
        a[4, 2] := 0;
        a[4, 3] := (-rlf79);
        a[4, 4] := (rlf97 + nclf91 + ilf9);
        a[4, 5] := nclf19;
      end;
  n := 4;
  for i := 1 to n do
    begin
      max := i;
      for j := i + 1 to n do
        if abs(a[j, i]) > abs(a[max, i]) then
          max := j;
      for k := i to n + 1 do
        begin
          t := a[i, k];
          a[i, k] := a[max, k];
          a[max, k] := t
        end;
      for j := i + 1 to n do
        for k := n + 1 downto i do
          a[j, k] := a[j, k] - a[i, k] * a[j, i] / a[i, i];

    end;

      for j := n downto 1 do
        if j = n then
          b[j] := a[j, n + 1] / a[j, j]
        else
          begin
                t := 0.0;
                for k := j + 1 to n do
                t := t - a[j, k] * b[k] / a[j, j];
                b[j] := a[j, n + 1] / a[j, j] + t;
          end;
      for i := 1 to 4 do
        begin
          E2 := b[1];
```

```
            E5 := b[2];
            E7 := b[3];
            E9 := b[4];
          end;
        e2 := sqrt(sqr(e2));
        e5 := sqrt(sqr(e5));
        e7 := sqrt(sqr(e7));
        e9 := sqrt(sqr(e9));
        m1e := 1 / n1;
        m2e := e2 / n2;
        m5e := e5 / n5;
        m7e := e7 / n7;
        m9e := e9 / n9;
  end;

  procedure S4imultsolve; {4 sub-system model}
  var
     a : array[1..3, 1..4] of real;
     r : array[1..3, 1..4] of real;
     b : array[1..3] of real;
     i, j, k, max, n : integer;
     t : real;
begin
    for i := 1 to 3 do
      for j := 1 to 4 do
        begin
          a[i, j] := 0;
          a[1, 1] := rlf21 + (4 * z * clf27) + ilf2;
          a[1, 2] := (-clf72 * 4 * z);
          a[1, 3] := 0;
          a[1, 4] := rlf12;
          a[2, 1] := (-clf27 * 4 * z);
          a[2, 2] := (clf72 * 4 * z) + rlf79 + ilf7;
          a[2, 3] := (-rlf97);
          a[2, 4] := 0;
          a[3, 1] := 0;
          a[3, 2] := (-rlf79);
          a[3, 3] := (rlf97 + nclf91 + ilf9);
          a[3, 4] := nclf19;
        end;
    n := 3;
    for i := 1 to n do
      begin
        max := i;
        for j := i + 1 to n do
          if abs(a[j, i]) > abs(a[max, i]) then
            max := j;
        for k := i to n + 1 do
          begin
            t := a[i, k];
            a[i, k] := a[max, k];
            a[max, k] := t
          end;
        for j := i + 1 to n do
          for k := n + 1 downto i do
            a[j, k] := a[j, k] - a[i, k] * a[j, i] / a[i, i];

      end;

        for j := n downto 1 do
          if j = n then
            b[j] := a[j, n + 1] / a[j, j]
          else
```

```
            begin
                t := 0.0;
                for k := j + 1 to n do
                t := t - a[j, k] * b[k] / a[j, j];
                b[j] := a[j, n + 1] / a[j, j] + t;
            end;
        for i := 1 to 3 do
          begin
            E2 := b[1];
            E7 := b[2];
            E9 := b[3];
          end;
        e2 := sqrt(sqr(e2));
        e7 := sqrt(sqr(e7));
        e9 := sqrt(sqr(e9));
        m1e := 1 / n1;
        m2e := e2 / n2;
        m7e := e7 / n7;
        m9e := e9 / n9;
end;

procedure S6imultsolve; {6 sub-system model}
    var
      a : array[1..5, 1..6] of real;
      r : array[1..5, 1..6] of real;
      b : array[1..5] of real;
      i, j, k, max, n : integer;
      t : real;
  begin
    for i := 1 to 5 do
      for j := 1 to 6 do
        begin
          a[i, j] := 0;
          a[1, 1] := rlf21 + (2 * z * rlf24) + (2 * z * clf25) + ilf2;
          a[1, 2] := (-rlf42 * 2 * z);
          a[1, 3] := (-clf52 * 2 * z);
          a[1, 4] := 0;
          a[1, 5] := 0;
          a[1, 6] := rlf12;
          a[2, 1] := (-rlf24 * 2 * z);
          a[2, 2] := 2 * z * (rlf42 + rlf45 + rlf47 + ilf4);
          a[2, 3] := (-rlf54 * 2 * z);
          a[2, 4] := (-rlf74 * 2 * z);
          a[2, 5] := 0;
          a[2, 6] := 0;
          a[3, 1] := (-clf25 * 2 * z);
          a[3, 2] := (-rlf45 * 2 * z);
          a[3, 3] := z * ((clf52 * 2) + (rlf54 * 2) + (clf57 * 2) + ilf5);
          a[3, 4] := (-clf75 * 2 * z);
          a[3, 5] := 0;
          a[3, 6] := 0;
          a[4, 1] := 0;
          a[4, 2] := (-rlf47 * 2 * z);
          a[4, 3] := (-clf57 * 2 * z);
          a[4, 4] := (rlf79 + (2 * z * clf75) + (2 * z * rlf74) + ilf7);
          a[4, 5] := (-rlf97);
          a[4, 6] := 0;
          a[5, 1] := 0;
          a[5, 2] := 0;
          a[5, 3] := 0;
          a[5, 4] := (-rlf79);
          a[5, 5] := (rlf97 + nclf91 + ilf9);
          a[5, 6] := nclf19;
```

```
        end;
    n := 5;
    for i := 1 to n do
      begin
        max := i;
        for j := i + 1 to n do
          if abs(a[j, i]) > abs(a[max, i]) then
            max := j;
        for k := i to n + 1 do
          begin
            t := a[i, k];
            a[i, k] := a[max, k];
            a[max, k] := t
          end;
        for j := i + 1 to n do
          for k := n + 1 downto i do
            a[j, k] := a[j, k] - a[i, k] * a[j, i] / a[i, i];
      end;
    for j := n downto 1 do
      if j = n then
        b[j] := a[j, n + 1] / a[j, j]
      else
        begin
          t := 0.0;
          for k := j + 1 to n do
            t := t - a[j, k] * b[k] / a[j, j];
          b[j] := a[j, n + 1] / a[j, j] + t;
        end;
    for i := 1 to 5 do
      begin
        E2 := b[1];
        E4 := b[2];
        E5 := b[3];
        E7 := b[4];
        E9 := b[5];
      end;
    e2 := sqrt(sqr(e2));
    e4 := sqrt(sqr(e4));
    e5 := sqrt(sqr(e5));
    e7 := sqrt(sqr(e7));
    e9 := sqrt(sqr(e9));
    m1e := 1 / n1;
    m2e := e2 / n2;
    m4e := e4 / n4;
    m5e := e5 / n5;
    m7e := e7 / n7;
    m9e := e9 / n9;
end;

 procedure results;
    var
      L1L9, L2L7, l215, l517, E1, l119non, tlnon, l112, l719 : real;
 begin
    L1L9non := 10 * log((nclf91 + ilf9) / nclf19);
    TLnon := l119non + (10 * log(A2 / (0.163 * V9 / rt9[freq])));
    E1 := 1;
    l112 := 10 * log(E1 / E2);
    l217 := 10 * log(E2 / E7);
    l719 := 10 * log(e7 / e9);
    L1L9 := 10 * log(E1 / E9);
    TL := L1L9 + (10 * log(A2 / (0.163 * V9 / rt9[freq])));
writeln(f[freq] : 2 : 1, ' :VLD = ', l217 : 2 : 5, ' :TL = ', TL : 2 : 1, ' :TLnon = ', tlnon : 2 : 1);
writeln(a, f[freq] : 2 : 1, ',', l217 : 2 : 5, ',', TL : 2 : 1, ',', tlnon : 2 : 1);
```

```
end;{results}

begin                                                    {PROGRAM BODY}
 init_long;
 init_tca;
 rewrite(a, 'data transfer');
 writeln('___SEA Diaphragm SOLID + RESONANT___');
 writeln;
 write('Do you wish to continue ? ');
 readln(answer);
 writeln;
 if (answer = yes) or (answer = y) then
    begin
      init_freq;
      inputs;
      critfreq;
      n_panel;

      for freq := -4 to 20 do
        begin {calculates Rrad at all frequencies except between fcxx anf fc}
          begin
           begin
             wavecrit := 343 / fc2;
             waveacoust := 343 / f[freq];
             alpha := sqrt(f[freq] / fc2);
             sqralpha := sqr(alpha);
             if f[freq] < (0.5 * fc2) then
               g1 := ((4 / pi4) * (1 - (2 * sqralpha))) / (alpha * sqrt(1 - sqralpha))
             else
               begin
                 g1 := 0;
               end
           end;
           begin
             if f[freq] < fcxx then
               begin
                 g2bottom := sqrt(1 - sqralpha);
                 g2bottoms := g2bottom * g2bottom * g2bottom;
                 g2 := ((1 / (sqr(2 * pi))) * ((1 - sqralpha) * ln((1 + alpha) / (1 - alpha)) + (2 * alpha)))
                 / g2bottoms; calc := (((wavecrit * waveacoust) / A2) * 2 * (f[freq] / fc2) * g1) + (((P2
                 * wavecrit) / A2) * g2); Rrad := A2 * impediance * calc;
               end
             else if (f[freq] > fcxx) and (f[freq] < fc2) then
               begin
                 rrad := 0;
               end
             else if f[freq] = fc2 then
               begin
                 calc := (1 / sqrt(Plen2 / wavecrit)) + sqrt(PHt2 / wavecrit);
                 Rrad := A2 * impediance * calc;
               end
             else if f[freq] > fc2 then
               begin
                 calc := 1 / sqrt(1 - (fc2 / f[freq]));
                 Rrad := A2 * impediance * calc;
                 rrad := 1 * impediance * A2;
                 {if catch = 1 then}
                   {begin}
                   {Rrad := 410;}
                   {catch := 2;}
                   {end;}
               end;
           end;
```

```
  end; {maidanik}
  datacollect; {stores Rrad values as s[freq]: all but those between fc2 and fcf}
end;

  begin {stores value of first and last Rrad and number of spaces between}
    wak := 0;
    logg := 0;
for freq := -4 to 20 do
  begin
      if (s[freq] <> 0) and (Wak = 0) then
      restart := s[freq]
    else if s[freq] = 0 then
      begin
        wak := 1;
        logg := logg + 1;
      end
    else if (s[freq] <> 0) and (wak = 1) then
      begin
        reend := s[freq];
        reend := 410 * A2;
        wak := 2;
      end
  end;

 begin {recalculates Rrad between fcxx anf fc by interpolation}
   restart := log(restart);
   reend := log(reend);
   diffs := (restart - reend) / (logg + 1);
   diff := sqrt(sqr(diffs));
   add := restart;
   for freq := -4 to 20 do
     begin
       if s[freq] = 0 then
         begin
           if reend > restart then
             begin
               add := add + diff;
               s[freq] := pow(add);
               writeln(f[freq] : 2 : 1, ' : ', s[freq] : 2 : 1);
             end
           else if reend < restart then
             begin
               add := add - diff;
               s[freq] := pow(add);
               writeln(f[freq] : 2 : 1, ' : ', s[freq] : 2 : 1);
             end
           else
         end
       else
     end;
  end;
end;

for freq := -4 to 20 do
  begin
    n_room;
    n_cavity;
    w := 2 * pi * f[freq];

    {radiation loss factors}
    rlf21 := s[freq] / (w * m2 * A2);
    rlf79 := s[freq] / (w * m7 * A7);
    rlf12 := rlf21 * (n2 / n1);
```

```
        rlf97 := rlf79 * (n7 / n9);
        rlf24 := s[freq] / (w * m2 * ((RibC / 2) * PHt2)); rlf42 := rlf24 * (n2 / n4);
        rlf74 := s[freq] / (w * m7 * ((RibC / 2) * PHt7)); rlf47 := rlf74 * (n7 / n4);
        rlf54 := s[freq] / (w * m5 * A5);
        rlf45 := rlf54 * (n5 / n4);
        ilfs;
        non_resonant;
        clfs;
        clfsa;
        s5imultsolve; {s4imultsolve or s6imultsolve}
        results;
        T[freq] := TL;
      end;                                                    {PROGRAM BODY}

{___Rating program__}
    begin
      write('Rating..... ');
      rating_curve;
      repeat
        begin
          devsum := 0;
          sum16 := 0;
          for freq := 4 to 19 do
            begin
              deviation[freq] := R[freq] - T[freq]; if deviation[freq] > 0 then
                begin
                  devsum := deviation[freq] + devsum;
                end
              else if deviation[freq] <= 0 then
            end;
          sum16 := devsum / 16;
          {writeln('Unfavourable Deviation = ', sum16 : 2 : 1);}
        end;
        for freq := 4 to 19 do
          begin
            R[freq] := R[freq] - 1;
          end;
      until sum16 <= 2;
      writeln;
      R[11] := R[11] + 1;
      writeln('Final Unfavourable Deviation = ', sum16 : 2 : 1); writeln('Dnt [', f[11] : 2 : 1, ' Hz] = ',
      R[11] : 2 : 1, ' dB');
    end; {rating calculation}

  end
else
  begin
  end;
writeln;
writeln('End of Program');
close(a);
end.
```

Figure A.7.1: 1:8 Scale perspex models of single, fin and diaphragm walls

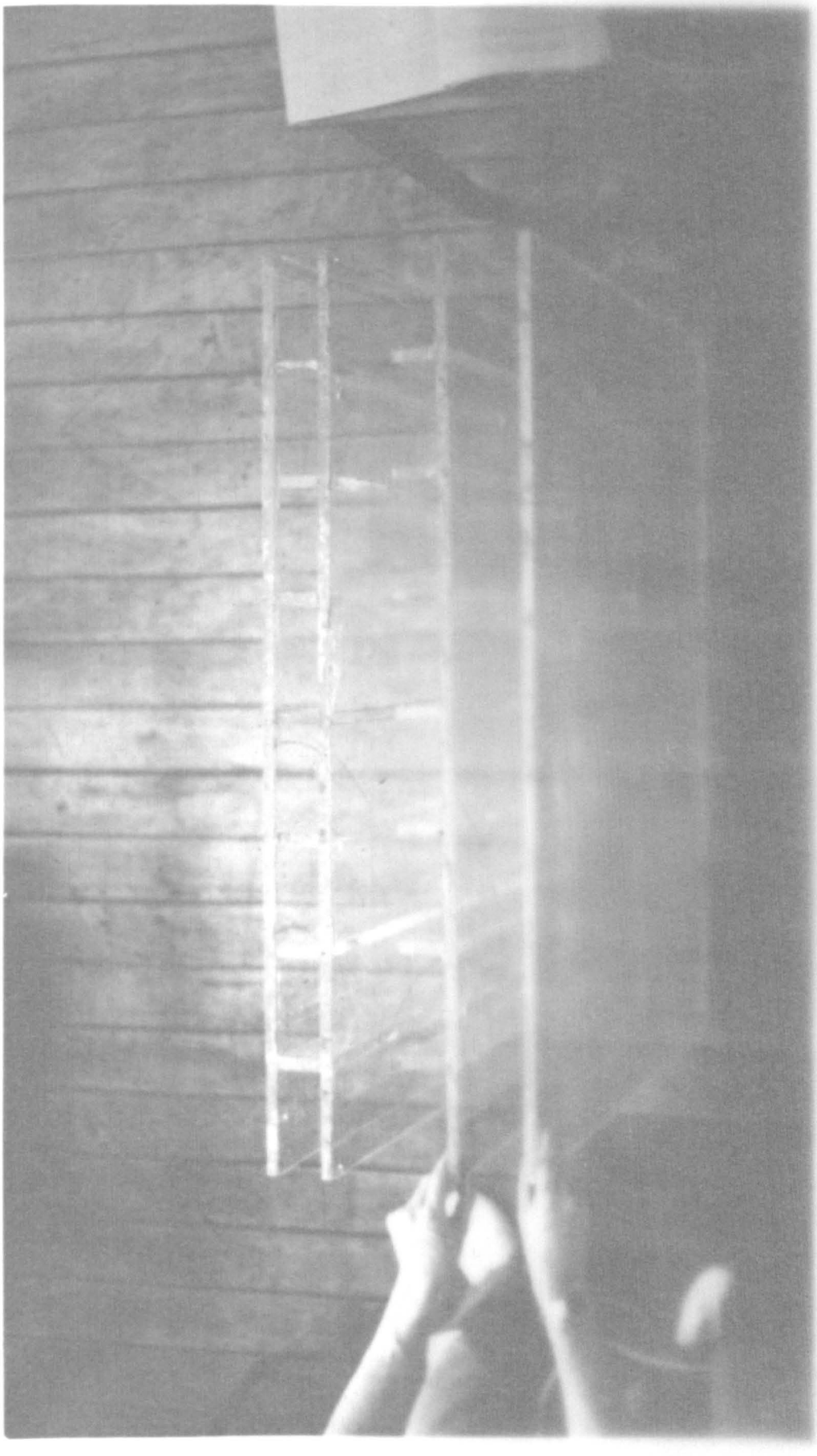

Figure A.7.1: 1:8 Scale perspex models of single, fin and diaphragm walls

Figure A.7.2: 1:4 scale diaphragm wall built into the large transmission suite

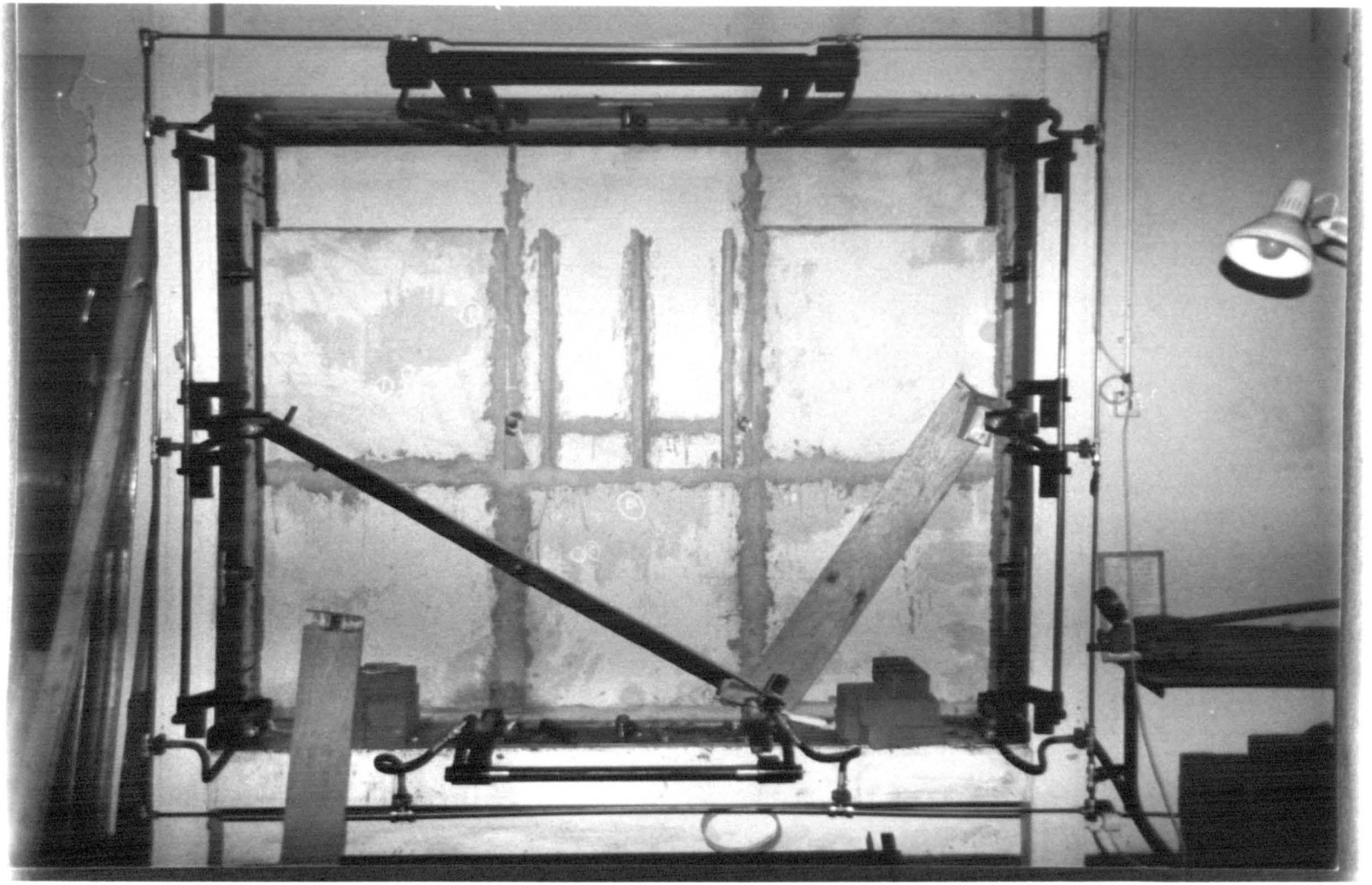

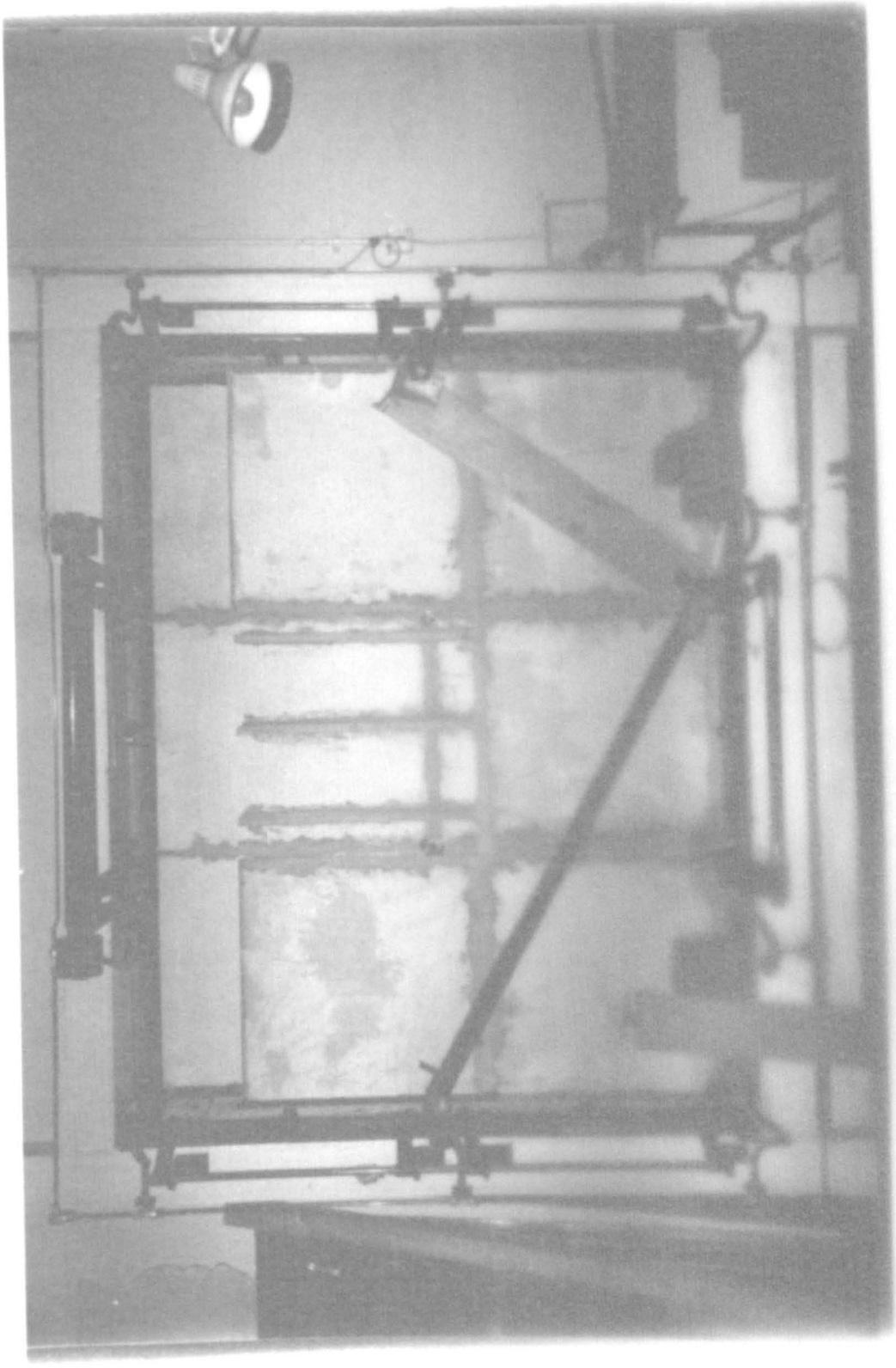

Figure A.7.2: 1:4 scale diaphragm wall built into the large transmission suite

Figure A.7.3: Transmission loss measurement of a perspex model by intensimetry

Figure A.7.3: Transmission loss measurement of a perspex model by intensimetry

Figure A.7.4: Transmission loss measurement by intensimetry of the single leaf masonry wall

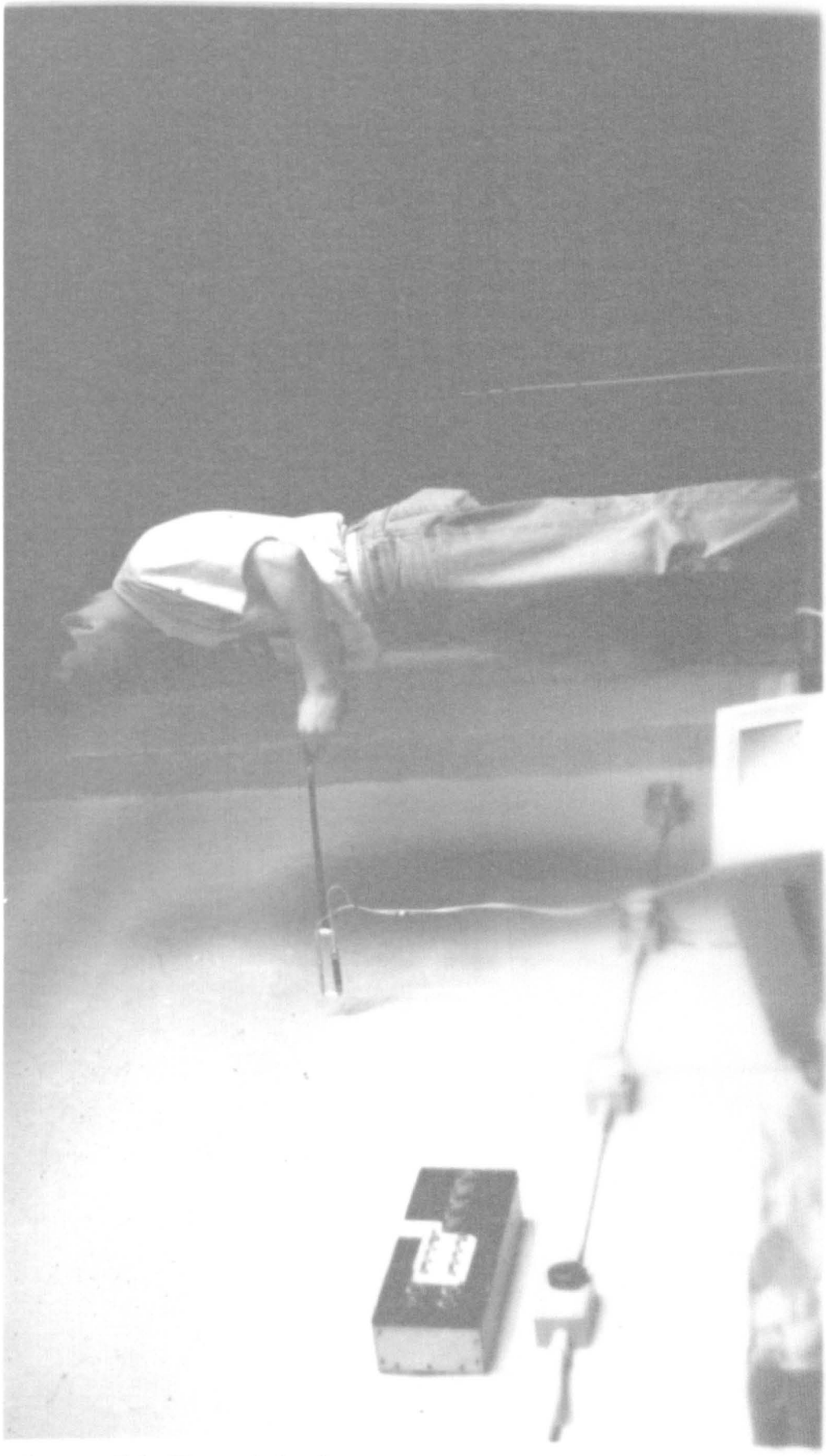

Figure A.7.4: Transmission loss measurement by intensimetry of the single leaf masonry wall

Figure A.7.5: Full scale diaphragm wall at St. Augustines R.C. High School

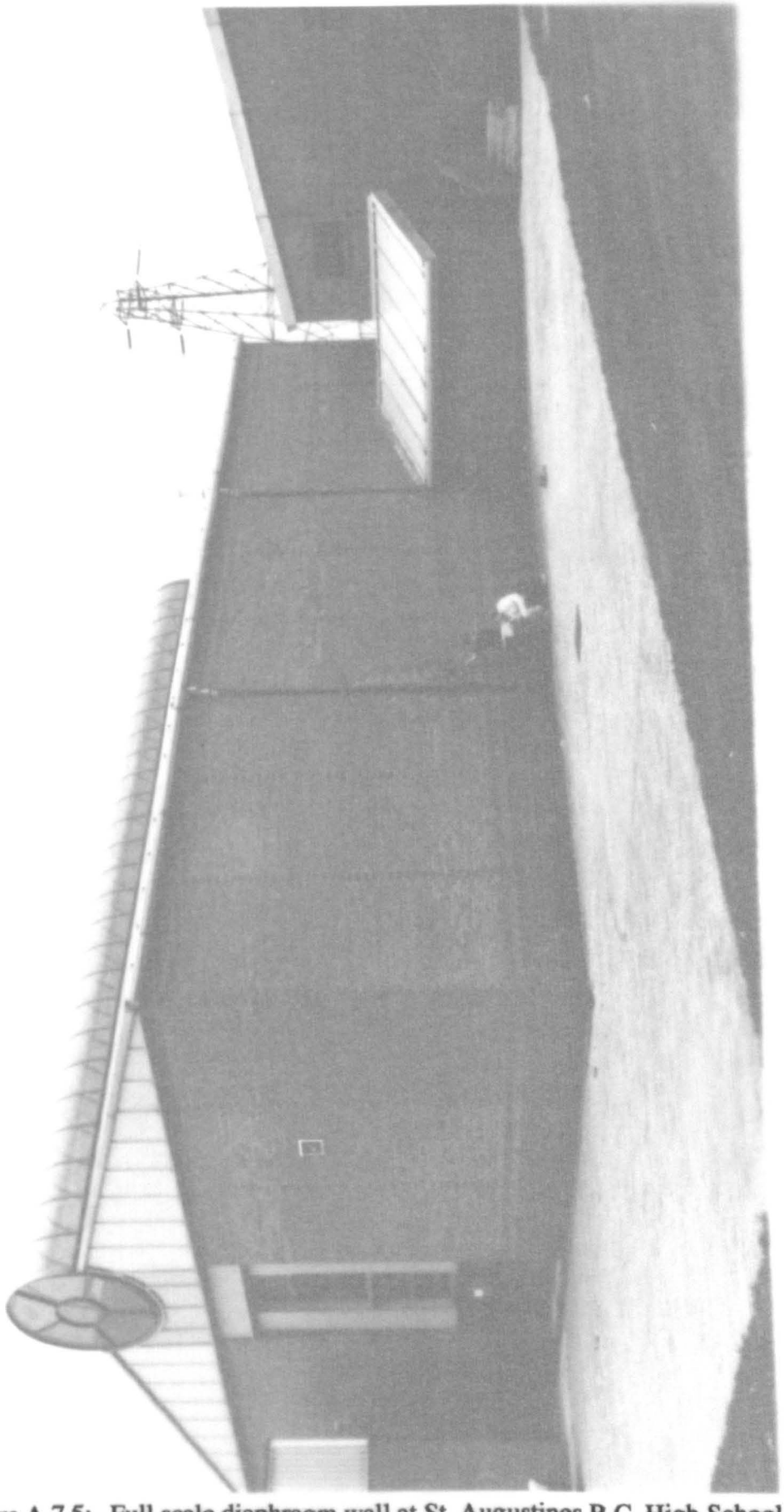

Figure A.7.5: Full scale diaphragm wall at St. Augustines R.C. High School

Figure A.7.6: **Measurement of sound pressure levels in the sports hall at AHS**


EXIT

Figure A.7.6: Measurement of sound pressure levels in the sports hall at AHS

Figure A.7.7: **Measurement of sound intensity through an in-situ diaphragm wall**

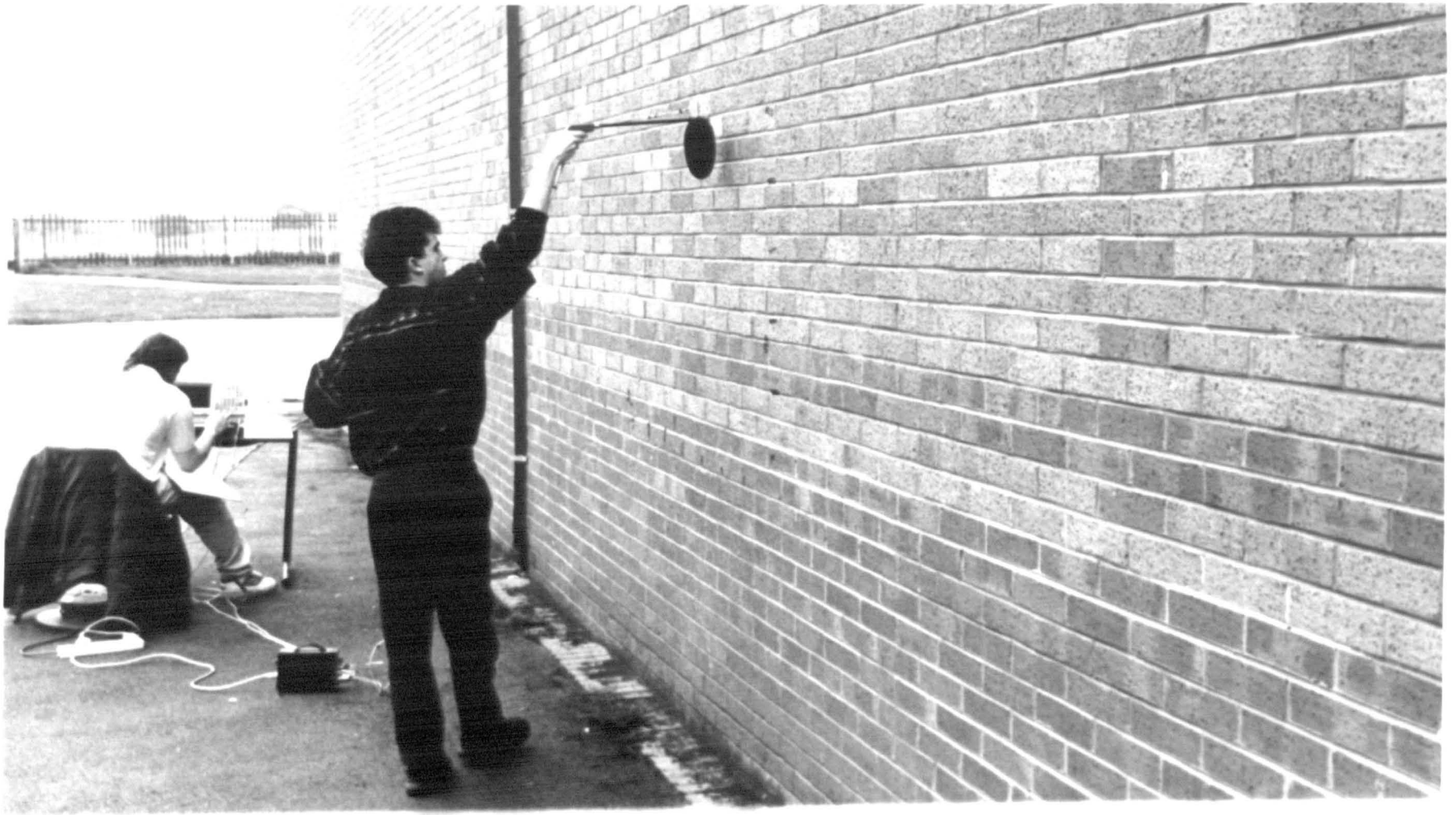

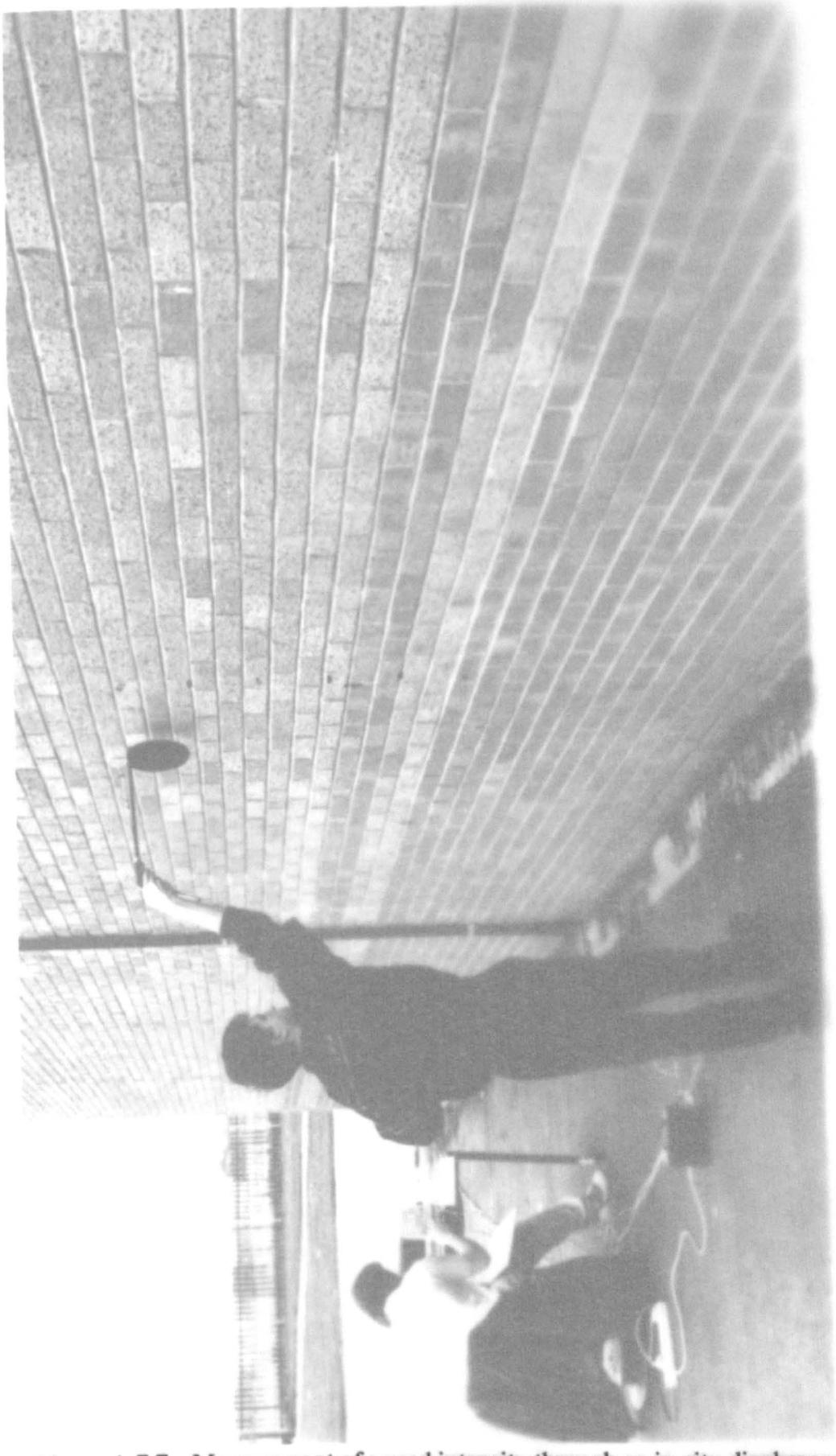

Figure A.7.7: Measurement of sound intensity through an in-situ diaphragm wall

Figure A.7.8: Free-standing, post-tensioned diaphragm and fin walls at CERAM research, Stoke-on-Trent

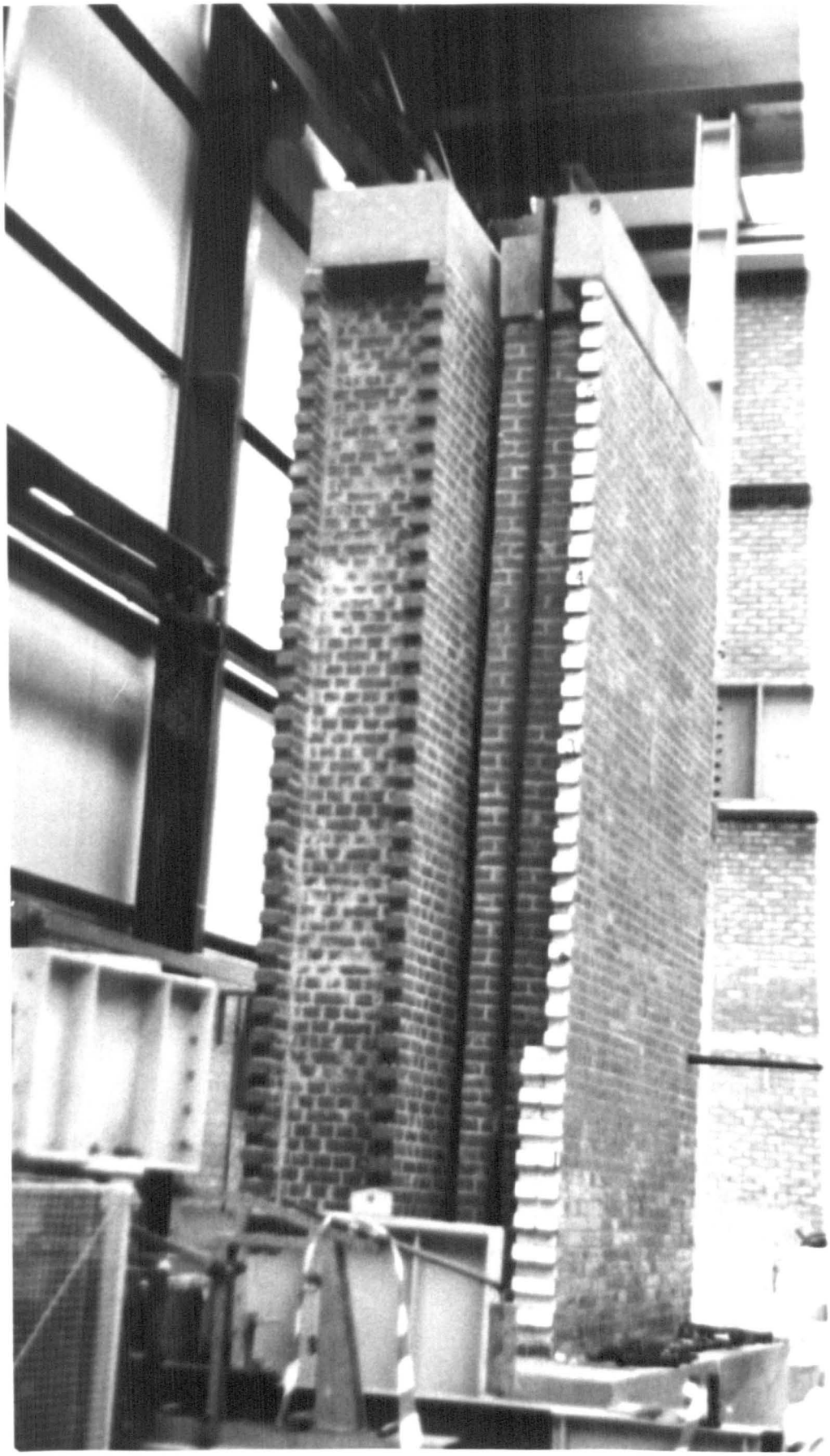

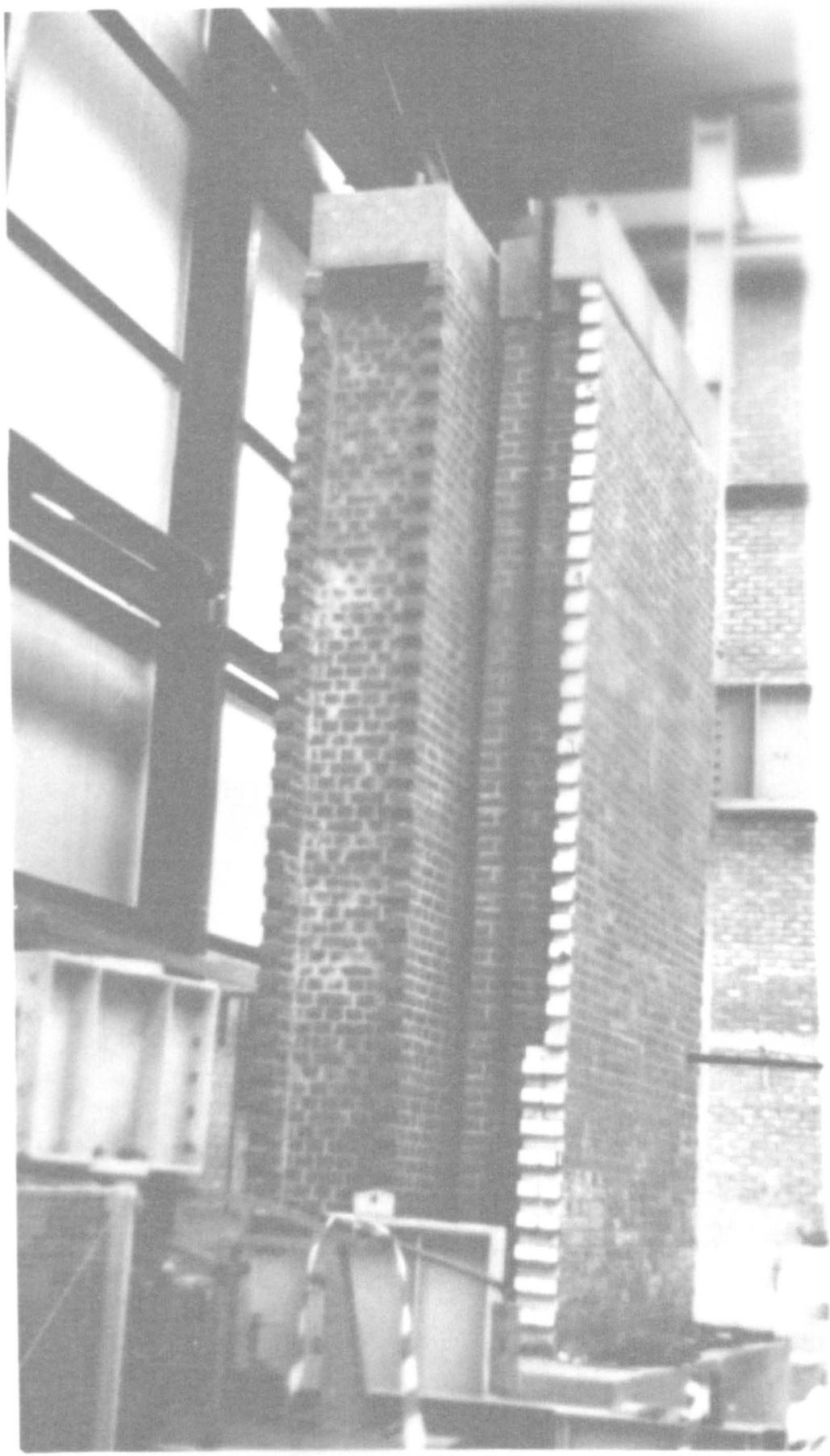

Figure A.7.8: Free-standing, post-tensioned diaphragm and fin walls at CERAM research, Stoke-on-Trent

BRITISH LIBRARY

IMAGING SERVICES NORTH

Boston Spa, Wetherby
West Yorkshire, LS23 7BQ
www.bl.uk

PAGE/PAGES EXCLUDED UNDER INSTRUCTION FROM THE UNIVERSITY

REFERENCES

Codes

A.C.B.A.	Aggregate Concrete Block Association
ANSI	American National Standards Institute
Appl. Acoust.	Applied Acoustics
ARU	Acoustics Research Unit
BS	British Standard
C.I.O.A.	Chinese Journal of Acoustics
DIS	Discussion (Draft standard)
IEC	International Electrotechnical Commission
ISO	International Standards Organisation
J. Acoust. Soc. Am.	Journal of the Acoustical Society of America
J. Eng. Ind.	Journal of Engineering for Industry
J. Inst. Quan. Surv.	Journal of the Institute of Quantity Surveyors
J. Sound Vib.	Journal of Sound and Vibration
Noise Cont. Eng.	Noise Control Engineering Journal
Proc. I.O.A.	Procedings of the Institute of Acoustics
Proc. Inst. Civil. Engrs.	Proceedings of the Institute of Civil Engineers
Struct. Eng.	Journal of Structural Engineering
S.N.T.R.I.	Swedish National Testing and Research Institute

1 BRICK DEVELOPMENT ASSOCIATION, 'Design of Brick Diaphragm Walls', March 1982

2 CURTIN W.G., 'Brick Diaphragm walls-development, application, design and future development', Struct. Eng. Vol. 58A, No. 2. Feb 1980

3 CURTIN W.G., 'Brick Diaphragm Walls: their application, structural design, procedures and problems., M. Eng. Thesis, University of Liverpool. (1978)

4 CURTIN W.G. & SAWKO F., 'Effective Thickness & Structural Efficiency of cellular walls and piers.', Proc. Inst. Civil. Engrs. Part 2, 1978

5 CURTIN W.G., 'Brick Diaphragm Walls, an alternative design for industrial buildings.'J. Inst. Quan. Surv. Vol. 34 (10) 1978

6 BRICK DEVELOPMENT ASSOCIATION, 'Design of Brick Fin Walls in tall Single-storey buildings',1980

7 HENDRY A.W., SINHA B.P. & DAVIES S.R., 'Load Bearing Brickwork Design', 2nd Ed. 1987 p15,Ellis Horwood Ltd. Publsh.

8 THE ARCHITECTURAL PRESS LTD., Specification 1987, 1. Technical. Building Methods & Products, (1987)

9 BRITISH STANDARDS INSTITUTE, 'Code of Practice for the structural use of masonry: Part 1, unreinforced masonry', London, 1978

10 BRITISH STANDARDS INSTITUTE, 'Structural recommendations for load-bearing walls', London, 1970

11 WILLIAMS, MORGAN, DURKA, 'Structural Mechanics'; Pitman Ed.Ltd.,

12 GERE & TIMOSHENKO, 'Mechanics of Materials', Wadsworth, Inc.

13 CURTIN W.G., SHAW G., BECK J.K., PARKINSON G.I., 'Structural Masonry Detailing', Granada Publishing 1984

14 CURTIN W.G., 'Discussion: Brick Diaphragm Walls - development, application, design and future development', The Structural Engineer. Vol. 59A, No.11. 1981

15 PHIPPS M.E. & MONTAGUE T.I., 'The Design of Concrete Blockwork Diaphragm Walls', A.C.B.A. CI/SfB (21.8) Ff, 1976

16 PHIPPS M.E. & MONTAGUE T.I., 'The Design of Prestressed Concrete Blockwork Diaphragm Walls', A.C.B.A. CI/SfB (21.9) Fg.2, 1976

17 GIBBS B.M. & LEWIS J., 'Sound Insulation of Brick Diaphragm Walls - I. Scale Model Measurement and Statistical Energy Analysis', Building and Environment, Vol. 26, No.2, pp 165-172, 1991

18 HUNG R., 'The Acoustic Insulation of Brick Diaphragm Walls', 1982 Dissertation

19 MA K. YEE-LAP, 'The Sound Transmission through a Model Diaphragm Wall', 1986 Dissertation

20 LLOYD J., 'Field Measurement of Airborne Sound Insulation offered by Brick Diaphragm Walls', 1987 Dissertations

21 WATTERS B.G., The Transmission Loss of Some Masonry Walls', J. Acoust. Soc. Am. Vol. 31, No. 7, pp 898-911 (1959)

22 KURTZE G. & WATTERS B.G., 'New Wall Design for High Transmission Loss or High Damping', J. Acoust. Soc. Am. Vol. 31 No. 6, pp 739-748 (1959)

23 PARKIN P.M., PURKIS M.J. & SCHOLES W.E., 'Field Measurement of Sound Insulation between Dwellings', Nat. Building Studies Research paper No. 33, H.M.S.O (1960)

24 ISO 717/1 Pt. 1 or BS 5821 Part 1 (1982) Method of rating the sound insulation in buildings and of interior building elements

25 LAWRENCE A., 'Acoustics and the Built Environment', Elsevier Applied Science

26 IEC Publication 225

27 RAYLEIGH L., 'The Theory of Sound Vol. 1 & 2', Macmillian Company {original publishers}, Dover Publications, Section 271 (1945)

28 LONDON A.J., 'Transmission of Reverberant Sound through Single Walls', Res. Nat. Bureau of Standards, Res. Paper RP 1998, Vol.42, June (1949)

29 SCHOCH A. & FEHER K., 'The Mechanism of Sound Transmission through Single Leaf Partitions', Acustica, Vol. 2, p289 (1952)

30 CREMER L., 'Calculation of Sound Propagation in Structures', Acustica Vol. 3, No. 5, p317-335, (1953)

31 BERANEK L.L. & WORK G.A., 'Sound Transmission through Multiple Structures', J. Acoust. Soc. Am., Vol. 21, p419, (1949)

32 SCHILLER K.K., 'Physical Aspects of Sound Insulation through Walls', J. Sound Vib. 6(3), pp283-295, (1967)

33 MULHOLLAND K.A., PRICE A.J. & PARBROOK H.D., 'Transmission Loss of Multiple Panels in a Random Incidence Field', J. Acoust. Soc. Am. 43(6), pp1432-1435, (1968)

34 SABINE P.E., 'Weight as a Determining factor in Sound Transmission', J. Acoust. Soc. Am., pp38-43, July (1932)

35 CREMER L., Akust. Z., Vol 7., p81 (1942)

36 BIES D.A. & HANSON C.H., 'Engineering Noise Control; Theory & Practice', Unwin Hyman Ltd (1988)

37 FAHY. F, 'Sound and Structural Vibration; radiation,transmission and response.' Academic Press (1985)

38 BERANEK L.L., 'Noise Reduction', McGraw-Hill (1960)

39 CREMER L.,HECKL M. AND UNGAR E.E.,'Structure-borne Sound', Springer-Verlag, Berlin (1973)

40 KOSTEN, C.W., 'Symposium on the Sound Insulation of Lightweight Structures', Acustica Vol. 4 pp263-273 (1954)

41 SHARP B.H., 'Prediction methods for the Sound Transmission of Building Elements', N. C. E. Vol. 11, No. 2, pp53-63 (1978)

42 LJUNGGREN S., 'Airborne Sound insulation of Thick Walls', J. Acoust. Soc. Am. 89(5), pp2338-2345 (1991)

43 WATTERS B.G. , 'Transmission Loss of some Masonry Walls', J. Acoust. Soc. Am. Vol. 31 No.7, pp898-911 (1959)

44 LONDON A. J.'Transmission of Reverberant Sound through Double Walls', Res. Nat. Bureau of Standards, Res. Paper RP 1998, Vol.44, pp77-88 Jan. (1950)
or
J. Acoust. Soc. Am. Vol 22. No. 2, pp270-279 (1950)

45 BERANEK. L.L. & WORK G.A., 'Sound transmission through multiple structures containing flexibility blankets,'J. Acoust. Soc. Am. Vol. 21, pp419-428 (1949)

46 CUMMINGS A. & MULHOLLAND K.A., 'The Transmission Loss of Finite Double Panels in a Random Incidence Sound Field,' J. Sound Vib. Vol. 8 (1) pp126-133 (1968)

47 MULHOLLAND K.A., PARBROOK H.D. & CUMMINGS A., 'The Transmission Loss of Double Walls', J. Sound Vib. Vol. 6 (3), pp324-334 (1967)

48 MULHOLLAND K.A., PRICE A.J. & PARBROOK H.D., 'Transmission Loss of Multiple Panels in a Random Incidence Field', J. Acoust. Soc. Am. Vol. 43 (6), pp1432-1435 (1968)

49 CUMMINGS A., ' The Mechanism of Sound Transmission through Single & Double Panels,' P.h.D Thesis, University of Liverpool (1968)

50 BRANDT O., 'Some Measurements of Lightweight Double Walls', Acustica Vol. 4, pp270-273 (1954)

51 NOVAK R.A. 'Sound Insulation of Light-weight Double Walls', Internal Docu. Dept .of Building Technology, the Royal Inst. of Tech., Stockholm, Sweden (1992)

52 WILSON R., 'Sound Transmission through Double walls', Ph.D Thesis, Heriot-Watt University (1992)

53 WHITE P.H. & POWELL A., 'Transmission of Random Sound and Vibration through a Rectangular Double Wall', J. Acoust. Soc. Am. Vol. 40, No.4 pp821-832 (1966)

54 SEWELL E.C., 'Two-dimensional Solution for Transmission of Reverberant Sound through a Double Wall', J. Sound Vib. Vol 12, pp33-57 (1970)

55 DONATO R.J., 'Sound Transmission through a Double Leaf', J. Acoust. Soc. Am. Vol. 51, pp807-815 (1972)

56 MULHOLLAND K.A., 'Sound Insulation Measurements on a series of Double Plasterboard Panels with Various Infills', Appl. Acoust. 4., pp1-12 (1971)

57 GU Q. & WANG J., 'Effect of Resilient Connection on Sound Transmission Loss of Metal Stud Double Panel Partitions', C.J.O.A. Vol. 2 No. 2, pp113-126 (1983)

58 LEE SIEW-EANG, 'The Transmission of Sound through Stud Partitions', Acoustics 84. Univ. of Swansea pp343-347 (1984)

59 LIN GAN-FENG & GARRELICK J.M., 'Sound Transmission through periodically framed parallel plates', J. Acoust. Soc. Am. Vol. 61. No. 4 pp1014-1018 (1977)

60 INGEMANSSON & KIHLMAN, 'Sound Insulation of Frame Walls', Trans. Chalmers Univ. Technol., Gothenburg. No. 222 (1959)

61 PIERCE G.W., 'Transmission and Reception of Sound Waves', U.S. patent No. 2,063,945 (1933)

62 SANDERS F.H., Canadian Journal of Research Vol. 1 (1939)

63 VON VENZKE G., DAMMING P & FISCHER H.W., Acustica 29(1) pp29-40 (1973)

64 VINOKUR R. YU, 'The influence of Linear Sound Bridges Linking panel Edges on the Airborne Sound Insulation of Double Partitions', Appl. Acoust. 34, pp19-35 (1991)

65 RINDEL J.H., 'Prediction of Sound Transmission through Thick and Stiff Panels', Proc. I.O.A. Vol. 10 Part 8, pp119-126 (1988)

66 CRAIK R.J.M., 'Scale Models for Determining the Performance of Buildings', Inter-Noise 83 pp1199-1201 (1983)

67 ISO 140/3 (1978) or BS 2750: Part 3 (1980) Methods of measurement of sound insulation in buildings and of building elements, 'Laboratory measurements of airborne sound insulation of building elements.'

68 ISO 140/1 (1978) or BS 2750: Part 1 (1980) Methods of measurement of sound insulation in buildings and of building elements, 'Recommendations for laboratories.'

69 HAMMAD R.N.S., 'The Acoustic Performance of Building Facades in Hot Climates', Ph.D Thesis Liverpool University (1982)

70 HARWOOD H.D. & BURD A.N., 'Acoustic Scaling of Studios and Concert Halls', Acustica Vol. 28 pp330-340 (1973)

71 DELANY M.E., RENNIE A.J. & COLLINS K.M., 'A Scale Model Technique for Investigating Traffic Noise Propogation', J. Sound Vib. 56 (3) pp325-340 (1978)

72 FUJIWARA K, ANDO Y. & MAEKAWA Z., 'Noise Control by Barriers - Part 1: Noise Reduction by a Thick Barrier', Appl. Acoust. Vol. 10 pp147-159

73 FUJIWARA K, ANDO Y. & MAEKAWA Z., 'Noise Control by Barriers - Part 2: Noise Reduction by an Absorptive Barrier', Appl. Acoust. Vol. 10 pp167-179

74 FOTHERGILL L.C., 'New European standards for measuring and rating sound insulation', proc. I.O.A. Vol. 13 Part 8 pp93-98 (1991)

75 SCHROEDER M.R. 'Effect of frequency response averaging on the transmission response of multi-modal media', J. Acoust. Soc. Am. 46(2) (1969)

76 SCHROEDER M.R. 'Frequency Autocorrelation Functions of Frequency Response in Rooms', J. Acoust. Soc. Am. 34 pp1819-1823 (1962)

77 CROCKER M. J & KESSLER F. M., 'Noise and Noise Control, Vol. 1, pp189, CRC Press (1975)

78 MEYER E. & KUTTRUFF H., Gottinger Nachr. Phys. Kl, No. 6 (1958)

79 CREMER L, MULLER H.A. & SCHULTZ T.J., Principles and Applications of Room Acoustics, Volume 1, Applied Science (1978)

80 LUBMAN D., 'Precision of Reverberant Sound Power Measurements', J. Acoust. Soc. Am. 56(2) pp523-533 (1974)

81 HALLIWELL R.E. & WARNOCK A.C.C., 'Sound Transmission Loss: Comparison of Conventional Techniques with Sound Intensity Techniques', J. Acoust. Soc. Am. 77(6), pp2094-2103 (1985)

82 CRAIK R.J.M., 'The Effect of Laboratory Design on Measured Wall Performance', Proc. I.O.A. Vol.13 Part 8, pp99-105 (1991)

83 ISO 140/2 (1978) or BS 2750 : Part 2 (1980) Methods of measurement of sound insulation in buildings and of building elements, 'Statement of Precision Requirements.'

84 ISO 3741 (1988) or BS 4196 : Part 1 (1991) 'Sound Power levels of Noise Sources', Part 1. Precision methods for determination of sound power levels for broad-band sources in reverberation rooms.

85 FAHY F.J., 'Sound Intensity,' Acoustics Bulletin, pp15-18, July (1986)

86 FAHY F.J., 'Sound Intensity', Elsevier Applied Science (1989)

87 OLSEN H.F., 'Fieldtype acoustic wattmeter, J. Audio Engng, Soc., 22 pp321-8 (1974)

88 CLAPP C.W. & FIRESTONE F.A., 'The Acoustic Wattmeter, an Instrument for Measuring Sound Energy Flow', J. Acoust. Soc. Am. Vol. 13, pp124-136 (1941)

89 SCHULTZ T.J., 'Acoustic Wattmeter', J. Acoust. Soc. Am. Vol. 28 No. 4, pp693-699 (1956)

90 ISO 9614-1 (1991) 'Determination of Sound Power Levels of Noise Sources using Sound Intensity Measurements - Part 1: Method of Measurement at Discrete Points'

91 ISO/DIS 9614-2 (1992) 'Determination of Sound Power Levels of Noise Sources using Sound Intensity Measurements - Part 2: Method of Measurement by Scanning'

92 ANSI S12.12-199X (1991) 'Engineering Method for the Determination of Sound Power Levels of Noise Sources using Sound Intensity.'

93 IEC 1043 Draft Standard (1991) 'Instruments for the Measurement of Sound Intensity - Instruments which measure intensity with pairs of pressure sensing microphones.'

94 COPS A. & MINTEN M., 'Comparitive study between the sound intensity method and the conventional two-room method to calculate the sound transmission loss of wall constructions.'

95 CHUNG J.Y., Cross-spectral method of measuring acoustic intensity without error caused by instrument phase mismatch', J. Acoust. Soc. Am. 64 (6) pp1613-1616 (1978)

96 VAN ZYL B.G. & ERASMUS P.J. & ANDERSON F., 'On the Formulation of the Intensity Method for Determining Sound Reduction Indices', Appl. Acoust. 22, pp213-228 (1987)

97 VAN ZYL B.G. & ERASMUS P.J. & VAN DER MERWE G.J.J., 'Determination of Sound Reduction Indices in the Presence of Flanking Transmission', Appl. Acoust. 19, pp25-39 (1986)

98 HALLIWELL R.E. & WARNOCK A.C.C., 'Sound Transmission Loss: Comparison of Conventional Techniques with Sound Intensity Techniques', J.A.S.A 77(6), pp2094-2103 (1985)

99 CROCKER M.J., RAJU P.K. & FORSSEN B., 'Measurement of Transmission Loss of Panels by the Direct Determination of Transmitted Acoustic Intensity', Noise Cont. Eng., pp6-11 (July-Aug 1981)

100 COPS A., MINTEN M. & MYNCKE H., 'Influence of the Design of Transmission Rooms on the Sound Transmission Loss of Glass - Intensity Versus Conventional Method', Noise Cont. Eng. Vol. 28 No. 5, pp121-129 (May-June 1987)

101 GUY R.W. & DE MEY A., 'Measurement of Sound Transmission Loss by Sound Intensity', A Preliminary Report.

102 GUY R.W & LI. J., 'Proposed ANSI S12.12: Engineering Method for the Determination of the Sound Power Levels of Noise Sources using Sound Intensity - towards limiting the Indicators ', (report 1992)

103 JACOBSEN F., 'Sound Field Indicators: Useful Tools', Noise Cont. Eng. pp37-46 (July-August 1990)

104 JONASSON H.G., 'Measurement of Sound Reduction index with Intensity Technique, Nordtest Project 746-88', SP Report 1991: 23 S.N.T.R.I. (1991)

105 'S.N.T.R.I., Measurement with Sound Intensity Technique', Nordtest, Annex E (informative) to ISO/140-3 (1992)

106 ISO 140/5 or B.S. 2750 Part 5 (1980) Methods of Measurement of Sound Insulation in Buildings and of Building Elements 'Field Measurements of Airborne Sound Insulation of Facade Elements and Facades'

107 RASMUSSEN, 'Phase Errors in Intensity Measurements', Intensity Measurements, B & K collection of papers, pp11-18 (1984)

108 GUY R.W. & LI J., 'Intensity Measurements in the Presence of Standing Waves', report (1992)

109 KRISHNAPPA G. & CHIU V.J. , 'Sound power determination using sound intensity scanning technique', pp1179-1182 Inter-noise 92, Toronto, Canada (1992)

110 LAI J.C.S. & BURGESS M., 'Application of the Sound Intensity Technique to Measurement of Field Sound Transmission Loss', Applied Acoust. 34, pp77-87 (1991)

111 FAHY F.J. private communication

112 'Sound Intensity ' Bruel & Kjaer information booklet

113 GIBBS B.M., 'The direct and indirect transmission of vibrational energy in building structures,' Thesis Ph.D. University of Aston (1974)

114 LEE S-E, 'The Transmission of Sound through Stud Partitions,' Proc. I.O.A. pp343-347 (1992?)

115 MAIDANIK G., 'Response of Ribbed Panels to Reverberant Acoustic Fields', J. Acoust. Soc. Am. Vol. 34. No.6, pp809-826 (1962)

116 KIHLMAN T., 'Fifty Years of "Development" in Sound Insulation Of Dwellings', Inter-Noise 91, pp 3-15 (1991)

117 BERANEK L.L., 'Noise and Vibration Control', McGraw-Hill , 1988 Revised Edition (1971)

118 PRICE A.J. & CROCKER M.J., 'The Theory and Measurement of the Radiation from Panels' Dept. of Building Science report BS/A/68-2 . A.R.C. 30 922 N.624 (1968)

119 LYON R.H., 'Statistical Energy Analysis of Dynamic Systems: Theory and Applications.', MIT Press (1975)

120 CROCKER M.J. & PRICE A.J., 'Sound Transmission using Statistical Energy Analysis', J. Sound Vib. No. 9, pp469-486 (1969)

121 CRAIK R.J.M., 'Course Notes - Msc/Diploma in Acoustics, Vibration & Noise Control: Distance Learning, Sound Insulation.' (1990)

122 NORTON M.P., 'Fundamentals of Noise and Vibration Analysis for Engineers', Cambridge Univ. Press (1989)

123 KIHLMAN T., 'Transmission of structure-borne sound in buildings. A theoretical and experimental investigation', Nat. Swedish Inst. for Build. Res., Report 9 UDC 699.844 (1967)

124 CRAIK R.J.M., 'A study of Sound Transmission through Buildings using Statistical Energy Analysis', Ph.D Thesis, Heriot-Watt Univ. (1980)

125 LYON R.H. & SCHARTON T.D., 'Vibrational-Energy Transmission in a Three-Element Structure', J.A.S.A, 38, pp253-261(1965)

126 BHATTACHARYA M.C., MULHOLLAND K.A. & CROCKER M.J., 'Propagation of Sound Energy by Vibration Transmission via Structural Junctions', J. Sound Vib. Vol. 18 (2), pp221-234 (1971)

127 CROCKER M.J., BHATTACHARYA M.C. & PRICE A.J., 'Sound and Vibration Transmission through Panels and Tie Beams using Statistical Energy Analysis', J. Eng. Ind., pp775-782 Aug. (1971)

128 CRAVEN P.G. & GIBBS B.M., 'Sound Transmission and Mode Coupling at Junctions of thin plates, Part 1: Representation of the Problem,' J. Sound Vib. Vol. 77 (3), pp417-427 (1981)

129 GIBBS B.M. & CRAVEN P.G., 'Sound Transmission and Mode Coupling at Junctions of thin plates, Part 2: Parametric Survey', J. Sound Vib. Vol. 77 (3), pp429-435 (1981)

130 WOHLE W., BECKMANN T.H. & SCHRECKENBACH H., 'Coupling Loss Factors for Statistical Energy Analysis of Sound Transmission a Rectangular Structural Slab Joints, Part 1', J. Sound Vib. Vol. 77 (3) pp323-334 (1981)

131 WOHLE W., BECKMANN TH. & SCHRECKENBACH H., 'Coupling Loss Factors for Statistical Energy Analysis of Sound Transmission at Rectangular Structural Slab Joints, Part 1', J. Sound Vib. Vol. 77 (3) pp335-344 (1981)

132 CRAIK R.J.M., 'Damping of Building Structures', Appl. Acoust. Vol. 14 pp347-359 (1981)

133 CRAIK R.J.M. & THANCANAMOOTOO A., 'The Importance of In-plane Waves in Sound Transmission through Buildings', Appl. Acoust. Vol. 37 pp85-109 (1992)

134 WOODHOUSE J., 'An Introduction to Statistical Energy Analysis of Structural Vibration', Appl. Acoust. 14 pp455-469 (1981)

135 SMITH P.W. Jr., 'Response and Radiation of Structural Modes excited by Sound', J. Acoust. Soc. Am., Vol. 34, No. 5 pp640-647 (1962)

136 EICHLER E., 'Thermal Circuit Approach to Vibrations in Coupled Systems and the Noise Reduction of a Rectangular Box', J. Acoust. Soc. Am. Vol. 37 (6) pp995-1007 (1965)

137 PRICE A.J. & CROCKER M.J., 'Sound Transmission through Double Walls using Statistical Energy Analysis', J. Sound Vib. Vol. 47 (3 pt.1) pp683-693 (1970)

138 CROCKER M.J., 'The Response of Structures to Acoustic Excitation and the Transmission of Sound and Vibration', Ph.D. Thesis. Univ. of Liverpool. (Aug. 1969)

139 BREKKE A., 'Calculation Methods for the Transmission Loss of Single, Double and Triple Partitions', Appl. Acoust. Vol. 14 pp225-240 (1981)

140 KIHLMAN T., 'Transmission of structure-borne sound in buildings. A theoretical and experimental investigation', Nat. Swedish Inst. for Building Res. Report 9, UDC 699.844 (1967)

141 BERANEK L.L., 'Interaction of Sound Waves with Solid Structures', Ver I.L. & Holmer C.I. Ch. 11, Noise & Vibration Control, McGraw-Hill (1971)

142 DAH-YOU MAA., 'Distribution of eigentones in a rectangular chamber at low frequency ranges', J.A.S.A (10) p235-238 (1939)

143 CRAIK R.J.M., 'The Noise Reduction of the Acoustic Paths between Two Rooms interconnected by a Ventilation Duct', Appl. Acoust. 12, pp161-179 (1979).

144 CRAIK R.J.M., 'Statistical Energy Analysis at Low Frequencies applied to Sound Transmission through Buildings', Cambridge, U.S.A. Inter-Noise 86, pp1287-1290, July 21-23 (1986)

145 EVANS D.I. & CRAIK R.J.M., 'Using Statistical Energy Analysis for Structure-borne Sound Transmission at Low Frequencies', Proc. I.O.A. Vol. 8 Pt. 3, pp471-474 (1986)

146 CRAIK R.J.M., J.A. STEEL & EVANS D.I., 'Statistical Energy Analysis of Structure-borne Sound Transmission at Low Frequencies', J.S.V 144(1), pp95-107 (1991)

147 ELMALLAWANY A., 'Improvement of the Method of Statistical Energy Analysis for the Calculation of Sound Insulation at Low Frequencies', Ap. Ac. 15 pp341-345 (1982)

148 WALLACE C.E., 'Radiation Resistance of a Rectangular Panel', J. Acoust. Soc. Am. Vol. 51 No.3 (Pt. 2) pp946-952 (1972)

149 EMMANUEL T., 'Measurement of the Sound Insulation of Facades and Facade Elements - A Comparison of the Intensity Technique with the Traditional Method.' Proc. I.O.A. Vol 15. Pt. 8 pp231-238 (1993)

150 SPERLING H. & CHRISTENSEN K.,' Measurements of Airborne Sound Insulation of Large Facades by means of Sound Intensity', Inter-Noise 92, July 29-22, Toronto, Canada pp963-966 (1992)

151 CRAIK R.J.M., 'The Measurement of Structure-borne Sound Transmission using Impulsive Sources', Appl. Acoust. Vol. 15 pp355-361 (1982)

152 CRAIK R.J.M. & EVANS D.I., 'Workmanship and its effect on Sound Insulation', Proc. I.O.A. Vol. 8 Pt. 3, pp463-466 (1986)

153 CRAIK R.J.M., 'The Measurement of the Material Properties of Building Structures', Ap. Ac. Vol. 15 pp 275-282 (1982)

154 ISO 717/3 or B.S. 5821 Part 3 (1980) Rating the sound insulation in buildings and of building elements 'Method for rating the airborne sound insulation of facade elements and facades'

155 Private communication with R. Grew, lecturer in structural design, University of Liverpool.

156 DAVIES H., LESTER M.R. & MORGAN J.R., 'Selective Conditioning for the Measurement of Sound Transmission Loss.' J. Sound Vib., 145(1) pp83-93 (1991)

157 MULHOLLAND K.A. & GILLIAM, MPBW Databank Project, Acoustics Research Unit, Liverppol University (1971)